Proceedings of the High Energy Density Matter (HEDM) Contractors' Conference Held 1-3 June 1997 in Chantilly, VA

Patrick G. Carrick, Editor
Capt. Neal T. Williams, Editor

March 1998

Special Report

19980804 078

AIR FORCE RESEARCH LABORATORY
AIR FORCE MATERIEL COMMAND
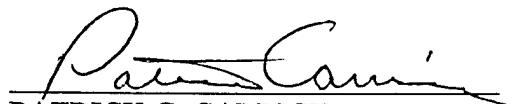**EDWARDS AIR FORCE BASE CA 93524-7048**

DTIC QUALITY INSPECTED 1

NOTICE

When U.S. Government drawings, specifications, or other data are used for any purpose other than a definitely related Government procurement operation, the fact that the Government may have formulated, furnished, or in any way supplied the said drawings, specifications, or other data, is not to be regarded by implication or otherwise, or in any way licensing the holder or any other person or corporation, or conveying any rights or permission to manufacture, use or sell any patented invention that may be related thereto.
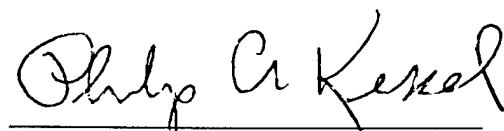
FOREWORD

This Conference Proceedings was compiled and edited by Dr. Patrick G. Carrick and Capt. Neal Williams, United States Air Force Research Laboratory, Propulsion Directorate, Edwards Site (formerly OL-AC Phillips Laboratory), Edwards AFB, CA.

This report has been reviewed and is approved for release and distribution in accordance with the distribution statement on the cover and on the SF Form 298.

PATRICK G. CARRICK
Project Manager

RANNEY G. ADAMS III
Public Affairs Director

PHILIP A. KESSEL
Technical Advisor
Propulsion Sciences and
Advanced Concepts Division

REPORT DOCUMENTATION PAGE

Public reporting burden for this collection of information is estimated to average 1 hour per response, including the time for reviewing instructions searching existing data sources gathering and maintaining the data needed, and completing and reviewing the collection of information. Send comments regarding this burden estimate or any other aspect of this collection of information, including suggestions for reducing this burden to Washington Headquarters Services, Directorate for Information Operations and Reports, 1215 Jefferson Davis Highway, Suite 1204, Arlington, VA 22202-4302, and to the Office of Management and Budget, Paperwork Reduction Project (0740-0188), Washington DC 20503,

1. AGENCY USE ONLY (LEAVE BLANK)	2. REPORT DATE March 1998	3. REPORT TYPE AND DATES COVERED Special Report 1 Jun 97 – 3 Jun 97

4. TITLE AND SUBTITLE

Proceedings of the High Energy Density Matter (HEDM) Contractors' Conference Held 1-3 June 1997 in Chantilly, VA

6. AUTHOR(S)

Patrick G. Carrick, Editor
Capt. Neal T. Williams, Editor

5. FUNDING NUMBERS

C:

PE: 62601F

PR: 1011

TA: 0046

7. PERFORMING ORGANIZATION NAME(S) AND ADDRESS(ES)

Air Force Research Laboratory (AFMC)
AFRL/PRS
10 E. Saturn Blvd.
Edwards AFB CA 93524-7680

8. PERFORMING ORGANIZATION REPORT NUMBER

PL-TR-97-3057

9. SPONSORING/MONITORING AGENCY NAME(S) AND ADDRESS(ES)

10. SPONSORING/MONITORING AGENCY REPORT NUMBER

11. SUPPLEMENTARY NOTES: Extended abstracts from the Eleventh High Energy Density Matter Contractors' Conference

COSATI CODE(S):

12a. DISTRIBUTION/AVAILABILITY STATEMENT	12b. DISTRIBUTION CODE
APPROVED FOR PUBLIC RELEASE DISTRIBUTION IS UNLIMITED	A

13. ABSTRACT (MAXIMUM 200 WORDS)

This report documents the information presented at the eleventh annual High Energy Density Matter (HEDM) Contractors' Conference held 1-3 June 1997 in Chantilly, VA. This report contains the extended abstracts of the oral, workshop, and poster presentations given by the Air Force funded contractors and by the in-house researchers from the Air Force Research Laboratory, Propulsion Directorate, Edwards Site (formerly Operating Location-AC Phillips Laboratory), Edwards AFB, CA.

14. SUBJECT TERMS

HEDM; high energy density matter; propellant; solid hydrogen; cryogenic materials; potential energy surfaces

15. NUMBER OF PAGES 254

16. PRICE CODE

17. SECURITY CLASSIFICATION OF REPORT	18. SECURITY CLASSIFICATION OF THIS PAGE	19. SECURITY CLASSIFICATION OF ABSTRACT	20. LIMITATION OF ABSTRACT
Unclassified	Unclassified	Unclassified	SAR

TABLE OF CONTENTS

TABLE OF CONTENTS, Cont'd

TABLE OF CONTENTS, Cont'd

Introduction

The main purpose of the High Energy Density Matter (HEDM) program is to research and develop advanced propellants containing increased energy densities (energy to mass ratio) to produce greater specific impulse (thrust per weight flow rate of propellant) which will enable significantly increased payloads for rockets and missiles. With these advanced propellants, future space-bound payloads could be potentially four times greater than those of current systems for the same overall size and weight. Theoretical and experimental research is carried out by in-house researchers at the Phillips Laboratory, Propulsion Directorate, at Edwards Air Force Base and through Air Force funded contracts with numerous researchers in academic and industrial laboratories.

The HEDM program is administered by a steering group made up of representatives from the Phillips Laboratory Propulsion Directorate (after 1 Oct 97 known as the Propulsion Directorate, Air Force Research Laboratory) and the Air Force Office of Scientific Research (AFOSR). A technical panel administered by Universal Energies Systems assisted the steering group in ensuring the high technical content of the program.

Annual conferences, hosted by the AFOSR and the Phillips Laboratory, are arranged in order to allow in-house and contract researchers to report on their progress and new developments. The 11th High Energy Density Matter Contractor's Conference was held 1-3 June 1997 at the Westfields International Conference Center, Chantilly, VA. The conference commenced with registration on Sunday followed by an introduction and then technical talks related to synthesis of new propellant ingredients. Sunday night ended with a reception and a HEDM poster session. Monday continued with technical sessions on theoretical investigations of HEDM and concluded with a theory/synthesis workshop in the evening. Tuesday was a continuation of technical talks on cryogenic solids and computational chemistry of HEDM molecules.

This report documents the information presented at this conference and contains extended abstracts of the oral presentations, special sessions, and poster session. The next HEDM conference is scheduled for 20-22 May 1998 at the Naval Postgraduate School, Monterey, CA in conjunction with the AFOSR Molecular Dynamics Conference.

1997 High Energy Density Matter Contractor's Meeting
Westfields International Conference Center
Chantilly, VA
1-3 June 1997

Sunday, 1 June 1997

12:00 - 1:00	Registration
1:00 - 1:30	Introductory Remarks: *Dr. Michael R. Berman, AFOSR*
1:30 - 2:00	Propellant R&D for the Integrated High Pay-Off Rocket Propulsion Technology (IHPRPT) Program *Dr. Patrick G. Carrick, Phillips Laboratory*
2:00 - 2:30	Solid Rocket Propellants Present and Future *Dr. Lou Cannizzo, Thiokol Corporation*
2:30 - 3:00	New Energetic Ingredients for High Performance Solid Propellants *Dr. Kenneth O. Hartman, Alliant Techsystems*
3:00 - 3:30	*Break*
3:30 - 4:00	Aspects of Solid and Liquid Propellant Development at Phillips Laboratory *Dr. Tom W. Hawkins, Phillips Laboratory*
4:00 - 4:30	Progress Towards Synthesis of Pentaprismane and Bicyclopropylidene: Potential Rocket Fuel Additives *Dr. Suresh C. Suri, Hughes-STX Corporation*
4:30 - 5:00	Extra-High Energy Oxidizers and Fuels *Dr. Robert J. Schmitt, SRI International*
6:00 - 9:00	Poster Session, Reception

Monday, 2 June 1997

8:30 - 9:00	New Methods for Excited States *Dr. Rodney J. Bartlett, University of Florida*
9:00 - 9:30	Theory and Synthesis of New High Energy Density Materials *Dr. Karl O. Christe, Hughes STX Corporation*
9:30 - 10:00	Synthesis of High-Energy Density Materials Based on Strained-Ring Compounds *Dr. William P. Dailey, University of Pennsylvania*
10:00 - 10:30	*Break*
10:30 - 11:00	Epoxidation Transition States and Stereoselectivity Modeling *Dr. Kendall N. Houk, University of California, Los Angeles*
11:00 - 11:30	Nitrogen Peroxides for HEDM Applications *Dr. D. Scott Bohle, University of Wyoming*
11:30 - 12:00	Models and Simulations of Energetic Materials *Dr. Donald L. Thompson, Oklahoma State University*
12:00 - 1:30	*Lunch*
1:30 - 2:00	The Role of Quantum Chemistry in the Design of High Energy Species *Dr. Mark S. Gordon, Iowa State University*
2:00 - 2:30	Reaction Field Cavity Optimization: A New Solvent Model for Electronic Structure Theory *Dr. Teresa Head-Gordon, University of California, Berkeley*
2:30 - 2:45	Direct Detection and Spectroscopy of O_4^* *Dr. Holly Bevsek, University of California, Berkeley*
2:45 - 3:15	*Break*

Monday, 2 June 1997 (Cont'd)

3:15 - 3:45   Computational Studies of High Energy Density Matter
                                         Dr. Gregory A. Voth, University of Utah

3:45 - 4:15   Spectral Theory of Physical and Chemical Binding:
                                           Aspects of Computational Implementation
                                           Dr. Peter W. Langhoff, Indiana University

4:15 - 4:45   Reactions of Laser-Ablated Boron Atoms with HCN. Infrared
                                           Spectra of BNC, BCN, HBNC and HBCN in Solid Argon.
                                           Reactions of Laser Ablated Aluminum Atoms with Ammonia.
                                           Infrared Spectra of $HAlNH_2$, $AlNH_2$ and $HAlNH$ in Solid Argon
                                           Dr. Lester Andrews, University of Virginia

TBD   Workshop - Theory/Synthesis
                                           Discussion Leader: *Dr. Jeffrey A. Sheehy, Phillips Laboratory*

Tuesday, 3 June 1997

8:30 - 9:00   Progress Towards the Production of Cryosolid HEDM Samples by
                                           Laser Ablation and Matrix Isolation Techniques
                                           Dr. Mario Fajardo, Phillips Laboratory

9:00 - 9:30   Characterization of Cryogenic Carbon and Boron HEDM
                                           Dr. C. William Larson, Phillips Laboratory

9:30 - 10:00   Theoretical Investigations of HEDM
                                           Dr. Jeffrey A. Sheehy, Phillips Laboratory

10:00 - 10:30   *Break*

10:30 - 11:00   Spectroscopy & Dynamics in Quantum Hosts
                                           Dr. V. Ara Apkarian, University of California, Irvine

11:00 - 11:30   Mass Spectrometry of Doped Helium Clusters
                                           Dr. Kenneth C. Janda, University of California, Irvine

11:30 - 12:00   Light Metal Atom Interations with Hydrogen and Helium Clusters:
                                           Solvation Dynamics and Non-Adiabatic Effects
                                           Dr. Kevin Lehmann, Princeton University

12:00 - 1:30   *Lunch*

Tuesday, 3 June 1997 (Cont'd)

1:30 - 2:00   Spectroscopic Characterization of Non-Bonding Interactions of the Boron Atom
Dr. Paul J. Dagdigian, Johns Hopkins University

2:00 - 2:30   Structure and Energetics of $B(Ar)_n$, $B(N_2)$, and $O(H_2)$ Clusters
Dr. Millard H. Alexander, University of Maryland

2:30 - 3:00   Fundamental Insights from HEDM Studies
Dr. David R. Yarkony, Johns Hopkins University

3:00 - 3:30   *Break*

3:30 - 4:00   **Calorimetric Measurements of O Atom Recombination**
Dr. Peter Taborek and Dr. James E. Rutledge, University of California, Irvine

4:00 - 4:30   Characterization of Metal Atom-Doped Cryogenic Solids
Dr. George M. Seidel, Brown University

4:30 - 5:00   Ozone in Solid Oxygen
Dr. Richard A. Copeland, SRI Interational

5:00 - 5:30   Advanced Cryogenic Solid Hybrid Rocket Engine Developments for HEDM and Non-HEDM Demonstrations
Mr. Eric E. Rice, Orbital Technologies Corporation (ORBITEC)

Air Force High Energy Density Matter
Contractor's Conference

1-3 June 1997
Westfields International Conference Center
Chantilly, Virginia

SPEAKERS

Dr. Millard H. Alexander
Dept. of Chemistry & Biochem
University of Maryland
College Park, MD 20742-2021
301-405-1823
301-314-9121
mha@mha-ibm4.umd.edu

Dr. Vartkess Ara Apkarian
Dept. of Chemistry
University of California, Irvine
Irvine, CA 92697-2025
714-824-6851
714-824-8571
aapkaria@uci.edu

Dr. Holly Bevsek
Dept of Chemistry
UC Berkeley
% Y.T. Lee Group
Berkeley, CA 94720
510-486-5471
510-486-5311
holly@leea.cchem.berkeley.edu

Dr. Louis F. Cannizzo
Science and Engineering
Thiokol Corporation
P.O. Box 707, M/S 244
Brigham City, UT 84302-0707
801-863-3782
801-863-2271
cannilf@tc.thiokol.com

Dr. W. Lester Andrews
Dept. of Chemistry
University of Virginia
McCormick Road
Charlottesville, VA 22901
804-924-3513
804-924-3710
lsa@virginia.edu

Dr. Rodney J. Bartlett
Dept. of Chemistry
University of Florida
P.O. Box 118435
Gainesville, FL 32611-8435
352-392-6974
352-392-8722
bartlett@qtp.ufl.edu

Dr. D. Scott Bohle
Dept. of Chemistry
University of Wyoming
Box 3838
Laramie, WY 82071-3838
307-766-2795
307-766-2807
bohle@uwyo.edu

Dr. Patrick G. Carrick
OL-AC PL/RKS
10 E. Saturn Blvd.
Edwards AFB, CA 93524-7680
805-275-5883
805-275-5471
patrick_carrick@ple.af.mil

Dr. Karl O. Christe
Phillips Laboratory
Hughes STX
Edwards AFB, CA 93524-7680
805-275-5194
805-275-5471
karl_christe@ple.af.mil

Dr. Paul J. Dagdigian
Dept. of Chemistry
Johns Hopkins University
34th & Charles Streets
Baltimore, MD 21218
410-516-7438
410-516-8420
pjdagdigian@jhu.edu

Dr. Mario E. Fajardo
OL-AC PL/RKS
Bldg 8451
Edwards AFB, CA 93524-7680
805-275-5946
805-275-5471
mario_fajardo@ple.af.mil

Dr. Kenneth O. Hartman
Allegheny Ballistics Lab
Alliant Technical Systems
Box 210, Rt 956
Rocket Center, WV 26726
304-726-5114
304-726-4730
ken_hartman@atk.com

Dr. Teresa L. Head-Gordon
Life Science Division
Lawrence Berkeley Nat'l Lab.
1 Cyclotron Rd., Donner 134
Berkeley, CA 94720
510-486-7365
510-486-6488
thg@water.lbl.gov

Dr. Richard A. Copeland
Dept. of Molecular Physics
SRI International
333 Ravenswood Ave.
Menlo Park, CA 94025-3493
415-859-6534
415-859-6196
rich@mplvax.sri.com

Dr. William P. Dailey, III
Dept. of Chemistry
University of Pennsylvania
231 S. 34th St.
Philadelphia, PA 19104-6323
215-898-2704
215-573-2112
dailey@dailey.chem.upenn.edu

Dr. Mark S. Gordon
Dept. of Chemistry
Iowa State University
201 Spedding Hall
Ames, IA 50011
515-294-0452
515-294-0105
mark@si.fi.ameslab.gov

Dr. Tom Hawkins
OL-AC PL/RKS
10 E. Saturn Blvd.
Edwards AFB, CA 93524-7680
805-275-5449
805-275-5435
tom_hawkins@ple.af.mil

Prof. Kendall N. Houk
Dept. of Chemistry & Biochem
University of California
405 Hilgard Avenue
Los Angeles, CA 90095-1569
310-206-0515
310-206-1843
houk@chem.ucla.edu

Dr. Kenneth C. Janda
Dept. of Chemistry
University of California, Irvine
Irvine, CA 92697-2025
714-824-5266
714-824-3168
kcjanda@uci.edu

Dr. Carl William Larson
OL-AC PL/RKS
10 E. Saturn Blvd.
Edwards AFB, CA 93524-7680
805-275-6104
805-275-5471
carl_larson@ple.af.mil

Dr. Eric Rice
Orbital Technologies Corporation
Space Center
1212 Fourier Drive
Madison, WI 53717
608-827-5000
608-827-5050
ricee@orbitec.com

Dr. Robert J. Schmitt
Functionally Designed Mat'ls
SRI International
333 Ravenswood Ave., PS 345
Menlo Park, CA 94025-3493
415-859-5579
415-859-4321
robert_schmitt@qm.sri.com

Dr. Jeffrey A. Sheehy
OL-AC PL/RKS
10 E. Saturn Blvd.
Edwards AFB, CA 93524-7680
805-275-5762
805-275-5471
sheehy@helium.ple.af.mil

Dr. Peter W. Langhoff
Dept. of Chemistry
Indiana University
Bloomington, IN 47405
805-275-5224
805-275-5471
langhoff@helium.ple.af.mil

Dr. Kevin K. Lehmann
Dept. of Chemistry
Princeton University
Frick Lab, William Street
Princeton, NJ 08544-1009
609-258-5026
609-258-6746
lehmann@chemvax.princeton.edu

Dr. James E. Rutledge
Dept. of Physics & Astronomy
University of California, Irvine
Irvine, CA 92697-4575
714-824-5141
714-824-2174
jrutledg@uci.edu

Prof. George M. Seidel
Dept. of Physics
Brown University
Box 1843
Providence, RI 02912
401-863-2584
401-863-2024
seidel@physics.brown.edu

Dr. Suresh C. Suri
OL-AC PL/RKS
10 E. Saturn Blvd.
Edwards AFB, CA 93524-7680
805-275-5952
805-275-5471
suresh_suri@ple.af.mil

Dr. Peter Taborek
Dept. of Physics
University of California, Irvine
Irvine, CA 92697
714-824-2254
714-824-2174
ptaborek@uci.edu

Prof. Gregory A. Voth
Dept. of Chemistry
University of Utah
4524 Henry Eyring Bldg
Salt Lake City, UT 84112
801-581-7272
801-581-4353
voth@chemistry.chem.utah.edu

Prof. Donald L. Thompson
Dept. of Chemistry
Oklahoma State University
Stillwater, OK 74078
405-744-5174
405-744-6007
dlt@osuunx.ucc.okstate.edu

Dr. David R. Yarkony
Dept. of Chemistry
Johns Hopkins University
3400 N. Charles St.
Baltimore, MD 21218
410-516-4663
410-516-8420
yarkony@jhuvms.hcf.jhu.edu

ATTENDEES

Dr. Tomas Baer
Dept. of Chemistry
University of North Carolina
Chapel Hill, NC 27599-3290
919-962-1580
919-962-2388
baer@unc.edu

Dr. William O. Berry
AFOSR/NL
110 Duncan Ave., Ste B115
Bolling AFB, DC 20332-8080
202-767-4278
202-404-7475
william.berry@afosr.af.mil

Dr. Jerry A. Boatz
OL-AC PL/RKS
10 E. Saturn Blvd.
Edwards AFB, CA 93524-7680
805-275-5364
805-275-5471
jerry@helium.ple.af.mil

Dr. Jeffrey C. Bottaro
Functionally Des Mat'ls Dept
SRI International
333 Ravenswood Avenue
Menlo Park, CA 94025-3493
415-859-4571
415-859-4321

Ms Galina Chaban
Dept. of Chemistry
Iowa State University
201 Spedding Hall
Ames, IA 50011
515-294-4604
515-294-4709
galina@si.fi.ameslab.gov

Dr. William R. Clayburgh
Space Transportation Division
NASA Headquarters
300 E. St., S.W.
Washington, D.C. 20546
202-358-1891
202-358-2900
sclaybau@mail.hq.nasa.gov

Ms. Michelle E. DeRose
OL-AC PL/RKS
10 East Saturn Blvd
Edwards AFB, CA 93524-7680
805-275-5798
805-275-5471
michelle_derose@ple.af.mil

Dr. Michael A. Dewey
Propellant & Adhesives Dev
Thiokol Corporation
P.O. 707, M/S 243
Brigham City, UT 84302-0707
801-863-2586
801-863-2271
deweyma@thiokol.com

Dr. Greg W. Drake
Phillips Laboratory
National Research Council
10 East Saturn Blvd.
Edwards AFB, CA 93524-7680
805-275-5759
805-275-5471
greg_drake@ple.af.mil

Dr. Bruce Garrett
Env Molecular Science Lab
Pacific Northwest Nat'l Lab
Battelle Blvd, MS K 1-96
Richland, WA 99352
509-375-2587
509-375-6631
bc_garrett@pnl.gov

Mr. Friedrich Grein
Dept. of Chemistry
Univ. of New Brunswick
Fredericton, NB, Canada E3B6E2
506-453-4776
506-453-4981
fritz@unb.ca

Dr. Sharon Hammes-Schiffer
Dept of Chem & Biochem
University of Notre Dame
Notre Dame, IN 46556
219-631-7434
219-631-6652
hammes-schiffer.1@nd.edu

Dr. Anatoli Korkin
Dept. of Chemistry
Univ of FL, Quan Theory Proj
362 Williamson Hall
Gainsville, FL 32611-8435
352-392-1597
352-392-8722
korkin@qtp.ufl.edu

Dr. John R. Lombardi
Dept. of Chemistry
City College of CUNY
Convent Ave & 138th St.
New York, NY 10031
212-650-6032
212-650-6848
lombardi@sci.ccny.cuny.edu

Dr. Robert W. Naylor
Alliant Techsystems
210 Rt. 956
Rocket Center, WV 26726
304-726-5405
304-726-5152

Mr. Steven R. Gwaltney
Quantum Theory Project
University of Florida
345 Williamson Hall
Gainesville, FL 32611-8435
352-392-6365
352-392-8722
gwaltney@qtp.ufl.edu

1Lt Jessica Harper
OL AC PL/RKS
10 E. Saturn Blvd.
Edwards AFB, CA 93524-7680
805-275-6278
805-275-5471
jessica_harper@ple.af.mil

Ms. Jennifer R. Krumrine
Chemical Physics Program
University of Maryland
College Park, MD 20742-2021
301-405-1822
301-314-9121
krumrine@mha-ibm5.umd.edu

Dr. Jeff D. Mills
OL-AC PL/RKS
10 East Saturn Blvd
Edwards AFB, CA 93524-7680
805-275-5224
805-275-5471
mills@helium.ple.af.mil

Dr. Bryan Palaszewski
Combustion Branch, MS 60-4
NASA Lewis Research Center
21000 Brookpark Road
Cleveland, OH 44135
216-977-7493
216-977-7545
bryan.a.palaszewski@lerc.nasa.gov

Mr. Saroj Patel
EE61
NASA Marsh Sp Flt Ctr
Huntsville, AL 35812
205-544-0591
205-544-3214
saroj.patel@msfc.nasa.gov

Dr. Stephen L. Rodgers
OL-AC PL/RKS
10 E. Saturn Blvd.
Edwards AFB, CA 93524-7680
805-275-5230
805-275-5471
stephen_rodgers@ple.af.mil

Dr. Steven D. Thompson
Defense Tech Security Adm
Department of Defense
400 Army Navy Drive, Suite 305
Arlington, VA 22202-2884
703-604-8061
703-602-5841
sthompson@dtsa.osd.mil

1Lt Neal T. Williams
OL-AC PL
10 East Saturn Blvd
Edwards AFB, CA 93524-7680
805-275-6270
805-275-5471
neal_williams@ple.af.mil

Mr. Xin Yang
Dept. of Chemistry
Johns Hopkins University
3400 N. Charles St., Remsen
Baltimore, MD 21218
410-516-4669
410-516-8420
yangxin@jhunix.hcf.jhu.edu

Dr. Mark A. Petrie
OL AC PL/RKS
10 E. Saturn Blvd.
Edwards AFB, CA 93524-7680
805-275-5759
805-275-5471
mark_petrie@ple.af.mil

Mr. Simon Tam
OL-AC PL/RKS
10 E. Saturn Blvd.
Edwards AFB, CA 93524-7680
805-275-6074
805-275-5471
simon_tam@ple.af.mil

Prof. David Weeks
AFIT/ENP
2950 "P" Street
WPAFB, OH 45433-7765
937-255-3636
937-255-2921
dweeks@afit.af.mil

Dr. William W. Wilson
PL, Hughes STX
Bldg. 8451
10 E. Saturn Blvd.
Edwards AFB, CA 93524-7680
805-275-5194
805-275-5471
william_wilson@ple.af.mil

Propellant R&D for IHPRPT

Dr Patrick G. Carrick
Chief, Propellants Research & Development
Air Force Research Laboratory
Edwards Air Force Base, CA
(805) 275-5883
Patrick_Carrick@PLE.AF.MIL

The Integrated High Payoff Rocket Propulsion Technology (IHPRPT) Program is a national effort to double the capabilities of rocket propulsion technology by the year 2010. It is a cooperative program involving the Department of Defense (DOD), the National Aeronautics and Space Administration (NASA), and the national aerospace industry. The program involves efforts to improve rocket propulsion technology in all aspects of launch, space propulsion, and missile propulsion. As such, the technical efforts are grouped by rocket technology area: Boost and Orbit Transfer (B&OT) propulsion, Spacecraft (SC) propulsion, and Tactical (TC) propulsion. Each technology area has specific goals set for three phases of the program – Phase I by 2000, Phase II by 2005, and Phase III by 2010. The goals were set by determining state-of-the-art baselines in 1995, and setting the desired gains in relation to these baselines. These program goals are listed below.

Boost and Orbit Transfer Propulsion	2000	2005	2010
• Reduce Stage Failure Rate	25%	50%	75%
• Improve Mass Fraction (Solids)	15%	25%	35%
• Improve ISP (sec)	14	21	26
• Reduce Hardware Costs	15%	25%	35%
• Reduce Support Costs	15%	25%	35%
• Improve Thrust to Weight (Liquids)	30%	60%	100%
• Mean Time Between Removal (Mission Life-Reusable)	20	40	100

Spacecraft Propulsion			
• Improve ISP (Chemical/Solar Thermal)	5/10%	10/15%	20/20%
• Improve Mass Fraction (Bipropellant)	5%	10%	20%
• Improve Density-Isp (Monopropellant)	30%	50%	70%

Tactical Propulsion			
• Improve Delivered Energy	3%	7%	15%
• Improve Mass Fraction (Without TVC/Throttling)	2%	5%	10%
• Improve Mass Fraction (With TVC/Throttling)	10%	20%	30%

The technology areas are divided into four technical working areas: Propellants, Propellant Management Devices, Combustion and Energy Conversion Devices, and Technology Demonstrators. There are specific objectives for each of these technical working areas that "roll up" to provide the goals (as listed above) for each technology area. The Propellants area objectives typically involve improvements in specific impulse (Isp), density (which effects mass fraction) and cost. The specific propellant area objectives are given below. Note that there are very few Phase I objectives. This is due to the long lead time in developing new propellant ingredients.

As stated above, the propellant objectives "roll up" into the overall IHPRPT goals. Since new propellants generally cost more than established propellants, the cost objectives were set to give no <u>overall</u> increase in propellants costs. Even if the new propellant ingredients cost more, this might be achieved by reducing manufacturing and/or handling costs.

There is also some overlap in objectives between areas, such as solids for Boost and Orbit Transfer and solids for Tactical. The overall Propellants R&D program is designed to take advantage of these overlaps when possible.

B&OT, Solids
- Phase II: 1.6% Isp, 2.6% Mass Frac., 0% Cost
- Phase III: 5.0% Isp, 5.1% Mass Frac., 0% Cost

B&OT, Hydrocarbon
- Phase II: 2% Isp, 0% Cost
- Phase III: 4% Isp, 0% Cost

B&OT, Cryogenic Booster
- Phase III: 5% Isp, 0% Cost

Tactical
- Phase I: 2.4% Del. Energy, 0.8% Mass Frac., 0% Cost
- Phase II: 5.6% Del. Energy, 2% Mass Frac., 0% Cost
- Phase III: 12% Del. Energy, 4% Mass Frac., 0% Cost

Spacecraft, Liq. Propellants & RCS
- Phase I: 1.6% Isp, 25% Mass Frac., -20% Cost
- Phase II: 4% Isp, 25% Mass Frac., -20% Cost
- Phase III: 8% Isp, 29% Mass Frac., -20% Cost

There are several Air Force propellant programs in the different technical areas. There are three contracted efforts and one in-house effort in B&OT, Solids: Advanced Oxidizers, Binders, & Fuels, which is a Phase II program that is investigating known "emerging" energetic ingredients; Advanced Propellant Formulation, which is a Phase II program to develop new formulations based on the "emerging" ingredients; and High Performance Oxidizers, Binders, & Fuels, which is a Phase III program to develop new energetic ingredients. These programs also support development of new propellants for Tactical propulsion.

There is currently one Air Force propellant program in B&OT, Hydrocarbon: Hydrocarbon Fuels & Additives. This project currently has very little Air Force development (6.2) effort. There is a component of our in-house and contracted basic research ("6.1" − type, AFOSR funded) that supports the investigation of new liquid ingredients for hydrocarbon-based rocket propulsion systems.

There is also currently one Air Force program in the B&OT, Cryogenic area: Cryogenic Solid Thruster. This in-house and university contracted project is supported solely by AFOSR basic research funding. There is little current activity in this area, although this area of research may be most productive in a timeframe beyond the IHPRPT program.

There is currently one Air Force program in Spacecraft, Liquid Propellants & RCS: New Monopropellant Ingredients. This project is primarily an in-house effort to development less toxic, higher performance, higher density monopropellant replacements for hydrazine and hydrazine-based propellants.

Solid Rocket Propellants Present and Future[*]

Lou Cannizzo
Thiokol Corporation, Science and Engineering
Brigham City, Utah 84302

ABSTRACT

The present ingredients used in solid rocket propellants are mostly commercial or semi-commercial materials whose properties in propellants are fairly well understood. Future demands in solid rocket propulsion, in terms of the solid propellant's performance, cost, and safety dictate that new ingredients need to be developed and examined. Several new energetic materials under investigation include CL-20 (a new high density nitramine), ADN (a high energy non-chlorine oxidizer), furazan-based high nitrogen compounds, and oxetane-based energetic polymers and plasticizers. The utilization of these materials and others will be the first step in improving solid propellant technology. The current status of these materials will be presented.

INTRODUCTION

Solid rocket propulsion technology has advanced significantly over the last fifty years, yielding reliable, relatively low cost motors ranging in size from hundred pound tactical motors to million pound Shuttle boosters. To advance this technology even further, the Integrated High Performance Rocket Propulsion Technology (IHPRPT) Program has targeted improvements in several areas of importance. One of these areas is delivered performance. To achieve the proposed increases in delivered performance, new energetic materials will have to be developed and evaluated as solid propellants ingredients. With the recent emphasis on safer propellants, the list of possible candidates to give high performance propellants has diminished greatly. New ingredients which can give the desired increases without the concurrent safety hazards are the ultimate goal of the current efforts.

The IHPRPT Alternate Oxidizers and Fuels Program is directed towards achieving the Phase II and III propellant performance goals of the IHPRPT Program for booster and orbit transfer solid propellants.[1] The approach to meeting these goals is through the evaluation of alternate high energy oxidizers and fuels. These materials can be used to develop entirely new formulations and also to modify existing ones. Among the available alternate materials, the non-chlorine oxidizer ammonium dinitramide (ADN) can give dramatic increases in calculated Isp values compared to baseline ammonium perchlorate (AP) propellants. Utilizing technology developed on the Navy's ADN MANTECH Program, ADN of suitable quality for propellant formulating is now available. In combination with energetic binders, aluminized propellants containing ADN give formulations which can achieve the performance goals of the program. The recent, intensive effort to develop new energetic materials (e. g. CL-20, TNAZ) has lead to the availability of a number of high density, high heat of formation compounds which can be applied towards increasing solid propellant performance. The combination of these new materials with ADN and energetic binders now makes it possible to formulate solid propellants which can met or exceed the predicted delivered performance of current metallized, AP-containing propellants in orbit transfer applications, without producing particulates or other products which might interfere with satellite systems.

RESULTS AND DISCUSSION

The high density, energetic nitramine CL-20 was first synthesized in 1987 at the Naval Weapons Center, China Lake.[2] Thousands of pounds have been produced in the last several years by Thiokol Corporation using a modified process. Propellant grade material is now readily available for formulation studies. Utilization of low levels of CL-20 in both booster and orbit transfer formulations can give significant increases in solid propellant performance without causing unacceptable propellant detonability characteristics.

Ammonium dinitramide (ADN) is currently under study by a number of researchers for various applications, including use as an oxidizer for solid rocket propellants.[3] The relatively good density and high heat of formation of this ingredient make it attractive for increasing the performance of booster and orbit transfer propellants. However, current properties of ADN which limit its use in solid propellants include poor thermal stability, deliquescence, and inferior particle morphology. The ADN MANTECH Program (sponsored by the Navy) has recently produced material which has significantly improved the above properties.[4] This has been accomplished by utilization of very low levels of additives combined with a prilling process to give spherical particles of ADN. Using these techniques, multi-pound batches of prilled ADN have been manufactured for formulation studies.
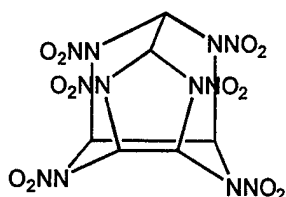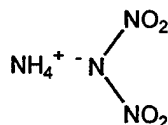
CL-20   **ADN**

Energetic compounds which contain nitrate ester and nitramine functional groups are inherently fairly sensitive to impact, friction and ESD stimuli due to the presence of these energetic moieties. However, other heteroatomic structures such as furazan, azoxy, azo and C-nitro groups can be used to construct energetic structures without the higher sensitivities noted above. Several such compounds are already known or in development.

For this program a series of materials based upon the starting compound 3,4-diaminofurazan (DAF)[5] are under investigation. These compounds were chosen because their energetic nature is derived from the alternate, less sensitive structures mentioned above. The first, 3-amino-4-nitrofurazan (ANF), is synthesized from DAF using sodium tungstate and 30% hydrogen peroxide.[6] The reported yield is 50%. The next compound, diaminoazofurazan (DAAF) is formed by the oxidation of DAF with ammonium persulfate in water.[7] The product is obtained in 49% yield. Alternatively, DAF can be oxidized with hydrogen peroxide in concentrated sulfuric acid to give the corresponding azoxy compound diaminoazoxyfurazan (DAAOF) in 90% isolated yield.[8] Further oxidation of DAAOF with ammonium persulfate and hydrogen peroxide in concentrated sulfuric acid yields dinitroazoxyfurazan (DNAF) in 60% yield.[9] The procedures listed above have been optimized at Thiokol to increase the yields and purities of the resulting products. In some cases this has resulted in reducing the quantities of reagents employed and switching to reagents which give improved procedures. These optimizations have been employed to produce multi-gram quantities of each of the above compounds. This has allowed measurement of initial safety properties, heats of formation, and densities of the compounds listed above. The results from these tests are presented in Tables 1 and 2. The initial safety properties indicate that most of the compounds are fairly insensitive,

except for DNAF. Although the initial measurements of the sensitivity of DNAF indicates that it is greater than RDX, the values are within the limits of acceptable materials to handle. Further development of DNAF will give a better indication of its bulk safety properties, including susceptibility to detonation. The heats of formation and densities of the series of compounds are attractive for energetic formulations. With the highest heat of formation and one of the highest densities, DNAF would be projected to give the largest increases in impulse values when employed in solid propellant formulations.
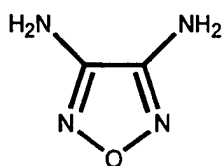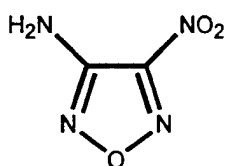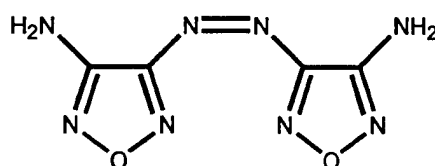
DAF   ANF   DAAF
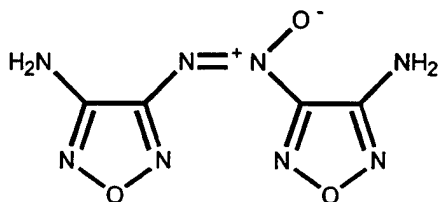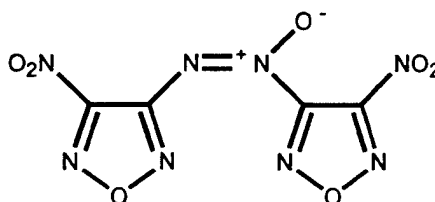
DAAOF   DNAF

Table 1. Safety Properties of ANF, DAAF, DAAOF, and DNAF*

compound	impact (inches)	friction (lbs)	ESD (joules)	DSC onset (°C)
ANF	42	>64	>8	220
DAAF	>46	>64	0.52	264
DAAOF	>46	>64	2.43	263
DNAF	15	13	>8	227
TNT	42	>64	>8	270
RDX	22	63	0.43	240

* Impact, friction, and ESD sensitivities were measured on Thiokol Corporation-designed instruments and are 50% levels. The relative sensitivities of TNT and RDX are given for comparison. DSC onsets were determined at scan rates of 20°C/minute.

Table 2. Heats of Formation and Densities of ANF, DAAF, DAAOF, and DNAF*

compound	ΔHf (kcal/mol)	density (g/cc)
ANF	+34	1.81 (c)
DAAF	+119	1.73 (p)
DAAOF	+101	1.74 (p)
DNAF	+185	1.81 (p)

* The heats of formation were determined from heat of combustion measurements. The densities were determined by pycnometer (p) or from the crystal structure (c).

The propellant effort on the IHPRPT Alternate Oxidizers and Fuels Program is directed toward meeting the Phase II/Phase III IHPRPT performance goals in both booster and orbit transfer applications. The overall system performance increases are +4% and +8% for Phase II and Phase III, respectively. The proportion of the increase directly resulting from propellant is a function of the propulsion application and industry approaches to improvements in other components such as case technology and nozzle technology.

The aggressive performance increase goals of IHPRPT can be met through the use of ADN oxidizer. Although the density of ADN is slightly lower than that of AP, 1.8 g/cc vs 1.95 g/cc, the Isp values for ADN formulations are typically substantially higher than their AP counterparts. Use of higher density energetic binders serves to offset the density losses. Energetic binders also enable performance needs to be met at lower solids which improves processing and mechanical properties. Propellant mechanical properties with the energetic binders would also be expected to be enhanced because of their polarity, which aids oxidizer-binder bonding without the need for bonding agents required of non-polar binders. Hazards properties of the propellants are a concern at the high performance levels required by IHPRPT.

Booster propellant applications must realistically address not only delivered Isp but also propellant density, i.e., propellant density-Isp. For booster applications, a typical weighting factor for density is density$^{(0.6)}$-Isp. Propellants based on energetic binders with ADN oxidizer and aluminum fuel show promising performance potential. As described earlier, a major effort in the PL IHPRPT Program is identification of high performance non-metal fuels. The new fuels avoid the generation of metal oxide exhaust products, and show interesting potential in orbit transfer applications. While the densities of the organic fuels are lower than aluminum, propellant density in many orbit transfer applications is less of a performance driver. The contribution of density varies by specific motor application, but density$^{(0.3)}$-Isp was selected as a moderate value. Formulations using an unplasticized energetic binder and ADN oxidizer in combination with several of these fuels can meet the Phase II IHPRPT performance goals and can approach the Phase III IHPRPT performance goals without any metal present. The organic fuels do not suffer the same 2-phase flow losses as their metallized counterparts. There is still some efficiency loss in performance, but significantly less than those in metallized formulations. For this reason, propellants containing higher performance organic fuels can exhibit the same delivered Isp as their metallized analogs.

SUMMARY AND CONCLUSIONS

As discussed in the previous pages, the utilization of new energetic oxidizers, fuels, and binders provides a viable approach to increasing the performance level of booster and orbit transfer propellants. ADN, when combined with energetic binder systems in aluminized propellants, give significant gains in predicted delivered performance compared to the baseline booster propellant. For orbit transfer non-particulate formulations consisting of ADN and new organic fuels show excellent performance potential without the use of metals. The absence of particulates or other harmful products in the exhaust from these orbit transfer propellants are very attractive characteristics for orbit transfer of satellites with sensitive optics and electronic packages onboard.

REFERENCES

1 . Contract #F04611-96-C-0005 with the Phillips Laboratory at Edwards AFB.

2. Arnold T. Nielsen, private communication.

3. Borman, S. "Advanced Energetic Materials Emerge for Military and Space Applications", *Chemical & Engineering News* **1994**, January 17, 1994.

4. ADN MANTECH Program, Contract Number N000174-95-C-0078.

5. DAF is readily available from glyoxal using a three step process.

6. Schmidt, R. D. (Lawrence Livermore National Laboratory), Private Communication.

7. Gunasekaran, A.; Boyer, J. H. *Heteroatom Chemistry* **1993**, *4*, 521.

8. Solodyuk, G. D.; Boldyrev, M. D.; Gidaspov, B. V.; Nikolaev, V. D. *Zh. Org. Khim.* **1981**, *17*, 861.

9. Gunasekaran, A.; Trudell, M. A.; Boyer, J. H. *Heteroatom Chemistry* **1994**, *5/6*, 441.

NEW ENERGETIC INGREDIENTS FOR HIGH PERFORMANCE SOLID PROPELLANTS[1]

R. W. NAYLOR
K. O. HARTMAN
ALLIANT TECHSYSTEMS
ALLEGANY BALLISTICS LABORATORY
ROCKET CENTER, WV 26726

The goal of our efforts has been the improvement of the performance level of existing propellants to and beyond 265 sec while maintaining a Class 1.3 shock sensitivity. To achieve the performance goals, our approach has concentrated on the synthesis and procurement of new, high energy density oxidizers. We have concentrated on oxidizers because these compounds comprise the largest propellant component and therefor offer the greatest opportunity for significant energy increases. A typical solid propellant contains 60-90% oxidizer, 10-40% binder, and up to 10% additives for acoustic and ballistic modification. The binders are composed of polymers and energetic plasticizers. Many polymers and energetic plasticizers exist, having a wide range of energies, from which an equally wide range of binder energies can be formulated.

In our focus on energetic oxidizers, we established certain criteria for our selection process. In addition to the performance goals, the following propellant requirements must be met: no chlorine, low metal content, environmentally compatible, and low cost. Following these requirements, a list of potential compounds was generated having the following characteristics. 1.) High densities through high nitrogen content and quaternary carbons 2.) Positive heats of formation. 3.) Energy content derived from the inclusion of small strained rings and carbon bonded nitro groups. Geminal nitro groups were included whenever possible since these have a measure of stability over gem-trinitro, nitramino, and nitrato groups. Nitramino groups were avoided because of their known shock sensitivity. 4.) Non ionic bonding, since salts have the potential for being highly hygroscopic.

A number of compounds that had these characteristics were identified and evaluated based on the following criteria: heat of formation, density, performance in the baseline binder, stability, sensitivity, ease of synthesis, and cost. The compounds listed below along with their densities and heats of formation were selected for consideration using the above criteria and evaluation system.
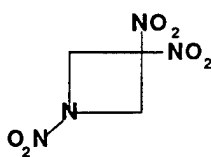
TNAZ

ΔH, (cal/mole)	8,000
(cal/g)	41.6
DENSITY (g/mL)	1.70
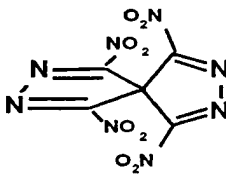
TNTSN

ΔH, (cal/mole)	117890
(cal/g)	393
DENSITY (g/mL)	1.55
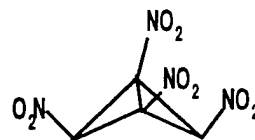
TNBB

ΔH, (cal/mole)	39,780
(cal/g)	170
DENSITY (g/mL)	1.55
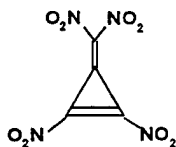
TNMCP

ΔH, (cal/mole)	57,000
(cal/g)	246
DENSITY (g/mL)	1.84
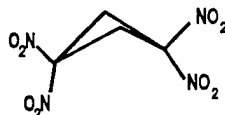
TNCB

ΔH, (cal/mole)	-5140
(cal/g)	-21.8
DENSITY (g/mL)	1.99

TNSP
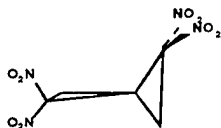
ΔH, (cal/mole)	28,300
(cal/g)	114
DENSITY (g/mL)	1.8
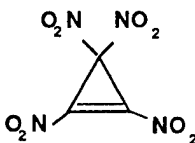
TNCP

ΔH, (cal/mole)	34,170
(cal/g)	155
DENSITY (g/mL)	1.85
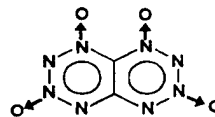
DTTO

ΔH, (cal/mole)	201,000
(cal/g)	1004.5
DENSITY (g/mL)	1.86
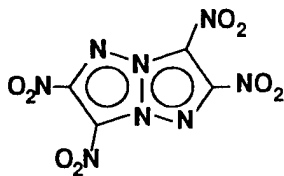
TNTAP

ΔH, (cal/mole)	120,600
(cal/g)	418
DENSITY (g/mL)	2.00

TNSPD
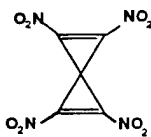
ΔH, (cal/mole)	90,000
(cal/g)	369
DENSITY (g/mL)	1.8
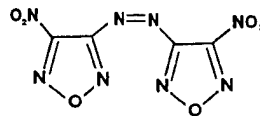
ABNF

ΔH, (cal/mole)	141,000
(cal/g)	551
DENSITY (g/mL)	1.86

To assure a high degree of efficiency in the operation of the program, an early sensitivity screening plan was devised to eliminate those materials which demonstrate incompatibility and or shock sensitivity. This will guarantee that time and resources will not be expended on materials which are unacceptable to the program. Ten gram samples of the synthesized/procured material is evaluated for compatibility with propellant components and for hazards sensitivity to impact, friction and ESD stimuli. Failure of any one of these tests will eliminate the material from further development. On passing the sensitivity and compatibility screening, the material is scaled up to the 100-g synthesis level, formulated in the selected baseline binder system and evaluated by the NOL card gap test for shock sensitivity. Acceptable shock sensitivity will allow development to continue toward full scale demonstrations. The schematic for the screening plan is illustrated below.

```
                              ┌──────────┐
                              │ ELIMINATE │
                              └──────────┘
                                   ▲
                                   │ FAIL
                                   │
 ┌─────────────┐           ┌──────────────┐          ┌──────────────┐
 │ LABORATORY  │           │ SENSITIVITY  │          │ PROPELLANT   │
 │ SYNTHESIS AND │ ──────▶  │ AND          │ ──────▶  │ FORMULATION  │
 │ PROCUREMENT │           │ COMPATIBILITY │          │ AND          │
 │             │           │ SCREENING    │          │ SCREENING    │
 └─────────────┘           └──────────────┘          └──────────────┘
                                                             │
                                                             ▼
 ┌─────────────┐          ◇──────────◇          ◇──────────────◇
 │ SCALE-UP    │          │ ≥35 DAYS │          │ <70 CARDS    │
 │ TAILORING AND │ ◀────── │ STABILITY │ ◀────── │ INSENSITIVITY │
 │ EVALUATION  │          │ @ 158-F  │          │ (NOL)        │
 └─────────────┘          ◇──────────◇          ◇──────────────◇
       │                       │ FAIL                 │ FAIL
       ▼                       │                      │
 ┌─────────────┐          ┌──────────────┐           │
 │ DEMONSTRATION │         │ REFORMULATE  │ ◀─────────┘
 └─────────────┘          └──────────────┘
```
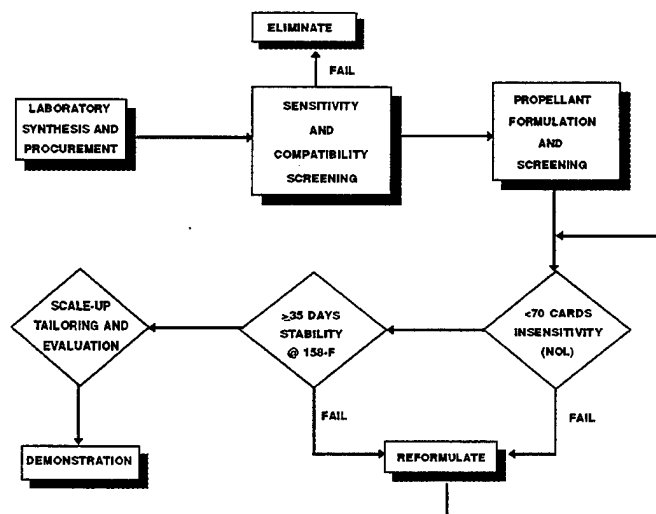
To date, two materials have been evaluated. 3,3,1-trinitroazetidine (TNAZ), a commercially available material, was evaluated for shock sensitivity at the 50% level in a PEG/nitrate ester binder (H_{ex} = 910 cal/g). The I_{sp} of the TNAZ propellant was 255 sec. The NOL card gap test demonstrated shock sensitivity of the propellant at 69 cards by punching a clean hole through a one-half inch thick, steel witness plate. In addition to the high shock sensitivity, the TNAZ propellant demonstrated a burn rate of 0.26 in/sec at 1000 psi and a high slope of 1.08. The non optimized propellant had a modulus of 311 psi, an elongation of 18%, and a tensile strength of 41 psi. The high sensitivity in the PEG propellant suggests that TNAZ will not meet the Class 1.3 goal in energetic binders.

The second compound evaluated, azo bis-nitrofurazan (ABNF) has been synthesized and found to be impact sensitive by the hammer test. In addition to its impact sensitivity, ABNF has a low melting point of 56°C and for that reason would pose production difficulties at the routinely used propellant processing temperatures of 50-60°C. Because of its low melting point and its high sensitivity, work on ABNF has been terminated.

Three additional materials are being synthesized. Tetranitrospiropentane is in the advanced stages of synthesis and the most recent precursor, spiropentane dicarboxylic acid, will be converted into the diaryl dinitrospiropentane dicarboxylate for nitration.

A synthesis route to octaazanaphthalenetetraoxide (DTTO) has been postulated and synthesis of this material is underway. DTTO propellant has an extremely high performance of 280 sec at

loadings below 40%. The thermal stability and shock sensitivity of DTTO will be evaluated upon its synthesis.

The fourth compound, tetranitrocyclobutane (TNCB) was reportedly synthesized, but its evaluation in propellant has not been reported. The compound meets the performance goal in energetic binders, and since its synthesis route has been demonstrated, we will manufacture and evaluate this material.

Aspects of Solid and Liquid Propellant Development at Phillips Laboratory

T.W. Hawkins, A. Brand, M. Petrie, D. Bach and M. McKay
Phillips Laboratory, Edwards AFB CA

Propellant development activities are underway at Phillips Laboratory in several areas including space boost and spacecraft propulsion. The Propellant Applications group is currently performing development work on solid, solution propellant for space boost and non-toxic monopropellant for spacecraft. Both efforts are part of the DoD Integrated High Payoff Rocket Propulsion Technology (IHPRPT) Program.

The advantages of the solution propellant approach to solid propulsion include : (1) The propellant does not require particulate oxidizer in several particle sizes to obtain a 'high solid loading' for a composite propellant; (2) Manufacturing costs for the propellant are expected to be less than that for conventional solid propellants; (3) Toxic curatives typically used in solid propellant formulations (e.g., isocyanates) are not required; and (4) Formulations with environmentally attractive benefits (e.g., simple demilitarization and ingredient reclamability) may be produced.

Efforts to further increase the performance capability of solution propellant have been spurred by the DoD Integrated High Payoff Rocket Propulsion Initiative. This initiative has set certain performance objectives for propulsion systems (including solid propulsion) to meet by the years 2000, 2005 and 2010. Among these objectives for solid propellants is that of increased energy. Propellant energy density is expected to attain 3.44 MJ/kg by 2005 and 3.66 MJ/kg by 2010 for solid booster propellants. One approach to improving the performance of solution propellants involves the development and application of more energetic, higher density oxidizers and fuels. An investigation is underway at Phillips Laboratory to characterize such oxidizers and fuels and the resulting solution propellant formulations. Results of this characterization and pertinent comparisons with HAN-based oxidizer and propellant are presented.

Hydrazine is the state-of-the-art monopropellant for RCS and satellite positioning propulsion systems. A combination of safety and environmental concerns have resulted in increases in operational cost for such hydrazine-based systems. This situation has resulted in a need for significantly less toxic and also higher performance alternatives. The IHPRPT Initiative has set objectives for performance for "non-toxic" monopropellants to be met by the years 2000, 2005 and 2010. Monopropellant energy density is expected to attain 3.25 MJ/kg by 2005 and 3.76 MJ/kg by 2010 for spacecraft monopropellants.

Experience gained in the U.S. Army's liquid gun propellant program (using HAN-based propellant) showed that such highly ionic, liquid propellants could have a significant performance, toxicity and handling advantage over hydrazine. In work at Phillips Laboratory, an examination of prospective alternative, non-toxic and highly ionic monopropellant candidates is underway. Theoretical and experimental evaluations of candidate HEDM ingredients (e.g. hydroxylammonium nitroformate) will be presented.

Progress Towards the Synthesis of Pentaprismane and Bicyclopropylidene: Potential Rocket Fuel Additives

Suresh C. Suri

HUGHES STX Corporation C/O Phillips Laboratory/RKS
10 East Saturn Blvd., Edwards AFB, CA 93524-7680

One of the current activities in rocket propulsion area has been directed towards improving the overall performance of the existing rocket fuel. The improvement in performance translates to increase of specific impulse (Isp) and increase in payload (high density of the propellant components). For increase in specific impulse, the fuel components should possess low exothermicity (high positive heat of formation) for the propellant components, high exothermicity (high negative heat of formation) of the combustion products.

The strain ring compounds is promising because of their compact structure that provides high density and incorporation of strain that serves to increase their heat of formation. The class of strain ring compounds that meet the above criteria are: (a) prismanes, (b) triangulanes, (c) propellanes and (f) spiro- pentane/hexane/ heptanes. The strain compounds belong to prismane[1] family are [3]-prismane (tetrahedron); [4]-prismane (cubane) and [5]-prismane. Turro and coworkers[2] achieved the synthesis of [3]-prismane in 15% yield. Eaton and Cole[3] achieved the synthesis of [4]-prismane in 1964. Over the years, improvements have been made to its synthesis to maximize the yield. Under the AFOSR sponsored HEDM program, the focus was directed towards practical synthesis of pentaprismane and bicyclopropylidene.

PENTAPRISMANE:. In the past two decades numerous chemists have employed diverse synthetic strategies to obtain elusive hydrocarbon "pentaprismane". Eaton et al.[4] prepared pentaprismane from tricyclic Diels-Alder adduct of 5,5-dimethoxy-1,2,3,4-tetrahydrocyclopenta-1,3-diene and benzoquinone in 17 steps. Dauben et al.[5] offered a new variant for the preparation of pentaprismane. None of the above synthetic routes offered by Eaton and by Dauben are practical for large production. The synthesis of 1,8,10-trichloro-11,11-dimethoxy-3α-hydroxy-tetracyclo[6.2.1.0^{2,7}.0^{4,10}]undec-5-ene-9-one (**3**)[6] was achieved via base promoted eliminative cyclization of **2**[7] (Scheme-1) which can be obtained by stereoselective reduction of abundantly

Scheme-1

1   NaBH₄/Ce(III)/MeOH   2   t-BuOK/t-BuOH   3
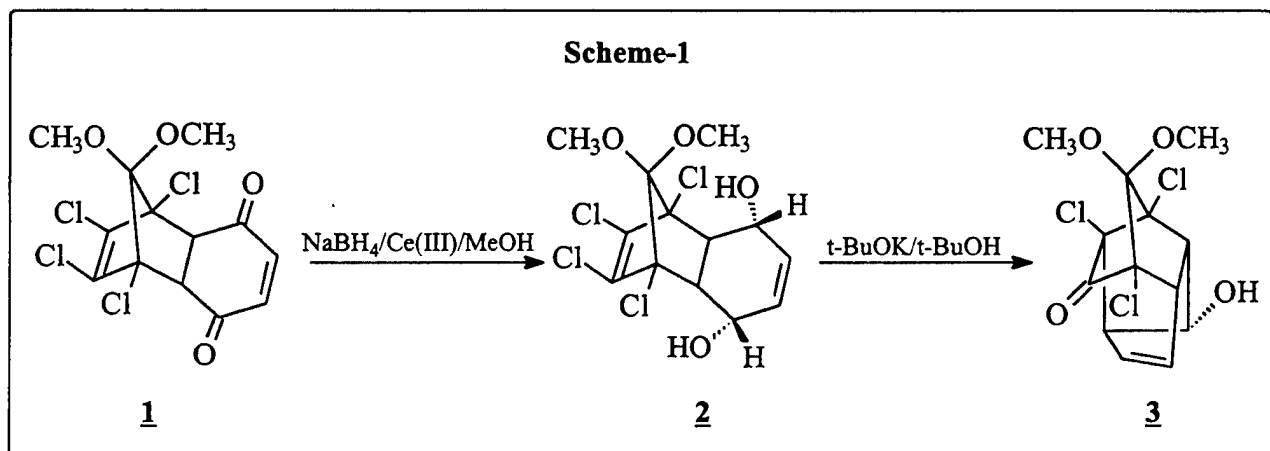
available material **1**. It is anticipated that carbons C9 & C5 and C3 & C6 can be stitched together chemically to

furnish substituted homopentaprismane which can be transformed to substituted pentaprismane via Favorskii ring contraction methodology. All attempts to form chemical bonds between C9 & C5 and C3 & C6 simultaneously were unsuccessful. However, It was demonstrated[8] that the chemical bond between C9 & C5 in **3** could be achieved to furnish substituted pentacycloundecane **5** via ketyl-olefin reductive coupling reaction using SmI$_2$. The formation of chemical bond between C6 & C3 was achieved under solvolytic conditions of tosylate/triflate with variety of internal/external nucleophiles. The C3 & C6 bond formation was demonstrated by treating the tosylate with LiAlH$_4$ to furnish substituted 3-oxahexacyclo[5.5.0.0^{2,6}.0^{4,11}.0^{5,9}.0^{8,12}]dodecane **6**.[9] The formation of **6** could be explained via tandem cyclization trigered by an internal oxy anion.

Scheme-2
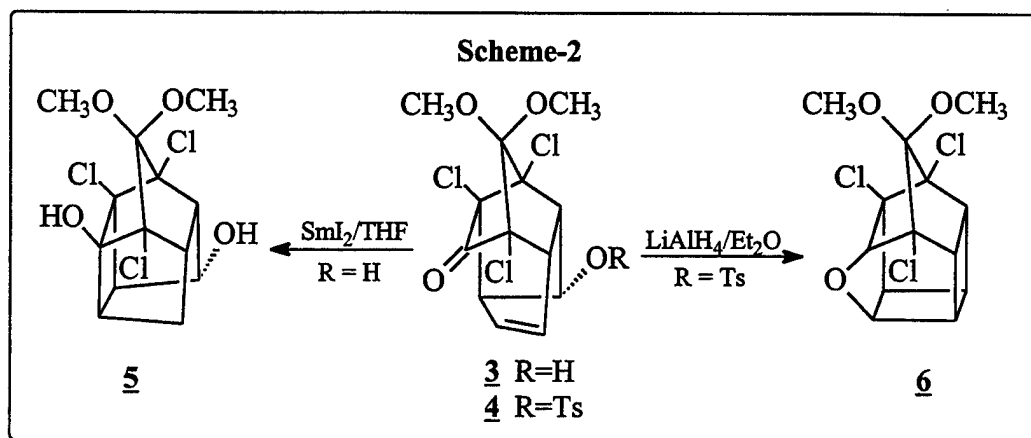
The solution of tosylate **4** in aqueous dimethylformamide (DMF) furnished formate **7**[10] in 74% yield. The fromation of formate can be explained via generation of a carbenium ion which is trapped by DMF to generate alkoxyformiminium intermediate followed by hydrolysis to give the corresponding formate. Treatment of formate **7** with Jones reagent (aqueous. Chromic acid) furnished corresponding dione **8** in respectable yield. Molecular mechanics calculations carried out on **8** suggested carbonyl carbons distance 2.54 A is within the range of carbon-carbon bond formation. It is anticipated that the dione **8** should furnish the homopentaprismane when it is subjected to variety of coupling reagents. The preliminary coupling experiment
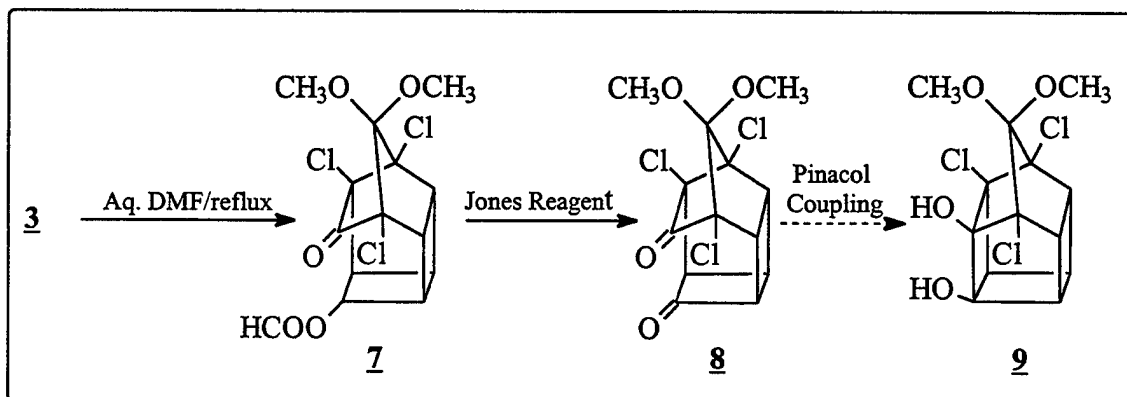
using Corey's reagent [Mg(Hg)/TiCl$_4$][11] was very promising. The experimental efforts to optimize the yield are

in progress. The coupling experiments using Sm-I$_2$-MeOH/Sm-I$_2$-Ti(Opr-i)$_4$/MeOH[12]and vanadium (II)[13] are in progress.

The formation of chemical bond was further demonstrated by treatment of **3** with Ph$_3$P/X$_2$/CH$_2$Cl$_2$ to furnish **10** which is suitable for intramolecular Barbier reaction to furnish substituted homopentaprismanes. Exposure of 10 (X= Br) to n-BuLi at room temperature furnished mixture of compounds which did not indicate the presence of starting material by tlc. The intramolecular Barbier-type reaction on **10** using SmI2/Fe(III) is
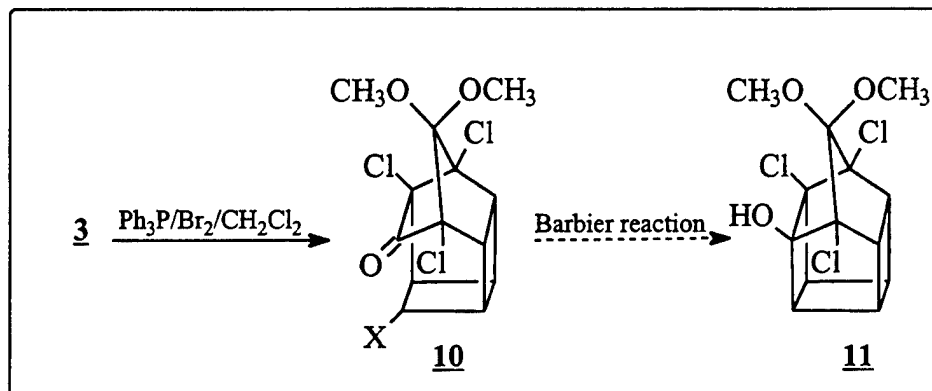
being considered for carbon-carbon bond formation.

BICYCLOPROPYLIDENE:. Based on theoretical Isp and heat of formation calculations, bicyclopropylidene (**15**) is a potential candidate to increase the performance of rocket fuel. Bicyclopropylidene is a precursor for "Triangulane" class of strain ring compounds. Many synthesis of bicyclopropylidene have been reported in the literature[14] but require major modification for pilot plant scale up. Meijere and coworkers[15] synthesized 1-cyclopropyl-1-cyclopropanol (**13**) from methyl cyclopropanecarboxylate (**12**) using Kulinkovich's methodology.[16] At Phillips Laboratory, the synthesis of 1-cyclopropyl-1-cyclopropanol (**13**) was modified without any loss of yield by generating the Grignard reagent (C$_2$H$_5$MgBr) *in situ*. This modification avoids handling of preformed hygroscopic and pyrophoric Grignard reagent used by Meijere[15]. The direct attempt to dehydrate alcohol using DMSO[17] or HMPT[18] at high temperature (~ 160°C) furnished cyclopropyl

28
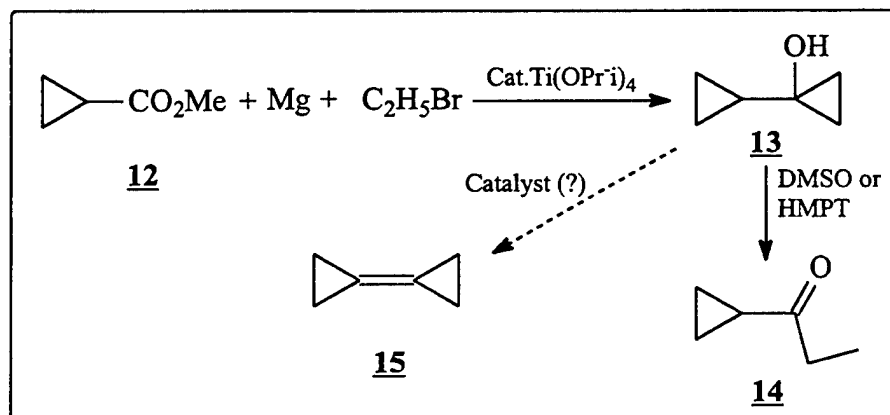
ethyl ketone **(14)**. Efforts are underway to dehydrate alcohol to bicyclopropylidene directly using different catalyst.

REFERENCES

1. For a comprensive review on prismanes: Mehta, G. in *"Strain and its Implications in Organic Chemistry"*, Meijere, A. de, Blechert, S. Eds. NATO ASI Series, Kluwer Academic Publishers; Dordrecht **1989**, <u>273</u>, 269; Mehta, G., Padma, S. *"Carbocyclic Cage Compounds"* Osawa, E., Yonemitsu, O. Eds, VCH Publishers, Inc., NY **1992**; Forman, M. A., Dailey, W. P. *"Organic Preparation and Procedures Int.* **1994,** <u>26</u>, 291.
2. Katz, T. Z., Acton, N. J. Am. Chem. Soc. 1973, 95, 2738; Turro, N. J., Ramamurthy, V., Katz, T. J. *Nouv. J. Chim.* **1977,** <u>1</u>, 363.
3. Eaton, P. E., Cole, T. W., Jr., *J. Am. Chem. Soc.* 1964, 86, 962; Eaton, P. E., Cole, T. W., Jr., *J. Am. Chem. Soc.* 1964, 86, 3157.
4. Eaton, P. E., Or, Y. S., Branca, S. J. J. Am. Chem. Soc. 1981,103, 2134; Eaton, P. E., Or, Y. S., Branca, S. J., Ravishankar, B. R., *Tetrahedron* **1986,** <u>42</u>, 1621.
5. Dauben, W. G., Cunningham, A. F. *J. Org. Chem.* **1983,** <u>48</u>, 2842.
6. Suri, S. C. *Tetrahedron Lett.* **1990,** <u>31</u>, 3695.
7. Marchand, A. P., LaRoe, W. D., Sharma, G. V. M., Suri, S. C., Reddy, D. S., *J. Org. Chem.* 1986, <u>51</u>, 1622.
8. Suri, S. C., Hardcastle, K. I., *J. Org. Chem.* **1992,** <u>57</u>, 6357.
9. Suri, S. C. *J. Org. Chem.* **1993,** <u>58</u>, 4153.
10. Suri, S. C., Rodgers, S. L., Radhakrishnan, K. V., Nair, V., *Synthetic Communications*, **1996,** <u>26</u>, 1031.
11. Corey, E. J., Danheiser, R. L., Chandrasekaran, S. *J. Org. Chem.* **1976,** <u>41</u>, 260.
12. Yanada, R., Negoro, N., Yanada, K., Fujita, T. *Tetrahedron Lett.* **1997,** <u>38</u>, 3271.
13. Raw, A. S., Pederson, S. F. *J. Org. Chem.* **1991,** <u>56</u>, 830.
14. Le Perchec, P., Conia, J. M., *Tetrahedron Lett.* **1970,** 1587; Schipperijn, A. J. *Rec. Trav. Chim. Pays-Bas* **1971,** <u>90</u>, 1110; Schipperijn, A. J. And Samel, P. . *Rec. Trav. Chim. Pays-Bas* **1973,** <u>92</u>, 1121; Fitzer, L. And Conia, J. M., *Angew. Chem.* 1973, <u>85</u>, 347; Fitzer, L. And Conia, J. M., *Angew. Chem.* 1973, <u>85</u>, 332; Schmitt, A. H., Schirmer, Conia, J. M., *Chem. Ber.* 1976, <u>109</u>, 2588; Weber, W., De Meijere, A., Synthetic Communications, **1986,** <u>16</u>, 837.
15. De Meijere, A., Kozhushkov, S. I., Spaeth, T., Zefirov, N. S., *J. Org. Chem.* **1993,** <u>58</u>, 502.
16. Kulinkovich, O. G., Sviridov, S. V., Vasilevski, D. A., Savchenko, A. I., Pritytskaya, T. S., *Zh. Org. Chem.* **1991,** <u>27</u>, 294; *J. Org. Chem.* **1991,** <u>27</u>, 294.; Kulinnkovich, O. G., Sviridov, S. V., Vasilevski, D. A., *Synthesis* **1991,** 234.
17. Traynelis, V. J., Hergenrother, W. L., Hanson, H. T., Valicenti, J. A., *J. Org. Chem.*, **1964,** <u>29</u>, 123.
18. Monson, R. S., Priest, D. N., *J. Org. Chem.*, **1971,** <u>36</u>, 3826.

29

EXTRA-HIGH ENERGY OXIDIZERS AND FUELS AND COMBINATORIAL SYNTHESIS OF ENERGETIC MATERIALS

R. J. Schmitt and J. C. Bottaro
Functionally Designed Materials Program
Chemistry and Chemical Engineering Laboratory
SRI Intentional, Menlo Park, CA 94025
(415) 859-5579 Voice
(415) 859-4321 Fax
Robert_Schmitt@qm.sri.com e-mail

SRI International's program is focused on the discovery and synthesis of new, extra-high energy oxidizers and fuels for the HEDM program. Our goals include the preparation of new compounds having unusual bonding to yield high energy, dense materials for propellant applications. Our requirements include simplicity of synthesis and good long-term stability to make these materials viable candidates for propellant applications. We have directed our work toward the synthesis of highly energetic fuels and fuel additives. Our focus this year has been on the synthesis of acetylene based materials as acetylenes have a higher heat of formation per gram than cubane or quadracyclane and are vastly simpler to prepare in bulk and on developing the new concept of combinatorial type synthesis of energetic materials..

Our goals for this program are:

- Develop new fuels and oxidizers for propellant applications. The materials must
    - Be simple to make (cubane is hard)
    - Be storable and usable
    - Have significantly improved performance over conventional materials
    - Develop burn rate accelerators to improve and accelerate combustion (better fuel efficiency)
- Invent new compositions of matter to meet needs.
- Use "non-classical" combinatorial methods to make materials

We have synthesized several new boroacetylene derivatives having exceptionally high energy density for use as fuels. The new boron derivatives are capable of taking advantage of the high heat of combustion of boron and acetylene while having a high

30

intrinsic positive enthalpy of formation. We hope that the use of boron-acetylide compounds will provide improved combustion of boron and solve some of the combustion issues associated with the use of boron. Next, we prepared a series of new acetylene based compounds having good (>0.9 g/cc) densities. The role of these acetylene compounds it to use them as the fuel or fuel additive in hydrocarbon fuels. We invite members of this community to test samples of these materials in propellant applications.

We list in Tables 1 and 2 the calculated performance values of various organic compounds. Table 1 lists the "standard" hydrocarbons, those usually considered for application in hydrocarbon systems. In table 2, we provide the calculated heat of formation and performance figures for compounds that have been prepared as well as our proposed new materials.

COMBINATORIAL APPROACH TO ENERGETIC MATERIALS

The current synthesis strategy for energetic materials is to conceive of a new material, to develop a route, and then to synthesize the compound. This neglects the possibility of serendipity (synthesis of a compound that wasn't predicted or planned on, see for example the synthesis of the CL-20 cage structure). This one at a time, custom synthesis method has been highly effective in the development of energetic materials. Dinitramide and it's salts is an example of this approach.

However, the strategy for synthesis in the pharmaceutical and biotherapeutics industry has undergone a paradigm shift by the use of combinatorial methods for the synthesis of new compounds. A combinatorial approach allows the preparation of many derivatives of a desired molecular structure for fast screening. A combinatorial approach has not been used for the synthesis of basic new ring structures, but complex structures can be built up using known functional parts. We suggest that a combinatorial approach should be applied to the synthesis of energetic compounds.

Combinatorial approaches are hardly new. In reality, at a certain level, this approach has been used when we vary the conditions of a reaction (solvent, pH, temperature, time, etc.) to optimize the yield of reaction. We also do combinatorial work when we combine different anion/cation pairings. Neither of these are formally described as combinatorial nor is the approach optimized to address the synthetic needs.

31

We believe that combinatorial approaches can be used for the synthesis of new energetic materials. Energetic fuels and oxidizers can be prepared this way. To build up a molecular structure based on known materials we could:

- Pick "interesting" energy dense functional groups
    - Use as building blocks

- Choose energetic functional groups that allow simple synthesis

- Use combinatorial approach to make molecules
    - Many different functional groups
    - Many different combinations
- Determine most desirable materials
    - Physical properties
    - Energy density
    - Oxidizer or fuel or combination of both

- Especially useful for salts or polymers (block or random)
    - Ion-exchange of anions and cations easy
    - Many good anions available
    - Energetic borates are good anions
    - Energetic groups in polymer backbones and side-chains

- Acetylide is an energy-dense moiety
    - Acidic hydrogen on acetylene provides convenient handle for synthetic modification
    - Acetylide is a convenient nucleophile for attack on metal-halides and on substituted organic halides
- Amines are good nucleophiles
    - Propargyl is easily substituted onto amines
    - Energetic cations can be prepared

Examples of energetic anions and cations are shown in table 1. This is a short set of charged moieties, but they are illustrative of the types of systems that are currently used in the energetics field for combinatorial type synthesis. This list can be expanded as well as a similar lists for energetic functional groups for fuels or oxidizers and a list for densiphores. As we develop new reactions for novel combinations of energetic functionalities, the cardinality of our combinatorial basis set will be expanded.

The combinatorial approach presented here is not yet completely thought out, but it offers a way of thinking and categorizing the synthesis of new materials. Ultimately, it may result in more choices of energetic materials if correctly applied.

Acknowledgments

TABLE 1: THE CLASSICS
Combustion With Oxygen

Compound	I_{sp}	Flame Temp.	H_f	H_f
	sec	K	kcal/mol	cal/gram
RP-1	300	3670		
Quadracyclane (C_7H_8)	308	3906	+60.5	658
Cubane (C_8H_8)	317	4039	+139	1,336
Acetylene (C_2H_2)	327	4116	+54.2	2,084

TABLE 2: PROPOSED NEW MATERIALS
Combustion With Oxygen

Compound	I_{sp} sec	Flame Temp. K	H_f kcal/mol	H_f cal/gram
$C_4H_4N_4$	304	3993	130 [a]	1,204
C_6H_6O	314	3958	75 [a]	798
C (Polycarbon)	334	6150	30 [c]	2,500
$C_{12}H_8N_4$	295		+43 [a]	688
$C_{24}H_{24}NB$	316	3967	440 [a]	1,306
$C_{28}H_{32}NB$	313	4023	400 [a]	1,017
C_9H_9N	316	4050	168 [a]	1,282
C_6H_7N	316	3947	111	1,196
$C_{20}H_{16}NB$	322	4198	480 [a]	1,708
$C_9H_6N_2$	301	3027	134 [a]	944
C_3H_2 (polymer)	312	4107	50	1,321
C_7H_5 (polymer)	308	4082	98	1,099
$C_{21}H_{18}N_6$	303	3986	331	936
$C_{16}H_{16}N_2$	315	3986	292	1,238
$C_{18}H_{16}N_2$	315	4096	347	1,335
C_5H_2 (polymer)	315	4377	105	1,697
$C_{11}H_6$ (polymer)	312	4192	206	1,490
$C_{12}Al_2$ (polymer)	306	4823	349	1,837
$C_{15}H_6Al_2$ (polymer)	311	4385	334	1,441
$HC{\equiv}CCH_2NH_2$	316		130	
$HC{\equiv}CCH_2OH$	305		10.7	
$(HC{\equiv}CCH_2O)2$	330		145	
$CH_3C{\equiv}C-CC{\equiv}CH_3$	318		104	
$C_2HN_4O_2F$ [b]	263	3761	32 [b]	242

[a] Calculated using Benson Additivity
[b] Monopropellant
[c] per carbon

TABLE 3: ANIONS AND CATIONS USED IN ENERGETIC MATERIALS

Cations	Anions
$N_2H_6^{+2}$	NO_3^-
NO^+	NO_2^-
M^{+n}	$N(NO_2)_2^-$
$N_2H_5^+$	ClO_4^-
NO_2^+	$C(NO_2)_3^-$
NH_3OH^+	
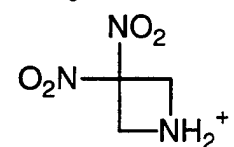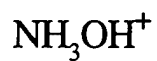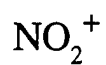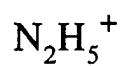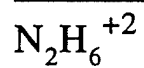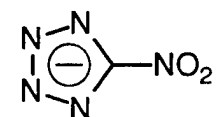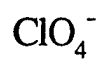
NEW METHODS FOR EXCITED STATES

Rodney J. Bartlett, Marcel Nooijen, Steve Gwaltney and Anatoli A. Korkin

Quantum Theory Project, University of Florida, Gainesville, Fl 32611-843

Recently, we have proposed and studied computationally a series of energetic molecules, as potentially interesting species for the HEDM program, e.g. nitrocyanide (I), nitrofulminate (II) and their trimeric forms, trinitrotriazine (III) and trinitrotriazine trioxide (IV) [1]. Related to this study, we have also investigated theoretically the mechanism of the gas phase reactions of NO (NO_2) and NCO radicals, which are key intermediate processes in the rapid reduction of nitrogen oxides ($RAPRENO_x$) [2] from the exhaust gases in the combustion of nitrogen containing fuels (Scheme 1).

For many of the potentially interesting energetic materials the "normal" synthetic route based on the ground state of substances are precluded because of the high reactivity of intermediates, expensive reagents, numereous steps and low yield of the final products. Although the idea of the direct attainment of energetic molecules via excited states is attractive, this way also has many practical limitations and hidden complications. Among other problems the questions to be answered are - how to predict (modify) the reactivity of excited species and how to direct the reaction toward a desired product. Compared to "ground state" chemistry, the mechanisms of photochemical reactions (chemistry of the molecules in electronically excited states) are far less known and based rather on qualitative orbital concepts (e.g. Woodward-Hoffman rules) and unproven semi-empirical studies rather than on rigorous *ab initio* theoretical investigations. Until recently there were no such methods, which allow both accurate computations of the excited state energies and the associated analytical gradients. This is now possible with the ACES II program.

Our particular emphaises over the last year and into the near future is the development of the similarity-transformed equation of motion coupled-cluster method (STEOM-CC) (Scheme 2), which permits accurate results to be obtained for quite large molecules [3]. Furthermore, it is conceptually appealing, as it retains the simplicity of the mono-excited CI method, yet now for fully correlated results.

An illustration is offered by the pyridine molecule (Table 1). The EOM-CCSD method requires the diagonalization of a matrix of dimension equal to single and double excitations. For Rydberg states and many other states dominated by single excitations, EOM-CCSD is quite accurate. However, for certain valence states and others with substantial double excitation character, some consideration of triple excitations seems warranted. The newest methods we have developed for this purpose are the iterative EOM-CCSDT-3 and its perturbation analogue, EOM-CCSD(T~) [4]. However, these highly accurate methods are also expensive. STEOM-CC has the advantage that at least for singly excited states it implicitly includes a triple correction [5], such that results fall between EOM-CCSD and EOM-CCSD(T~). In the final stage of a STEOM calculation excited states are obtained by diagonalizing a transformed Hamiltonian over the space of singly excited determinants. The resulting method is highly efficient as shown by the timing for the pyridine calculation (Table 2). We have also used STEOM-CC in our study of the potential oxidizer, NO_4^+, · which has a high multi-reference character [6]. We are currently working on analytical gradients for the STEOM-CC method.

[1] (a) A.A. Korkin, J. Leszczynski, R.J. Bartlett, J. Phys. Chem., 100 (1996) 19846; (b) A.A. Korkin, R.J. Bartlett, J. Am. Chem. Soc. 118 (1996) 12244; (c) A. A. Korkin, A. Lowrey, J. Leszczynski, D.B. Lempert, R.J. Bartlett, J. Phys. Chem., 101 (1997) 2709.

[2] (a) R.A. Perry, D.L. Sibers, Nature, 324 (1986) 657; (b) J.A. Miller, C.T. Bowman, Int. J. Chem. Kinet., 23 (1991) 289.

[3] M. Nooijen, R.J. Bartlett, J. Chem. Phys., 106 (1997) 6441; (b) M. Nooijen, R.J. Bartlett, J. Chem. Phys., 106 (1997) 6441.

[4] (a) J.D. Watts, R.J. Bartlett, Chem. Phys. Lett. 258 (1996) 581. (b) J.D. Watts, S.R. Gwaltney, R.J. Bartlett, J. Chem. Phys. 105 (1996) 6979.

[5] M. Nooijen, R.J. Bartlett, J. Chem. Phys. (submitted)

[6].A.A. Korkin, R.J. Bartlett, M. Nooijen, K.O. Christe (to be published).

I: $\Delta H^{o}_{f} = 60$ kcal/mol

II: $\Delta H^{o}_{f} = 71$ kcal/mol

III: $\Delta H^{o}_{f} = 46$ kcal/mol

IV: $\Delta H^{o}_{f} = 108$ kcal/mol

NCO + NO

33.3

13.9

13.1

$N_2 + CO_2$

NCO + NO_2

35.4

11.2

11

2.4

0.8

13

12

$N_2O + CO_2$

8

Scheme 1

39
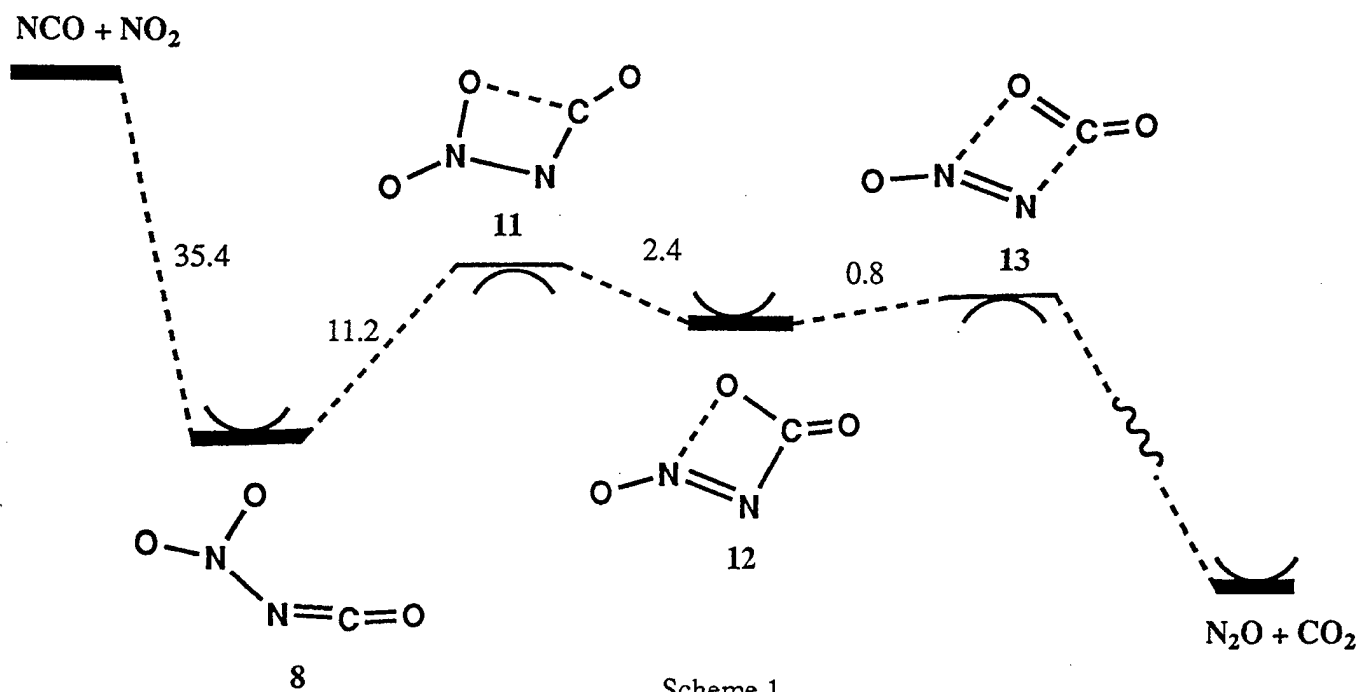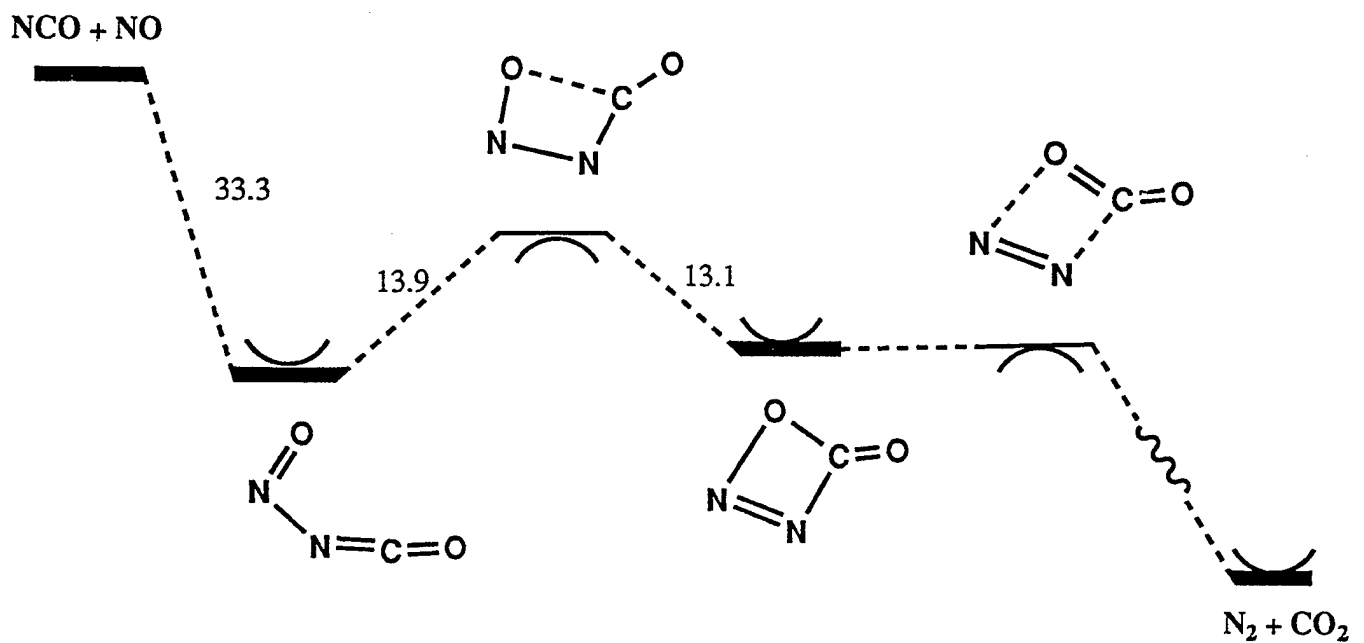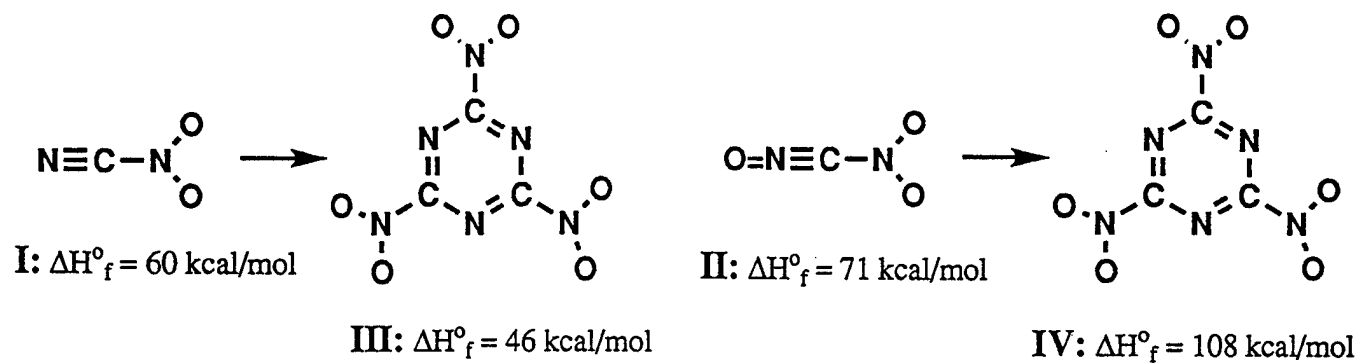
1. Similarity Transformed Equation-of-Motion Coupled-Cluster Theory (STEOM-CC).

Perform two transformations of second-quantized Hamiltonian such that excitation components of new Hamiltonian are zero.

1. Solve CCSD equations: $\langle \Phi_\lambda | e^{-T} H e^{T} | 0 \rangle = 0$.

2. Transform Hamiltonian: $\bar{H} = e^{-T} H e^{T}$.

3. a. Choose active *occupied* orbitals and solve IP-EOMCC equations (diagonalize $\bar{H}$ over *1h* and *2h1p* configurations.) $\longrightarrow S^{-}$.

   b. Choose active virtual orbitals and solve EA-EOMCC equations (diagonalize $\bar{H}$ over *1p* and *2p1h* conf.) $\longrightarrow S^{+}$.

4. Obtain doubly transformed Hamiltonian

$$G = \left\{ e^{\left(S^{-} + S^{+} \right)} \right\}^{-1} \bar{H} \left\{ e^{\left(S^{-} + S^{+} \right)} \right\} \tag{1}$$

5. Diagonalize G over very small set of configurations.

   a. DIP-STEOM: Diagonalize over $\hat{i}\hat{j}|0\rangle$ $\longrightarrow$ states with 2 electrons less than $|0\rangle$.

   b. DEA-STEOM: Diagonalize over $\hat{a}^\dagger \hat{b}^\dagger |0\rangle$ $\longrightarrow$ states with 2 electrons more than $|0\rangle$.

   c. EE-STEOM: Diagonalize over $\hat{a}^\dagger \hat{i} |0\rangle$ $\longrightarrow$ excited states.

STEOM-CC: Efficient and accurate method to include both dynamical and non-dynamical correlation.

Sheme 2

Table 1.

Pyridine singlet excitation spectrum for valence states. Excitation energies are given in eV, oscillator strengths in a.u., between brackates.

State	EOMCC		STEOM		CASPT2	Exp.
	SD	SD(T)	PT	CC		
$^1B_1$ n→π*	5.17 (0.05)	4.80	5.01 (0.006)	4.91 (0.006)	4.91 (0.009)	4.59 (0.003)
$^1B_2$ π→π*	5.22 (0.029)	4.81	5.01 (0.026)	4.82 (0.023)	4.84 (0.018)	4.99 (0.029)
$^1A_2$ n→π*	5.61	5.26	5.36	5.31	5.17	5.43
$^1A_1$ π→π*	6.70 (0.006)	6.36	6.69 (0.013)	6.62 (0.006)	6.42 (0.005)	6.38 (0.085)
$^1B_2$ π→π*	7.48 (0.52)	7.14	7.37 (0.65)	7.29 (0.61)	7.23 (0.82)	7.22 (0.90)
$^1A_1$ π→π*	7.50 (0.23)	7.26	7.43 (0.67)	7.37 (0.66)	7.48 (0.64)	

Table 2.

Timing and dimensions for pyridine calculation on Cray YMP.

Procedure	Relevant dimensions	Time (min : sec)
Integrals		10:39
SCF	169 AO's	00:57
Transformation + Sorting	15 occupied, 142 virtuals	14:14
CCSD/MBPT(2)	598,659	21:55/ 0
H-bar		03:55
Lambda/MBPT(2)	598,659	16:15/ 0
IP-EOMCC	9,125; 9 eigen vectors	00:19
EA-EOMCC	82,426; 18 eigenvectors	12:55
G		01:05
STEOM+ properties	667; 598,659	02:25

THEORY AND SYNTHESIS OF NEW HEDM RELATED MATERIALS

K. CHRISTE, W. WILSON, G. DRAKE, M. PETRIE, J. SHEEHY and J. BOATZ

**HUGHES STX AND PROPULSION DIRECTORATE, PHILLIPS LABORATORY,
EDWARDS AIR FORCE BASE, CA 93524**

This paper describes some of the work carried out during the past year by both the HEDM Synthesis Group at the Phillips Laboratory and the assoiated program at USC, which is partially supported by the Air Force. It exemplifies the benefits and synergism which can be derived from the successful combination of theory and synthesis.

In the area of novel anions, our study of the novel and elusive POF_4^- anion was completed. This anion, which is stable only at -140 °C, was characterized, in collaboration with Prof. Schrobilgen from McMaster University, by multinuclear NMR spectroscopy. In collaboration with Dr. Dixon from Pacific Northwest Laboratories, the geometry, NMR shifts, activation barriers for the Berry inversion, vibrational spectra, force field and thermodynamic data were calculated. In the course of our efforts to rationalize the very different dismutation behavior of POF_4^- and isoelectronic SOF_4, (POF_4^- dismutates at -140 °C to $PO_2F_2^-$ and PF_6^-, whereas SOF_4 does not dismutate at all to SO_2F_2 and SF_6), it was shown by our ab initio calculations that the thermodynamic data published for several phosphous and sulfur oxofluorides are in error by as much as 60 kcal/mol. It was shown that the different dismutation behavior of POF_4^- and SOF_4 is due to mechanistic and not thermodynamic reasons. The results were published in the Journal of the American Chemical Society, **1997**, *119*,3918.

In the area of high coordination number chemistry, we have succeeded to prepare and characterize a number of new heptacoordinated anions. Among these are IF_5^{2-}, IF_5O^{2-}, $IF_5O_2^{2-}$, IF_7^{2-}, SbF_7^{2-}, and BiF_7^{2-}. Since all these ions possess very little solubility and therefore are not amenable to crystal growing or NMR studies, they were characterized by infrared and Raman spectroscopy. Ab initio calculations, carried out by Dr. Dixon, were used to confirm their identities, stuctures and vibrational assignments. The IF_5^{2-} anion contains two and IOF_5^{2-} contains one sterically active free valence electron pairs

on the iodine central atom. They are only the second known examples of pentagonal planar and pentagonal pyramidal AX_5E_2 and AX_5OE species, respectively. The $IF_5O_2^{2-}$ ion is the first known example of an AX_5O_2 species and contains two axial oxygen atoms in trans positions. The IF_7^{2-} anion possesses one free valence electron pair on the iodine central atom, but this pair is sterically inactive. The resulting structure is that of a monocapped octahedron which normally is found only for heptacoordinated transition metal compounds. The SbF_7^{2-} and BiF_7^{2-} anions represent the first known examples of heptacoordinate AX_7 pnictogen species and are very remarkable because SbF_6^- and BiF_6^- had been known for a long time. More details on this work are given in the poster abstract by Dr. Drake.

In the process of synthesizing $[N(CH_3)_4]_2IF_5O_2$ from $N(CH_3)_4IF_4O_2$ and F^-, it became necessary to better characterize this salt. This shock sensitive material, which also explodes on heating, exhibits very interesting polymorphism, phase transitions and rotational disorder. The crystal structures and Raman spectra of its low temperature and room temperature phases were studied and demonstrate that the phase transitions in this molecule are due to the onset of free ion rotation, rather than positional disorder of the rotational oscillation axes. This finding confirms a proposal, made in 1930 by Linus Pauling and repeatedly critized since then. These results were summarized in manuscript form for publication in Inorganic Chemistry.

Attempts were made to synthesize NF_2-substituted fullerenes by reacting C_{60} with NF_2 radicals, which were generated by uv-photolysis of N_2F_4. However, no NF_2-substituted fullerenes could be obtained under these conditions. The only product obtained were fluorinated fullerenes and dinitrogen.

In collaboration with Dr. Korkin and Prof. Bartlett from the University of Florida, the feasibility of preparing NO_4^+, a bicyclic spiro compound of D_{2d} symmetry, was studied by ab initio calculations. It was found that this cation is vibrationally stable, having a heat of formation of 370 kcal/mol and an N-O bond length of 1.349 Å, but that its barrier towards decomposition to NO_2^+ and groundstate dioxygen is less than 20 kcal/mol due to potential energy surface crossings. Therefore, no experimental efforts were undertaken to synthesize this molecule. In collaboration with the USC team (Drs. Wagner, Rasul, Prakash and Olah), the novel trimethylperoxonium cation was prepared

44

by methylation of dimethylperoxide with methylfluoride and SbF_5 in SO_2 solution and was characterized by multinuclear NMR spectroscopy. The identity and chemical NMR shifts were confirmed by ab initio calculations. A manuscript has been written and submitted to JACS for publication.

Several extremely energetic, but also extremely shock sensitive, triazidocarbenium salts have been prepared and characterized. These incude $C(N_3)_3^+N(NO_2)_2^-$, $C(N_3)_3^+ClO_4^-$ and $C(N_3)_3^+BF_4^-$. They were characterized by vibrational and NMR spectroscopy and the data were confirmed by ab initio calculations. Their heats of formation were calculated as 252, 218 and -128 kcal/mol, respectively, and show that their energy densities approache that of hydrazoic acid. Theoretical calculations and synthesis efforts on the protonation of the $C(N_3)_3^+$ cation were also carried out and show that protonation should occur on the alpha nitrogen atom and that the protonated dication should be vibrationally stable. The results were summarized in manuscrpt form and submitted to JACS for publication.

Structural studies of three new monopropellant candidates, $H_3NO \cdot H_3NOH^+C(NO_2)_3^-$, $K^+O_2N-N-CN^-$, and $H_2NO-CH_2-ONH_3^+C(NO_2)_3^-$ were carried out, using single crystal x-ray diffraction, vibrational spectrocopy and ab initio calculations. More details on this work are given in Dr. Petrie's poster abstract.

In collaboration with Dr. Zhang from USC, the crystal structures of a number of highly energetic cations, including ClF_6^+, BrF_6^+, KrF^+, $FN-NF_2^+$ and ONF_2^+, will be studied. For this purpose, most of these salts have been synthesized, and a special low-temperature device for the handling and mounting of unstable and air-sensitive materials has been designed and built.

In collaboration with Dr. Hoge from USC, the synthesis of ClF_5O is being pursued. This compound would be the highest performing, earth-storable liquid oxidizer with an I_{sp} which is about 10 sec higher than ClF_5. The potential of HOF to act as a powerful oxygenating agent will be explored, and construction of the necessary hardware for this program has been about 60% completed.

SYNTHESIS OF HIGH-ENERGY DENSITY MATERIALS BASED ON STRAINED-RING COMPOUNDS

William P. Dailey
Department of Chemistry
University of Pennsylvania
Philadelphia, PA 19104-6323

We have been investigating the synthesis of new strained-ring hydrocarbons as potential high energy fuels and fuel additives. Cyclobutane contains almost exactly the same amount (26.5 kcal/mol) of strain energy as cyclopropane (27.5 kcal/mol) yet four membered rings are chemically and thermally much more stable than cyclopropane derivatives. We have investigated two different areas this past year which focus on the synthesis of molecules that contain multiple four membered rings.

We have been interested in the synthesis of higher order prismanes[1] and have recently reported the preparation of bishomohexaprismanedione (3).[2] Our synthesis started with conversion of the conveniently available bishomosecoheptaprismanedione (1)[3] to diene 2 followed its further manipulation to 3. As we reported, diene 2 does not undergo [2+2] photochemical ring closure to produce the bishomoheptaprismane ring system of 4 under either sensitized or direct irradiation conditions. We attributed this failure to the 80 kcal/mol increase in strain energy which accompanies the transformation of 2 to 4. This value is above the 55 kcal/mol threshold suggested as the maximum increase in strain energy tolerated in the photoreaction.
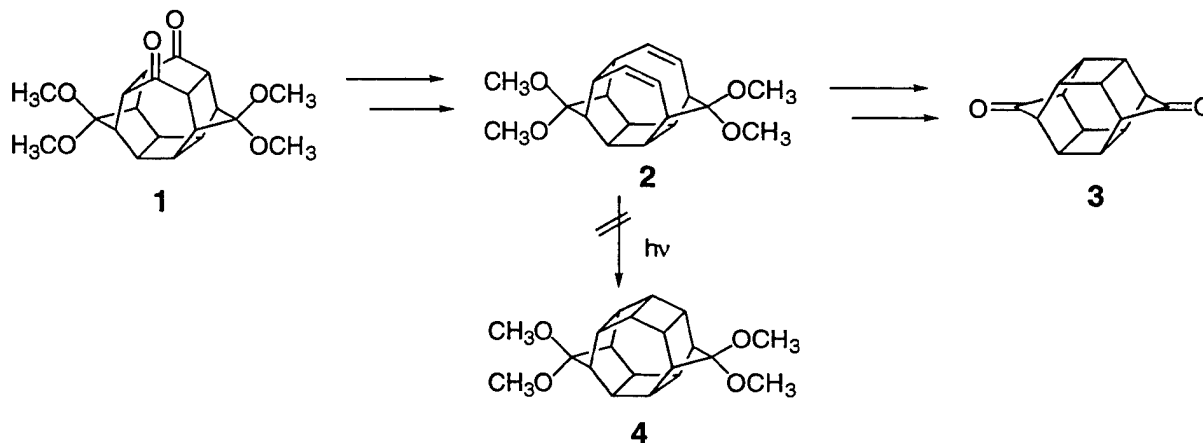
Here we report the conversion of diene 2 to tetraene 10. The photochemistry of tetraene 10 and its conversion to 11 the previously unreported hexacyclo[8.5.1.1^{4,7}.0^{5,14}.0^{6,12}.0^{11,15}.0^{16,17}]-heptadecane ring system of 14 are described.

Fragmentation of 1 to diene 2 was accomplished via a multi-step sequence similar to that reported for the compound lacking methoxy groups.[4] Diketone 1 was converted to diol in high yield using sodium borohydride. Treatment of the diol with mesyl chloride gave the dimesylate 6

which when treated with sodium iodide in 2-butanone produced a diastereomeric mixture of diiodides **7** and **8** in good yield. If desired, the two diastereomers could be separated by careful flash chromotagraphy but the mixture was routinely carried through to the next reaction. Reductive fragmentationof the diastereomeric mixture of diiodides **7** and **8** with 2:1 sodium-potassium alloygave the diene **2** in high yield. Mild hydrolysis using aqueous oxalic acid gave a high yield of ketone **9**. When irradiated using a medium pressure mercury arc through Pyrex, **9** smoothly underwent decarbonylation/fragmention to produce tetraene **10** in 60% yield.
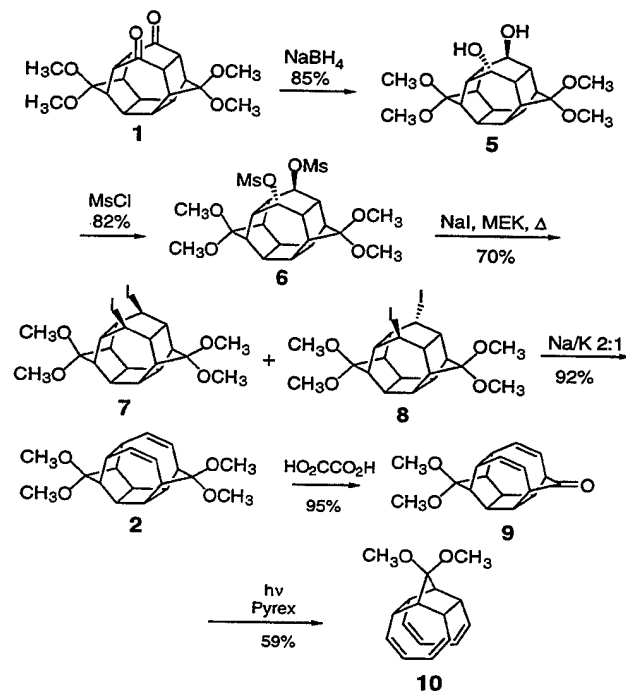
Further direct irradiation ($\lambda > 220$ nm) of tetraene **10** produced the [4+4]cycloadduct **11** in low yield. The identity of **11** was determined by analysis of the ^{1}H and ^{13}C NMR spectra which revealed the symmetrical nature of the compound. Diene **11** was resistant to further photochemical ring closure and yielded no traces of the homoheptaprismane ring system of **12** even upon extended photolysis. This result was expected based on the large increase in strain energy for the reaction.
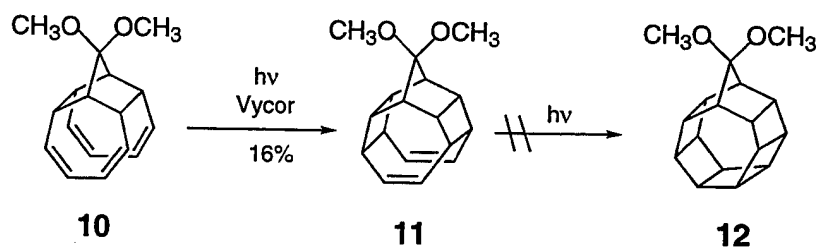
We were intrigued by the possibility of performing tandem Diels-Alder reactions[5] with tetraene **10**. By analogy to the pagodane synthesis we have investigated the reaction of **10** with maleic anhydride and have found that the reaction proceeds in excellent yield to give **13**, the domino Diels-Alder adduct. Analysis of the crude reaction mixture by ^{1}H NMR produced no evidence for any other isomer in the reaction. The stereochemistry of the product was confirmed by single crystal x-ray analysis, although the R factor was poor. Diene **14** was produced in modest yield via a oxidative decarboxylation. Hydrolysis gave ketone **15** which was subjected to single crystal x-ray analysis. For comparison, the structure of **15** was calculated using ab initio molecular orbital theory at the HF/6-31G* level and a comparison of some selected bond lengths are shown in Table I. The agreement is quite satisfactory.

Table I. Experimental and Calculated Bond Lengths in **15**.

Bond	X-ray(Å)	HF/6-31G*
C1-C2	1.568	1.571
C1-C5	1.548	1.545
C4-C5	1.544	1.545
C5-C6	1.482	1.507
C6-C7	1.305	1.319
C4-C15	1.536	1.551
C10-C11	1.528	1.523
C11-O1	1.208	1.186
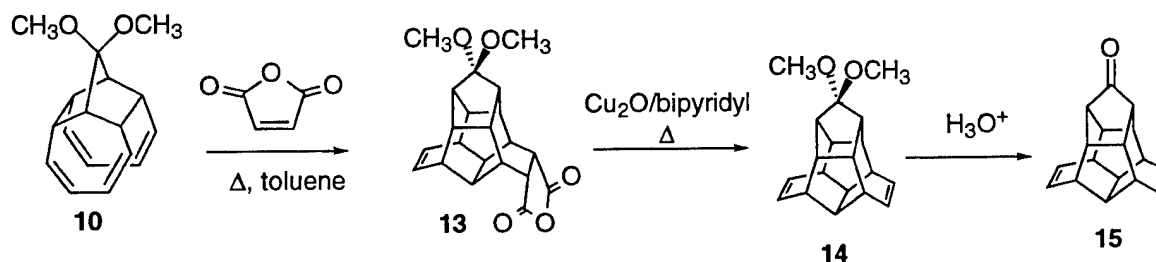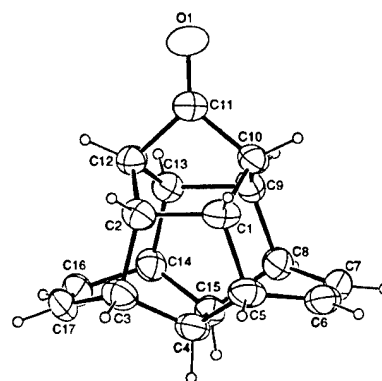
A second area of study concerns the conversion of [1.1.1]propellane (**16**) to stable high energy materials. The remarkably direct Szeimies synthesis[6] of [1.1.1]propellane (**16**) has allowed the investigation of many reactions of this compound on a preparative scale. The Szeimies method involves addition of dibromocarbene to commercially available 3-chloro-2-(chloromethyl)-1-propene (**17**) followed by methyl lithium induced ring closure of 1,1-dibromo-2,2-bis(chloromethyl)cyclopropane (**18**).
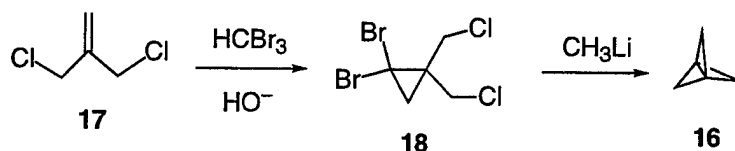
We recently reported an optimized protocol for the preparation of large quantities of intermediates **17** and **18**.[7]

Several of the compounds that can be derived from [1.1.1]propellane and that may be useful as high energy densitry materials are shown below along with their calculated heats of formation and predicted I_{sp} values. All of these compounds have been prepared, although procedures for efficient large scale preparation are still under development.

ΔH_f = 83 kcal/mol
I_{sp} =316.6

ΔH_f = 51 kcal/mol
I_{sp} =313.9 sec

ΔH_f = 45 kcal/mol
I_{sp} =311.2

ΔH_f = 95 kcal/mol
I_{sp} =309.9

ΔH_f = 26 kcal/mol
I_{sp} =308.0
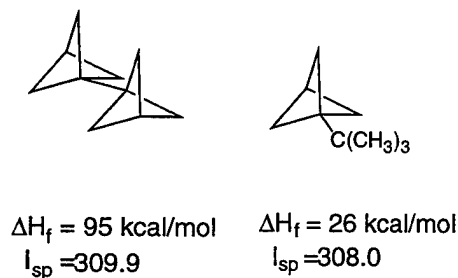
References

1   For three recent [n]-prismane reviews see a.) Forman, M. A.; Dailey, W. P. *Org. Prep. Proc. Int.* **1994**, *26*, 291. b.) Mehta, G.; Padma,S., *Carbocyclic Cage Compounds*, Osawa, E.; Yonemitsu, O., Eds., VCH Publishers Inc., 1992.

2   Golobish, T. G.; Dailey, W. P. *Tetrahedron Lett.* **1996**, *37*, 3239.

3   Forman, M. A.; Dailey, W. P. *J. Org. Chem.* **1993**, *58*, 1501.

4   Mehta, G.; Padma, S.; Jemmis, E. D.; Leela, G.; Osawa, E.; Barbiric, D. A. *Tetrahedron Lett.* **1988**, *29*, 1613.

5   Winkler, J. D. *Chem. Rev.* **1996**, *96*, 167.

6   Semmler, K.; Szeimies, G.; Belzner, J. *J. Am. Chem. Soc.* **1985**, *101*, 6410.

7   Lynch, K. M.; Dailey, W.P. *J. Org. Chem.* **1995**, **60**, 4666.

EPOXIDATION TRANSITION STATES AND STEREOSELECTIVITY MODELING

K. N. Houk

Department of Chemistry and Biochemistry, University of California,

Los Angeles, CA 90095-1569

Abstract: The transition structures for the epoxidations of ethylene by performic acid, dioxirane, and oxaziridine have been located with density functional theory methods using the Becke3LYP functional and 6-31G* basis set. All of the epoxidations have spiro transition states; those with performic acid and dioxirane are early and involve synchronous oxygen transfer, while that with oxaziridine is later with asynchronous oxygen transfer. The results from Becke3LYP/6-31G* theory are compared with MP2/6-31G* literature values. Substitution on ethylene by methoxy, methyl, vinyl, and cyano groups changes the transition state geometries toward asynchronous spiro structures. The activation energies are lowered by all substituents except the cyano group in reactions of performic acid and dioxirane. Experimental stereoselectivities are rationalized using transition state models based upon these transition structures.

Synthesis and Thermochemistry of Stable Nitrogen Peroxides and Nitrite Pseudochalcogenide Salts

Navamoney Arulsamy; D. Scott Bohle[*]; Bernhard Hansert; Patrick A. Sand, and Peter Schwerdtfeger[†]

Department of Chemistry, University of Wyoming, Laramie, Wyoming 82071-3838, USA; and

†Department of Chemistry, University of Auckland, Private Bag, Auckland, New Zealand.

Derivatives of the nitrogen oxides often exhibit marked kinetic stabilization and have positive enthalpies of formation. In is therefore not too surprising that many have found applications as propellants and explosives. In spite of their long history, and seemingly thorough characterization, there remain many unsolved problems and surprises associated with this class of compounds. Our research concerns two long standing problems in this field: 1) the characterization of stable nitrogen peroxides; and 2) the generation of pseudochalcogenide nitrite and nitrate analogues of Nitrosodicyanomethanide, $[ONC(CN)_2]^-$ and nitrodicyanomethanide, $[O_2NC(CN)_2]^-$. Salts of all of these species decompose exothermally with different DSC onset temperatures, and are possible HEDM candidates.

<u>Nitrogen peroxides:</u> There are two "simple" peroxyanions of nitrogen, peroxynitrite, $ONOO^-$, 1, and peroxynitrate, O_2NOO^-, 2. The characteristic properties of these two species are contrasted in Table 1; neither the free acid nor the salts of 2 have been isolated.[1] On the other hand, peroxynitrite was first muted almost a century ago in what is now a classic study by Baeyer and Villiger.[2] Since then, development of its systematic chemistry has been hampered by the absence of a suitable synthesis of pure, isolable peroxynitrite salts.[3] Recently we developed a synthesis of the tetramethylammonium peroxynitrite salt of 1 by treating $[NMe_4][O_2]$ with nitric oxide in liquid ammonia, equation 1.[4] This preparation allows for the isolation of $[NMe_4][ONOO]$ as an analytically pure bright yellow-orange hygroscopic solid.
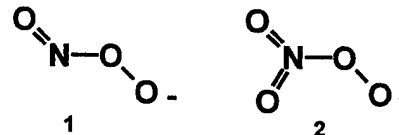
Table 1 Peroxynitrogen Anions Contrasted

	pKa	Stability($\tau_{1/2}$)		UV bands(nm)		δ ^{15}N NMR	Vibrational Bands(cm^{-1})	
		pH = 2	pH = 14	pH = 2	pH = 14		ν(NO$_x$)	ν(OO)
ONOO[−] pernitrite	7	1.5 sec	116 days	240(sh)	302	203.3	ν(NO) 1496	932
O₂NOO[−] pernitrate	5	30 min.	70 sec	220(sh)	-	-28.3	ν(NO$_2$)$_s$ 1301 ν(NO$_2$)$_a$ 1707	945

$$[NMe_4][O_2] \;+\; NO \;\xrightarrow[-40°C]{NH_3}\; [NMe_4][OONO] \quad \text{equation 1}$$
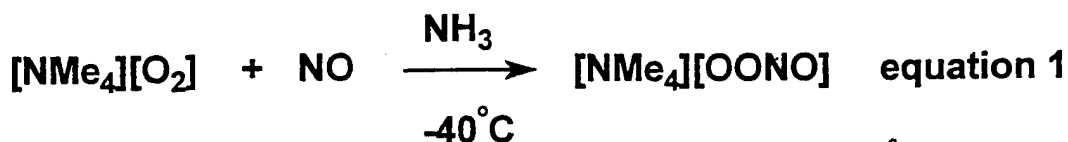
While the reaction in equation 1 is rapid and straightforward, the synthesis of the tetramethylammonium superoxide precursor has limited the quantities of $[NMe_4][ONOO]$ that can be prepared to ca. 500 mg per lot. This is due to the reaction conditions employed in the formation of $[NMe_4][OO]$, as a solid state mixture stirred in an oscillation reactor for three days, equation 2, which is followed by a tedious extraction of the tetramethylammonium superoxide by liquid ammonia.[5] A significant improvement on this method combines the two separate solid state stir/ammonia extraction steps into one solvent mediated procedure.[6] Thus a suspension of a slight excess of potassium superoxide and the pentahydrate of tetramethylammonium hydroxide are stirred in liquid ammonia at -40 °C for a minimum of 48 hours and the resulting pale yellow solution is separated from the off-white solid directly by a careful filtration. Pure tetramethylammonium peroxynitrite can then be readily prepared by treating this solution with dry nitric oxide followed by careful removal of the ammonia under vacuum. In this manner multi-gram quantities of tetramethylammonium peroxynitrite can be prepared and isolated. These hygroscopic materials have been stored for six months at -4 °C without significant decomposition.

$$[NMe_4][OH]\cdot 5H_2O \;+\; 11KO_2 \;\longrightarrow\; [NMe_4][OO] \;+\; 11KOH \;+\; 7.5\,O_2 \quad \text{equation 2}$$

The thermochemical properties of 1 suggest that it is of particular interest as a HEDM material. Theses salts decompose exothermally when heated, with the reaction course being markedly dependent upon conditions. For example, the DSC thermograms shown in Figure 1 indicate that

Figure 1 DSC Thermograms for [NMe₄][ONOO]

$T_{min} = 114$ °C

$\Delta H = -37.8 \pm 0.4$ kcal mol^{-1}

$\Delta H = -60.3 \pm 0.4$ kcal mol^{-1}

5 degrees/minute
20 degrees/minute

TEMPERATURE (K)

52
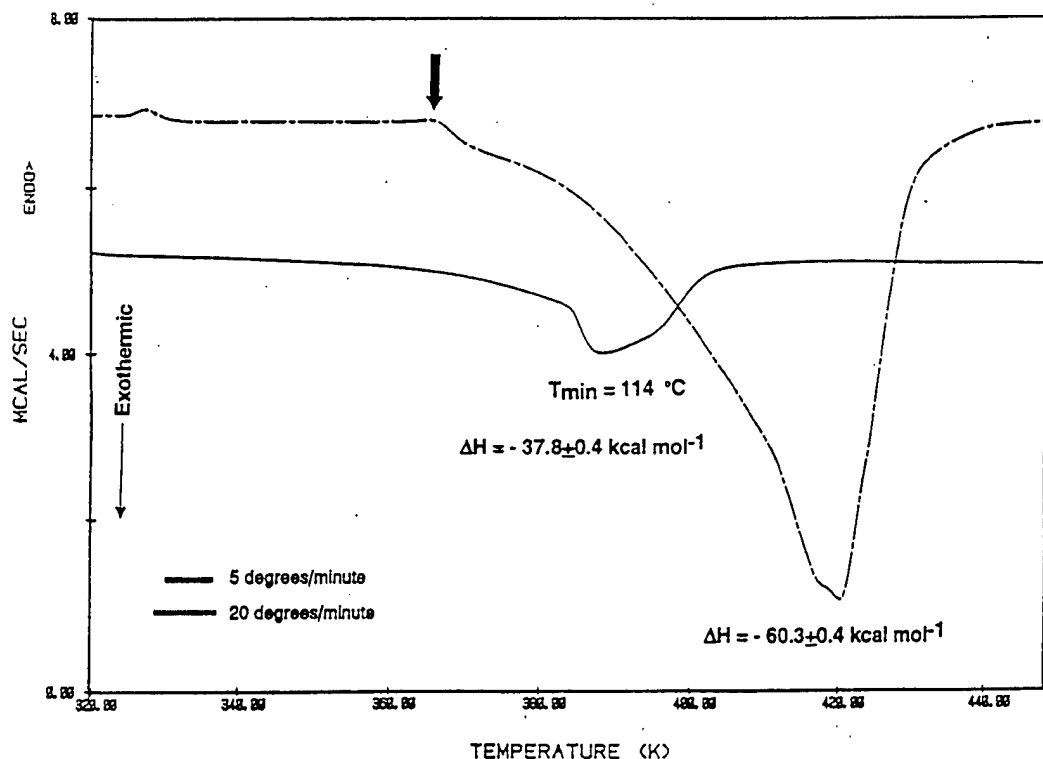
For dicyanomethanide, the second of these anions, a number of nitroso and nitro derivatives have been prepared and characterized, Scheme 1.[8]

Scheme 1 Synthesis of Dicyanomethanide Derivatives

$$H_2C(CN)_2 + HNO_2 \xrightarrow[\text{2. Ag}^+]{\text{1. pH = 4.5}} Ag\{ONC(CN)_2\}$$

NMe₄Cl

KMnO₄

$[NMe_4][ONC(CN)_2]$

$K\{O_2NC(CN)_2\}$
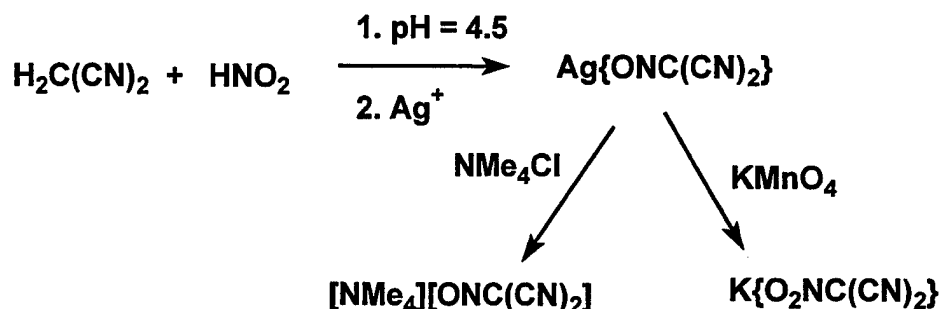
Preliminary thermochemical results for the nitrosodicyanomethanides from DSC indicate that its salts all decompose exothermally with varying heats and onset temperatures, Table 2. Of these derivatives the potassium salt is not only the most exothermic, but it is also the most kinetically stabilized.

Table 2 Thermochemistry of Nitrosodicyanomethanide Salts.

Compound	DSC Onset and Peak Temperatures, K		ΔH, kcal/mole
$K[ONC(CN)_2]$	560	636	-58.12
$NH_4[ONC(CN)_2]$	400	447	-33.72
$Ag[ONC(CN)_2]$	490	502	-32.38
$NMe_4[ONC(CN)_2]$	430	464	-41.44

<u>Conclusions and future directions:</u> Tetramethylammonium peroxynitrite can be readily prepared by an improved synthesis in gram quantities. The energy released from the peroxy form is markedly increased as compared to that from the nitrate isomer, and this makes peroxynitrite salts especially attractive for HEDM applications. While the syntheses shown in equations 1 and 2 are probably too expensive and the tetramethylammonium salt too hygroscopic for routine propellant use, it is worth noting that the photolysis of most nitrate salts yields lattice trapped peroxynitrite.[9] These salts are much more hydrolytically and thermally stable and have excellent storage properties. These photolyzed materials and the family of dicyanamide derivatives are currently being prepared and tested for possible HEDM applications and will be described in future HEDM meetings.

the exotherm depends markedly upon the heating rate with slow heating rates, *i.e.* 5 °C/min, having an exotherm of -38 kcal/mole, whereas faster heating rates of 20 °C/min results in the release of 68 kcal/mole of energy. The first enthalpy corresponds to the theoretical and solution isomerization enthalpies and this is consistent with the product of the slow decomposition which is almost solely tetramethylammonium nitrate. However, the product of the rapid thermolysis reaction is mostly evolved gas with a trace of residual soot left in the DSC cup afterwards. As is marked by the arrow in Figure 1, the main decomposition onset in this thermogram is preceded by a small endothermic process. We suggest that this corresponds to a radical initiation step which would be required to rupture the C-H and C-N bonds·in the cation.

Figure 2 Rotation Barriers in ONOO⁻

Ab initio calculations at either the MP2 or DFT levels of theory with large triple zeta basis sets indicate that the *cis* isomer of peroxynitrite is more stable than the *trans* conformer by *ca.* 3-4 kcal/mole. The predicted rotational barrier for the *cis* ↔ *trans* isomerization is shown in Figure 2 at both the Hartree-Foch and Møller-Plesset Level 2 energies as a function of the ON-OO torsion angle. The MP2 calculation predicts that the barrier is 27 kcal, and this suggests that conformer interconversion will be slow on the ^{15}N NMR time scale. It is significant then that only a single sharp resonance at 191.4 ppm is observed in the ^{15}N NMR for 1 at room temperature in water at pH=14.0. Similar results are found in acetonitrile at -40 °C, in liquid ammonia at -70 °C, or in water at 5 °C. This can be due to either one of two cases: first, we are at the low temperature limit and only a single isomer forms during the radical-radical condensation of NO and O_2^-; or, that this system corresponds to the low temperature limit where there is rapid interconversion of the two conformers at all of these temperatures. Clearly the latter interpretation is inconsistent with theory; we currently favor the former with the proviso that until both resonances are observed by ^{15}N NMR spectroscopy this experiment alone is not able to distinguish between these two scenarios.

Pseudochalcogenide Oxynitrogen Anion Analogues: While the relationships between the halides and the pseudohalides are widely recognized a similar concept, that is the relationship of dianionic species, the pseudochalcogenides, has been little exploited. This idea was first formulated by Langmuir in the form of his isosteric theory,[7] which relates the family of pseudochalcogenides:
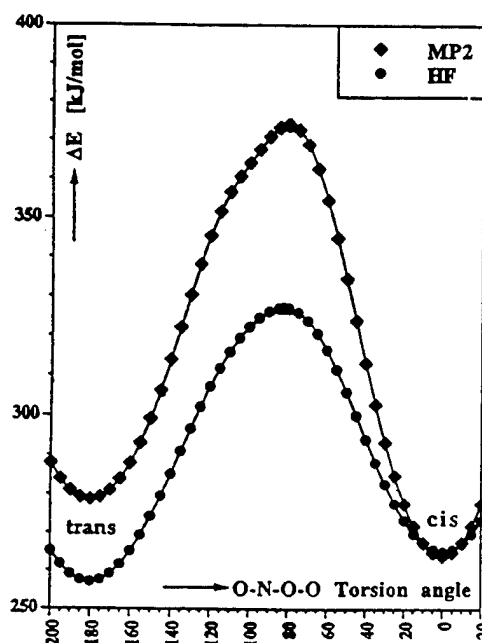
$$O^{2-} \Leftrightarrow \{C(CN)_2\}^{2-} \Leftrightarrow \{NCN\}^{2-} \Leftrightarrow \{CNN\}^{2-}.$$

References

1. Appelman, E.H.; Gosztola, D.J.; *Inorg. Chem.* **1995**,*34*,787.
2. Baeyer, A.; Villiger, V.; *Chem. Ber.* **1901**,*34*,755.
3. Hughes, M.N.; Nicklin, H.G.; *J. Chem. Soc.(A)* **1968**,450.
4. Bohle, D.S.; Glassbrenner, P.A.; Hansert, B.; *Meth. Enzymol.* **1996**,*269B*,302.
5. Yamaguchi, K.; Calderwood, T.S.; Sawyer, D.T.; *Inorg. Chem.* **1986**,*25*,1269.
6. Koppenol, W.H., *Private communication.*
7. Langmuir, I.; *Science* **1921**,*54*,59.
8, Bohle, D.S.; Conklin, B.J.; Hung, C.-H.; *Inorg. Chem.* **1995**,*34*,2569.
9. Plumb, R.C.; Edwards, J.O.; *J. Phys. Chem.* **1992**,*96*,3245.

Models and Simulations of Energetic Materials

Donald L. Thompson and Dan C. Sorescu

Department of Chemistry
Oklahoma State University
Stillwater, OK 74078

We are developing models and performing simulations of both isolated molecules and molecular crystals of energetic materials. The emphasis is on NTO (5-nitro-2,4-dihydro-3H-1,2,4-triazol-3-one) and related compounds, and ammonium nitrate. We are developing realistic potential energy surfaces (PESs) for molecules and crystals by using *ab initio* quantum chemistry calculations in conjunction with the available experimental data. Classical molecular dynamics simulations are being used to characterize the static and dynamic properties of these systems.

NTO Molecule. In our first study[1] we calculated the structure and vibrational spectra of the NTO molecule by using Hartree-Fock (HF), second-order Möller-Plesset theory (MP2) and density functional theory (DFT). Geometry optimizations were performed with a variety of basis sets ranging from 3-21G (split valence) to 6-311G** (triple-ζ-valence plus dp-polarization). The structure was first optimized under C_s symmetry at the restricted HF level using analytical gradients and then refined at the MP2 level.

We have also investigated the use of efficient DFT codes for predicting the geometry and harmonic vibrational frequencies. We used Becke's three parameter exchange functional in combination with the Lee, Yang, and Parr correlation functions (B3LYP) with 6-311G** and 6-311++G** bases. There are marked changes in geometric parameters going from HF/3-21G and HF/6-31G* to MP2/6-31G*, indicating significant effects of electron correlations. However, there is little change in going from MP2/6-31G* to MP2/6-311G**.[1] The B3LYP functional provides an excellent description of the NTO molecule compared to the MP2 calculations. The maximum difference in bond lengths for the MP2/6-311G** and B3LYP/6-311G** results are less than 0.01 Å. There is similar good agreement for the bond angles; the maximum difference is 1.13°.

Comparing the structure computed at the MP2/6-31G** level to the crystallographic X-ray structure[2] shows that most of the measured bond lengths for the crystal are smaller than those calculated for the gas-phase geometry; the maximum difference is 0.0285 Å. The maximum difference in bond angles being 3.53°. Both theoretical and experimental structures are planar.

The experimental IR spectrum of NTO isolated in an argon-matrix at 21 K and in the neat NTO films were measured by C. A. Wight's group at the University of Utah.[1] The neat NTO spectrum exhibits much broader features indicative of strong intermolecular interactions, with some red- or blue-shifts of 100 cm^{-1} or more. For example, the N-H

stretching band observed at 3489 cm^{-1} for the matrix-isolated NTO shifts down to 3200 cm^{-1} in the pure NTO film due to hydrogen bonding. However, we need to emphasize that the differences between the neat films and matrix-isolated NTO go far beyond that expected for hydrogen bonding, where only a limited number of frequencies are expected to be modified. Indeed, the influences of crystal defects, twinning, dipole-dipole interactions, and random orientations of the crystallites with respect to the polarization of the IR beam serve to broaden and shift the spectral lines. This means that the observed frequencies correspond not only to the intramolecular motions, but to collective motions of groups of molecules as well.

We compared the *ab initio* and experimental vibrational frequencies for NTO isolated in an Ar matrix.[1] The root-mean-square (rms) deviations for the 18 measured frequencies is 39.4 cm^{-1} at the MP2/6-31G** level and 28.4 cm^{-1} at the MP2/6-311G** level. Also, there is close agreement between the scaled frequencies determined at the B3LYP/6-311G** level and the corresponding scaled MP2/6-311G** values, with rms deviations of 20.9 cm^{-1}.

The values of the geometric and spectroscopic data described above were used to construct equilibrium force fields for the isolated NTO molecule (PES1) and for NTO in the neat solid (PES2). The PES function is written as a sum of harmonic bond stretches, harmonic bond and wag angles, and a truncated cosine series for the torsions. In the case of gas phase NTO the equilibrium geometry parameters for PES1 were adjusted to reproduce the MP2/6-311G** equilibrium geometry, and the force constants were adjusted to yield reasonable agreement with the scaled *ab initio* MP2/6-311G** frequencies. The second force field, PES2, was constructed to reproduce both the experimental[2] geometry of β-NTO and the experimental vibrational frequencies measured for thin solid films.[1] The accuracies of these two force fields were verified by the results of normal mode analyses and power spectra.

NTO Crystal. We have developed an intermolecular potential for the NTO crystal within the approximation of rigid molecules.[3] The potential used to describe the intermolecular interactions was constructed as a sum of pairwise additive 12-6 Lennard-Jones (LJ), 12-10 LJ (for hydrogen bonding), and Coulombic potentials. The electrostatic charges assigned to the atoms in the molecules were determined by fitting *ab initio* results calculated (using GAUSSIAN) at the MP2/6-31G** level (CHELPG technique). The values of the other parameters were taken from the literature[4] or chosen such that the overall potential reproduces both the crystallographic structure and the lattice energy.

Crystal packing calculations performed with the potential acceptably reproduce the main crystallographic features and yield very good agreement with the estimated lattice energy. The accuracy of the model is also supported by the results of isothermal-isobaric molecular dynamics (MD) simulations at zero pressure for temperatures ranging from 4.2-400 K; the results indicate that at 300 K the model reproduces the experimental unit cell dimensions within 6.9 %. Also, little rotation or translation disorder occurs in unconstrained trajectories for thermal conditions based on analyses of center-of-mass fractional positions and the radial distribution function. Throughout the MD simulations the average structure of the crystal maintains the same space group symmetry as the one determined experimentally.

57

The thermal expansion coefficients of the crystal were determined from the averages of lattice dimensions extracted from trajectory calculations. The linear expansion coefficients for lattice dimensions a, b, and c are, respectively, 5.0×10^{-6}, 50.7×10^{-6} and 79.3×10^{-6} K^{-1} at T = 300 K, and the corresponding volume expansion coefficient is 142.8×10^{-6} K^{-1}. These results indicate anisotropic behavior of the crystal with expansions preferentially along the b and c axes.

This model could be refined by including the effects of intramolecular motions by incorporating the potential in Ref 1. Also, the model could be extended to reproduce not only geometry and energy parameters, but also spectroscopic data for the NTO lattice.

ANTA. The structure, tautomerism and vibrational spectra of the 3-amino-5-nitro-1,2,4-triazole (ANTA) molecule were studied by *ab initio* molecular orbital calculations at the HF, MP2, and MP4 levels and DFT.[5] The results show that the most stable tautomer for isolated molecule is 2H-ANTA (3-amino-5-nitro-1,2,4-2H-triazole) at the HF level, while at the MP2, MP4, and DFT levels the most stable tautomer is 1H-ANTA (3-amino-5-nitro-1,2,4-1H-triazole). For the 2H-ANTA tautomer, the calculated MP2 and DFT structures agree well with the experimental X-ray values,[6] but with twists of the nitro and amino groups much larger than in the solid state. The calculated fundamental vibrational frequencies at the DFT level are in good agreement with the MP2 results. The IR spectra for all tautomers have also been calculated, however, there are no experimental data to which they can be compared. In the case of 2H-ANTA, the $C-NO_2$, $C-NH_2$ and N-H bond dissociation energies were estimated to be 70, 117 and 88 kcal/mol, respectively. A classical force field for gas phase 2H-ANTA has developed based on the structural and spectroscopic results calculated at the MP2 level.

Ammonium Nitrate. A long-standing problem concerns the phase transitions in ammonium nitrate (AN). There are five crystal phases of AN over the temperature range -18 to 170 °C. Of particular importance are the transitions between phases III and IV which occur near 32 °C. The phase transitions, which are affected by heating, cooling, water content, and various dopants, result in undesirable changes in the properties of the material and its performance in energetic materials applications. We have initiated studies to investigate the fundamental changes that can occur in crystalline AN. The goal is to develop models which can be used to simulate these phases transitions. We have begun this work by performing ab initio studies of isolated AN molecules.

Our initial studies are focusing in the molecule. The structure of NH_4NO_3 has been determined at both the MP2 and DFT levels using basis sets as large as 6-311++G**. In the DFT calculations both exchange and correlation functionals of the density gradient, in addition to the density itself, are used because of they are essential for describing the hydrogen bonding. We have used a number of exchange-correlation functionals: B3LYP, BP86 and BPW91. The first uses the exchange functional described by the fitted three-parameter hybrid of Becke and the correlation functional of Lee, Yand, and Parr (B3-LYP); the second uses the exchange functional of Becke and the correlation functional of Perdew (BP86); and BPW91 is based on the exchange functional of Becke and the correlation functional of Perdew and Wang. All geometry optimizations were done using the default convergence criteria in the Gaussian94 programs.

The calculated (optimized) structures of gas-phase AN show that the hydrogen atom closest to the NO_3 group is pulled away from the NH_4 group by about 0.6 Å toward the NO_3 group. The ammonia nitrogen to nitrate hydrogen distance is 1.68 Å at MP2/6-311++G** level compared to 1.66 Å at B3LYP/6-311++G**, 1.61 Å at BP86/6-311++G** and 1.63 Å at BPW91/6-311++G** levels.

Generally there is a good correspondence between the predicted MP2 values and those determined at DFT levels. The B3LYP values are closest to the MP2 results with deviations generally below 0.5% and with a maximum deviation of 1.2 %. The other two exchange-correlation methods give larger differences: up to 4.1 % in the case of BP86 and 3.1 % in the case of BPW91. We ascertained that the critical points correspond to minima by performing frequency calculations. The B3LYP results are closer to the corresponding MP2 frequencies than those for the other two DFT functionals.

In order to obtain a description of the solid phases of AN, we are beginning calculations based on DFT theory in the pseudopotential approximation with periodically repeating geometries. In the first stage of these calculations we will focus on the following topics: (a) Determination of the optimized bulk structures of AN in different phases, particularly phases IV and III in the phase diagram of AN. (b) Characterization of the band structure, density of states, and electrostatic potential distribution for these phases. (c) Determination of the properties of AN surfaces. In this case we will investigate the possible relaxations that take place on AN surface relative to the ideal bulk configuration and the possible modifications on the band structure and density of states introduced by the presence of the surface. (d) We will also investigate the energetics of defects and the role played by different impurities in bulk AN.

References

1. D. C. Sorescu, T. R. L. Sutton, D. L. Thompson, D. Beardall, and C. A. Wight, J. Mol. Struct. **384**, 87 (1996).
2. K. Y. Lee and R. Gilardi, in *Structure and Properties of Energetic Materials*, vol. 296, edited by D. H. Lienbenberg, R. W. Armstrong and J. J. Gilman, (Materials Research Society, Pittsburgh, PA, 1993), p. 237.
3. D. C. Sorescu and D. L. Thompson, J. Phys. Chem. B **101**, 3605 (1997).
4. K. D. Gibson and H. A. Scheraga, J. Phys. Chem. **99**, 3752 (1995).
5. D. C. Sorescu, C. M. Bennett, and D. L. Thompson, in preparation.
6. S. Miertus, E. Scrocco, and J. Tomasi, Chem. Phys. **55**, 117 (1981).

THE ROLE OF QUANTUM CHEMISTRY IN DESIGNING HIGH ENERGY SPECIES
EXTENDED ABSTRACT FOR HEDM MEETING, JUNE 1-3, 1997
BOULDER, COLORADO
MARK S. GORDON
DEPARTMENT OF CHEMISTRY
IOWA STATE UNIVERSITY

Three areas that are related to HEDM will be considered: (1) A review of the current status of studies of N_2O_2 potential energy surfaces; (2) consideration of an investigation of a possible high energy compound proposed (but not yet synthesized) by Dr. Rob Schmitt (SRI); and (3) discussion of the importance of solvation in the synthesis of high energy species.

1. N_2O_2

We have identified four isomers of N_2O_2 (1 - 4 in Figure 1) that are candidates for high energy species[1]. The energies of each of these structures relative to 2 NO are summarized in Figure 1. All four are quite high in energy, ranging from 49 to 52 kca/mol above 2 NO at the highest level of theory: second order multi-reference perturbation theory (CASPT2) with the 6-311+G(2d) basis set. In order to further assess their viability as HEDM candidates, the minimum energy paths (MEP) connecting each of these species with 2 NO, via the intervening transition state has been explored. These MEP's are shown in Figures 2-5, respectively (note that Figure 4 actually shows the MEP connecting isomers 3 with 4). The adiabatic barrier heights separating the four isomers from products are 40, 20, 18, and 7 kcal/mol, respectively. So, isomer 4 is not likely to be a viable HEDM candidate.

One also must consider the crossings of the MEP with higher lying repulsive states (usually triplet states), since such crossings may lower the operational barriers, depending on where they occur. These triplet curves are also shown in Figures 2-5. For isomer 1, the repulsive triplet crosses the singlet surface at about 10 kcal/mol below the singlet transition state. Depending on the strength of the non-adaibatic (i.e., spin-orbit) coupling between the two electronic states, this crossing could effectively reduce the barrier to dissociation by 10 kcal/mol, to about 30 kcal/mol. This is still a healthy barrier

height. Such triplet crossings have no effect on the barriers for the other isomers, so **2** and **3** may be viable candidates.

1. *New HEDM Candidates*

In the 1996 HEDM Synthesis/Theory workshop, Rob Schmitt (SRI) proposed several (not yet synthesized) nitrogen-containing compounds as potential HEDM species, and requested that theorists provide some information about them. One such compound is shown below.
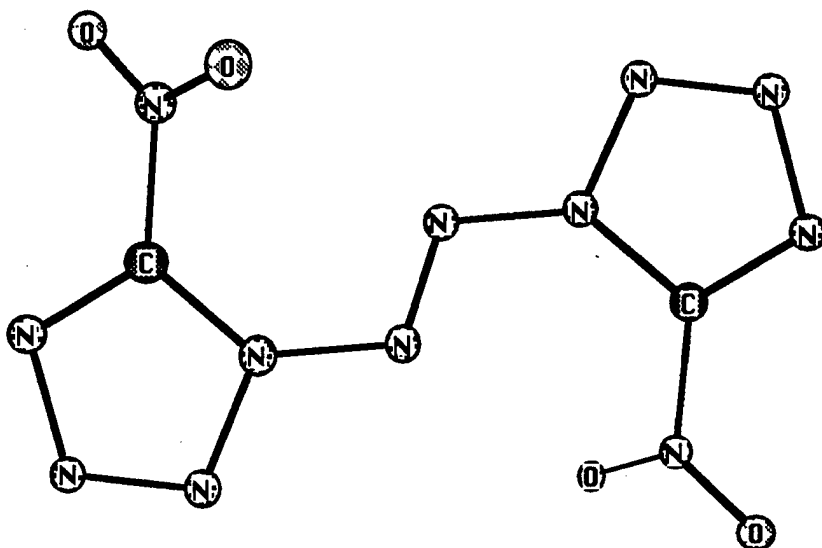
The geometry and vibrational frequencies of this compound have been determined at the SCF/6-31G(d) level of theory. Its heat of formation was predicted to be 456.8 kcal/mol, using a combination of isodesmic reactions and the G2 (MP2,SVP) model. This amounts to just under 1.8 kcal/g and to an I_{sp} of 329 sec, assuming decomposition to N_2 and CO_2. This may be compared to I_{sp}'s of 240 for hydrazine and 300 for LOX/RP1. So, this proposed compound may be a viable monopropellant. The next steps in the study of this species will be to investigate its stability with respect to hydrolysis, oxidation, and attack by acid or base.

3. *Synthesis/Solvation*

Polyhedral oligomeric silsesquioxanes (POSS) are of considerable interest, because of their use as viscosity modifiers and and precursors to ceramic fibers and SiC coatings. Synthesis of POSS is initiated by hydrolysis of trichlorosilanes, $RSiCl_3$, but the mechanism of POSS formation is not well understood. In particular, the role of the R group, of solvent, and of acid and base catalysis is unknown. In an attempt to understand the mechanism of POSS formation, we have initiated a broad investigation of this mechanism, and the role of solvent and catalysts[2].

Table 1 summarizes the predicted energetics for the three steps in the hydrolysis of $SiHCl_3$. The intrinsic MP4/6-31G(d) barrier heights for the three steps are 31, 31, and 19 kcal/mol, respectively. However, the addition of just one water (solvent) molecule reduces these barriers to 9, 10, and 3 kcal/mol, respectively. This very large reduction in barrier height is caused by the direct participation of the solvent molecule in the initial step - the transfer of a hydrogen atom to Cl, in order to elminiate HCl.

Table 2 summarizes the precited energetics for the condensation of SiH_3OH and $HSi(OH)_3$. As for the hydrolysis step, the intrinsic barrier heights for these two species are fairly high: 21 and 12 kcal/mol, respectively, at the MP2/6-31G(d) level of theory. However, the addition of just one solvent molecule lowers these barriers to 3 and -7 kcal/mol, respectively. So, for both key steps in the mechanism, solvent plays a critical role. It is therefore essential to obtain a more general understanding of the effect of solvation on this mechanism. A roadblock to such an investigation is the large computational cost of adding successive solvent molecules at the current high level of theory.

We have therefore embarked on a continuing development of a sophisticated and highly successful model for treating solvation. This is a discrete solvent model in which the solvent molecules are represented by one-electron terms in the *ab initio* Hamiltonian[3,4].

$$\mathcal{H} = V_{el} + V_{pol} + V_{rep-ct}$$

Here, V_{el} represents the contribution from electrostatics, determined using a *distributed multipolar expansion* through octupoles. The expansion points are the atom centers and the bond midpoints for each solvent molecule. V_{pol} represents the polarizability, determined by a tensor sum of localized orbital dipole polarizabilities centered at the localized orbital centroids of charge. This is iterated to self-consistency within the Hartree-Fock iteration process. V_{rep-ct} is the contribution from exchange repulsion plus charge transfer. This is determined by subtracting the electrostatic and polarizability terms from the Hartree-Fock energies at 192 water dimer geometries, and then fitting the remainder to a simple functional form. All tests of this *effective fragment potential*

(EFP) method have been highly successful. Geometries, energetics, vibrational frequencies and minimum energy reaction paths are all reproduced to a high level of accuracy for a wide range of applications. These include the effect of successive addition of water molecules to the internal rotation of formamide, the dissociation of NaCl to Na^+ + Cl^- and the Menshutkin reaction (NH_3 + CH_3Br -> $CH_3NH_3^+$ + Br^-), as well as the structure and energetics of water clusters. In order to extend this model to general solvents, we have derived a new method that is not dependent on the fitting procedure discussed above for V_{rep-ct}^5.

REFERENCES

1. G. Chaban, M.S. Gordon, and K.A. Nguyen, J. Phys. Chem., in press.

2. T. Kudo and M.S. Gordon, in preparation.

3. P.N. Day, J.H. Jensen, M.S. Gordon, S.P. Webb, W.J. Stevens, M. Krauss, D. Garmer, H. Basch, and D. Cohen, J. Chem. Phys., 105, 1968 (1996).

4. W. Chen and M.S. Gordon, J. Chem. Phys., 105, 11081 (1996).

5. J.H. Jensen and M.S. Gordon, Mol. Phys., 89, 1313 (1996).

TABLE 1. EFFECT OF H$_2$O ON HYDROLYSIS REACTIONS

Computational Level	Monomer x 2	Transition State (kcal/mol) Gas Phase	1 H$_2$O
A. HSiCl$_3$ + H$_2$O -> HSiCl$_2$OH + HCl			
RHF/6-31G(d)	0.0	36.8	21.5
MP2/6-31G(d)[a]	0.0	29.7	6.5
MP4/6-31G(d)[a]	0.0	30.6	8.8
B. HSiCl$_2$OH + H$_2$O -> HSiCl(OH)$_2$ + HCl			
RHF/6-31G(d)	0.0	37.6	22.8
MP2/6-31G(d)[a]	0.0	30.6	7.3
MP4/6-31G(d)[a]	0.0	31.5	9.6
C. HSiCl(OH)$_2$ + H$_2$O -> HSi(OH)$_3$ + HCl			
RHF/6-31G(d)	0.0	24.9	9.9
MP2/6-31G(d)[a]	0.0	18.5	1.3
MP4/6-31G(d)[a]	0.0	19.4	2.7

a. RHF/6-31G(d) geometry

TABLE 2. EFFECT OF H₂O ON CONDENSATION REACTIONS

Computational Level	Monomer x 2	Transition State (kcal/mol) Gas Phase	1 H₂O
A. H₃SiOH x 2 -> H₃Si-O-SiH₃			
RHF/6-31G(d)	0.0	35.8	23.5
MP2/6-31G(d)	0.0	20.5	0.4
MP4/6-31G(d)[a]	0.0	21.7	2.9
MP2/6-311+G(d,p)[a]	0.0		3.2
MP4/6-311+G(d,p)[a]	0.0		5.3
B. HSi(OH)₃ x 2 -> H(OH)₂Si-O-Si(OH)₂H			
RHF/6-31G(d)	0.0	30.4	18.9
MP2/6-31G(d)[b]	0.0	11.7	-7.2
MP4/6-31G(d)[b]	0.0	12.7	

a. MP2/6-31G(d) geometry

b. RHF/6-31G(d) geometry

Figure 1. N_2O_2 high energy isomers

1. D_{2h}

2. C_{2v}

MCSCF(10,10)/6-31G(d) geometry

Relative energy, kcal/mol

	1. D_{2h}	2. C_{2v}
MCSCF(10,10)/6-31G(d)	71.0	41.6
CASPT2/MCSCF(10,10)/6-31G(d)	49.0	47.7
MCSCF(10,10)/6-311+G(2d)	71.7	47.0
CASPT2/MCSCF(10,10)/6-311+G(2d)	48.7	53.1

3. C_{2v}

4. C_s
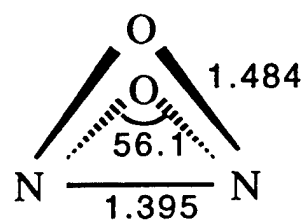
D(ONNO)=57.6 deg.
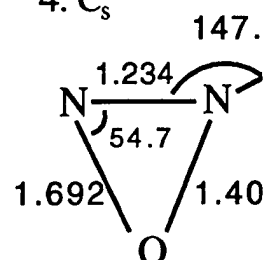
	3. C_{2v}	4. C_s
MCSCF(10,10)/6-31G(d)	71.2	66.0
CASPT2/MCSCF(10,10)/6-31G(d)	77.3	53.0
MCSCF(10,10)/6-311+G(2d)	73.2	68.4
CASPT2/MCSCF(10,10)/6-311+G(2d)	81.9	55.7

Fig. 2. Reaction path for decomposition of D2h isomer (1) to 2 NO

——— MCSCF(14,12)/6-31G(d) IRC path
— ⬦ — CASPT2(14,12)/6-31G(d) single point energies (singlet 1A'))
- - ♦ - - CASPT2(14,12)/6-31G(d) single point energies (triplet 3A"))
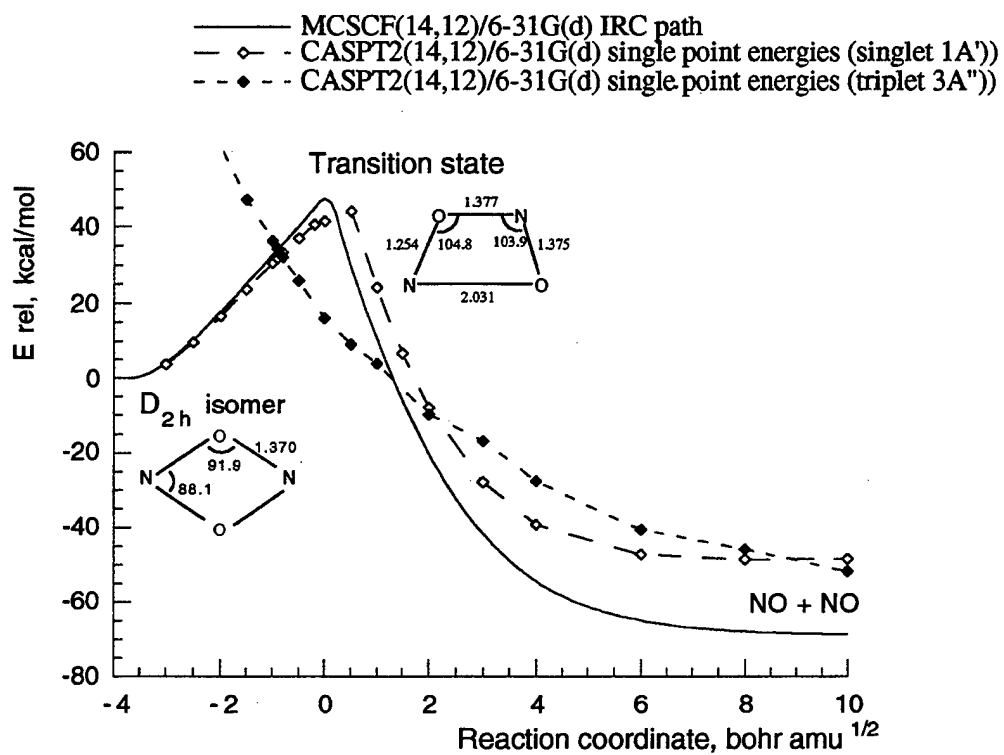
Fig. 3. MCSCF(10,10) reaction path for decomposition of C₂ᵥ isomer (2) to two NO molecules

Singlet - MCSCF(10,10)/6-31G(d)
Singlet - CASPT2(10,10)/6-31G(d)
Triplet - CASPT2(10,10)/6-31G(d)
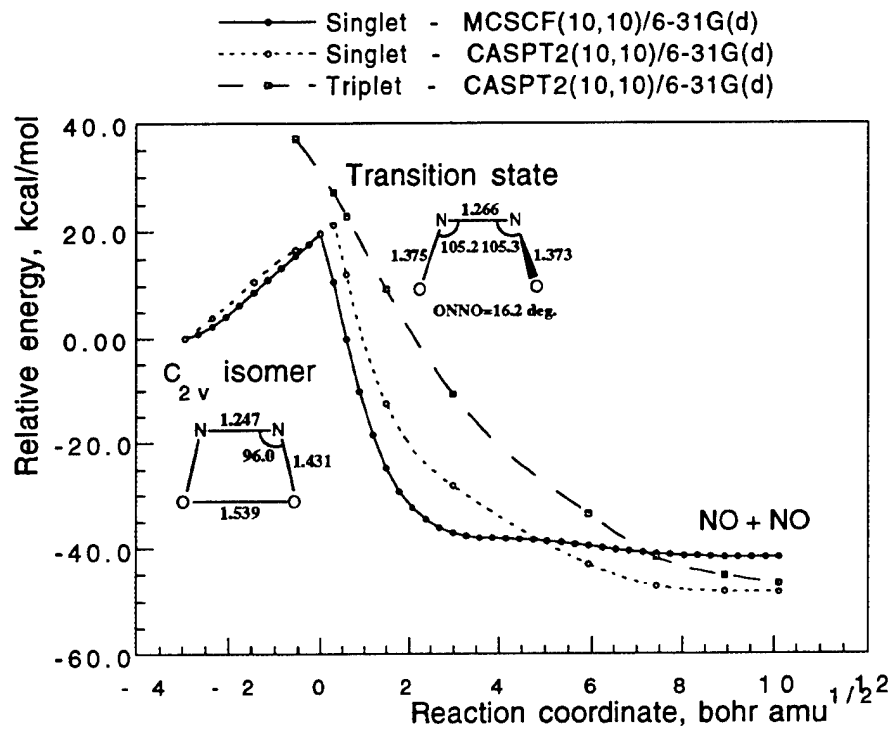
Fig. 4. MCSCF(10,10)/6-31G(d) reaction path
for isomerisation 3 -> 4
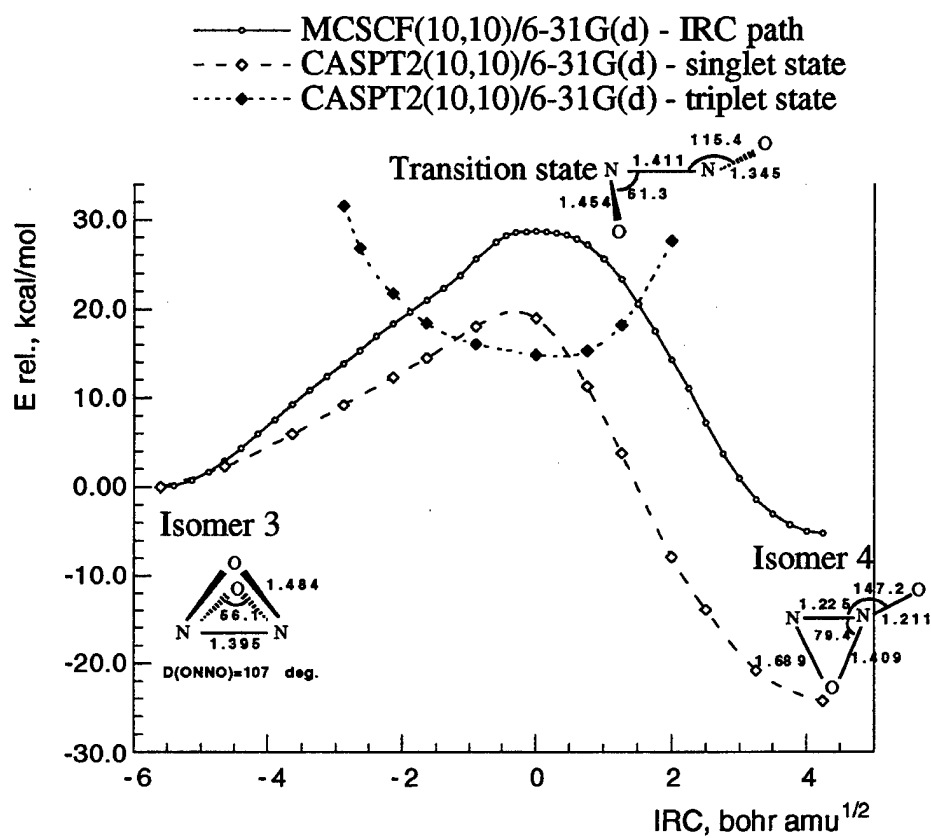
Fig. 5. MCSCF(14,12)/6-31G(d) reaction path for decomposition of isomer 4 to two NO molecules

· MCSCF(14,12)/6-31G(d) IRC path

——•—— singlet A' - CASPT2(14,12)/6-31G(d)

·····•···· triplet A" - CASPT2(14,12)/6-31G(d)

70
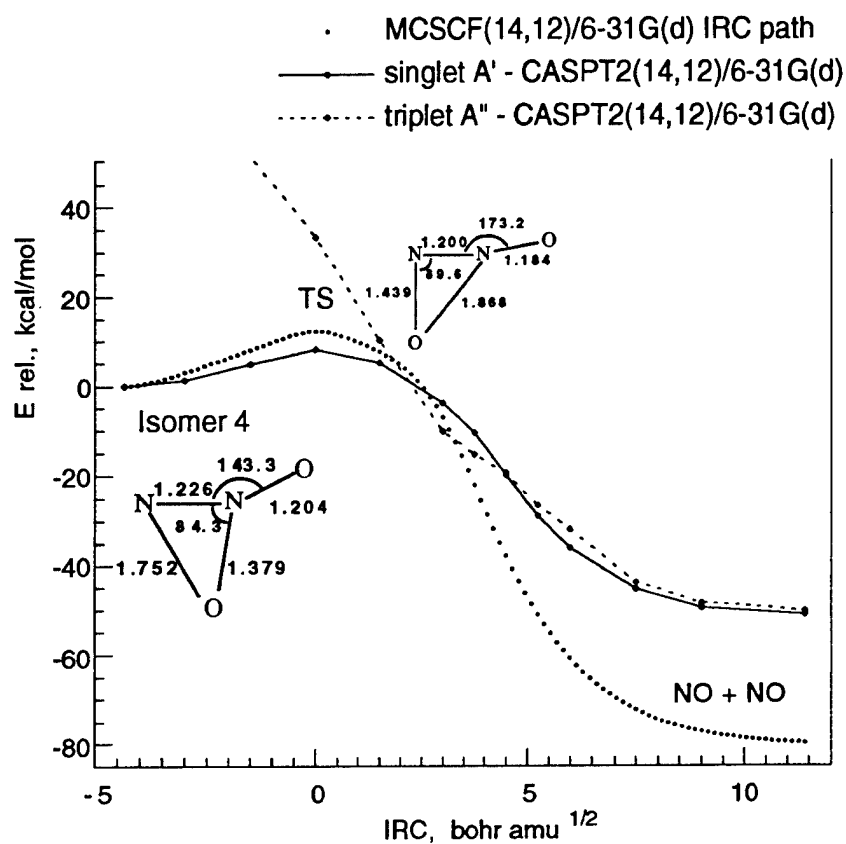
Reaction Field Cavity Optimization:
A New Solvent Model for Electronic Structure Theory
by

Teresa Head-Gordon
Life Sciences Division
Lawrence Berkeley National Laboratory
Berkeley, California 94720

Martin Head-Gordon
Department of Chemistry
U California, Berkeley
Berkeley, California 94720

The ability to explore potential energy surfaces, to characterize barriers, and to evaluate excited state properties with inclusion of a reaction field solvent environment are tools which will be useful for synthesis of new materials in general. A fully quantum, molecular description of solvation is still prohibitively expensive, however. Quantum reaction field (QRF) models provide an attractive alternative since the solvent is treated classically while only the solute is treated quantum mechanically. Solute-solvent separability should be manifested by wholly containing the solute wavefunction in an empirically defined cavity geometry. The primary disadvantages of the QRF models are the large sensitivity of the solvation free energy, Gsol, to the classical description of solvent and the solutes cavity shape and size. Therefore, the necessity for parameterizing the cavity volume or aspects of the classical solvent to reproduce experimental data limits the predictive use of the QRF models.

We are developing a new QRF model, available for both ground and excited states, which will no longer require empirical specification of the cavity shape and size. Instead, the cavity geometry is to be treated as a set of variables which can be optimized. This yields a more predictive solvation model, which also enables the physical consequences of the assumption of solute-solvent separability to be explored for the first time. Cavity optimization can be realized by two solvation models which we outline below, and will be implemented initially for Density Functional Theory (DFT) and Hartree-Fock (HF) ground state methods, and the single excitation configuration interaction (CIS) excited state method. We will present our current results on the optimization of cavity geometry for the isoelectronic species K+ and Cl- using HF theory, and discuss future improvements to the model to correctly predict the free energy of hydration of these ions.

Direct Detection and Spectroscopy of O$_4^*$

Holly M. Bevsek, F. Cortney Sailes, and Arthur G. Suits
Department of Chemistry
University of California-Berkeley
and
Chemical Sciences Division
Lawrence Berkeley National Laboratory
Berkeley, CA 94720

Abstract

We report the first direct detection of a metastable state of tetraoxygen, O$_4^*$. A covalently bound form of O$_4$ has long been theorized to exist[1-7] with two proposed structures: a cyclic form (D$_{2d}$) predicted to lie 100 kcal/mol above two isolated O$_2$ molecules[2-4], and a D$_{3h}$ structure, most recently predicted to be 54 kcal above this asymptote[5-7]. However, the only experimental observation of this system has been through detecting the O$_2$ dissociation products found in charge transfer[8] to O$_4^+$ and photodetachment[9] of the electron in O$_4^-$. In the present study, our excitation source produces a molecular beam of O$_4^*$ with significant intensity and a lifetime exceeding 80 µs, while detection is accomplished via (1+1) REMPI. Based on a tentative assignment of the spectrum, which consists of a complex series of vibrational bands, we believe the system is cyclic as predicted in refs. 1-4. We will also discuss the energetics of this system and hypothesize on possible mechanisms for its formation.

1. G. N. Lewis, J. Am. Chem. Soc., **46** 2027 (1924).
2. a) V. Adamantides, D. Neisius, and G. Verhaegen, Chem. Phys., **48** 215 (1980); b) V. Adamantides, Chem. Phys., **48** 221 (1980).
3. a) E. T. Seidl and H. F. Schaefer, J. Chem. Phys., **88** 7043 (1988); b) K. M. Dunn, G. E. Scuseria, and H. F. Schaefer, J. Chem. Phys., **92** 6077 (1990); c) E. T. Seidl and H. F. Schaefer, J. Chem. Phys., **96** 1176 (1992).
4. M. Zhao and B. M. Gimarc, J. Phys. Chem., **97** 4023 (1993).
5. I. Røeggen and E. W. Nilssen, Chem. Phys. Lett., **157** 409 (1989).
6. M. Hotokka and P. Pyykkö, Chem. Phys. Lett., **157** 415 (1989).
7. E. Ferreira, P. Gardiol, R. M. Sosa, and O. N. Ventura, J. Molec. Struct., **335** 63 (1995).
8. H. Helm and C. W. Walter, J. Chem. Phys., **98** 5444 (1993).
9. a) C. R. Sherwood, M. C. Garner, K. A. Hanold, K. M. Strong, and R. E. Continetti, J. Chem. Phys., **102** 6949 (1995); b) K. A. Hanold, M. C. Garner, and R. E. Continetti, Phys. Rev. Lett., **77** 3335 (1996).

Computational Studies of High Energy Density Matter

Gregory A. Voth

Department of Chemistry and Henry Eyring Center for Theoretical Chemistry, University of Utah, Salt Lake City, Utah 84112

I. INTRODUCTION

Two topics related to high energy density matter (HEDM) are currently under investigation in our group. These are described below.

A. Low Temperature HEDM Simulations

Solid hydrogen doped with energetic impurities may form the basis for HEDM to be used in rocket propulsion. A key research priority is therefore the largescale computer simulation of impurity diffusion and recombination in HEDM in order to better understand the reasons for its stability, or instability, as the case may be. The recombination of these atomic impurities is an extremely exothermic reaction, and therefore thermodynamically favored. Theoretical developments within our research group allow the (otherwise impossible) quantum dynamical simulation of these systems which is necessary to properly treat the problem. Classical molecular dynamics simulations, while less computationally challenging, predict qualitatively incorrect properties for low temperature liquid and solid hydrogen because of the highly quantum nature of hydrogen matrix, and are therefore inadequate.

The rate of recombination of two impurities in a low temperature solid can be characterized in terms of both their intrinsic recombination rate when they have diffused to within some well-defined separation, and the rate at which the two impurities diffuse into the required proximity with one another. If the intrinsic rate of recombination is very fast compared with the impurity self-diffusion rate, the overall recombination process will be limited by the impurity self-diffusion. The latter rate is proportional to the impurity self-diffusion constant, and it is a possible limiting factor in the undesirable impurity recombination process. Conversely, the recombination rate will be limited by the intrinsic recombination step if there is a large free energy barrier for that process.

The immediate goal of the our group's Air Force-supported low temperature HEDM research program is to calculate directly from largescale computer simulation the relevant rates for the impurity recombination rate. In low temperature hydrogen HEDM, quantum effects are enormous, so a highly specialized method is required for these demanding computer simulations.

B. Solvent Effects in HEDM Synthesis

In this aspect of the our group's AFOSR-supported research, *ab initio* molecular dynamics (AIMD) methodology is being developed and employed to study solvent effects in the synthesis of highly strained multicyclic organic compounds (HEDM). Such compounds can be used as an energy source in propellants, explosives, or other devices. Synthesis of these compounds is challenging, often requiring extreme and quite specific solvent environments. Solvent effects may thus play an important role in optimizing the production and stabilization of HEDM. The Diels-Alder reaction is an excellent candidate for the study of such solvent effects because it has been shown to have a strongly enhanced reaction rate in aqueous solution and it is an important mechanism in the synthesis of many strained compounds. It is therefore presently under

investigation by our group in an AIMD study of solvent effects on reaction rates and mechanisms within the context of the AFOSR HEDM Program.

In order to obtain an accurate picture of the nuclear dynamics, all nuclear forces and energies are obtained using *ab initio* density functional theory (DFT) as has been employed in "on-the-fly" AIMD techniques such as Car-Parrinello (CP) molecular dynamics. The reaction rate is then obtained using the reactive flux approach with some key and novel modifications (described below). Once these calculations are completed, it will be possible to go further in exploring optimal solvents for rate enhancement since the solvent properties can be varied easily on the computer. Though the initial object of study is the paradigmatic Diels-Alder reaction between methyl vinyl ketone (MVK) and cyclopentadiene (CPD), subsequent studies will focus on reactions whose products have sufficiently high strain energy that they are clearly HEDM. The long term goal of this part of the work is thus to construct *and* implement a computational AIMD methodology capable of probing solvent effects in the bimolecular reactions leading to HEDM products.

In the following pages, the scientific background behind our HEDM effort will be described in some detail, along with various results.

II. SCIENTIFIC METHODOLOGY AND RESULTS

A. Low Temperature HEDM Simulations

As stated in the Introduction, the computer simulation of impurity trapping and mobility in quantum solids represents an extraordinary challenge because the solid is so strongly influenced by nuclear quantum effects. For example, the self-diffusion constant D is obtained from a *quantum dynamical time correlation function for velocity*. Low temperature HEDM systems thus require an explicit quantum dynamical treatment to calculate their relevant dynamical properties. Classical molecular dynamics (MD) approaches are completely inadequate.

A novel quantum dynamical approach which makes the study of HEDM systems possible has been developed in our group which is called "Centroid Molecular Dynamics" (CMD) [1]. In the CMD approach, the impurity self-diffusion constant can be obtained through the correlation functions by running classical-like trajectories for the quantum particles on an effective, temperature-dependent potential [2-4]. In the "exact" CMD algorithm, the effective potential is calculated "on the fly" by performing equilibrium quantum averaging simultaneously with the time-integration of the CMD equations. In fact, we have recently developed a "hyper-parallel" CMD algorithm [5] which has exhibited near linear performance scaling over 64 or more IBM SP2 nodes in our simulations of liquid and solid hydrogen. As an alternative, the quantum centroid potential has been represented by an effective pairwise pseudopotential [6], allowing for extremely efficient quantum dynamical simulation of large systems (i.e., once the potential is specified in the pairwise form, the simulation is no more time-consuming than a classical MD simulation). The theoretical breakthrough of CMD is now allowing our group to directly simulate the dynamics of quantum liquids and solids, as well as impurity diffusion and recombination in potential HEDM and related systems.

As a first step, the quantum barrier for the intrinsic recombination step between two lithium impurities has been determined [7]. The lithium atoms were initially placed in well-separated single substitutional sites in the para-hydrogen hcp lattice at 4 K and equilibrated. The barrier calculation then involves the computation of the equilibrium mean centroid force between the two lithium atoms for fixed distances, and then this force is integrated to determine the quantum free energy barrier by virtue of the reversible work theorem. Shown in Fig. 1 is the barrier as a function of the internuclear Li-Li separation. The barrier occurs at a separation of 8.28 Angstroms and has a height of 80 K. It is interesting that the lithium nuclei actually tunnel due to their strong binding interaction. From the barrier height, the intrinsic recombination rate is estimated to be 1800 per second, which is significantly higher than the overall recombination rate observed in the experiments of Fajardo and co-workers at Edwards AFB. These results thus suggest that the

lithium recombination may be diffusion-limited in the experiments, so this issue will be explored in the future.

As a second step, the recombination of lithium impurities in "loaded" para-hydrogen solids was probed through the quantum dynamics simulations. Two systems were studied. The first was at 2.5 mole percent lithium impurity concentration, while the second was at 3.3 mole percent. Dramatically different behavior was observed between the two systems. Shown in Fig. 2 are time-dependent Li-Li radial distribution functions obtained from a long quantum trajectory for the 2.5 mole percent system. While the lattice exhibits some relaxation, the system is clearly stable on the timescale of the simulation (several nanoseconds). On the other hand, in the 3.3 mole percent system a local recombination event between two lithium atoms occurs after the first ten picoseconds of the trajectory which, in turn, triggers a global instability of the system, leading to recombination and eventual clustering of all of the lithium impurities. This behavior can be seen in Fig. 3 from the time-dependent behavior of the peak around 3 Angstroms in the Li-Li radial distribution function (i.e., the lithium dimer distance). These results suggest the lithium loaded para-hydrogen solid may be stable up to approximately 3 mole percent impurity concentration. In the future, the effects of pressure and temperature will be examined, and the loading of boron in solid hydrogen will begin to be explored.

B. Solvent Effects in HEDM Synthesis

The Diels-Alder is an important class of organic reactions, allowing the formation of six-membered rings with a high degree of stereo- and regio-specificity. This makes it useful in a wide variety of synthetic applications, including the production of strained molecules. It consists of two carbon-carbon bond forming events between a *diene*, characterized by a pair of conjugated double bonds, and a *dienophile*, characterized by a single double bond with little steric hindrance to reaction. A Diels-Alder reaction may be classified as having *normal electron demand* if it has an electron-donating group (EDG) on the diene and an electron-withdrawing group (EWG) on the dienophile. In the case of cyclic dienes, the product is predominantly *endo*, meaning that a substituent on the dienophile is adjacent to the dienophile, as opposed to *exo*, in which it is further away. Considerable evidence [8] suggests that it is a concerted reaction with both bonds forming simultaneously. In the language of transition state theory, it possesses only one transition state, rather than two, as would be true in the case of a stepwise mechanism.

One piece of evidence supporting the concerted mechanism is the weak solvent dependence of reaction rates, indicating little charge build-up in the transition state. In 1980, though, it was discovered that an aqueous solvent can have a very dramatic effect on Diels-Alder reaction rates [9]. It can also strongly enhance the *endo/exo* selectivity [10,11]. This finding attracted considerable interest, both as a key to improve synthetic methodologies, and as a challenge for our understanding.

Explanations may be either qualitative or quantitative in nature. Qualitatively, the aqueous effects have been attributed to certain solvent properties, with proponents arguing for either *hydrophobicity* or *hydrogen bonding* as the determining property of the solvent. Substantial anecdotal evidence has appeared to support each viewpoint. Using standard measures of these properties various workers have tried to make the discussion more quantitative, by correlating reaction rates and selectivities with measures of solvophobicity or Lewis acidity. A more advanced level of quantitative investigation has used molecular level simulations of varying degrees of sophistication in conjunction with transition state theory to reproduce reaction rate trends. Interpretation of these results in terms of hydrophobicity and hydrogen bonding has yielded some more clues to the mechanism of solvent effects. The best of these simulations, which use a gas phase description of the solute interacting with the solvent through calculated partial charges and an empirical interaction model, appear to be commanding much respect and influence in the work and interpretations of later workers [12,13].

75

Despite the quantitative nature of recent simulations, that work is in a different sense still qualitative. The numbers generated for reaction rates are approximately correct, but they cannot be expected to be highly accurate as long as they rely only upon transition state theory, which is a very useful yet inherently approximate theory, and as long as they rely upon simplified models of the solute-solvent interactions, without allowing for explicit polarization of the solute by the solvent (and vice versa). The solution to these problems is one focus of the our group's research.

First-principles modeling

Earlier shortcomings in modeling are being overcome by simulations in which the electronic structure of both the reacting species and the solvent are performed self-consistently for all relevant configurations using the Car-Parrinello AIMD method. In this approach, the ground state electronic structure (forces) appropriate to the nuclei, in the Born-Oppenheimer approximation, is calculated at each configuration, "on-the-fly" so to speak.

Corrections to semi-empirical TST

Most estimates of rate constants are based on empirical or semi-empirical modeling of the potential energy surface and transition state theory. Furthermore, transition state theory assumes that all reactants which move off the transition state dividing surface will go on to become products. This does not allow for barrier recrossings and thus gives an upper limit to the true rate constant. To correct for this one must be able to calculate some actual dynamics in order to throw out the non-reacting trajectories within the framework of a *reactive flux calculation*. To perform an exact rate constant calculation, one needs to first recognize that much of the effort in such a calculation goes into the determination of a good estimate of the condensed phase activation free energy--such calculations are not feasible within a completely *ab initio* approach--and that the transition state approximation itself may not be a good one due to recrossing effects. Our group's method to calculate exact rate constants recognizes not only the above facts, but also that AIMD calculations are extremely challenging and time-consuming. To address these challenges, a novel reactive flux approach is being employed in which (1) a "simple" estimate of the transition state rate constant derived from semi-empirical potential energy function modeling is used to significantly reduce the necessary degree of explicit *ab initio* dynamics calculations; and (2) the initial conditions for the reactive flux calculation are generated using a flux-weighted canonical distribution function as determined by the zeroth-order semi-empirical potential energy function. The statistical weighting of the initial conditions are therefore accomplished using a dynamics propagated by the semi-empirical potential and not the *ab* initio forces, while selectively determining the exact electronic wavefunction to compute the correct statistical weighting of initial conditions without having to do a full *ab initio* energy calculation at each step. This method provides a substantial saving in the computer resources needed to prepare the initial points and hence compute the rate constant *accurately*. The actual short-time *ab initio* dynamics to quantify the deviations from the approximate transition state rate constant derived from the semi-empirical potential energy function are determined with the AIMD methods described above. This approach also allows one to probe the reaction pathway (i.e., mechanism).

A theoretical approach to the challenge of studying solution phase chemical reactions with AIMD methods is fully underway in our group and is now described in more detail. In 1985 Car and Parrinello [14] proposed and developed the use of DFT within an AIMD framework which can be used practically for systems large enough to contain solvent motions [15-17]. Instead of using an on-the-fly brute force calculation of the *ab initio* forces--entailing a full electronic structure calculation at each step--the Car-Parrinello method treats the coefficients of the electronic wavefunction in some given basis as dynamical variables which must be propagated in analogy with the nuclear variables. Hence the total energy consisting of both the real nuclear energy plus a fictitious electronic coefficient energy is necessarily conserved. As long as the system is far from

76

Born-Oppenheimer breakdown, the electrons and nuclei are essentially decoupled, and there is no energy transfer between them. Thus the CP method conserves the nuclear energy for long times.

Since extensive statistical averaging using CP dynamics is prohibitive, the reactive flux method for computing rate constants must be *reformulated* to maximize the things one can do easily and minimize the input required from the CP dynamics. Fortunately, empirical and semi-empirical potentials can provide a good "first guess" at the nature of the transition state, the value of an "approximate" TST rate constant, and even the effect of the solvent (e.g., as in the work of Jorgenson and co-workers [18,19]). Our group has therefore reformulated the reactive flux algorithm to calculate with AIMD (CP) methods the correction factor to an *approximate* rate constant which is calculated from a semi-empirical potential model. To this end, the *exact* rate constant can be rewritten in terms of the semi-empirically generated rate constant and a correction factor which is dynamically determined from AIMD trajectories, but using a flux-weighted statistical average over initial conditions from the simpler "reference" semi-empirical Hamiltonian, $H_0 = T + V_0$. The reference Hamiltonian H_0 is constructed, e.g., by using a semi-empirical potential described by partial charges in analogy to the empirical potentials of Jorgenson *et al.* [18], but using results from gas phase or cluster DFT studies to be consistent with our overall approach. The initial dividing surface is chosen to correspond to a plane which satisfies the constraint suggested by, e.g., Jorgenson [19]. The statistical averages in the reformulated expression are obtained using molecular dynamics with respect to H_0 constrained to the dividing surface for a time long enough to have sampled the dividing surface ergodically. On the other hand, the trajectories for the recrossing dynamics are generated with the CP method for the "true" Hamiltonian, so they reflect the real dynamics around the transition state. This novel reformulation of the reactive flux method allows for the extensive statistical averaging over initial conditions to be carried out with the help of the semi-empirical potential, while the computationally demanding CP trajectories to calculate the recrossing effects are carried out for only a short period of time (usually less than a picosecond) since these trajectories are rapidly depart the barrier region. Applications of this methodology are presently underway.

REFERENCES

1 J. Cao and G. A. Voth, J. Chem. Phys. **99**, 10070 (1993).
2 J. Cao and G. A. Voth, J. Chem. Phys. **100**, 5106 (1994).
3 J. Cao and G. A. Voth, J. Chem. Phys. **101**, 6157 (1994).
4 J. Cao and G. A. Voth, J. Chem. Phys. **101**, 6168 (1994).
5 A. Calhoun, M. Pavese, and G. A. Voth, Chem. Phys. Lett. **262**, 415 (1996), accepted.
6 M. Pavese and G. A. Voth, Chem. Phys. Lett. **249**, 231 (1996).
7 S. Jang and G. A. Voth, J. Chem. Phys. (in press).
8 J. Sauer and R. Sustmann, Angew. Chem. Int. Ed. Engl. **19**, 779 (1980).
9 D. C. Rideout and R. Breslow, J. Am. Chem. Soc. **102**, 7817 (1980).
10 R. Breslow, U. Maitra, and D. Rideout, Tet. Lett. **24**, 1901 (1983).
11 P. A. Grieco, J. J. Nunes and M. D. Gaul, Tet. Lett, **24**, 1897 (1983).
12 J. J. Gajewski, J. Org. Chem. **57**, 5500 (1992).
13 S. Otto, W. Blokzijl, and J. B. F. N. Engberts, J. Org. Chem. **59**, 5372 (1994).
14 R. Car and M. Parrinello, Phys. Rev. Lett. **55**, 2471 (1985).
15 R. Car and M. Parrinello, in *Simple Molecular Systems at Very High Density*, edited by A. Poliani, P. Louberyre, and N. Boccara (Plenum, New York, 1989), p. 455.
16 D. K. Remler and P. A. Madden, Mol. Phys. **70**, 921 (1990).
17 G. Galli and M. Parrinello, in *Computer Simulations in Material Science*, edited by M. Meyer and V. Pontikis (Kluwer, Dordrecht, 1991), p. 283.

[18] J. F. Blake and W. L. Jorgenson, J. Am. Chem. Soc. **113**, 7430 (1991).

[19] J. F. Blake, D. Lim and W. L. Jorgenson, J. Org. Chem. **59**, 803 (1994).

FIGURE CAPTIONS

Figure 1: The quantum centroid potential of mean force for the intrinsic recombination step between two lithium impurities in solid para-hydrogen at 4 K. Also shown are the error bars. The barrier height is 80 K which corresponds to an intrinsic rate of recombination of 1800 per second.

Figure 2: Time-dependent Li-Li radial distribution function calculated from a long quantum MD trajectory for the 2.5 mole percent lithium impurity system at 4 K. The dashed line is the integrated distribution function, i.e., the number of lithium atoms.

Figure 3: Time-dependent Li-Li radial distribution function calculated from a long quantum MD trajectory for the 3.3 mole percent lithium impurity system at 4 K. The growth in the peak at three Angstroms reflects the impurity dimerization process, and later the impurity clustering process. The dashed line is the integrated distribution function, i.e., the number of lithium atoms.
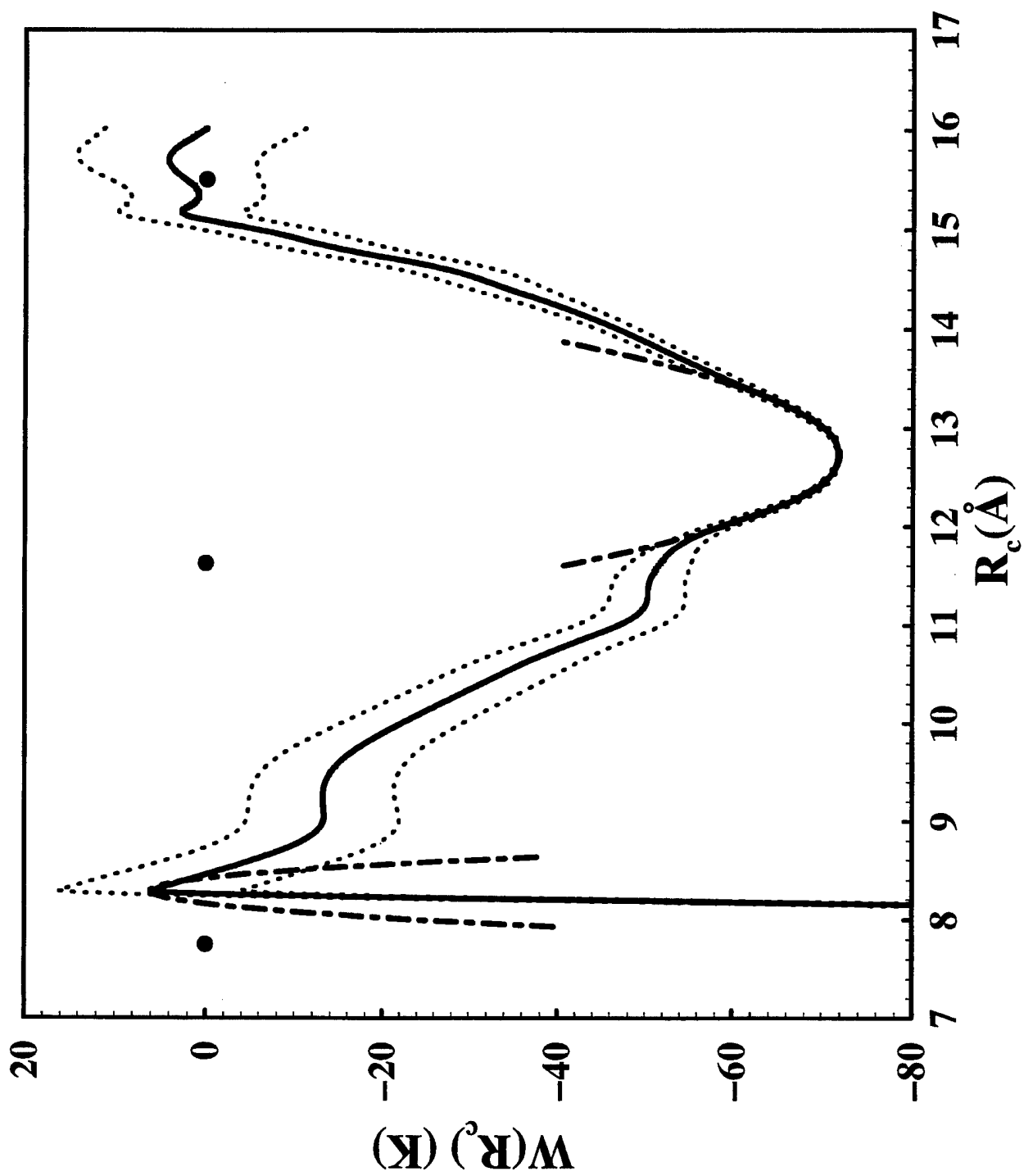
36 Lithium Atoms
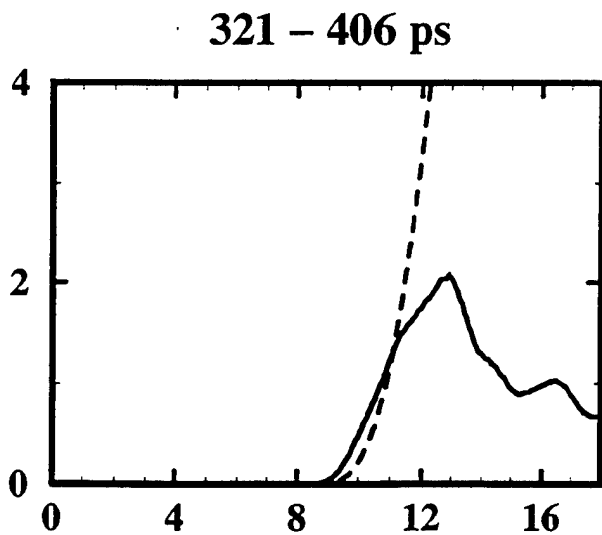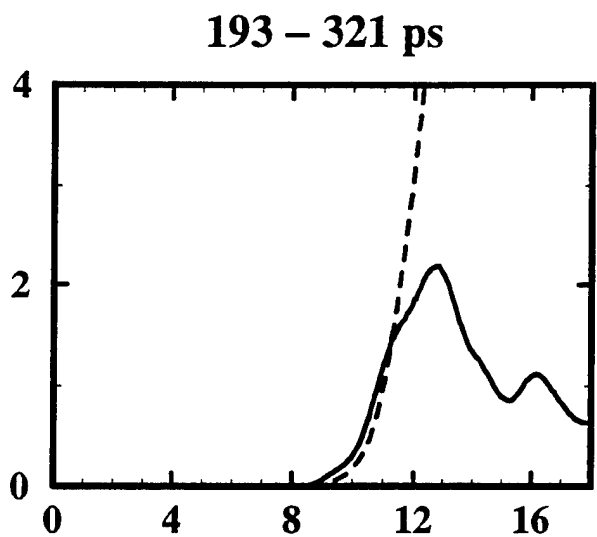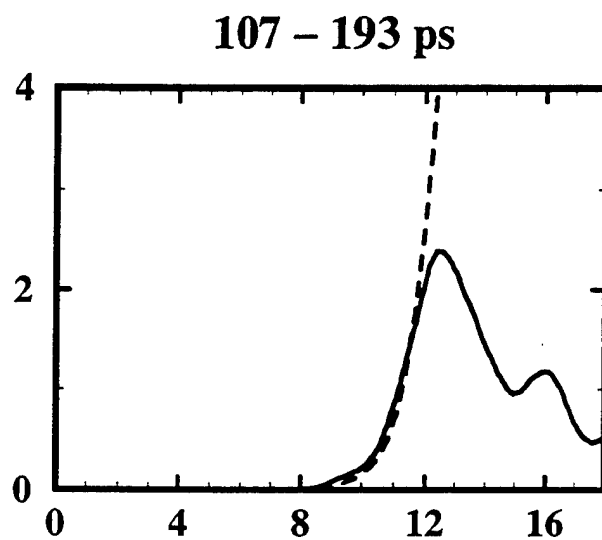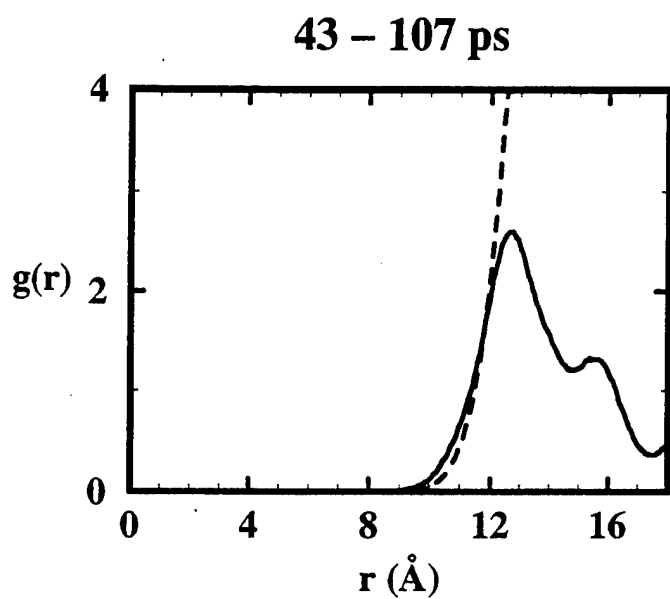
48 Lithium Atoms
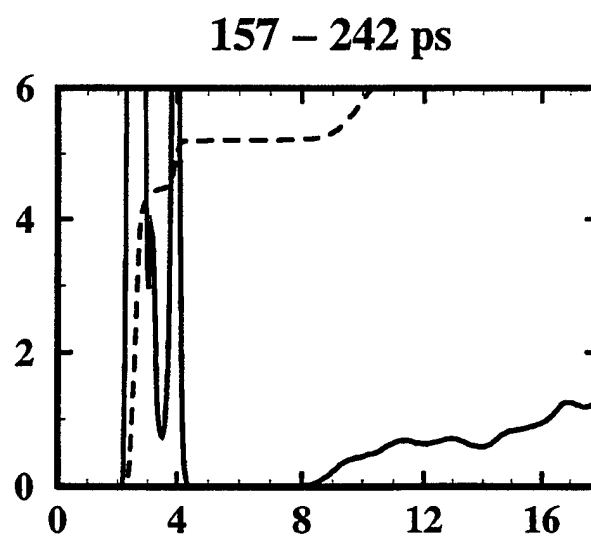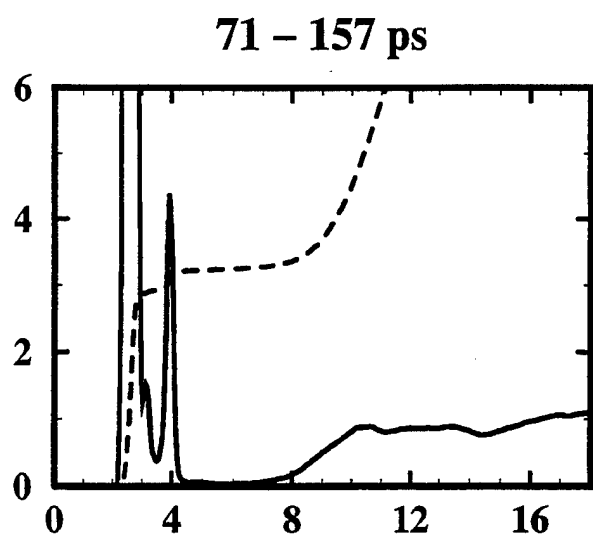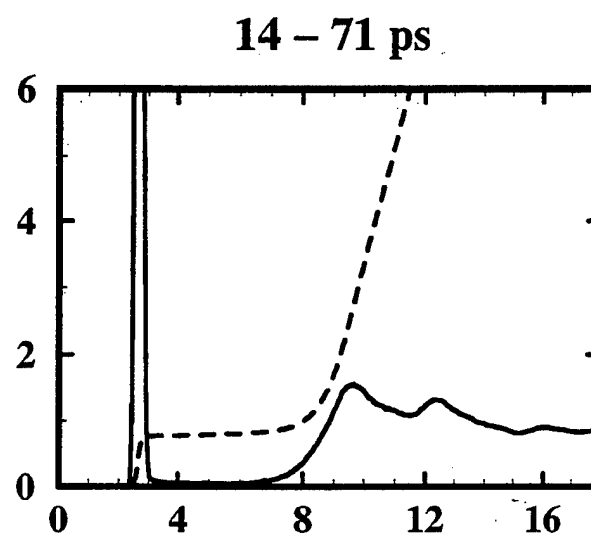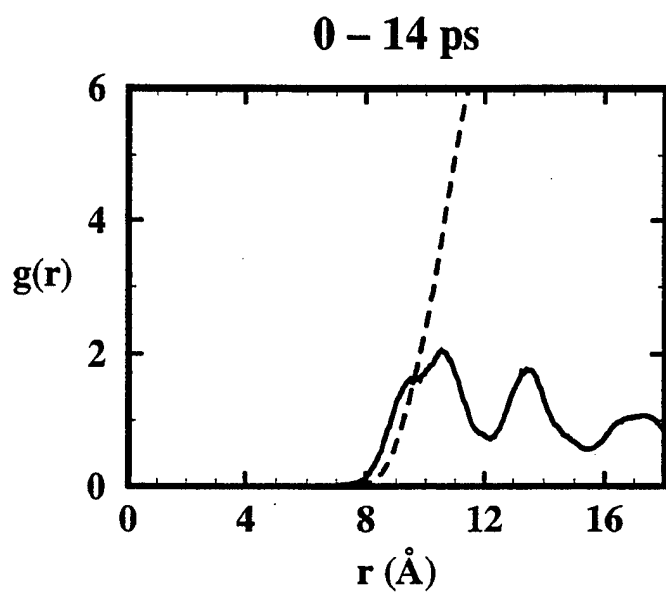
0 – 14 ps

14 – 71 ps

71 – 157 ps

157 – 242 ps

SPECTRAL THEORY OF PHYSICAL AND CHEMICAL BINDING: ASPECTS OF COMPUTATIONAL IMPLEMENTATION[a]

P. W. Langhoff[b]

Department of Chemistry
Indiana University
Bloomington, IN 47405-4001

and

J.A. Boatz and J.A. Sheehy

Propulsion Sciences Division
USAF Phillips Laboratory - OLAC PL/RKS
10 East Saturn Blvd.
Edwards AFB, CA 93524-7680

ABSTRACT

Progress is reported in the development and implementation of a spectral method for constructing the adiabatic electronic potential energy surfaces of large heterogeneous aggregates of physically or chemically interacting atoms. The work carries forward a program of study initiated some years ago by W. Moffitt to describe aggregate electronic structure solely in terms of the properties of atoms and their pairwise interactions. Necessary and sufficient conditions are described for construction of the transformation from diatomic to spectral-product states, and of the corresponding pair-interaction Hamiltonian matrices required in the development, employing representatives of the diatomic spectral response operator obtained from Fourier expansion of the Coulombic interactions. These conditions help to advance the development of the spectral method as a practical computational tool for electronic structure determinations employing conventional irreducible-symmetry methodology. The approach is illustrated with computational studies of avoided crossings in the potential energy surfaces of small van der Waals bonded $NaAr_N$ aggregates, which serve as useful prototypes for understanding selected attributes of cryogenic high energy density matter (HEDM). An outline is provided of work in progress on general implementation of the spectral method and of its application to cryogenic fuels and oxidizers seeded with trace metals which may exhibit improved combustion performance.

I. Introduction

Development of high-specific-impulse cryogenic fuel-oxidizer combinations employing metal or other seedant materials is an important and continuing focus of the USAF high energy density matter (HEDM) program [1]. Accurate adiabatic electronic potential energy surfaces can provide information useful for understanding the structure, stability, and other attributes of such heterogeneous systems. Accordingly, methods for constructing *ab initio* potential energy surfaces which are applicable to large aggregates of physically or chemically interacting atoms are presently under development employing a previously described spectral method devised specifically for this purpose [2].

In the present report, development and implementations are described of the spectral method, and illustrative computational applications are presented in cases of avoided crossings in the potential energy surfaces of physically bonded (van der Waals) inert-gas Ar_N aggregates seeded with metal Na radicals [3]. The general spectral method, which carries forward a program of study initiated some years ago by W. Moffitt [4] and developed and modified by others [5-10], employs a direct product of complete sets of atomic spectral eigenfunctions to represent the total adiabatic electronic wave functions. The representation of the electronic degrees of freedom obtained in this way is not symmetrical [11], and individual terms in the many-electron product basis are not explicitly antisymmetric in the electronic spin and spatial coordinates [12,13]. The Hamiltonian matrix obtained in the spectral-product representation is rigorously pairwise additive in the individual atomic-interaction matrices, which can be obtained by performing calculations on a limited number of appropriate diatomic molecules employing conventional computational methodology. This attribute of the spectral method can provide significant computational advantages for large aggregates of interacting atoms, although issues associated with convergence to antisymmetric states must addressed in the course of its general implementation.

Methods are described here for constructing the required spectral-product basis and the associated pairwise-additive atomic-interaction Hamiltonian matrices from diatomic molecular eigenstates and previously defined spectral response matrices [2] calculated employing conventional computational techniques at finite and asymptotic ($R \to \infty$) internuclear separations. These methods provide an explicit prescription for constructing the unitary transformation from diatomic to spectral-product representations, advancing the development of the spectral method as a computational tool for electronic structure determinations. The attributes of the approach are illustrated quantitatively with calculations of avoided crossings in the potential energy surfaces of $NaAr_N$ clusters employing diatomic states constructed for this purpose in a finite representational basis.

Aspects of the formal theoretical development are briefly reviewed in Section II, the necessary and sufficient conditions for explicit construction of the unitary transformation from diatomic to spectral-product basis representations are reported in Section III, and illustrative applications to avoided crossing situations in ($NaAr_N$) van der Waals aggregates are reported in Section IV. Concluding remarks and an outline of work in progress on general implementation of the spectral method and its application to physically and chemically bonded HEDM systems is given in Section V.

II. Review of the Theoretical Development

The theoretical development employs a direct product basis of the spectral eigenstates of the individual atoms to represent the correctly antisymmetric aggregate states, which basis provides certain advantages in the study of interacting atoms [2]. Specifically, when the product basis

$$\Phi(1;2;\ldots;n) = \left\{ \Phi^{(1)}(1) \otimes \Phi^{(2)}(2) \otimes \cdots \Phi^{(N)}(n) \right\}_O \tag{1}$$

is employed in a conventional linear variational solution of the many-electron Schrödinger equation for an aggregate of atoms 1 to N, the Hamiltonian matrix takes the form

$$\mathbf{H}(\mathbf{R}) = \sum_{\alpha=1}^{N} \left\{ \mathbf{H}^{(\alpha)} + \sum_{\beta=1}^{N} (\beta > \alpha) \, \mathbf{V}^{(\alpha,\beta)}(\mathbf{R}_{\alpha\beta}) \right\}, \tag{2}$$

where

$$\mathbf{H}^{(\alpha)} = \left\{ \mathbf{E}^{(\alpha)} \otimes \mathbf{I}^{(\beta)} \otimes \mathbf{I}^{(\gamma)} \otimes \cdots \mathbf{I}^{(N)} \right\}_O, \tag{3a}$$

$$\mathbf{E}^{(\alpha)} = \langle \Phi^{(\alpha)}(i) | \hat{H}^{(\alpha)}(i) | \Phi^{(\alpha)}(i) \rangle, \tag{3b}$$

are the atomic terms, and

$$\mathbf{V}^{(\alpha,\beta)}(\mathbf{R}_{\alpha\beta}) = \left\{ \mathbf{v}^{(\alpha,\beta)}(\mathbf{R}_{\alpha\beta}) \otimes \mathbf{I}^{(\gamma)} \otimes \mathbf{I}^{(\delta)} \otimes \cdots \mathbf{I}^{(N)} \right\}_O, \tag{4a}$$

$$\mathbf{v}^{(\alpha,\beta)}(\mathbf{R}_{\alpha\beta}) = \langle \Phi^{(\alpha,\beta)}(i;j) | \hat{V}^{(\alpha,\beta)}(i;j) | \Phi^{(\alpha,\beta)}(i;j) \rangle, \tag{4b}$$

are the pair-interaction terms. In Eqs. (1) to (4), $\hat{H}^{(\alpha)}(i)$ is the atomic Hamiltonian operator for the atom α containing the set of electrons i, $\hat{V}^{(\alpha,\beta)}(i;j)$ is the Coulombic interaction operator for atoms α and β, $\Phi^{(\alpha,\beta)}(i;j)$ is the spectral-product basis for the indicated pair, a semi-colon is employed to separate sets of distinguishable electrons $(i;j)$, the bracket symbol $\{\cdots\}_O$ implies choice of a particular ordering rule for the indices of the direct product ($\otimes$) functions, and the vector $\mathbf{R}$ specifies the atomic positions.

Because the representation of Eqs. (1) to (4) is not symmetrical [11], the individual products in the basis of Eq. (1) are not totally antisymmetric [12,13], and the Hamiltonian matrix of Eq.(2) can contain terms which do not correspond to physically meaningful (totally antisymmetric) aggregate eigenstates. These can be removed by performing a series of pairwise unitary transformations on the spectral-product basis and the associated Hamiltonian matrix which leave the physical eigenvalues and vectors invariant, but which allow unphysical components to be discarded. The result of these transformations is to replace the matrix elements of Eq. (4b) with the generally different quantities $v_{sp}^{(\alpha,\beta)}(\mathbf{R}_{\alpha\beta})$ given by the expression

$$\mathbf{v}_{sp}^{(\alpha,\beta)}(\mathbf{R}_{\alpha\beta}) = \mathbf{T}^{(\alpha,\beta)}(\mathbf{R}_{\alpha\beta})^{\dagger} \cdot \mathbf{v}_d^{(\alpha,\beta)}(\mathbf{R}_{\alpha\beta}) \cdot \mathbf{T}^{(\alpha,\beta)}(\mathbf{R}_{\alpha\beta}), \tag{5a}$$

where

$$\mathbf{v}_d^{(\alpha,\beta)}(R_{\alpha\beta}) = \langle \Psi^{(\alpha,\beta)}(i,j) | \hat{V}^{(\alpha,\beta)}(i;j) | \Psi^{(\alpha,\beta)}(i,j) \rangle \tag{5b}$$

is the pair-interaction matrix in the physically meaningful portion of the diatomic eigenstate basis $\Psi^{(\alpha,\beta)}(i,j)$. Here, $\mathbf{T}^{(\alpha,\beta)}(R_{\alpha\beta}) = \mathbf{U}^{(\alpha,\beta)}(R_{\alpha\beta}) \cdot \mathbf{D}^{(\alpha,\beta)}(\omega_{\alpha\beta})$, where $\mathbf{D}^{(\alpha,\beta)}(\omega_{\alpha\beta})$ is a product of Wigner rotation matrices for the atoms α and β, the angles $\omega_{\alpha\beta}$ specify the direction of atom β from atom α, and $\mathbf{U}^{(\alpha,\beta)}(R_{\alpha\beta})$ is the unitary transformation from the physically meaningful (antisymmetric) diatomic states to the spectral-product basis in a pair of rotated atomic coordinate systems having co-linear quantization axes [7].

III. Construction of the Pairwise Rotations

Necessary and sufficient conditions for *ab initio* construction of the pair transformations $\mathbf{U}^{(\alpha,\beta)}(R_{\alpha\beta})$ are obtained from the expression

$$\mathbf{v}_d^{(\alpha,\beta)}(R_{\alpha\beta}) = \frac{1}{4\pi^2} \int_{\mathbf{k}} d\mathbf{k} \left\{ \mathbf{q}_d^{(\alpha,\beta)}(\mathbf{k}, R_{\alpha\beta}) \cdot \mathbf{q}_d^{(\alpha,\beta)}(-\mathbf{k}, R_{\alpha\beta}) - \mathbf{q}_d^{(\alpha,\beta)}(\mathbf{k}, \infty) \cdot \mathbf{q}_d^{(\alpha,\beta)}(-\mathbf{k}, \infty) \right\} \tag{6a}$$

for the interaction matrix $\mathbf{v}_d^{(\alpha,\beta)}(R_{\alpha\beta})$, where

$$\mathbf{q}_d^{(\alpha,\beta)}(\mathbf{k}, R_{\alpha\beta}) = \langle \Psi^{(\alpha,\beta)}(i,j) | \sum_p (q_p/k) e^{i\mathbf{k} \cdot \mathbf{r}_p} | \Psi^{(\alpha,\beta)}(i,j) \rangle \tag{6b}$$

is the previously defined spectral response matrix in the diatomic basis [2], and the sum over particles (p) in Eq. (6b) includes all electrons ($q_p = -e$) and nuclei ($q_p = +Z_\alpha e$ and $+Z_\beta e$) in the molecule. Equations (6a) and (6b) follow from the Fourier transform of the interaction operator appearing in Eq. (5b). In the limit of large internuclear separation ($R_{\alpha\beta} \to \infty$)

$$\mathbf{q}_d^{(\alpha,\beta)}(\mathbf{k}, R_{\alpha\beta} \to \infty) \to \mathbf{M}^\dagger \cdot \mathbf{q}_{sp}^{(\alpha,\beta)}(\mathbf{k}, R_{\alpha\beta}) \cdot \mathbf{M}, \tag{7}$$

where $\mathbf{q}_{sp}^{(\alpha,\beta)}(\mathbf{k}, R_{\alpha\beta})$ is the spectral response matrix in the pair product basis, and $\mathbf{M}$ is a known constant matrix that accounts for possible diatomic state degeneracy in the large $R_{\alpha\beta}$ limit. Accordingly, the calculated diatomic eigenstates are seen to provide the spectral response matrix in both diatomic and spectral-product representations, which matrices can be employed to determine the unitary transformation matrix $\mathbf{U}^{(\alpha,\beta)}(R_{\alpha\beta})$ that connects them

$$\mathbf{q}_{sp}^{(\alpha,\beta)}(\mathbf{k}, R_{\alpha\beta}) = \mathbf{U}^{(\alpha,\beta)}(R_{\alpha\beta})^\dagger \cdot \mathbf{q}_d^{(\alpha,\beta)}(\mathbf{k}, R_{\alpha\beta}) \cdot \mathbf{U}^{(\alpha,\beta)}(R_{\alpha\beta}). \tag{8}$$

It is seen from the expression of Eq. (6a) that the transformation of Eq. (8) also provides the transformation of Eqs. (5). Because the transformation matrix $\mathbf{U}^{(\alpha,\beta)}(R_{\alpha\beta})$ satisfying Eq. (5a) also satisfies Eq. (8), the latter provides necessary and sufficient conditions for determination of the transformation from the physically meaningful diatomic states to the spectral-product basis.

85

IV. Illustrative Applications - NaAr_N Clusters

Applications of the foregoing development are reported for physically bonded Ar_N clusters seeded with Na atoms. For this system, the rotations [Eq. (8)] are solved in the $\mathbf{k} \rightarrow 0$ limit, appropriate for long-range interactions, in which case $\mathbf{q}_d^{(\alpha,\beta)}(\mathbf{k}, R_{\alpha\beta})$ becomes the diatomic dipole transition matrix $\boldsymbol{\mu}_d(R_{\alpha\beta})$, and $\mathbf{q}_{sp}^{(\alpha,\beta)}(\mathbf{k}, R_{\alpha\beta})$ becomes the corresponding dipole transition matrix, $\boldsymbol{\mu}_{sp}(R_{\alpha\beta})$, in the spectral-product basis. Solution of Eq. (8) is obtained in the form

$$\mathbf{U}^{(\alpha,\beta)}(R_{\alpha\beta}) = \mathbf{U}_d^{(\alpha,\beta)}(R_{\alpha\beta}) \cdot \mathbf{U}_{sp}^{(\alpha,\beta)}(R_{\alpha\beta})^\dagger, \tag{9}$$

where $\mathbf{U}_d^{(\alpha,\beta)}(R_{\alpha\beta})$ is the unitary matrix that diagonalizes $\boldsymbol{\mu}_d(R_{\alpha\beta})$ and $\mathbf{U}_{sp}^{(\alpha,\beta)}(R_{\alpha\beta})$ is the unitary matrix that diagonalizes $\boldsymbol{\mu}_{sp}(R_{\alpha\beta})$. Equation (9) is valid in the limit that closure has been achieved in the diatomic and spectral-product representations and the eigenvalues of $\boldsymbol{\mu}_d(R_{\alpha\beta})$ and $\boldsymbol{\mu}_{sp}(R_{\alpha\beta})$ are accordingly identical.

Employing the transformation of Eq. (9) in Eq. (5a) gives the final expression

$$\mathbf{v}_{sp}^{(\alpha,\beta)}(R_{\alpha\beta}) = \mathbf{T}^{(\alpha,\beta)}(R_{\alpha\beta})^\dagger \cdot \mathbf{E}_d^{(\alpha,\beta)}(R_{\alpha\beta}) \cdot \mathbf{T}^{(\alpha,\beta)}(R_{\alpha\beta}) - \mathbf{E}_d^{(\alpha,\beta)} \tag{10}$$

for the pair-interaction matrices, where the substitution $\hat{V}^{(\alpha,\beta)}(i;j) = \hat{H}^{(\alpha,\beta)}(i;j) - \hat{H}^{(\alpha)}(i) - \hat{H}^{(\beta)}(j)$ has been employed, $\mathbf{E}_d^{(\alpha,\beta)}(R_{\alpha\beta})$ is the diagonal matrix of diatomic energies, and $\mathbf{E}_d^{(\alpha,\beta)}$ is its $R_{\alpha\beta} \rightarrow \infty$ limit.

In Fig. 1 are shown diatomic potential energy curves for the ground and low-lying excited states of $NaAr$ calculated as functions of internuclear distance employing multi-reference configuration-interaction methods [14]. Evidently, the excited F and H states undergo an avoided crossing, whereas the other states within a symmetry class (Σ, Π, Δ) are generally well separated at all $R_{\alpha\beta}$. The associated electric dipole and transition matrix elements required in Eq. (8), shown in Figs. 2 and 3 for selected Σ and Π states, are seen to be strong functions of internuclear separation, consequent of atomic-product-state mixings at all $R_{\alpha\beta}$. Also shown in these figures are the eigenvalues of the matrices $\boldsymbol{\mu}_d(R_{\alpha\beta})$ for Σ and Π states, which are significantly less dependent upon internuclear separation than are the matrix elements themselves. Moreover, these eigenvalues are in very good accord with those of the matrices $\boldsymbol{\mu}_{sp}(R_{\alpha\beta})$, which are also shown in the figures, and which should be entirely independent of $R_{\alpha\beta}$. In the limit of closure in the diatomic and spectral-product basis sets, the eigenvalues of the two matrix representatives of the transition moment operator become identical and independent of $R_{\alpha\beta}$.

The transformation matrices obtained for Na-Ar interactions from the results of Figs. 1 to 3 and Eqs. (6) to (10) with $\mathbf{k} \rightarrow 0$ are employed in calculations of potential energy surfaces for the aggregates of interest, whereas the Ar-Ar interactions are treated as pairwise additive in the ground-state potentials. Note that the matrix $\mathbf{M}$ becomes the unit matrix for the states of interest in $NaAr$. In Fig. 4 are shown sections of the potential energy surfaces of $NaAr_2$ (C_{2v} symmetry) as functions of the Ar-Na-Ar angle for states associated with Na $3s \rightarrow 3d, 4p$ excitations. Also shown in the figure are the corresponding

states obtained from the present development employing a unit matrix for the required transformation $[U^{(\alpha,\beta)}(R_{\alpha\beta}) = 1]$, which corresponds to the so-called Balling & Wright approximation commonly employed in collisional broadening studies and trapped radical spectroscopy [3]. Evidently, the spectral method provides avoided crossings in the calculated $^2A_1$ and $^2B_2$ energy surfaces associated with $Na\ 3s \rightarrow 3d, 4p$ excitations, whereas the simpler model does not. Similar observations apply to the more complicated energy surfaces for larger $NaAr_N$ aggregates, also obtained from the present development employing the single Na-Ar transformation matrix of Eqs. (9) and (10). These results suggest that non-additive contributions to the potential energy surfaces of large van der Waals aggregates can be determined quite generally in terms of the underlying pairwise-interaction matrices by employing the computational prescription of Eqs. (9) to (10) for constructing the required pair transformation matrices. In the case of chemical interactions, the more general spectral response matrices of Eqs. (6) to (8) are preferred over the dipole matrices employed for van der Waals aggregates.

V. Concluding Remarks - General Implementation and HEDM Applications

The spectral method and procedures described here for computational implementations have been employed in studies of the effects of non-additivity in the potential energy surfaces on the structure and optical absorption spectra of $NaAr_N$ [$N = 2$ to 147] van der Waals aggregates, results that will be reported subsequently. Some indication of the nature of the approach is provided by the illustrative results reported in Figs. 1 to 4, which employ a limit ($k \rightarrow 0$) appropriate for long-range interactions. Evidently, avoided crossings are obtained from the spectral method in the potential surfaces of these aggregates employing accurate diatomic potential curves.

When the development of Eqs. (6) to (10) is employed, rather than the dipole limit employed in the applications reported here, the spectral method and its implementation is generally applicable to both physical and chemical interactions. Evaluation of the spectral response matrix of Eqs. (6a) and (6b) in the large electronic basis sets required for diatomic calculations will entail development of appropriate computer code routines for this purpose. Additionally, adoption of previously described Stieltjes methods for construction of complete sets of spectral states will allow applications of the spectral method in the limit of closure [15]. These issues are presently under study and will be topics of subsequent HEDM reports.

Applications of the spectral method are in progress to potential cryogenic HEDM systems which may improve the specific impulse of H_2/O_2 propulsion systems. Specifically, the potential energy surfaces of $Li(H_2)_N$ and $Al(H_2)_N$ aggregates are under study in order to clarify the natures of the physical (van der Waals) trapping sites in these cases, and to determine stabilities of the trapping configurations to chemical reactions that can produce the stable products LiH and AlH when the aggregates are subjected to thermal or other influences. Additionally, in view of the importance of cryogenic He_N clusters as potential vehicles for pickup and transport of trace metals into cryogenic fuel or oxidizer matrices, studies of the potential energy surfaces of $LiHe_N$ and $AlHe_N$ aggregates will be undertaken.

Acknowledgments

References

[1] M.E. Fajardo, in *Proceedings of the High Energy Density Matter Contractor's Conference*, Edited by P.G. Carrick and N.T. Williams (1997), PL-TR-96-3037.

[2] P.W. Langhoff, J. Phys. Chem. **100**, 2974 (1996).

[3] J.A. Boatz and M.E. Fajardo, J. Chem. Phys. **101**, 3472 (1994).

[4] W. Moffitt, Proc. Roy. Soc. (Lond.) **A210**, 245 (1951).

[5] F.O. Ellison, J. Am. Chem. Soc. **85**, 3540 (1963).

[6] F.O. Ellison, N.T. Huff, and J.C. Patel. J. Am. Chem. Soc. **85**, 3544 (1963).

[7] J.C. Tully in, *Modern Theoretical Chemistry*, Edited by G.A. Segal, (Plenum, NY, 1977), Vol. 7, pp. 173-200.

[8] P.J. Kuntz in, *Atom-Molecule Collision Theory*, Edited by R.B. Bernstein, (Plenum, NY, 1979).

[9] J.C. Tully, Adv. Chem. Phys. **42**, 63 (1980).

[10] P.J. Kuntz in, *Theory of Chemical Reaction Dynamics*, Edited by M. Baer, (Chemical Rubber, Boca Raton, 1985).

[11] P.A.M. Dirac, *The Principles of Quantum Mechanics* (Oxford University Press, New York, 1958), 4th Edition, Chapter IX.

[12] A.T. Amos and J.I. Musher, Chem. Phys. Letters **1**, 149 (1967).

[13] J.I. Musher and A.T. Amos, Phys. Rev. **164**, 31 (1967).

[14] J.A. Sheehy, in *Proceedings of the High Energy Density Matter Contractor's Conference*, Edited by P.G. Carrick and N.T. Williams (1997), PL-TR-96-3037.

[15] P.W. Langhoff, in *Mathematical Frontiers in Computational Chemical Physics*, Edited by D.G. Truhlar (Springer, Berlin, 1988), pp. 85-135.

Figure 2. Electric-dipole and dipole transition matrix elements (- - -) for *Na Ar* II states obtained from the calculations reported in Fig. 1. Also shown are the eigenvalues of the transition matrices in the diatomic (——) and spectral product (· · ·) representations.
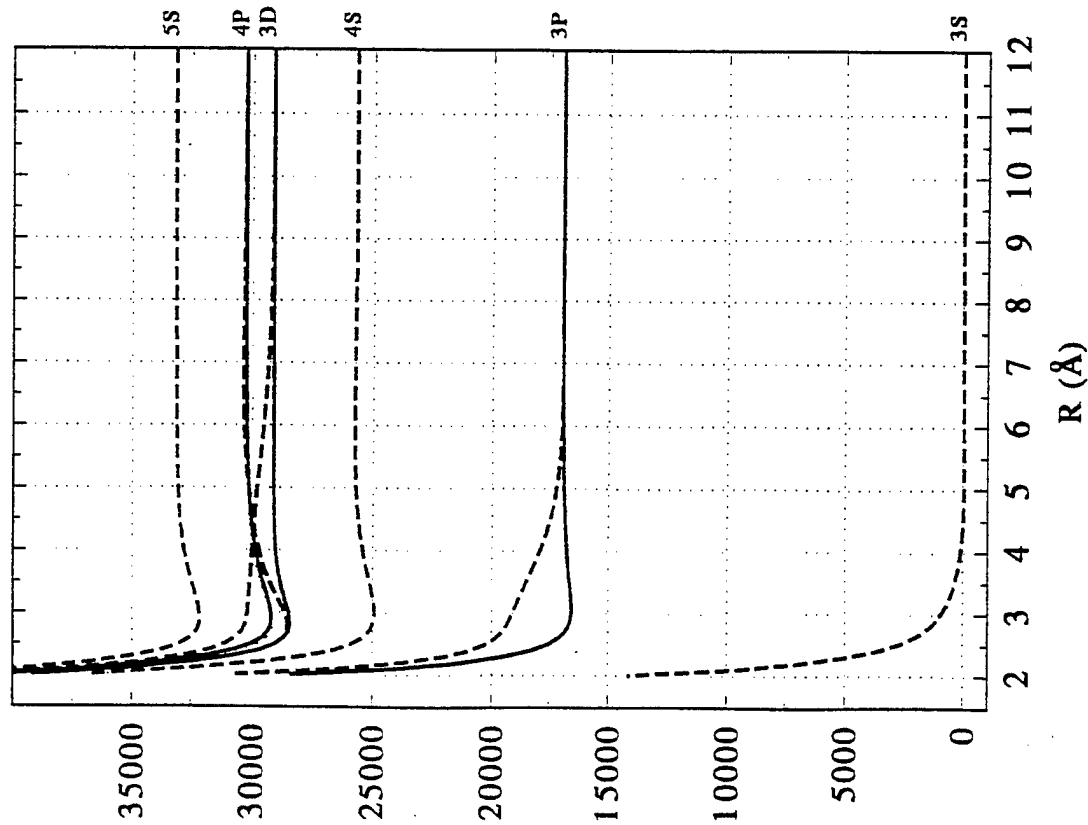
Figure 1. Potential energy curves for the ground- and low-lying-excited states of *NaAr* obtained from multi-reference configuration-interaction calculations [14]; (- - -) Σ states; (——) Π states; (· · ·) Δ state.

Figure 4. Potential energy surfaces for C_{2v} symmetry $NaAr_2$ as functions of the molecule apex angle: Balling & Wright - values obtained employing a unit matrix in place of the transformation of Eq. (9); Spectral Theory - values obtained from the spectral method employing the unitary transformation of Eq. (9).

Figure 3. Electric-dipole and dipole transition matrix elements (- -) for $NaAr$ Σ states obtained from the calculations reported in Fig. 1. Also shown are the eigenvalues of the dipole transition matrices in the diatomic (—) and spectral product ($\cdot \cdot$) representations.

Reactions of Laser-Ablated Boron Atoms with HCN. Infrared Spectra of BNC, BCN, HBNC and HBCN in Solid Argon.

Reactions of Laser Ablated Aluminum Atoms with Ammonia. Infrared Spectra of HAlNH2, AlNH2 and HAlNH in Solid Argon

Dominick V. Lanzisera and Lester Andrews

Department of Chemistry

University of Virginia

Charlottesville, VA 22901

email: lsa@virginia.edu

ABSTRACT

Laser ablated boron atoms (^{10}B, ^{11}B) have been reacted with hydrogen cyanide (HCN, H^{13}CN, DCN) during condensation in excess argon at 6-7 K. The major products observed in the matrix infrared spectrum are BNC and BCN with minor products HBNC, HBCN and HB(CN). Although DFT calculations predict product vibrational frequencies reasonably well, CCSD(T) and CASSCF calculations are superior in predicting both frequencies and intensities. In particular, CCSD(T) calculations by Martin and Taylor of anharmonic frequencies for BNC correctly predicted the strong Fermi resonance interaction observed in the matrix spectrum.

The stable BNC and BCN molecules contain fuel components and merit consideration as possible fuel additives.

Pulsed laser ablated Al atoms react with NH$_3$ to give two major products, HAlNH$_2$ and AlNH$_2$, which are trapped in solid argon and identified from infrared spectra through isotopic substitution (NH$_3$, ^{15}NH$_3$, ND$_3$) and MP2 calculations of product structures and isotopic frequencies. The bent HAlNH molecule was a minor product. In contrast, the linear HBNH molecule was a major product in the boron atom-ammonia reaction.

EXPERIMENTAL

The apparatus for laser ablation and matrix isolation spectroscopy has been described previously.[1,2] Mixtures of 0.3% HCN, $H^{13}CN$ or DCN in argon were codeposited at 3 mmol/h for 2h onto a CsI window at 6-7 K along with laser ablated boron (^nB, ^{11}B or ^{10}B). Analogous experiments were performed with laser-ablated aluminum and ammonia (NH_3, $^{15}NH_3$, ND_3).[3,4]

RESULTS AND DISCUSSION

The results for boron and HCN are summarized in Table 1 and illustrated in the $C\equiv N$ stretching in Figure 1a for ^nB and Figure 1b for ^{10}B. Common peaks to both spectra include HCN, HNC, CN and $(CN)_2$. The strongest absorption in the ^nB spectrum, at 2055.2 cm^{-1} (labeled A) grows 30% on photolysis and decreases 30% on annealing to 25 K. A potential ^{10}B counterpart at 2068.0 cm^{-1} (also labeled A) tracks with this band and is the major band in the ^{10}B spectrum. The next strongest product band in the ^nB experiment, at 2170.8 cm^{-1} (labeled B), has a blue shoulder at 2171.5 cm^{-1}. For the ^{10}B experiment, the 2171.5 cm^{-1} band (labeled B) dominates and decreases 30% on photolysis and 20% on 25 K annealing.

In the lower frequency region, several product bands were observed. One set tracks with the BNC bands and another set with the BCN bands, which are identified in Table 1. The assignments to BNC and BCN are based on agreement with quantum chemical frequency calculations. Martin and Taylor predicted the spectra of BNC and BCN from CCSD calculations and accounted for a strong Fermi resonance in BNC through anharmonic frequency calculations.[5] Table 1 also gives the results of B3LYP density functional theory calculations of harmonic frequencies. The agreement between observed and calculated isotopic frequencies of BNC and BCN confirms the identification of these interesting new molecules.

The consequences of Fermi resonance in BNC but not BCN can be seen in Figure 1. The $C\equiv N$ fundamental for BCN exhibits a 0.7 cm^{-1} boron isotopic shift and in the absence of Fermi resonance, the same should be the case for BNC. However, a 12.8 cm^{-1} boron isotopic shift is found for this mode in $^{10}BN^{12}C$ because of Fermi resonance with the overtone of the lower frequency stretching mode at 1995.8 cm^{-1}. The Fermi resonance is weak for $^{11}BN^{12}C$, but it is even stronger for the $^{10}BN^{13}C$ isotopic molecule as the unperturbed upper stretching fundamental and overtone of the lower frequency fundamental are closer in frequency position.

The C and D bands in Figure 1 are due to the insertion products HBCN and HBNC, respectively, as will be discussed in a later publication.[6]

Davy and Jaffrey performed *ab initio* molecular electronic structure calculations to determine geometries, energies, and vibrational frequencies of compounds expected in the Al+NH$_3$ reaction.[7] The most stable species were found to have the AlNH$_2$ and HAlNH$_2$ structures, and these molecules were the major products identified in the reaction of laser-ablated Al atoms with NH$_3$. Both molecules exhibited NH$_2$ bending and Al-N stretching modes, but the latter direct insertion product also gave strong Al-H stretching and deformation modes. Frequencies for the ^{15}N and D-substituted molecules at the MP2 level were calculated for comparison with observed values.[8] The bent HAlNH molecule was a minor product; in contrast, the linear HBNH molecule was a major product of the B+NH$_3$ reaction.[4]

CONCLUSIONS

In conclusion, laser-ablated B and Al atoms are <u>very reactive</u>. New, simple high energy molecules that have possible application as fuel additives have been prepared. Experiments are in progress to explore these reaction mechanisms. The comparison of calculated and observed isotopic frequencies is necessary to confidently identify new molecules; in this manner normal modes, as well as frequency positions, can be matched.

ACKNOWLEDGMENT

REFERENCES

(1)   Lanzisera, D. V.; Andrews, L. *J. Phys. Chem. A* **1997**, *101*, 824.

(2)   Lanzisera, D. V.; Andrews, L. *J. Phys. Chem. A* **1997**, *101*, 1482.

(3)   Andrews, L.; Burkholder, T. R.; Yustein, J. T. *J. Chem. Phys.* **1992**, *96*, 10182.

(4)   Thompson, C. A.; Andrews, L.; Martin, J. M. L.; El-Yazal, J. *J. Phys. Chem.* **1995**, *99*, 13839.

(5)   Martin, J. M. L.; Taylor, P. R. *J. Phys. Chem.* **1994**, *98*, 6105.

(6)   Lanzisera, D. V.; Andrews, L., *J. Phys Chem. A* **1997**, in press.

(7)   Davy, R. O.; Jaffrey, K. L. *J. Phys. Chem.* **1994**, *98*, 8930.

(8)   Lanzisera, D. V.; Andrews, L. *J. Phys Chem. A* **1997**, in press.

Table 1. Observed and Calculated Vibrational Frequencies (cm^{-1}) for BNC and BCN Using B3LYP (Harmonic) and CCSD (Anharmonic).[a]

BNC	11-14-12	10-14-12	11-14-13	10-14-13	assign
Obs	2055.2	2068.0	2021.6	2039.6	v_1
B3LYP	2115.0	2116.8	2078.5	2080.5	
CCSD	2076.0	2102.2			
Obs		1995.8		1972.4	$2v_2$
Obs	984.3	1016.6	976.1	1008.2	v_2
B3LYP	1012.0	1045.9	1002.6	1034.4	
CCSD	991.0	1023.0			
BCN	11-12-14	10-12-14	11-13-14	10-13-14	assign
Obs	2170.8	2171.5	2122.1	2122.8	v_1
B3LYP	2262.5	2263.5	2210.8	2211.5	
CCSD	2165.5	2166.4			
Obs	800.0	826.2	796.0	822.4	v_2
B3LYP	800.8	828.0	797.9	825.3	
CCSD	809.9	836.4			

[a]CCSD (anharmonic) calculations from Ref. 5.

Figure 1. Matrix infrared spectra in the 2200-1940 cm^{-1} C≡N stretching region following pulsed laser ablation of B atoms codeposited with Ar/HCN (300/1) samples on a CsI window at 6-7 K; (a) $^{n}B + H^{12}CN$ and (b) $^{10}B + H^{12}CN$.
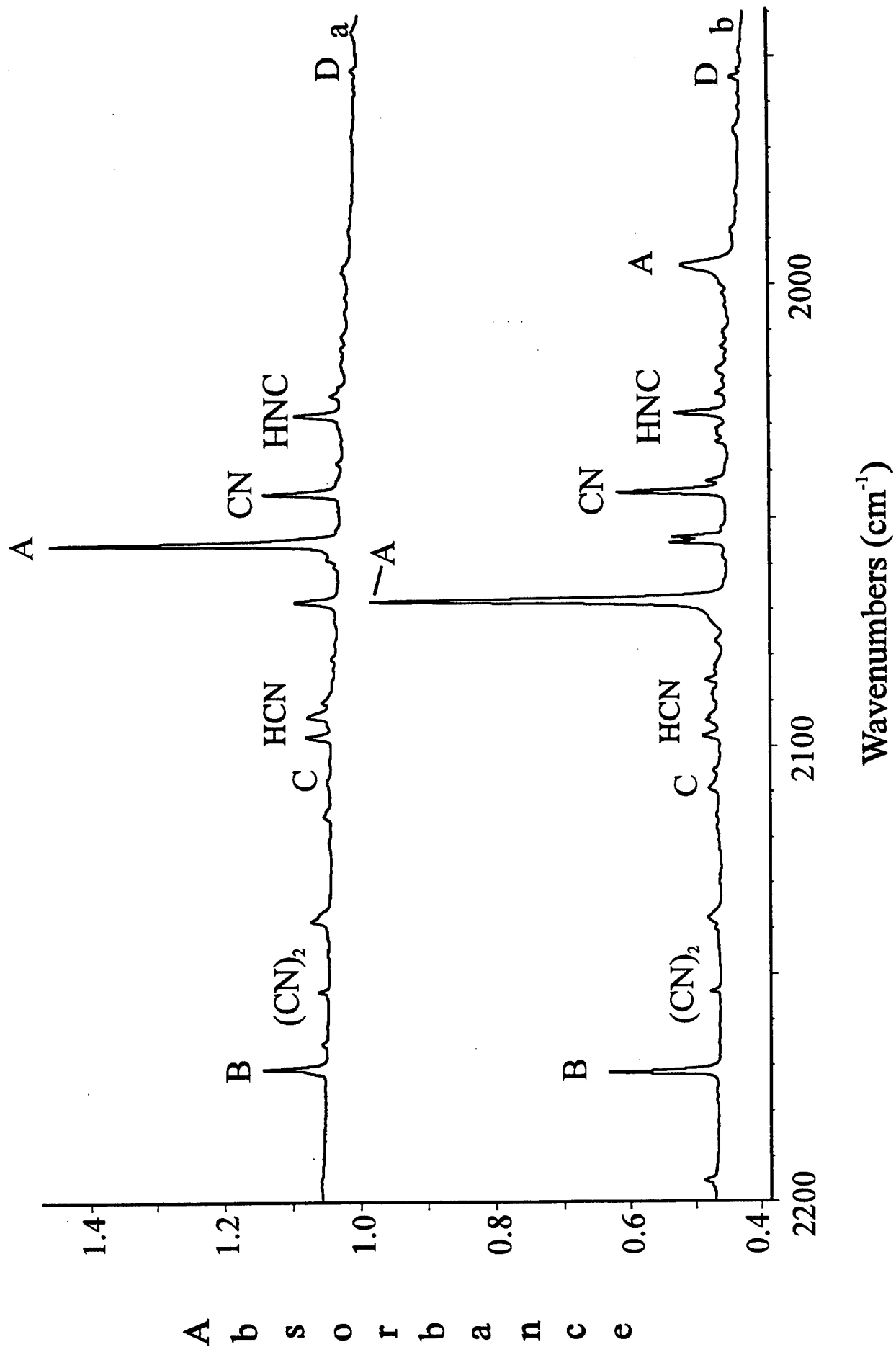
Figure 1

HIGH ENERGY DENSITY MATTER (HEDM) CONTRACTORS' CONFERENCE
Chantilly, VA 1-3 June 1997

Progress Towards the Production of Cryosolid HEDM Samples by Laser Ablation and Matrix Isolation Techniques

Mario E. Fajardo, Michel Macler, and Simon Tam

Propulsion Sciences Division, Propulsion Directorate, Phillips Laboratory
(OLAC PL/RKS Bldg. 8451, Edwards AFB, CA 93524-7680)

ABSTRACT

We report a newly developed method for rapid in-vacuum deposition of thick solid parahydrogen (pH_2) samples which are remarkable for their excellent optical qualities. These experiments were driven by the technological requirement of scaling up HEDM sample production while retaining the desirable aspects of the matrix isolation method for introducing energetic dopants (simplicity, versatility, etc.). The scientific result is a pronounced improvement in the quality of spectroscopic information obtained from these millimeters thick pH_2 samples.

Infrared absorption spectra of pure pH_2 samples suggests a hexagonal close-packed (hcp) microscopic structure§. The excellent optical and thermal properties suggest an overall polycrystalline structure, with large (~ 1 mm ?) crystallites.

We have obtained clean, reproducible spectra of the 200-220 nm electronic absorptions of B atoms in pH_2. We have observed the infrared (IR) absorptions of several molecular species produced either directly by ablation (*e.g.* carbon clusters) or by reactions with the matrix host. We have also observed a variety of novel **induced** IR absorptions of the pH_2 matrix host itself; transitions induced by the presence of atoms, molecules, and ions.

These results constitute the most important scientific and technological advances achieved by our group over the past few years. We expect significant impacts both on the field of condensed phase spectroscopy, and on the prospects of producing useful quantities of HEDM doped cryosolid propellants.

§ Throughout the text this symbol refers the reader to the **Addendum** following the **References**.

INTRODUCTION

Our previous efforts at using optical absorption spectroscopy to demonstrate the trapping of Li, B, Na, Mg, and Al atoms in cryogenic solid hydrogen matrices [refs. 1-3] have been made all the more difficult by the strong optical scattering properties of vapor deposited hydrogen films [ref. 4]. Such films are typically polycrystalline, with microcrystallites having dimensions comparable to optical wavelengths; the optical scattering results from abrupt changes in the solid's refractive index at microcrystallite boundaries. In the ultraviolet (UV) spectral region, e.g.: $\lambda \approx 0.2$ μm, optical scattering losses can easily exceed 90% in vapor deposited normal hydrogen films only ~ 10 μm thick (normal hydrogen, nH_2, is the room temperature equilibrium mixture of 75% ortho hydrogen $\{oH_2\}$ and 25% para hydrogen $\{pH_2\}$ [ref. 5]). Absorption spectra of dopant species obtained from such matrices suffer from poor signal-to-noise ratios and wavelength dependent baseline correction errors.

Our first approach to producing transparent solid hydrogen matrices involved cooling and converting the hydrogen host gas to nearly pure (99.99%) pH_2 by passing room temperature nH_2 gas through a cold (15 K) catalyst bed, followed immediately by deposition of the pH_2 onto a 2 K substrate [refs. 6, 7 and *vide infra*]. Unfortunately, matrices deposited in this manner at conventional matrix host gas flow rates of ~ 1 mmol/hr still exhibited significant optical scattering. Because of the strong wavelength dependence of the scattering phenomenon [ref. 8] the losses are less dramatic in the infrared (IR) spectral region than in the UV, but are still a nuisance. For example, a ≈ 50 μm thick pH_2 matrix deposited at ~ 1 mmol/hr, doped with C_n and hydrocarbon species by laser ablation of graphite, exhibited scattering losses of $\approx 20\%$ at $\lambda = 2.0$ μm [ref. 7].

Motivated by the technological requirement of establishing the scaling characteristics of HEDM sample production techniques, we recently attempted a number of pH_2 depositions at host gas flow rates of 10 to 200 mmol/hr. We anticipated great difficulties in performing absorption experiments in these thicker samples. However, we were pleasantly surprised to find that the resulting millimeters thick solid hydrogen samples are amazingly transparent even at vacuum UV wavelengths! We speculate that the higher deposition rates somehow allow for "self-annealing" of the accreting surface of the matrix during deposition, resulting in larger and fewer crystallites, and hence in greatly reduced optical scattering. Furthermore, and potentially of great significance to both the HEDM cryosolid effort and to matrix isolation spectroscopy in general, we have

demonstrated the trapping and isolation of numerous atomic, molecular, and ionic species in these rapidly deposited samples.

In what follows we describe: (1) the new experimental apparatus and sample preparation conditions, (2) demonstration of control over the ortho:para ratio of the hydrogen matrix host, (3) the remarkable optical, thermal, and spectroscopic properties of these rapidly deposited samples, (4) UV and IR absorption spectra of trapped B atoms and C_n molecules, respectively, and finally (5) novel IR absorptions of the H_2 host itself induced by the presence of atomic, molecular, and charged dopants.

EXPERIMENTAL

We employ an ortho-to-para hydrogen converter consisting of an 1/8 inch OD by 1.5 m long copper tube packed with 1.4 g of APACHI catalyst [ref. 5] wound and potted with conductive epoxy onto a copper bobbin (Figure 1) which can be cooled to below 10 K by a closed-cycle cryostat. This setup allows for continuous H_2 flow rates at 15 K in excess of 1 mol/hr, yielding a flow of pre-cooled 99.99% pH_2 which is deposited directly onto a BaF_2 substrate cooled to 2 K by a separate liquid helium bath cryostat (Figure 2). Because of the sample-in-vacuum design of our cryostat, sample thickness growth rates are limited to < 1 cm/hour by the pumping speed of the small turbomolecular pump which maintains the
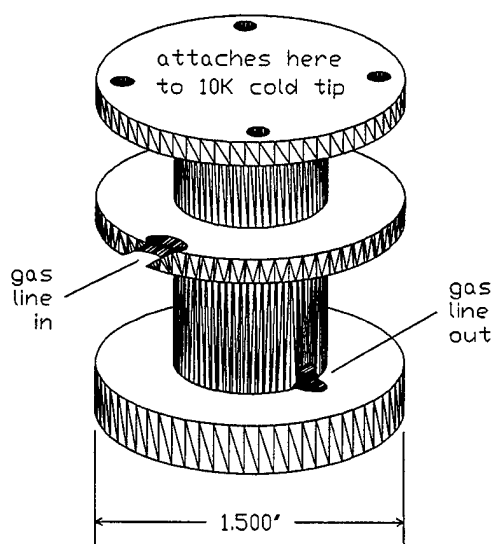
Figure 1. ortho/para Converter Bobbin.
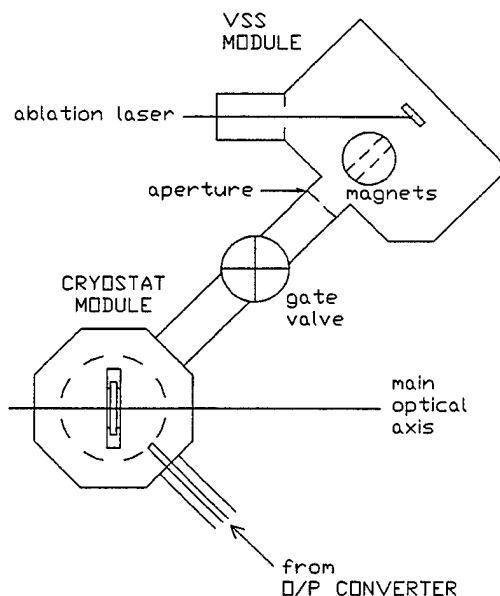
Figure 2. Experimental Schematic.

cryogenic thermal isolation vacuum ($P < 10^{-4}$ Torr uncondensed H_2 required to avoid thermal runaway); ultimate sample thickness is limited by the 3 liter capacity of the liquid helium bath cryostat. The uncondensed H_2 results in an additional complication: the deposition of a second solid H_2 film on the back side of the BaF_2 substrate, amounting to 8 to 9% of the main front side sample thickness; this front:back thickness ratio is independent of H_2 inlet flow rate.

Figure 2 also depicts the arrangement of our laser ablation dopant source. The Temporally and Spatially Specific PhotoIonization (TASSPI) Velocity Selected Source (VSS) module [refs. 9-12] is attached to the deposition chamber of our liquid helium bath cryostat. While no velocity selected atomic depositions are reported in this manuscript, it is important to note that the VSS module includes a pair of removable magnets which can be used to eliminate charged species from the laser ablated plume. For depositions in which the dopants are volatile at room temperature, such as CO, N_2, and CH_3OH, the VSS module was replaced by a simple copper tube inlet connecting the deposition chamber with a separate gas handling manifold.

Back-reflection HeNe laser interferograms taken during deposition, and matrix UV and IR absorption spectra, are obtained along the main optical axis. These diagnostics simultaneously probe both front and back side H_2 samples. To accommodate the IR diagnostic, most of the apparatus resides inside a 0.5 m^3 polycarbonate box purged with a constant flow of dry N_2 gas.
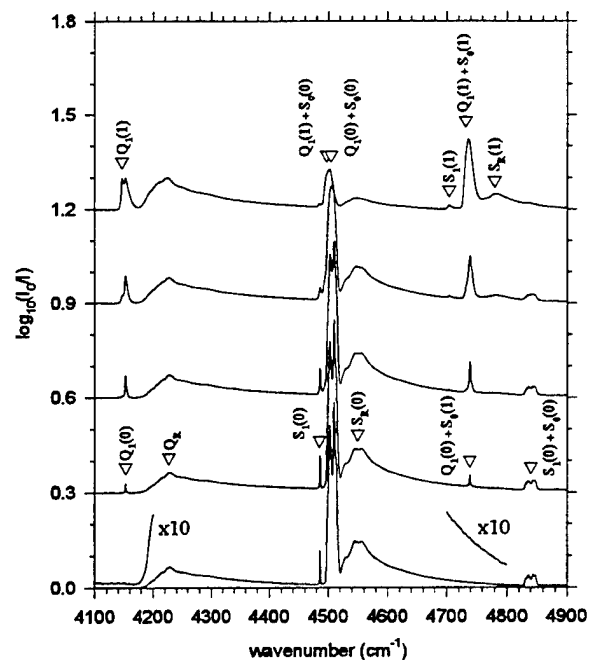
Figure 3. Ortho/para composition of ≈ 0.9 mm total (front + back) thickness vapor deposited solid hydrogen samples at T = 2 K. The oH_2 concentrations increase from bottom to top in the sequence: 0.01%, 2%, 8%, 25%, and 70%, corresponding to o/p converter bobbin temperatures of: 15 K, 28 K, 37 K, 52 K, and 135 K. In each case $\approx 55(\pm 3)$ mmol of hydrogen were deposited in a 1 hour period. The absence in the bottom trace of the $Q_1(0)$ (4153 cm^{-1}) and $Q_1(0)+S_0(1)$ (4740 cm^{-1}) absorptions is evidence of the very low oH_2 concentration (< 0.1%) in that sample. The spectra are presented at 1 cm^{-1} FWHM resolution.

100

RESULTS AND DISCUSSION

Figure 3 shows absorption spectra ($A = \log_{10}[I_0/I]$) of five different rapidly deposited solid hydrogen samples, of different oH_2 compositions obtained by adjusting the temperature of the ortho/para converter bobbin. Infrared activity in the homonuclear diatomic H_2 molecules arises from dipoles induced by intermolecular interactions in the condensed phase environment [refs. 13, 14]. The observed spectral changes with increasing oH_2 concentrations match exactly those reported for solid hydrogen crystals grown from the liquid [ref. 15]. None of these samples exhibited appreciable optical scattering, either visually or in the form of a wavelength dependent scattering background across the 1000 to 5000 cm^{-1} range.

Figure 4 shows the linearity of the sample thickness growth rates for two of the highest H_2 inlet flow rates used in this study. Both traces show similar ratios of H_2 host gas inlet amount to final total (back + front) sample thickness of about 60($\pm$5) mmol/mm, the same as for the slower
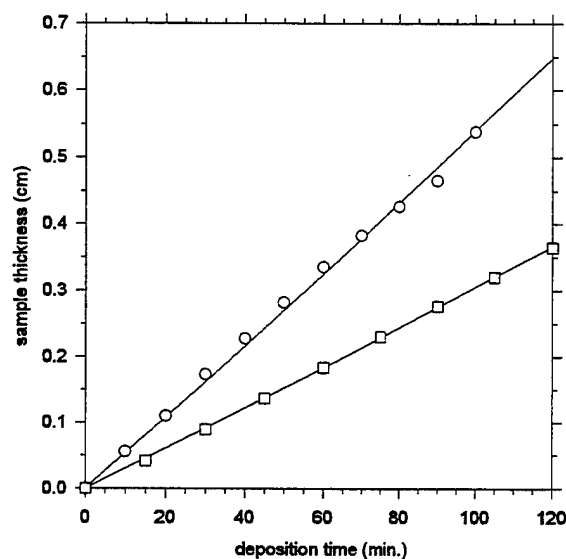
Figure 4. Linear Growth of Rapidly Deposited pH_2 Samples. Total (front+back) thicknesses are calculated from the absorption intensities of the $S_1(0)+S_0(0)$ band integrated over the 4825 to 4855 cm^{-1} range. The total H_2 gas inlet amounts were: 0.38 moles for the top trace, and 0.22 moles for the bottom trace. During the depositions, the BaF_2 substrate holder temperature rose from a baseline of 1.9 K, to 2.8 K and 2.5 K for the top and bottom traces, respectively.
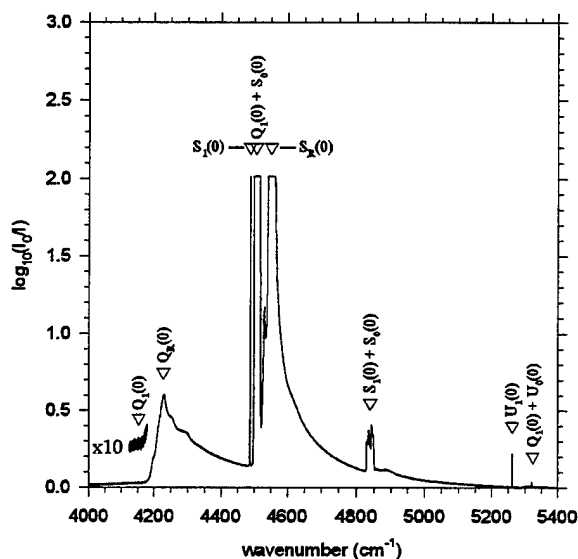
Figure 5. IR Absorption Spectrum of $\approx$ 6 mm Thick pH_2 Sample. The sample's growth history is shown in the top trace (open circles) of figure 4. Observation of the $S_1(0)$ transition at 4486 cm^{-1} combined with the non-observation of the $Q_1(0)$ transition at 4153 cm^{-1} demonstrates that the microscopic crystal structure is hcp§. The spectrum is presented at 0.15 cm^{-1} FWHM resolution, without any corrections whatsoever for optical scattering losses.

H_2 inlet rates depicted in figure 3. The observed linear growth rates and constant deposition efficiencies indicate that any additional thermal impedance due to the presence of the several millimeters thick pH_2 sample is a negligible component of the overall thermal impedance between the matrix accretion layer and the liquid helium bath.

Figure 5 shows the absorption spectrum of the same 99.99% pH_2 sample as depicted in the top trace of figure 4. At these very low oH_2 concentrations, the absorption spectrum yields quantitative information about the symmetries of the sites occupied by the pH_2 molecules. The close similarities between our observed solid pH_2 absorption lineshapes and those for large single crystal pH_2 samples [refs. 15-17] suggest that the vast majority of the H_2 molecules in our samples exist in an environment very similar in short-range structure to that found in hexagonal close-packed (hcp) pH_2 crystals[§]. More specifically: observation of the $S_1(0)$ absorption demands the absence of inversion symmetry in the H_2 molecules' local environment, while non-observation of the $Q_1(0)$ absorption demands that the sum of the vectors connecting each H_2 molecule with all of its nearest neighbors vanishes [ref. 18]. These observations are consistent with an hcp host structure, but not with face-centered cubic (fcc) or other centrosymmetric lattices, nor are they consistent with amorphous structures, or with the presence of large numbers of vacancy defects. We conclude that over 99.95% of the H_2 molecules in our samples exist in effectively hcp sites[§].

These spectroscopic observations, combined with the samples' excellent optical transparency and thermal properties, suggest an overall polycrystalline hcp structure[§] with fairly large (~ 1 mm ?) crystallites. We are preparing to confirm this assertion by performing visual inspections of thick vapor deposited pH_2 samples between crossed-polarizers [ref. 5].

We began studying vapor depositions of hydrogen samples in the first place to allow for the deliberate introduction of isolated energetic dopant species. Growing pH_2 crystals from the melt results in very pure samples, as few species (*e.g.*: oH_2, HD, D_2, HT, DT, T_2, and to a lesser extent: He, Ne) have any appreciable solubility in liquid pH_2, or survive phase separation upon freezing [ref. 4]. Furthermore, some reactive species are quite mobile in *solid* hydrogen at temperatures above ≈ 5 K [ref. 1] and are thus subject to loss via recombination. Fortunately, vapor deposition is an effective way of preparing doped solid samples which additionally allows us to take advantage of the myriad of dopant production techniques developed in previous matrix isolation spectroscopic studies [ref. 19].

Figure 6 shows IR absorptions of carbon clusters (and probably also hydrocarbons) trapped in a 1.2 mm thick pH₂ sample at T = 2 K. The signal:noise ratio of ≈ 100:1 for the main C_3 peak is significantly improved over recently published results [refs. 7, 20]. The observed irreversible changes in the intensities of the "C_3" peaks upon annealing to 4 K contradicts previous observations [ref. 20] and argues for the existence of multiple trapping sites for C_3 in pH₂ (or for a reassignment of the lines in the 2030 to 2040 cm⁻¹ region).

Figure 7 shows broad UV absorptions centered at 209 and 217 nm which we have previously assigned to B atoms isolated in solid hydrogen [ref. 2]. This spectrum as well represents a vast improvement in signal:noise ratio over our previous efforts (the estimated B atom concentrations are still low, but the optical path lengths are ~ 10 to 100 times longer than before). The improved optical quality of our new samples should be a great help in our ongoing efforts to prove conclusively the trapping of B atoms in pH₂.

In addition to yielding improved spectra of dopant species, the increased optical path
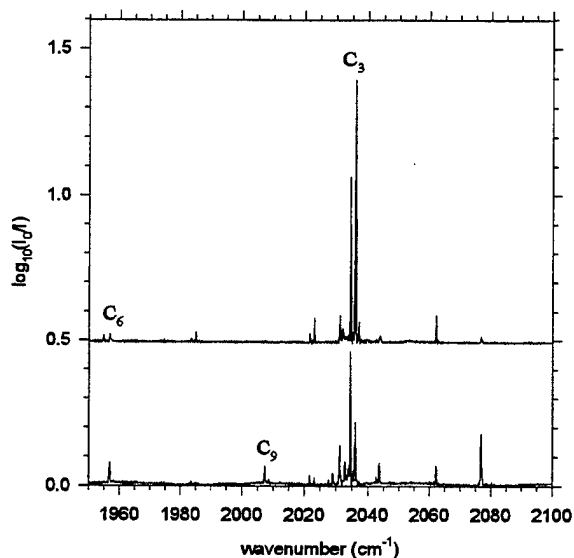
Figure 6. IR Absorptions of Carbon Clusters in pH₂ at T = 2 K. The sample was prepared by laser ablation of graphite. The top trace shows the as-deposited sample, with: T = 2 K, λ_{abl} = 308 nm, $\Phi_{abl} \approx 8\times10^7$ W/cm², 100 mJ/pulse, 10 Hz repetition rate, 30 minute C_n deposition time, H₂ inlet flow rate ≈ 120 mmol/hr, l = 1.2 mm. The bottom trace shows the sample again at 2 K, after warming to 4 K. Resolution is 0.15 cm⁻¹ FWHM.
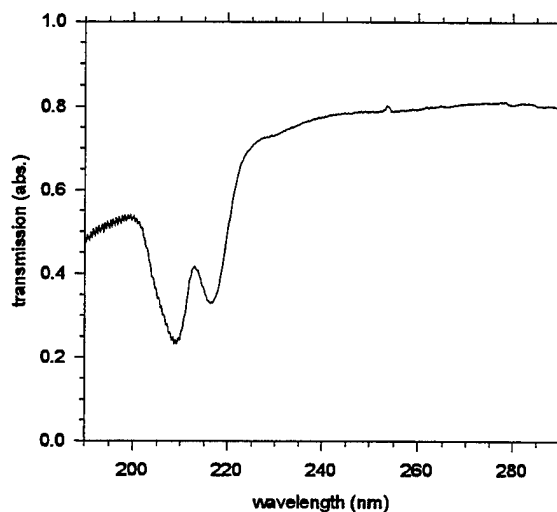
Figure 7. UV Transmission Spectrum of B/H₂ at T = 2 K. The sample was prepared by laser ablation of solid boron with: T = 2 K, λ_{abl} = 308 nm, $\Phi_{abl} \approx 9\times10^7$ W/cm², 110 mJ/pulse, 10 Hz repetition rate, 60 minute B deposition time, H₂ inlet flow rate ≈ 55 mmol/hr, l = 1.0 mm.

103

lengths provided by our rapidly deposited samples enables us to detect the weak IR activity induced by the dopant species in the solid hydrogen host itself. Perhaps the most familiar example of this impurity-induced IR activity is that due to oH_2 impurities in pH_2, as shown in figure 3. This effect is absent in rare gas atom host matrices, but is a topic of current interest in doped N_2 matrices [refs. 21, 22].

Figure 8 shows IR absorptions induced by the presence of neutral dopants. The complexity of the spectral pattern seems to increase as the dopant changes from atomic to diatomic to polyatomic, perhaps reflecting an increase in the number of dissimilar H_2 molecular environments. All the peaks appear within $\pm$ 10 cm^{-1} of the position of the $Q_1(0)$ line in the 2% oH_2 sample. Figure 9 shows IR absorptions induced by charged dopants. The large decrease in absorbance near 4150 cm^{-1} is the so-called "interference" feature due to trapped excess electrons,
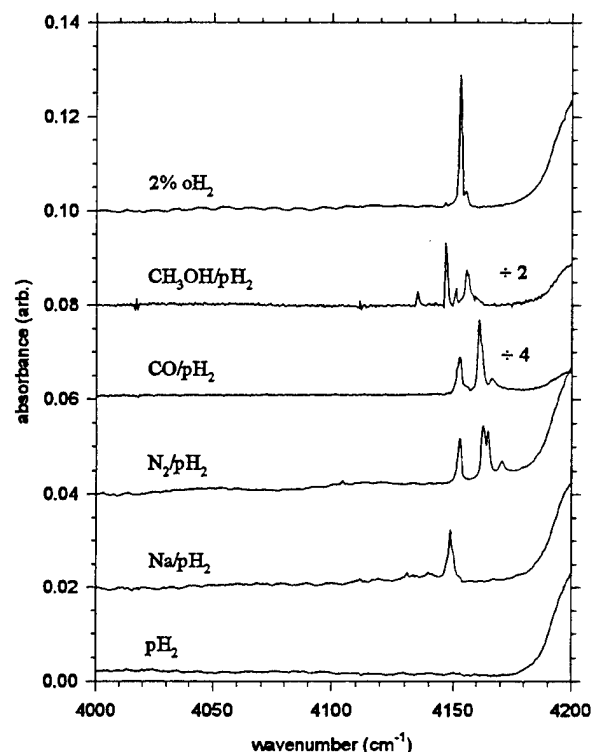
Figure 8. Neutral-Dopant Induced H_2. IR
Absorptions at T = 2 K. The pure pH_2 and the 2% oH_2 traces are the same data as shown in figure 3. All samples are between 0.7 and 0.9 mm thick. The Na/pH_2 sample was prepared by laser ablation with the ion rejection magnets in place.
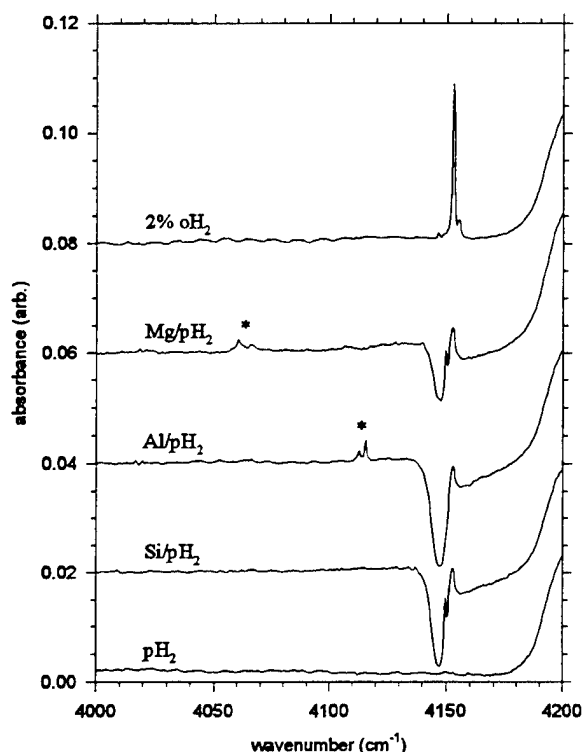
Figure 9. Charged-Dopant Induced H_2 IR
Absorptions at T = 2 K. All samples are between 0.8 and 1.0 mm thick. The metal doped samples were prepared by laser ablation without the ion rejection magnets. The features marked by asterisks are likely induced by positively charged species.

104

and is well known from studies on irradiated solid hydrogen samples [ref. 23]. The strongly red-shifted features marked by asterisks are likely due to trapped positively charged dopants, either metal ions or their reaction products. A similar positive ion induced feature has been observed at 4149.7 cm^{-1} in γ-ray irradiated pH_2 crystals [ref. 24]. Stark shifts for the ro-vibrational energy levels of H_2 adjacent to a positive charge have been calculated [ref. 25]; direct application of these results to the data in figure 9 yields reasonable ion-H_2 separations of 2.7 Å and 3.2 Å for the Mg/pH_2 and Al/pH_2 samples, respectively. Our experiments and analysis of these induced absorptions are still in progress. We ultimately expect to show that this induced IR activity can provide spectroscopic information complementary to the dopant absorptions, which will be key to the quantitative characterization of the microscopic structures of these samples.

CONCLUSIONS

We have developed a new method for rapid vacuum deposition of millimeters thick, doped, solid pH_2 samples. Unlike typical vacuum deposited hydrogen films, these samples exhibit very little optical scattering, even at vacuum UV wavelengths. Details of the IR absorption spectra of the pure pH_2 samples are consistent with an hcp crystal structure§.

The longer paths lengths afforded by this new sample preparation approach offer a significant improvement in signal:noise ratio for weak absorptions over traditional matrix isolation spectroscopy in thin rare gas host films. Additionally, IR activity induced in the pH_2 host by the dopants provides complimentary information about the dopant trapping environment, information unobtainable from rare gas matrix experiments.

REFERENCES

1. M.E. Fajardo, J. Chem. Phys. **98**, 110 (1993).

2. M.E. Fajardo, S. Tam, T.L. Thompson, and M.E. Cordonnier, Chem. Phys. **189**, 351 (1994).

3. S. Tam and M.E. Fajardo, unpublished B, Mg, and Al matrix isolation data.

4. P.C. Souers, Hydrogen Properties for Fusion Energy (University of California Press, Berkeley, 1986).

5. I.F. Silvera, Rev. Mod. Phys. **52**, 393 (1980).

6. M.E. Fajardo, M. Macler, and S. Tam, "Progress Towards Deposition of Velocity Selected Aluminum Atoms into Cryogenic para-Hydrogen Matrices" in Proceedings of the High Energy Density Matter (HEDM) Contractors' Conference held 5-7 June 1996 in Boulder CO, ed. P.G. Carrick and N.T. Williams, PL-TR-96-3037 (Phillips Lab, Edwards AFB, CA, 1997).

7. S. Tam, M. Macler, and M.E. Fajardo, J. Chem. Phys. **106**, 8955 (1997).

8. M. Born and E. Wolf, Principles of Optics, 6th edition (Pergamon Press, Oxford, 1987).

9. M. Macler and M.E. Fajardo, MRS Symp. Proc. **285**, 105 (1993).

10. M. Macler and M.E. Fajardo, Appl. Phys. Lett. **65**, 159 (1994).

11. M. Macler and M.E. Fajardo, Appl. Phys. Lett. **65**, 2275 (1994).

12. M. Macler and M.E. Fajardo, MRS Symp. Proc. **388**, 39 (1995).

13. J. Van Kranendonk, Physica **23**, 825 (1957).

14. J. Van Kranendonk and G. Karl, Rev. Mod. Phys. **40**, 531 (1968).

15. H.P. Gush, W.F.J. Hare, E.J. Allin, and H.L. Welsh, Can. J. Phys. **38**, 176 (1960).

16. A. Crane and H.P. Gush, Can. J. Phys. **44**, 373 (1966).

17. S.Y. Lee, Ph.D. thesis, The Ohio State University (1987).

18. J. Van Kranendonk and H.P. Gush, Phys. Lett. **1**, 22 (1962).

19. D.W. Ball, Z.H. Kafafi, L. Fredin, R.H. Hauge, and J.L. Margrave, A Bibliography of Matrix Isolation Spectroscopy 1954-1985 (Rice University Press, Houston, TX, 1988).

20. M. Miki, T. Wakabayashi, T. Momose, and T. Shida, J. Phys. Chem. **100**, 12135 (1996).

21. D.P. DiLella and D.E. Tevault, Chem. Phys. Lett. **126**, 38 (1986).

22. F. Legay and N. Legay-Sommaire, J. Phys. Chem. **99**, 5277 (1995).

23. S.K. Bose and J.D. Poll, Can. J. Phys. **65**, 58 (1987).

24. T. Momose, K.E. Kerr, D.P. Weliky, C.M. Gabrys, R.M. Dickson, and T. Oka, J. Chem. Phys. **100**, 7840 (1994)

25. J.D. Poll and J.L. Hunt, Can. J. Phys. **63**, 84 (1985).

§ Addendum

Discussions with other members of the HEDM community brought to our attention a flaw in our arguments for a nearly pure hcp structure. Our IR absorption spectra demonstrate the presence of some hcp pH_2, but do not preclude the presence of fcc or random-stacked close packed structures. Since the 1997 conference we have recorded the spontaneous Raman scattering spectrum of our rapidly deposited samples. These new data show that the as-deposited microscopic structure is in fact a mixture of fcc and hcp, with the possible inclusion of random-stacked close packed structures as well. These observations are in complete agreement with the results reported by Collins, et al., Phys. Rev. B **53**, 102 (1996).

Studies of Cryogenic Carbon and Boron HEDM

J.D. Presilla-Márquez
24147 20 Mule Team Road, Apt. 304, Boron, Alta California 93516

P.G. Carrick, J.D. Mills, J.A. Sheehy and C.W. Larson
OLAC Phillips Laboratory/RKS, Edwards AFB, California 93524-7680

ABSTRACT

A variety of cryogenic argon matrices were produced that contained carbon or carbon/boron in the ratio C/B ~ 3/1. The goal was to produce atomic densities approaching 1.2×10^{21} atoms per cubic centimeter, which is 5% of the 10K argon matrix density. FTIR spectra of C_n and/or B_xC_y clusters were measured between ~ 950 to 2200 cm^{-1} at a resolution where FWHM ~ 1.2 cm^{-1} at 1700 cm^{-1}. Over this wavelength range C-C and C-B stretching is intense. Gas phase intensities of linear C_n clusters (n = 3 to 9) were predicted at the DFT/B3LYP/cc-pVDZ level of ab initio theory to range between about 200 to 7000 km/mole; similarly the intensities of cyclic-C_n (n = 4,6, 8, 10, 12) clusters ranged from ~ 300 to 1500 km/mole. Vibrational frequencies of B_xC_y clusters (x + y = 3, 4) were predicted [DFT/B3LYP/6-31G*, DFT/B3LYP/6-311G(2df), DFT/B3LYP/6-311G(2d)] with intensities of ranging from ~ 7 km/mole (B_2C) to ~ 1000 km/mole (B_2C_2). The experimentally measured absorptivity of the ith species, $a_i(v)$, was combined with the calculated intensity, I_i, to produce overall average values of the column density $<\rho_i \, l>_{matrix}$:

$$<\rho_i \, l>_{matrix} = \frac{N}{I_i} \int_{v_1}^{v_2} a_i(v) dv$$

where the absorptivity, $a_i(v) = - \ln [I(v)/I_o(v)]$, and N is Avogadro's number. An average density of the clusters was obtained from the estimated average thickness of the matrix, l ~ 60 microns.

Comparison of the theoretical isotopomer shifts of cyclic-C_n and B_xC_y clusters to the shifts measured in various matrices with differing $^{10}B/^{11}B$ and $^{13}C/^{12}C$ ratios led to the unequivocal identification of five new molecules: cyclic-C_6, cyclic-C_8, BC_2, BC_3 and B_2C_2. Complete families of isotopomers were produced in some of the matrices where $^{10}B \sim ^{11}B$ and $^{13}C \sim ^{12}C$. Conclusive assignment of numerous FTIR absorptions measured in these matrices to additional new molecules, i.e., BC_y and B_2C_y (y > 1) and cyclic-C_n (n = 10, 12), or to overtones or absorptions of low-lying electronic states of cyclic-C_n (n = 6, 8), are being carried out with the support of new theoretical calculations.

Successive annealing of the carbon/boron matrices for around one-minute to temperatures around 28 K, 30 K, 32 K, 34 K, etc. revealed that they were extremely reactive. Generally, small clusters disappeared and larger clusters initially grew and then disappeared. No B_2C_2 was produced upon deposition of the matrix. After the first

annealing to 27.5 K/1-minute, $B_2C_2 \sim 0.8 \times 10^{17}$ molecules cm^{-3} was produced. Appearance of B_2C_2 was accompanied by disappearance of BC_2, which decreased from $\sim$ 1.2 to 0.9×10^{18} molecules cm^{-3}. This finding is consistent with the hypothesis that the scavenging of boron atoms by BC_2 occurs when the matrix is warmed and boron atoms become mobile. The equivalent carbon atom densities (in units of 10^{18} atoms cm^{-3}) of the identified species in a representative initial matrix were $BC_2 \sim 2.5$, $C_3 \sim 2.4$, $BC_3 \sim .75$, $C_4 \sim 0.44$, $C_6 \sim 0.11$, $C_5 \sim 0.045$, $C_7 \sim 0.028$, $C_9 \sim 0.0032$, and $B_2C_2 < .001$.

Annealing of the matrices with the largest carbon densities produced a condensation in which cyclic-C_6 and cyclic-C_8 played the dominant role. Their yields generally doubled upon the first annealing, and their yields exceeded the combined yield of all linear C_n clusters (n = 3 to 9) by a factor of three! The first two annealings of the most dense matrix resulted in increases in the equivalent carbon atom density of $\sim 25 \times 10^{18}$ atoms cm^{-3} for cyclic-C_6 and 15×10^{18} atoms cm^{-3} for cyclic C_8. During annealing, these high density carbon matrices emitted a characteristic green glow, reminiscent of the green emission of the Swan bands of the C_2 molecule in flames. The matrices were allowed to freely warm to temperatures greater than 40K after annealing studies were completed. Video tape recordings at frame rates up to 3000 frames per second revealed spectacular intense emission of visible light, which was emitted over time scales less than 0.3-millisecond. Initially, randomized and intermittent emission from areas less than 1-mm^2 occurred all over the matrix. This evolved over time into organized emission from a large area, about 3-mm by 20-mm. The organized emission appeared to track a critical isotherm that moved across the matrix as the matrix temperature increased. This intense emission, which occurred for about 30-seconds at the rate of one burst per second, was, in the most dense carbon matrices, preceded by a period of intense and homogeneous green glow for about 10-seconds, followed by about 10-seconds of no activity.

This study was enabled by the development of a new high temperature oven (~3000 K) that would, under conditions of ideal operation, produce carbon atoms from a 1-mm diameter orifice at a flux of $\sim 7 \times 10^{20}$ atoms/cm^2-s, where the pressure of carbon atoms is about 1-Torr. Under these conditions, the mean free path of C in a carbon atom gas is ~ 1.1 cm, about the size of the oven itself, so that the orifice itself acts as an atom selector, separating out larger species with smaller mean free path. At the orifice, the temperature is about 200 K or more higher than at the evaporating carbon surface. Thus, the vapor in equilibrium with condensed phase, dominated by C_3, is dissociated to carbon atoms at the orifice. The purity of the atomic plume leaving the oven increases with the temperature difference, ΔT, between the orifice and condensed phase surface. The most dense carbon matrices were produced as multilayered sandwiches containing as many as ten regions of high density carbon separated by layers of pure solid argon. Production of these matrix sandwiches was accomplished by thermally cycling the furnace, which enhanced the purity of the atomic plume because the transient ΔT following the initial sudden application of furnace power persisted for a significant amount of time before relaxing to the steady state ΔT.

Previously, in 1991, Vala's group produced moderately high density carbon/argon matrices by laser ablation of graphite that were estimated to contain about 0.5 mole percent carbon. Although the cyclic-C_n (n = 6 and 8) absorptions were observed, they were not assigned. Their annealing studies to temperatures similar to ours but for

amounts of time ten times longer than ours showed condensation behavior somewhat similar to ours. However, cyclic-C_6 greatly exceeded cyclic-C_8 in their matrices, and cyclic-C_6 increased about six-fold upon first annealing compared to the doubling of cyclic-C_6 we observed. Also, their measured absorbances were more than seven times smaller than ours. The column density, $<\rho_i \, l>_{matrix}$, was more than seven times larger in this work, indicating that the matrices of this work approach the five mole percent goal of the Air Force HEDM program. Our independent estimate of the carbon density, based on an estimate of the matrix thickness of 60-microns, is that the carbon density observed as condensed species (i.e., not including atoms and dimers) is as high as 2 mole percent carbon.

References

1. J. Szczepanski and M. Vala, J. Phys. Chem 95 (1991) 2792.
2. BC_2 molecule in J.D. Presilla-Márquez, C.W. Larson, P.G. Carrick and C.M.L. Rittby, J. Chem Phys. 105 (1996) 3398.
3. B_2C_2 molecule in J.D. Presilla-Márquez, P.G. Carrick and C.W. Larson, J. Chem Phys. (to be published).
4. BC_3 molecule in J.D. Presilla-Márquez, P.G. Carrick and C.W. Larson, J. Chem Phys. (to be published).
5. cyclic-C_6 molecule in J.D. Presilla-Márquez, J.A. Sheehy, J.D. Mills, P.G. Carrick and C.W. Larson, Chem. Phys. Lett. 274, 439 (1997).
6. cyclic-C_8 molecule in J.D. Presilla-Márquez, J.A. Sheehy, J.D. Mills and C.W. Larson, Chem. Phys. Lett.(to be published).

Theoretical Investigations of HEDM

Jeffrey A. Sheehy[a], Jerry A. Boatz, Jeffrey D. Mills, and Peter W. Langhoff[b]

Propulsion Sciences Division
Air Force Research Laboratory
10 E. Saturn Blvd.
Edwards AFB, CA 93524-7680

Introduction

The computational and theoretical chemistry group in the Propulsion Sciences Division at the Air Force Research Laboratory (AFRL) is engaged in several projects that support experimental research in the high energy density matter (HEDM) program. The spectral theory of chemical binding continues to be developed and implemented, providing a new framework for constructing adiabatic potential-energy surfaces for aggregates of interacting atomic or molecular species and giving insights into the structural and spectroscopic properties of HEDM-seeded cryogenic propellants. Preliminary applications to metal-doped rare gas matrices, such as sodium and aluminum atoms in argon, are invaluable to guiding theoretical understanding and computational implementation of the method. Secondly, calculations of structures and infrared spectra are assisting in the identification of new HEDM and other molecules produced by co-deposition of argon with the vapor from high-temperature evaporation of elemental powders, such as carbon and boron. Several new B_mC_n and C_n species (m = 1-4; n = 2-13) have been produced; the first identification of cyclic forms of small neutral polycarbons (C_6 and C_8) are notable accomplishments made possible by close interaction between theoreticians and experimentalists. Thirdly, the structures, spectra, and thermodynamic properties of proposed and synthesized new oxidizers, fuels, and monopropellants are also being calculated. An overview and highlights of these efforts are presented in this report, with further details on specific topics provided in other contributions to these proceedings [1-6].

Spectral Theory of Chemical Binding

A prominent goal of the HEDM program is to determine whether cryogenically solidified propellants (particularly H_2 or O_2) can be used as matrix materials in which significant quantities of atomic or small molecular additives can be trapped, thereby increasing the energy content of the propellant [7]. The spectral theory of chemical binding, which has been under development for about two years [8,9], aims to provide accurate electronic potential-energy surfaces for such aggregates, which in turn reveal their structural and spectroscopic properties, as well as information related to their stabilities and reactivities. Details of the theoretical approach are

provided elsewhere in these proceedings [1,2], but its key features are as follows: (1) it treats physical and chemical binding on a common basis; (2) it gives a rigorous theoretical foundation for a class of methods, loosely known as "atoms-in-molecules" or "diatomics-in-molecules" aproaches, which build potential surfaces from information related to component fragments [10-12]; (3) it requires only diatomic molecule calculations from conventional quantum chemistry, and these can be performed once and for all for any pair of atoms; and (4) it is potentially applicable to systems of 1000 or more atoms.

Due to the availability of experimental data on the spectroscopy of alkali atoms trapped in rare-gas matrices [13], these systems have been studied as prototypes of proposed HEDM fuels, such as atom-seeded solid H_2. Potential-energy, dipole-moment, and transition-moment functions for the ground and lowest nine excited states of NaAr are calculated employing multireference configuration interaction (MRCI) from complete-active-space self-consistent-field (CASSCF) wave functions in large Gaussian atomic basis sets [14] supplemented with suitable diffuse functions. The NaAr potential-energy curves and selected dipole and transition moments so obtained are highlighted elsewhere in these proceedings [1]. Similar calculations for AlAr are in progress; preliminary results obtained employing MRCI from selected CASSCF configurations are shown in another abstract in this volume [2]. These data are used directly in computational implementations of the spectral theory and in ensuing simulations of the structures and absorption spectra of $NaAr_n$ and $AlAr_n$ clusters [1,2].

Identification of New Molecules

Another significant effort within the HEDM program at AFRL is the preparation and identification of new molecules that might prove to be suitable energetic additives to solidified propellants [7]. Additionally, it is essential to understand how HEDM additives deposited in cryogenic matrices might recombine to form larger systems, which requires identifying condensation products and mechanisms. In the course of experiments aimed at depositing a few mole percent carbon atoms in cryogenic matrices, a novel condensation chemistry has been observed with cyclic C_6 playing a leading role [15].

Pure carbon molecules (polycarbons) have received considerable experimental and theoretical attention over the past forty years. Several reasons were indicated by Weltner and Van Zee in their comprehensive review [16], including the possible role of polycarbons as soot precursors and their significance in astrophysical processes. More recently, the discovery of methods for producing macroscopic quantities of fullerenes in the laboratory [17,18] and the exploration of mechanisms for their formation have excited new interest. Vibrational and electronic spectra of linear C_6 have been extensively studied [19-29], but experimental data concerning possible cyclic forms are inconclusive. Several researchers have considered the question of why no cyclic forms of any small neutral polycarbons have been directly identified [23,30]; their elusiveness constitutes a long-standing experimental challenge.

The measurement and assignment of cyclic C_6 in argon matrices is discussed elsewhere in these proceedings [4]; here the focus is on the details of the calculations. Previous studies of C_6 isomers employing extensive electron-correlation treatments [30-34], including single- and double-excitation coupled-cluster calculations with a noniterative treatment of connected triple

excitations [denoted CCSD(T)], indicate that the distorted hexagon ($^1A_1'$, D_{3h} symmetry) is ~8 kcal/mol lower in energy than the regular hexagon ($^1A_{1g}$, D_{6h}) and ~11 kcal/mol lower than the linear chain ($^3\Sigma_g^-$, $D_{\infty h}$). Additionally, application of density-functional theory (DFT) methods to cyclic C_6 [35,36] yields structures, frequencies, and intensities that are in good accord with the CCSD(T) results [30,34]. Whereas harmonic frequencies and infrared intensities for cyclic $^{12}C_6$ have been published [33-37], the ^{13}C isotopic shifts essential for the definitive identification of matrix-isolated species are not in the literature. Consequently, density-functional (B3LYP) calculations in several atomic basis sets were performed, as were CCSD(T) calculations in the cc-pVDZ basis set, largely following the work of Martin and co-workers [34,36].

Vibrational frequencies and intensities were computed for the complete set of isotopomers; those for the vibrational modes of cyclic $^{12}C_6$ are reported in Table 1. These data are evidently insensitive to the choice of atomic basis set or correlation treatment, and the B3LYP/cc-pVDZ results are in complete agreement with those from the identical calculation of Martin et al. [36]. Our CCSD(T)/cc-pVDZ frequencies (Table 1), however, differ significantly from those reported by Martin and Taylor [34], even though we obtained the same minimum energy structure is obtained. These results were confirmed using two different program systems [38,39], strongly indicating that the CCSD(T)/cc-pVDZ frequencies for cyclic $^{12}C_6$ reported by Martin and Taylor (Table 3 of Ref. 34) should be replaced by the values listed in Table 1. The scale factor for the $v_4(e')$ mode that brings the calculated CCSD(T)/cc-pVDZ frequency into coincidence with the measurement is 0.9762, sufficiently near unity to tentatively assign the 1694.7 cm^{-1} band to cyclic $^{12}C_6$. Conclusive assignment, however, is based on the ^{13}C isotopomer data, which is also in excellent accord with experimental observations [4]. Similar studies of cyclic C_8 and several mixed boron/carbon clusters are in progress.

Properties of New Propellant Ingredients

A third prominent area of research within the HEDM program is the synthesis and characterization of new fuels, oxidizers, and monopropellants to supplement or replace current propellants. Calculations support synthesis efforts by providing accurate structural parameters and thermodynamic data, as well as infrared, Raman, and nuclear magnetic resonance spectra. Additionally, potential-energy surfaces may be examined to determine transition states and barriers to decomposition. Several calculations related to current chemical synthesis at AFRL are reported in other abstracts in these proceedings [3,5,6]; compounds examined include molecules such as nitrocyanamide anion [6], triazidocarbenium cation [5], and spiro-bis-oxetane [4]. In general, these studies involve computing structures, spectra, and heats of formation employing Hartree-Fock, density-functional, and coupled-cluster methods in double- or triple-zeta atomic basis sets. For nitrocyanamide anion and its protonated form, heats of formation of -2 and +55 kcal/mol were found by the Gaussian-2 ("G2") method [6], which compare with the value of -29 kcal/mol calculate for dinitramide anion $[(NO_2)_2N]^-$. The heat of formation of spiro-bis-oxetane, calculated at the MP2/6-31G(d)//HF/6-31G(d) level, is -28 kcal/mol [4]. Data such as this is useful in determining whether proposed or synthesized molecules are suitable candidate ingredients for energetic propellants.

Conclusion

The computational and theoretical chemistry group at AFRL is supporting a wide variety of experimental research within the HEDM program; Table 2 gives a summary of these efforts. The methods employed range from the development of new theories and associated computer programs to the application of well-known techniques and codes to problems in energetic material synthesis and characterization. The impact of these calculations included screening of candidate synthesis targets and identification of unknown molecules, along with predictions of their properties and stabilities. It is clear that *ab initio* quantum chemistry contributes to one of the missions of AFRL -- to create technologies for the war fighter to control and exploit space -- by pointing the way to new chemical propellants with increased performance characteristics.

References

[1]   P.W. Langhoff, J.A. Boatz, and J.A. Sheehy, "Spectral Theory of Physical and Chemical Binding: Aspects of Computational Implementation," these proceedings.

[2]   J.A. Boatz, J.A. Sheehy, and P.W. Langhoff, "Monte Carlo Simulations of the Structures and Optical Absorption Spectra of Al/Ar$_N$ Clusters: Applications of Spectral Theory of Chemical Binding," these proceedings.

[3]   J.A. Boatz and J.D. Mills, "Theoretical Determination of the Heats of Formation of Prospective Strained-Ring Rocket Fuels," these proceedings.

[4]   J.D. Presilla-Marquez, P.G. Carrick, J.D. Mills, J.A. Sheehy, and C.W. Larson, "Studies of Cryogenic Boron and Carbon HEDM," these proceedings.

[5]   K.O. Christe, W.W. Wilson, G.W. Drake, and M.A. Petrie, "Theory and Synthesis of New High Energy Density Materials," these proceedings.

[6]   M.A. Petrie, T.W. Hawkins, and K.O. Christe, "Progress in the Synthesis of Novel Energetic Salts," these proceedings.

[7]   See, for example, Proceedings of the High Energy Density Matter (HEDM) Contractors Conference Held 5-7 June 1996 in Boulder CO, eds. P.G. Carrick and N.T. Williams (Phillips Laboratory, Edwards AFB, CA, 1997), report PL-TR-96-3037.

[8]   P.W. Langhoff, J. Phys. Chem. 100 (1996) 2974.

[9]   J.A.Sheehy, J.A. Boatz, M.E. Fajardo, and P.W. Langhoff, pp. 48-57 in Ref. 7.

[10]   W. Moffitt, Proc. Royal Soc. London A210 (1951) 245.

[11]   F.O. Ellison, J. Am. Chem. Soc. 85 (1963) 3540.

[12]   J.C. Tully, in Semiempirical Methods of Electronic Structure Calculation, Part A: Techniques, ed. by G.A. Segal (Plenum, New York, 1977), pp. 173-200.

[13]   See, for example, J.A. Boatz and M.E. Fajardo, J. Chem. Phys. 101 (1994) 3472.

[14]   P.-O. Widmark, B.J. Persson, and B.O. Roos, Theoret. Chim. Acta 79 (1991) 419.

[15] J.D. Presilla-Marquez, J.A. Sheehy, J.D. Mills, P.G. Carrick, and C.W. Larson, Chem. Phys. Lett., in press.

[16] W. Weltner, Jr. and R.J. Van Zee, Chem. Rev. 89 (1989) 1713.

[17] W. Krätschmer, L.D. Lamb, K. Fostiropoulos, and D.R. Huffman, Nature (London) 347 (1990) 354.

[18] H.W. Kroto, J.R. Heath, S.C. O'Brien, R.F. Curl, and R.E. Smalley, Nature (London) 318 (1985) 162.

[19] K.R. Thompson, R.L. Dekock, and W.Weltner, Jr., J. Am. Chem. Soc. 93 (1971) 4688.

[20] M. Vala, T.M. Chandrasekhar, J. Szczepanski, and R. Pellow, High Temp. Sci. 27 (1990) 19.

[21] R.H. Kranze and W.R.M. Graham, J. Chem. Phys. 98 (1993) 71.

[22] H.J. Hwang, A. Van Orden, K. Tanaka, E.W. Kuo, J.P. Heath, and R.J. Saykally, Mol. Phys. 79 (1993) 769.

[23] R.J. Van Zee, R.F. Ferrante, K.J. Zeringue, W.Weltner, Jr., and D.W. Ewing, J. Chem. Phys. 88 (1988) 3465.

[24] J. Szczepanski and M. Vala, J. Phys. Chem. 95 (1991) 2792.

[25] D.W. Arnold, S.E. Bradforth, T.N. Kitsopoulos, and D.M. Neumark, J. Chem. Phys. 95 (1991) 8753.

[26] C.C. Arnold, Y. Zhao, T.N. Kitsopoulos, and D.M. Neumark, J. Chem. Phys. 97 (1992) 6121.

[27] D. Forney, J. Fulara, P. Freivogel, M. Jakobi, D. Lessen, and J.P. Maier, J. Chem. Phys. 103 (1995) 48.

[28] P. Freivogel, J. Fulara, M. Jakobi, D. Forney, and J.P. Maier, J. Chem. Phys. 103 (1995) 54.

[29] J. Szczepanski, S. Ekern, C. Chapo, and M. Vala, Chem. Phys. 211 (1996) 359.

[30] Z. Slanina, Chem. Phys. Lett. 142 (1987) 512.

[31] J. Hutter and H.P. Lüthi, J. Chem. Phys. 101 (1994) 2213.

[32] V. Pless, H.U. Suter, and B. Engels, J. Chem. Phys. 101 (1994) 4042.

[33] K. Raghavachari, R.A. Whiteside, and J.A. Pople, J. Chem. Phys. 85 (1986) 6623.

[34] J.M.L. Martin and P.R. Taylor, J. Phys. Chem. 100 (1996) 6047.

[35] J. Hutter, H.P. Lüthi, and F. Diederich, J. Am. Chem. Soc. 116 (1994) 750.

[36] J.M.L. Martin, J. El-Yazal, and J.-P. François, Chem. Phys. Lett. 242 (1995) 570.

[37] K. Raghavachari and J.S. Binkley, J. Chem. Phys. 87 (1987) 2191.

[38] Gaussian 94, Revision D.4, M.J. Frisch, G.W. Trucks, H.B. Schlegel, P.M.W. Gill, B.G. Johnson, M.A. Robb, J.R. Cheeseman, T. Keith, G.A. Petersson, J.A. Montgomery, K. Raghavachari, M.A. Al-Laham, V.G. Zakrzewski, J.V. Ortiz, J.B. Foresman, J. Cioslowski, B.B. Stefanov, A. Nanayakkara, M. Challacombe, C.Y. Peng, P.Y. Ayala, W. Chen, M.W.

Wong, J.L. Andres, E.S. Replogle, R. Gomperts, R.L. Martin, D.J. Fox, J.S. Binkley, D.J. Defrees, J. Baker, J.P. Stewart, M. Head-Gordon, C. Gonzalez, and J.A. Pople, Gaussian, Inc., Pittsburgh, PA, 1995.

[39] ACES II, Quantum Theory Project, University of Florida. Authors: J.F. Stanton, J. Gauss, J.D. Watts, M. Nooijen, N. Oliphant, S.A. Perera, P.G. Szalay, W.J. Lauderdale, S.R. Gwaltney, S. Beck, A. Balková, D.E. Bernholdt, K.-K. Baeck, P. Rozyczko, H. Sekino, C. Hober, and R.J. Bartlett. Integral packages included are VMOL (J. Almlöf and P.R. Taylor), BPROPS (P.R. Taylor), and ABACUS (T. Helgaker, H.J.Aa. Jensen, P. Jørgensen, J. Olsen, and P.R. Taylor).

Table 1. Calculated harmonic frequencies (cm^{-1}) of cyclic $^{12}C_6$. Infrared intensities (km/mol) of the active modes are given in parentheses.

Mode	B3LYP/6-311G($2d$)	B3LYP/cc-pVDZ	B3LYP/cc-pVTZ	CCSD(T)/cc-pVDZ
$\nu_1(a_1')$	1218	1222	1223	1183
$\nu_2(a_1')$	646	659	647	556
$\nu_3(a_2')$	1393	1437	1412	1371
$\nu_4(e')$	1751 (424)	1769 (404)	1761 (436)	1736 (420)
$\nu_5(e')$	1234 (1)	1219 (1)	1232 (1)	1178(1)
$\nu_6(e')$	650 (24)	633 (25)	645 (22)	576 (43)
$\nu_7(a_2'')$	425 (7)	419 (8)	435 (6)	380 (7)
$\nu_8(e'')$	534	519	538	492

Table 2. Summary of HEDM-related computations at AFRL.

Area of Interest	Type of Calculation	Impact of Calculations	Applications
Synthesis of new propellant ingredients	Calculations of stationary points on potential surfaces	Exploration of efficient synthetic routes and dissociation pathways	Cubane (C_8H_8), pentaprismane ($C_{10}H_{10}$)
Stabilities of proposed and synthesized new propellants	Calculations of structures, spectra, properties	Effective screening of proposed compounds; determine which merit experimental study	$[(N3)C]^+$, $[NCNNO2]^-$, $C_5H_8O_2$, $C_{17}H_{24}N_4O_8$
Discovery and characterization of new cryogenic HEDM additives	Calculations of infrared frequencies and intensities; spectral modeling	Predict whether candidate molecules can be isolated; aid in data analysis	Li_xB_y, Li_xC_y, Si_xC_y (x,y = 1,2,3); cyclic C_6 and C_8
Characterization of doped cryogenic solid propellants	Spectral theory of chemical binding in conjunction with molecular dynamics simulations	Predict structures, densities, dopant concentrations, and stabilities of cryogenic HEDM propellants	Na/Ar_n, Al/Ar_n (prototypes); Li/H_2, B/H_2, LiB/H_2, $B/H_2/He_{(l)}$

116

Spectroscopy and Dynamics in Quantum vs. Classical Hosts
Presentation Made at The 1997 HEDM Contractors Meeting

V. A. Apkarian
Department of Chemistry
University of California
Irvine, CA 9697-2025.

This extended abstract is made to summarize the presentation I gave at 1997 HEDM meeting in Washington DC. I broadened the titled subject in my presentation to discuss the broader challenges of characterizing chemical interactions and dynamics in condensed media, and our contributions to this general field.

As a model of quantum hosts, and a prototypical cryogenic HEDM, we have carried out extensive studies of solid hydrogens doped with atomic and molecular oxygen.[1-4] The main conclusions regarding HEDM considerations remain: $O(^3P)$ is stable in solid hydrogens, it stabilizes the solid lattice and increases the overall density, atomic centers remain until changes in gross morphology of the lattice and self-diffusion of the host. The more surprising aspect of the experimental findings is that $O(^1D)$ is also observed in spectra, via the $O(^1S) \rightarrow O(^1D)$ transition, and this UV induced fluorescence is observed to not bleach with irradiation time. To provide an understanding of this observation, through a collaboration with L. Harding, we have recalculated $O+H_2$ pair potentials via high level *ab initio* theory, and used these surfaces for dynamical calculation in solid H_2.[2] This task is non-trivial since dynamical calculations in quantum hosts can only be carried out via approximate methods. We devised such a method, classical simulations over pseudo-potentials, which we first tested in spectroscopic simulations of solids doped with molecular oxygen.[3,4] Despite the simplicity of its construct, the method has been highly successful in explaining vibronic spectra of O_2 doped solid $D_2(H_2)$. One of the more important results of these simulations has been the establishment of distortion-coupled-rotation in quantum solids as the analog of translation-coupled-rotation in classical hosts, as the mechanism of reorientations.[4] In terms of observables, the mechanism explains the observed librational progressions in O_2 doped solid H_2 and the polarized nature of the emission bands. Despite the development of this methodology, it has not been possible to convincingly rationalize the absence of reactivity of $O(^1D)$ in solid hydrogens. This, despite the fact that a clear demonstration of the many-body effect of isolation in symmetric sites emerges from the investigation.[2] Namely: The anisotropic $O(^1D)$ - H_2 potential can be expanded as a Legendre polynomial series. The even terms in this expansion are non reactive, the odd terms are. As long as the local symmetry of the lattice remains high, there will be no reaction, since upon summation the odd terms

disappear. However, the thermal fluctuations of the cage are of sufficiently large amplitude to mix in the odd terms, to lead to reaction. In effect, while qualitatively we recognize the origin of a many-body barrier to reaction, quantitatively we cannot reproduce the experiment with the existing potentials. This, however, should not be very disturbing. The combined demands on accuracy of the pair potentials and the reliability of the construct of many-body surfaces from them have never been put to as rigorous a test as in the present case. This challenge has now been taken by other groups. In particular, P. Kuntz, who had previously constructed DIM surfaces for H_2O, and has recognized the inadequacy of many-body constructs that neglect ionic configurations, is now testing the expanded bases set treatment of the problem. His initial results indicate that inclusion of ionic states immediately lead to a higher barrier than what we had predicted,[5] and it will be interesting to see if, as in our prior experience,[6] the inclusion of ionic surfaces in DIM will lead to a more reliable many-body surface.

More recently, in a collaboration with N. Schwentner at the Berlin Synchrotron Facility, we carried out exploratory studies of NO doped solid H_2. The experiments allowed access to the sample by VUV and IR sources, the latter being used to record FTIR spectra of the irradiated spot. One motivation for this work was the alternate means of producing O and N doped solid hydrogens, again systems of interest as cryogenic HEDM. Within the sensitivity of our analysis, no photodissociation could be observed: neither was there a detectable loss of NO absorption intensity, nor could we observe atomic emissions due to O or N in hydrogen, although in experiments with over-layers of Ar we could clearly see the production of OH from residual H_2O doped in the Ar layer (ppm). The experiments did however provide novel science. VUV irradiation of the NO bands leads to dimerization, along with irradiation induced conversion of ortho to para hydrogen. The converted hydrogen could be distinguished as nearest neighbors to the NO dopant, by a ~2 cm^{-1} blue-shift relative to the bulk hydrogen absorption. Moreover, nearly 50% of the ortho population could be converted, a number representative of the sites visited by NO during its diffusion in the solid. The softness of the quantum host in this instant is demonstrated by the facile photomobility of the molecular impurity, a process not observed in classical hosts, moreover, the experiments illustrate that diffusion of the guest should be possible to follow with unprecedented detail since the nearest neighbors are marked by their conversion and spectral shift. These preliminary studies will be continued.

The above are but some examples of our ignorance in the details of interactions and dynamics in condensed media. This state of affairs is the result of the absence of mastery of fundamentals, in part due to the absence of detailed observables. Detailed time and frequency domain observables are required, along with the tools for their theoretical inversion into science. The flow chart below shows the logical iterative process that may yield the required fundamental understanding.

The fundamental quest is the understanding of the many-body potentials, $V(\{q_i\})$. Where chemistry is involved, where electronic configurations are changed, we note that multiple electronic states with their couplings are a necessary ingredient, thus most generally, V is a matrix of diagonal and off-diagonal electronic Born-Oppenheimer surfaces. It is inconceivable that one may guess such a function of hundreds of degrees of freedom, let alone its refinement. The logical approach is the construction of such matrices from what is known from pair interactions, $V_{ij}(q)$. Learning how to construct many-body potentials from pair potentials is one of the fundamental challenges to descriptions of condensed phase microscopics. The framework of diatomics in ionic systems has provided some astounding results in this regard, and it would seem that the inclusion of lowest lying charge transfer states of a system allows the reliable accounting of nonadditivities of interactions. We have shown this in three case studies to date, HF-Ar,[7] Cl$_2$-Rg,[6] and HF-dimer,[8] in the latter case showing quantitative reproduction of all the known features of the potential energy surface in full dimensionality.
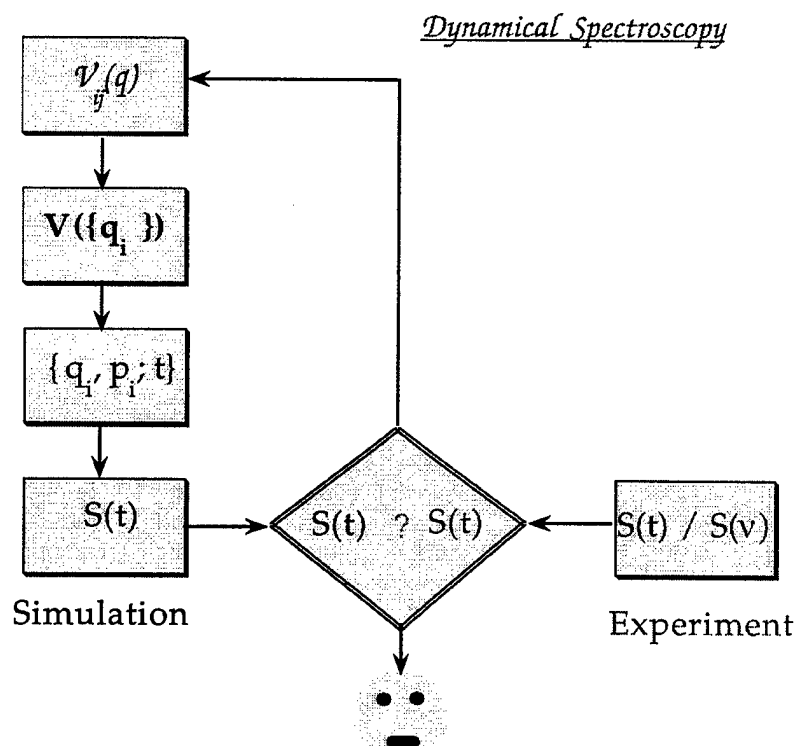
Given V, to obtain spectroscopic observables in frequency domain, one needs to propagate the quantum Hamiltonian of a multidimensional system, a system of hundreds of degrees of freedom to obtain a reliable rendition of the extended solid or liquid at issue. There are no exact methods to accomplish such a feat.

We recently developed the formalism of mixed-order semi classical dynamics, first in coordinate representation,[9] and more recently in coherent state representation,[10] to compute quantum time correlation functions which correspond to observables (absorption, emission, resonant Raman) by explicitly propagating quantum amplitudes of ~300 degrees of freedom. Nearly exact results are obtained by the method, which has the transparency of molecular dynamics calculations, with its sole input being potentials. Quantum time correlation functions, and their Fourier transforms, yield the observables that can be measured in experiments. To learn about these convoluted systems, detailed observables are necessary, and the combination of ultrafast time resolved measurements,[11] and classic optical scattering measurements, in recent years have provided unprecedented detail in our vision of microscopia in condensed media – to date, mostly in model systems. What may be less obvious in the challenges ahead is the step of iteration between experiment and theory. Since the observables are so far removed from the multi-variable pair potential parameters that are used as building blocks of the many-body matrices, the iteration process is time intensive and will require special methods, such as artificial intelligence to become practicable.

Fundamental challenges link the boxes in the flow chart designed for understanding many-body interactions and dynamics. Most of these links have now been made due to the model studies in which experiment and theory could be carried out on a commensurate level.

DEDICATION

I would like to dedicate this manuscript to the memory of Zhiming Li, who passed away on July 4, 1997, in a freak accident. He was one of the most dedicated scientists with whom I have had the pleasure to work. His contributions, published and not, have been seminal to the development of most of the topics discussed above.

REFERENCES

1. A. V. Danilychev, V. E. Bondybey, V. A. Apkarian, S. Tanaka, H. Kajihara, S. Koda, *J. Chem. Phys. 103*, 4292 (1995).
2. Z. Li, V. A. Apkarian, L. B. Harding, *J. Chem. Phys. 106*, 942 (1997).
3. M. Sterling, Z. Li, V. A. Apkarian, *J. Chem. Phys. 103*, 5679 (1995).
4. Z. Li, and V. A. Apkarian, *J. Chem. Phys. 107*, 1544 (1997).
5. P. Kuntz, (private communication).
6. B. L. Grigorenko, A. V. Nemukhin, and V. A. Apkarian, *Chem. Phys. 219*, 161 (1997).
7. B. L. Grigorenko, A. V. Nemukhin, and V. A. Apkarian, *J. Chem. Phys. 104*, 5510 (1996).
8. B. L. Grigorenko, A. V. Nemukhin, and V. A. Apkarian, (submitted).
9. M. Ovchinnikov, and V. A. Apkarian, *J. Chem. Phys. 105*, 10312 (1996); M. Ovchinnikov, and V. A. Apkarian, *J. Chem. Phys., 106*, 5775 (1997).

10. M. Ovchinnikov, and V. A. Apkarian, *J. Chem. Phys.*, (submitted).
11. Z. Li, R. Zadoyan, V. A. Apkarian, and C. C. Martens, *J. Phys. Chem. 99*, 7453 (1995).

Mass Spectrometry of Doped Helium Clusters

Kenneth C. Janda, Berton Callicoatt, Kirk Forde, Lilian Jung and V. A Apkarian
Department of Chemistry, University of California, Irvine, California 92697

Our group has been investigating the usefulness of liquid helium clusters as a medium for the synthesis of high energy density materials. Liquid helium clusters have exciting prospects in this regard since they offer a unique low temperature, high thermal conductivity environment for stabilizing reactive species. However, one difficulty with working with these clusters is that it is difficult to analyze their content. In this regard, we have been investigating the ionization and fragmentation of liquid helium clusters with and without dopant molecules. In particular, we have been investigating the mass spectra that are observed when clusters that contain between 500 and 10,000 atoms are ionized by 65 volt electrons.

Even the mass spectrum of pure helium clusters has proved to be quite surprising. Of course, one expects significant fragmentation when such clusters are ionized, since it takes only about 0.001 eV to evaporate a helium atom from a large cluster. Even so, the extent of fragmentation is surprising. An example of a mass spectrum is shown in Figure 1. Although the cluster starts out with 1100 atoms, the most intense peak after fragmentation is He_2^+. For 10,000 atom clusters, the most prominent ion in the mass spectrum is still He_2^+. Why is this surprising? Consider the fact that the energy of formation of He_2^+ is 2.5 eV. Even if all of this energy went into the evaporation of He atoms, and as little energy as possible were consumed in the evaporation of each atom, this would only account for the evaporation of about 2,000 atoms. For He_2^+ to be observed upon ionization of a 10,000 atom cluster, evaporation can not be the main fragmentation mechanism. We conclude that the dynamics of cluster ionization must be considerably more complicated than we had expected. Although He_2^+ is the most common product ion that is observed, He_n^+ ions with n up to 90 appear in the mass spectrum. There are "magic numbers" for n = 10 and 14. The last of these magic numbers corresponds to a He_2^+ core surrounded by a first shell of 12 helium atoms. It is not obvious that such shell structure should occur for a quantum liquid. The magic number at 10 indicates that the small ionized clusters can not be described by a simple combination of two body forces between the shell atoms and the He_2^+ or a He_3^+ core.
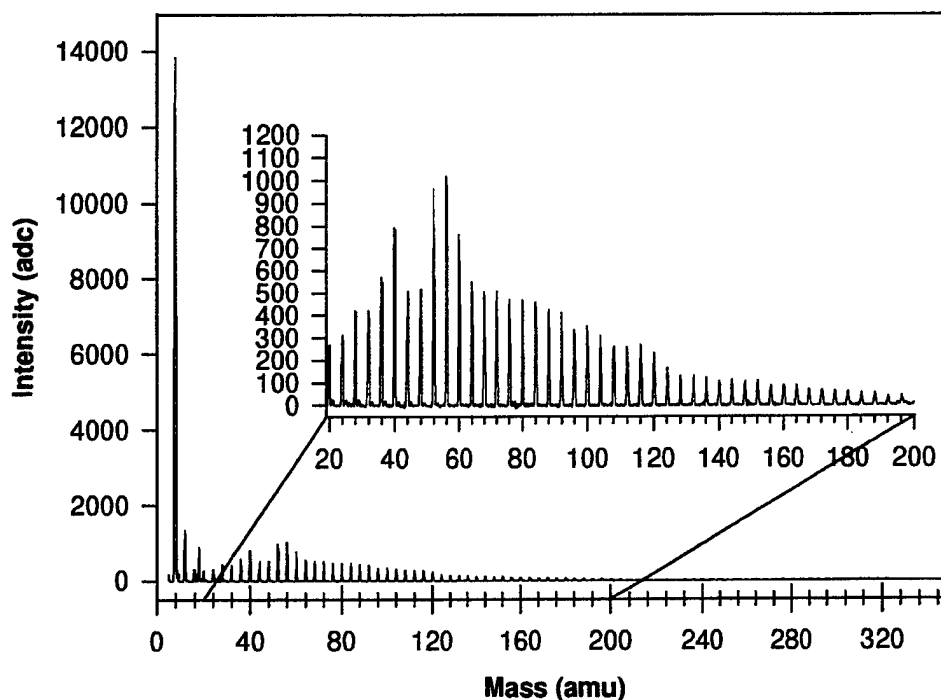

Pure Helium Cluster Mass Spectrum

Fig. 1 This figure shows a mass spectrum that results when a 1100 atom He cluster is ionized with 65 eV electrons. About half the total intensity is in the He_2^+, and He_3^+ is the next most intense peak. The peaks for He_{10}^+ and He_{14}^+ are also more intense than the adjacent peaks. This indicates that there are specific chemical interactions that determine the stability for ionic He clusters in this size range. The mass spectrum continues to about He_{90}^+ before the signal completely disappears into the base line. To our surprise, this pattern of fragmentation results even for ionization of much larger clusters. This indicates that the energy dissipated by the "charge localization" is not dissipated simply as heat.

We have also made extensive studies of liquid helium clusters that contain Ar and NO dopant species. Among our observations are the following phenomena. When a cluster containing 1100 helium atoms and a single Ar atom is ionized, the chance that the Ar atom ends up being ionized is about 20%, and this chance drops very quickly with increasing numbers of helium atoms. The Ar^+ ion tends to be formed with a shell of helium atoms around it. When a cluster that contains 1100 helium atoms and two Ar atoms is ionized, the chance that Ar_2^+ is formed is 30%, and no helium atoms tend to stick to the Ar_2^+ species. Finally, when a cluster that contains 1100 helium atoms and 3 Ar atoms is ionized, the chance that Ar_3^+ is formed is close to zero! The liquid helium cluster is surprisingly inefficient at "caging" this

species. An example of data from which these types of conclusion are drawn is shown in Figure 2. In contrast, ionization of helium clusters that contain NO is much more likely to result in the observation of NO^+ than N^+ in spite of the fact that the NO^+ is created 2.5 eV above its dissociation limit. In this case, the helium clusters are very efficient at "caging" a high energy species. We will present preliminary models that help us explain some, but not all, of these phenomena.

Ion Signal vs. Argon Pressure
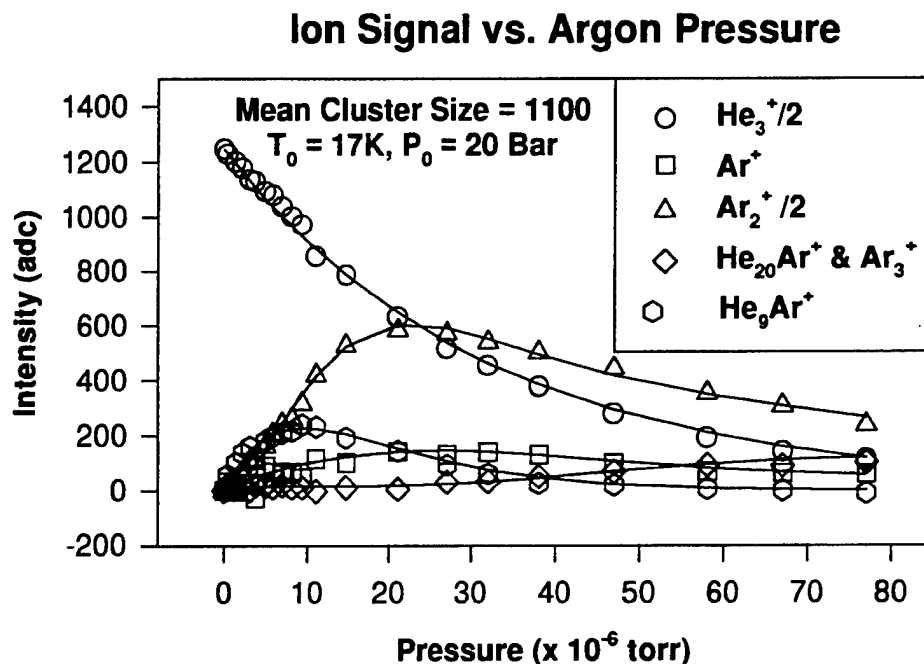
Fig. 2. This figure shows several ion signal intensities as a function of the Ar pressure in the pick up cell. The lines through the data points result from statistical modeling of the data. The fit to the data shows, for instance, that if the cluster contains a single Ar atom, then the probability that the charge ends up on that atom is 20%.

We believe that we have made important progress in understanding how to use He clusters to prepare the type of species that are important to the HEDM program. However, the analysis of the system may not be straight forward. For example, Figure 3 shows both a raw mass spectrum of a 1100 atom He cluster that has passed through a pick-up cell containing 3.1×10^{-6} torr of Ar. The raw data shows no obvious indication that the cluster has picked up an Ar atom. However, when the mass spectrum of a pure helium cluster beam is subtracted

from that shown in Figure 3, the difference spectrum in Figure 4 results. This difference spectrum mainly consists of mass peaks of the type Ar^+He_n with $1 < n < 13$. We would expect similar phenomena to occur if boron atoms were being picked up. The mass spectrometry will have to be worked out on a case by case basis.

Argon Pickup in He Clusters
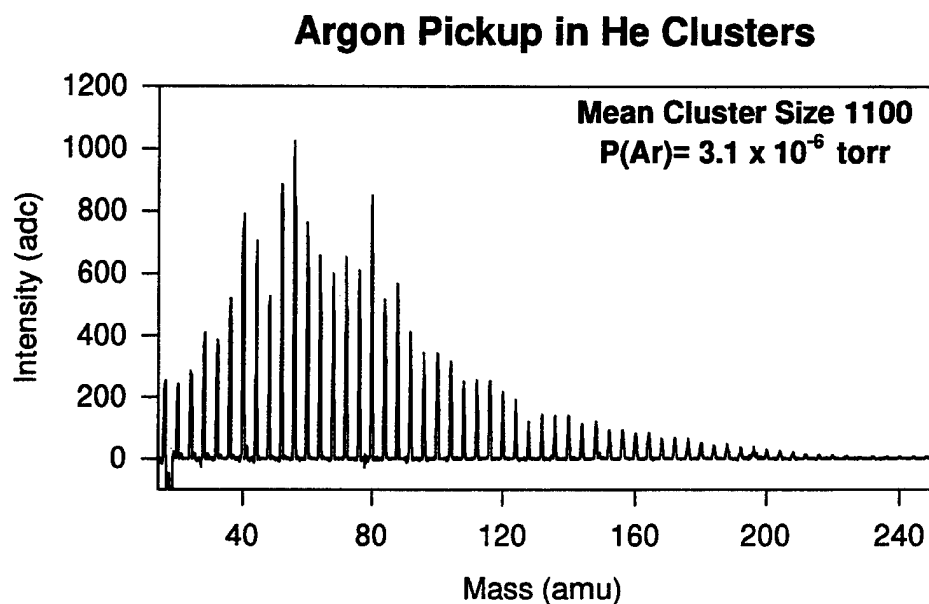
Figure 3. This figure shows a portion of the mass spectrum that results if an 1100 helium atom cluster passed through a pick-up cell containing 3.1×10^{-6} torr of argon. The spectrum is almost unchanged from that of Figure 1. It is not obvious that any argon has been picked up by the cluster.

Argon Pickup in He Clusters Pure He Subtracted

Mean Cluster Size 1100
$P(Ar) = 3.1 \times 10^{-6}$ torr
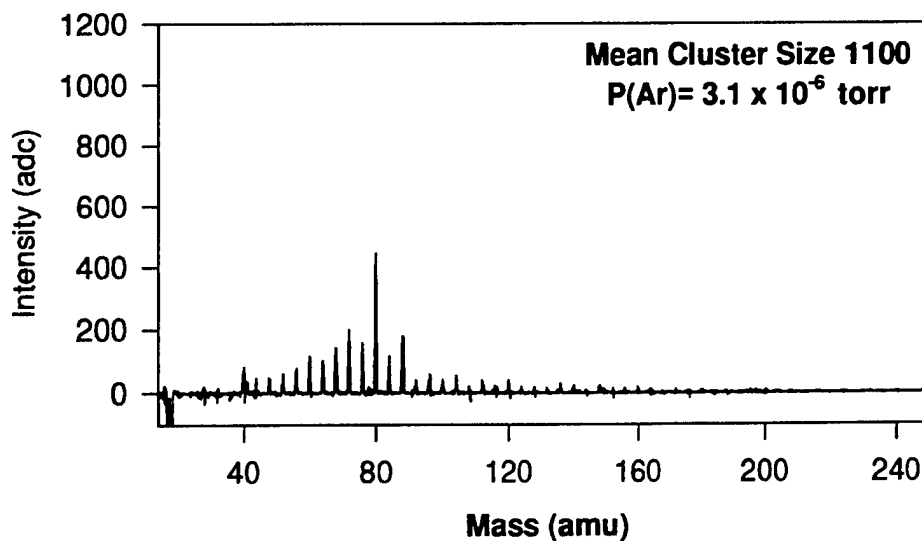
Figure 4. This figure shows a difference spectrum in which data from Figure 1 is subtracted from that in Figure 3. The difference spectrum shows that Ar has been picked up, and that the resulting mass peaks are mostly of the type Ar^+He_n with $1 < n < 13$.

We believe that the data we have obtained to date would allow us to design the cluster synthesis part of an apparatus to form boron/hydrogen HEDM materials. We recommend that work proceed to determine whether the condensation part of the technique is feasible.

NON-ADIABATIC EFFECTS IN THE INTERACTION OF LIGHT METAL ATOMS WITH H_2 AND He CLUSTERS.

C. Callegari, W.E. Ernst[*], J. Higgins, K. K. Lehmann, J. Reho, and G. Scoles

Chemistry Department, Princeton University, Princeton, NJ 08544

I. INTRODUCTION

Light-atom-doped solid hydrogen has been in recent years one of the main themes of research within the HEDM program. Substantial effort has been directed towards determining the maximum atom concentrations achievable, the dopant-hydrogen interactions, and the mobility of dopants in solid hydrogen. Our contribution has been the introduction and development of a new experimental method suitable for the study of metal atoms interacting with medium-large ($n \approx 10^4$) hydrogen and helium clusters. In analogy with matrix-isolation spectroscopy, we call this method cluster-isolation spectroscopy. As in matrix isolation, cluster isolation allows for the synthesis and stabilization of unstable molecules and van der Waals complexes, but offers additional advantages such as the improved control on seeded species aggregation, the absence of walls and windows in contact with the "matrix" and the possibility, in helium, of achieving extremely high cooling rates and even rotational resolution [1].

We form the clusters in supersonic expansions at low temperatures and we dope them by passing the collimated cluster beam in a scattering box containing a relatively small pressure ($\approx 10^{-5} - 10^{-4}$ torr) of the dopant gas. The doped clusters are excited by tunable laser radiation and three different type of spectra are obtained: a) Laser Induced Fluorescence (LIF) excitation spectra; b) Dispersed Fluorescence spectra; c) Laser Induced Beam Depletion (LIBD) spectra. In addition, we have recently acquired the capability to carry out time resolved fluorescence measurements (using time correlated photon counting) with time resolution of ≈ 20 ps. For the latter type of measurement, the bandwidth of the detected fluorescence can be restricted to about ± 5 nm.

Using Li, Na and K attached to hydrogen clusters, we have shown the very high probability with which radiation quenching occurs and the consequent large difference between LIF and LIBD. Because of the overwhelming predominance of quenching, the latter type of spectra is likely to represent rather closely the true absorption spectra for these metal/cluster combinations. While the absorption (LIBD) spectra are not very structured, in the

*Department of Physics, Pennsylvania State University, 104 Davey Laboratory, University Park, PA 16802

LIF spectra we have found the presence of a pronounced frequency-dependent structure and also a strong influence of the ortho-para composition of the hydrogen substrate. These results have shown the need of more precise theoretical investigations on both the interaction potentials and the dynamics of the atom/cluster interactions [2].

In contrast to what happens on H_2 clusters, alkali atom fluorescence quenching on He clusters appears to be negligible as LIF and LIBD spectra are in this case identical both representing the true absorption spectra. When more than one alkali is picked up by the He cluster, the lack of spin relaxation allows for the selective storing of high spin alkali oligomers as the strongly bound lower spin species (singlet dimers and doublet trimers) evaporate from, or destroy, the cluster due to the accommodation of the recombination energy. Exploiting this phenomenon, we have been able to carry out spectroscopic measurements on several triplet alkali dimers and quartet trimers obtaining new information on the potential energy surfaces of these species including, in the case of the trimer, their three-body interactions [3–7].

During the last year we have made progress in the following areas (some of which are described in greater detail here below):

a) We have studied the quenching of $P \rightarrow S$ fluorescence in Na atoms attached to He clusters as produced by H_2 impurities introduced in the He by gas phase pick-up.

b) We have interpreted the red shifted emission spectrum of $3P$ Na atoms excited on an He cluster as being due to the emission of the Na*He excimer which forms in those cases when the $P \leftarrow S$ excitation is not followed by immediate evaporation of the excited atom from the cluster (bound-bound transitions). Using a recently assembled time correlated photon counting apparatus, the rise time of this red shifted fluorescence has also been measured, uncovering the presence of a delay in the formation of the excimer (700 ps) when the excitation occurs in the neighborhood of the $3P_{1/2}$ (as opposed to what happens near or above the $3P_{3/2}$ line where the excimer formation occurs in a time shorter than our time resolution: 30-70 ps). The data obtained under a) and b) are presented and discussed below.

c) We have also studied the phonon tail of the spec-

trum of the $A \leftarrow X$ transition of singlet Na_2 molecules attached to He clusters, isolating the contributions due to the excitations (rotons and maxons) generated into the liquid He substrate at the moment of the excitation. In addition, we have also identified a third feature at lower energy (≈ 2 cm^{-1}) which has not yet been assigned, but could conceivably be due to the excitation of ripplons on the surface of the cluster which consists of a sphere of $\approx 10^4$ He atoms at 0.37 K.

d) Finally, we have measured that it takes from 1.2 to about 0.5 ns (depending on the excited vibronic state) for an optically excited quartet sodium trimer to cross the doublet state potential energy surface and dissociate into $Na_2^* + Na$ or $Na^* + Na_2$. These data are, potentially, an excellent state selective test for dynamical calculations of the non-adiabatic behavior of a dissociating three particle system, which is simple enough for the potential energy surface to be calculated with sufficient accuracy. The experiments briefly summarized under c) and d) will not be discussed further in this report.

II. ALKALI FLUORESCENCE QUENCHING BY H_2: ALKALI/H_2 COMPLEXES IN He CLUSTERS.

As we have explained in the preceding section, hydrogen clusters have shown a remarkable ability to quench the fluorescence of the excited alkali atoms. Although the efficiency of H_2 at quenching excited alkali atoms is well established [8], one point still needs to be clarified: whether in our case quenching is due to a collective contribution of the entire cluster (as appears to be the case for alkali atoms in bulk liquid He [9]), or rather due to the interaction of the alkali atom with only one (or few) H_2 molecule(s). In order to answer this question the most direct route is to obtain the spectrum of alkali-atom/hydrogen complexes containing only one or a few H_2 molecules. These complexes are however nearly impossible to prepare with conventional techniques. He clusters are instead particularly suitable to prepare unstable and weakly bound species. Therefore we used a multiple pick-up technique to prepare $Na(H_2)_n$ complexes attached to He clusters.

Since H_2 has an interaction with alkali atoms roughly a factor of 10 stronger than He does, H_2 molecules picked up by the cluster are expected to find the alkali atom and form weakly bound complexes. We found that hydrogen has only moderate effects on LIBD spectra, which are broadened, but not considerably reduced in intensity. Far greater are the effects on LIF spectra, which are blue shifted and more importantly dramatically reduced in intensity. The total amount of fluorescence is
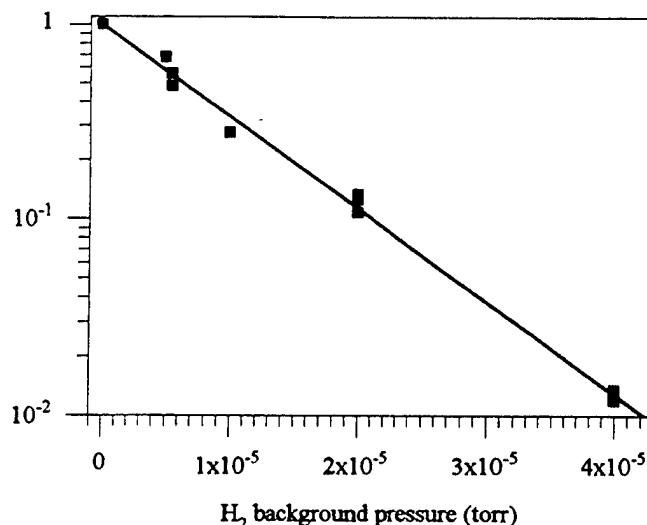

FIG. 1. Integrated LIF signal of Na-$(H_2)_n$ complexes on the surface of He clusters as a function of background H_2 pressure. The straight line is a fit to an exponential.

found to decrease exponentially with the H_2 background pressure (Fig. 1). We calculate that less than 10 H_2 molecules per cluster need to be picked up in order to reduce the fluorescence to $1/e$ of its initial value. This is however a very conservative estimate (e.g. it assumes a sticking probability of 1 for H_2 colliding with He clusters), and therefore the real limit is probably even lower. What is important is that these results point to a "single molecule" quenching mechanism, rather than to some collective effects involving the entire cluster. In analogy with the relaxation dynamics of alkali atoms on He clusters (see below), it is likely that excimers are formed in the case of H_2 clusters too. Contrary to the He case, Na-H_2 excimers would not return their excitation energy by emitting red-shifted fluorescence, but rather undergo non-radiative intersystem crossing, in analogy to what has been observed in collisional experiments [8].

III. THE Na^*-He EXCIMER

A. Demonstration of its Formation

The excitation and dispersed emission spectra of Na atom on He clusters were previously measured in our laboratory [10]. The excitation spectrum obtained integrating over the complete emission spectrum is illustrated in Figure 2. It is seen that the spectrum begins slightly to the red of the free Na D ($3P_{1/2,3/2}$) lines and has a long tail on the blue side. The dispersed emission consist of two main features the relative intensity of which changes as a function of the excitation frequency. The first feature can be described as emission from free sodium atoms,
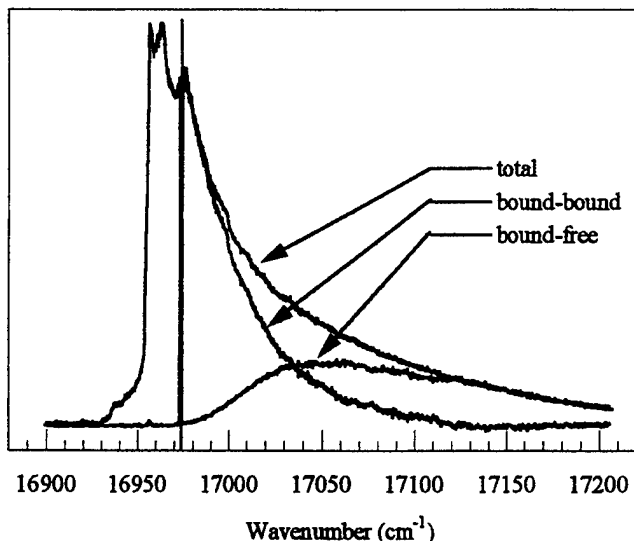
FIG. 2. Emission-wavelength-selected excitation spectra of Na atoms on He clusters. The bound-free contribution is measured by monitoring fluorescent emission at the gas phase lines. The bound-bound contribution by monitoring red shifted fluorescent emission.

FIG. 3. Na-He potential curves as calculated by J. Pascale [11].

while the second is a broad, structured, feature spanning the range 14200 cm^{-1} to 16800 cm^{-1}. In our earlier publication [10] the excitation spectrum was modeled with contributions arising both from bound-free and bound-bound transitions of the Na - cluster potential.

The atomic emission was assigned to gas phase Na* atoms produced by the bound-free transition while Na atoms excited in bound-bound transitions were assigned as the source of the "red" emission. This allows for an empirical way to separate the bound-bound and bound-free contributions to the absorption by emission-wavelength-selected excitation spectra, which are also shown in Fig. 2. It can be seen that the free atom emission (bound-free excitation) does not begin until 18 cm^{-1} above the wave number of the $P_{1/2}$ line. This provides a direct measure of the binding energy of the ground state Na on the cluster. The observation of emission from bound-bound transitions is perhaps surprising given the well established fact that the light alkali atoms do not give detectable fluorescence from bubble states in bulk liquid He. It is believed that in the bulk the excited Na atom is rapidly quenched due to the attraction of a ring of about four He atoms around the nodal plane of the P orbital, which allow them to "feel" much of the Na$^+$ core without excessive Pauli repulsion [9]. At such distances the ground state He-Na interaction is highly repulsive, possibly resulting in a curve crossing which would lead to quenching.

The interaction potentials of both Na ground state and excited Na with He have been calculated by J. Pascale [11]. Experimental information on these curves is also available from studies of the red tail of the emission of

Na* in high pressure He gas [12]. Figure 3 shows the calculated curves, neglecting spin-orbit effects. We see that we have a repulsive $^2\Sigma$ state and a moderately attractive $^2\Pi$ state correlating to the atomic Na(3p) asymptote. The ground state is very weakly attractive with a well depth of under 3 cm^{-1}.

The bound levels of the $^2\Pi$ state, and the expected bound-free emission from each of them, were calculated in the Condon approximation (i.e. constant electronic transition moment) from Pascale's potentials using LeRoy's BCONT code [20], which numerically solves the radical Schrödinger equation by use of the Numerov-Cooley algorithm. We then performed a fit of the observed spectrum, varying only the relative populations of the vibrational levels of the $^2\Pi$ state. While the potential supports a total of 7 vibrational states, only the lowest four have been used for the fit; the contribution from higher states is either negligible or masked by gas phase emission.

Figure 4 shows the dispersed emission spectrum observed following excitation of Na at 16975.2 cm^{-1} in which a structure with four peaks is seen. As one can see the agreement with the fitted emission spectrum (superimposed) is excellent. We have performed similar fits to observed emission spectra following excitation from several different wavelengths. In all cases we obtain an

129

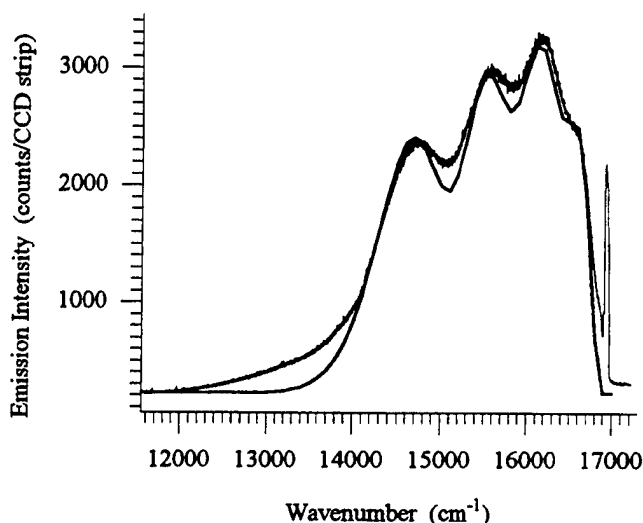FIG. 4. Dispersed fluorescence spectrum of Na*-He excimers desorbed from He clusters after excitation of Na atoms on the surface of the cluster. The excitation energy is 16975 cm^{-1}. The thick line is a simulated emission spectrum (using Pascale's potentials [11]).

	Excitation energies (cm^{-1})				
	16954.6	16960.7	16975.2	17046.7	17150.7
v=0	0.35	0.33	0.30	0.24	0.10
v=1	0.34	0.34	0.32	0.25	0.22
v=2	0.24	0.25	0.26	0.26	0.27
v=3	0.07	0.08	0.12	0.25	0.41

TABLE I. Na*He vibrational levels populations after excitation of Na atoms on He clusters at different excitation energies.

excellent simulation of the observed spectrum.

Table 1 shows the relative $^2\Pi$ vibrational populations that result. We see that, as expected, excitation with higher excess energy results in formation of the Na*-He with higher vibrational excitation.

Based upon these observations, it appears fairly safe to state that the red emission arises from emission of Na* bound to a single He atom. It is less obvious that this species is in the gas phase, instead of still bound to the surface of the cluster. In fact, the unassigned red tail of the observed emission could be construed as evidence that a relatively small exciplex population interacts with more than one He atom.

B. Experimental Setup for Time-Resolved Fluorescence Experiments

Reported below is the description of our apparatus for time resolved laser spectroscopy of doped He clusters (see Figure 5). A mode-locked, frequency-doubled YAG laser

(Quantronix 416) sync-pumps a folded-cavity dye laser (Spectra Physics 3500), producing pulses of 10-12 ps full width at half maximum (FWHM). The linewidth of the laser is 2 cm^{-1}, which is twice the Fourier Transform limit value. Given the 16 ns radiative lifetime of the sodium "D" lines, use of the dye laser's 76 MHz repetition rate will lead to substantial overlap of the emission from several excitation pulses. A home-built "pulse-picker" is used to reduce the repetition rate to 12.6 MHz.

Laser-induced fluorescence from the Na-doped He clusters is collected by a high collection efficiency double mirror optic and transported to a microchannel plate detector (MCD) (Hamamatsu R2807U-07) through a multimode, incoherent fiber bundle (Edmund Scientific). In order to allow for wavelength selection, band pass filters are introduced in front of the microchannel plates. Lifetime measurements use the reversed time-correlated single photon counting technique [13]. The fluorescence signal from the MCD is amplified (Minicircuits ZFL-2000), passes through a constant fraction discriminator (Tennelec TC454), and then provide the start signal of a time-to-amplitude converter (TAC) (Ortec 457). The stop pulse for the TAC is provided by the output of a fast photodiode that monitors the laser pulse train. This signal is amplified and then sent through a constant fraction discriminator. This "reverse" method insures that the each "start" pulse is followed by a "stop" pulse inside the time window of the TAC. The output of the TAC is processed by a multichannel analyzer (Nucleus II) and binned, thus compiling our experimental histograms which give the emission intensity as a function of time after each excitation pulse. The multichannel analyzer contains 8192 channels which we have set to cover a 100 ns region in time.

We have measured the instrument response function by passing a H$_2$ beam through a 34.7 K nozzle at backing pressures in excess of 300 psi. This beam, comprised of large frozen hydrogen particles, acts as a scatterer of our laser light probe. We thus define the histogram of this cold (H$_2$)$_n$ beam scatter signal as a measure of the instrument function. The FWHM of the instrument function is determined by the broadening and resulting timing jitter of the various components which comprise the detection system, and is presently estimated at 170 ps. Modeling of the data is carried out through an iterative convolution method in which the numerical instrument function (measured by H$_2$ cluster scattering with all other experimental conditions the same) is convolved with a kinetic model by use of a pair of Fast Fourier Transforms. The following kinetic model is used:

$$G(t) = A(e^{-t/\tau_1} - e^{-t/\tau_2}) + D \qquad (1)$$

in which τ_1 and τ_2 represents the fall and rise times, respectively, of the population of the fluorescing species. D is a background factor that accounts for dark counts
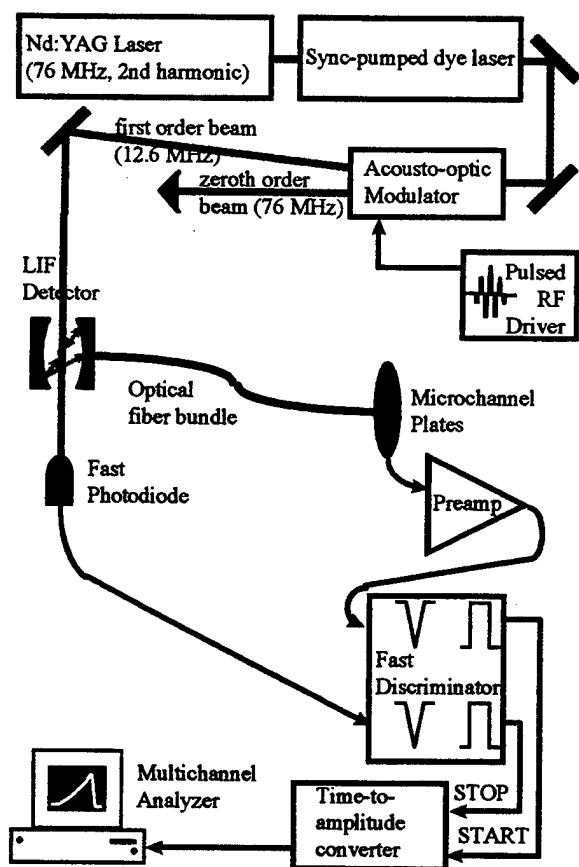
FIG. 5. Time-resolved fluorescence set-up.

Fluorescence at 589 ± 5 nm (free atoms)		
Excitation energy (cm^{-1})	Rise Time (ps)	Fall Time (ns)
17041	50 ± 30	16.3 ± 0.1
17084	50 ± 30	16.3 ± 0.1
17127	70 ± 30	16.3 ± 0.1
17385	70 ± 30	16.2 ± 0.1
Fluorescence at 633 ± 5 nm (excimers)		
Excitation energy (cm^{-1})	Rise Time (ps)	Fall Time (ns)
16945	700 ± 30	18.2 ± 0.1
16956	700 ± 30	18.2 ± 0.1
16973	80 ± 30	20.1 ± 0.1
16994	70 ± 30	20.7 ± 0.1
17041	80 ± 30	21.2 ± 0.1

TABLE II. Time-resolved fluorescence rise and fall times for Na atoms on He clusters.

in the MCD, calculated from the measured total dark count rate and the total signal averaging time for each bin. When the fit to this function is found unsatisfactory, a model which is biexponential in rise and fall is used.

$$G(t) = A(e^{-t/\tau_1} - e^{-t/\tau_2}) + B(e^{-t/\tau_3} - e^{-t/\tau_4}) + D \quad (2)$$

The amplitudes A and B as well as the exponential arguments τ_i (i.e., the rise and fall times) of the model are parameters in a weighted least squared fit to the observed fluorescence decay curve. Following Cova et al. [15], we claim that the ultimate resolution attained by deconvolution is a factor of 10 better than the FWHM of the instrument function (i.e. ≈ 20 ps).

C. Time Resolved Excimer Formation and Non-Adiabatic Effects

Rise and fall time measurements were made at several points in the excitation spectrum, looking at either atomic (16980 ± 145 cm^{-1}) or red-shifted (15800 ± 125 cm^{-1}) fluorescence. The results of these fits are presented in table 2. We will first discuss the results of fits to decays observed at the atomic wavelength. These gave decay times centered around 16.3 ± 0.1 ns, in excellent

agreement with the well known Na ^2P lifetime [14], confirming the ability of our instrument to provide accurate lifetimes. Times of 50 ps and 70 ps were found for the fluorescence rise times (i.e., mean time of the onset of fluorescence) under the same conditions. These values are less than the width of the instrument function (170 ps), but larger than the claimed resolution (≈ 20 ps). Fits to emission from excitation of gas phase Na atoms (which should give an infinitely fast rise for the model that is convolved with the instrument function) gave rise times of under 20 ps. For a bound-free transition, we expect the free atom emission to rise with a time on the order of the vibrational period of the Na*-cluster attractive potential. Based upon the previous estimates of this potential [10], this period should be ≈ 15 ps. On the other hand, the He cluster is not rigid and its response times are very difficult to predict a priori.

In summary, at this point in time, we note that the expulsion times of the excited Na atoms from the cluster appear to be longer than our instrumental resolution, but we stop short of making the claim with confidence. We are presently setting up pump and probe experiments in which rise times larger than a few picoseconds should be easily resolved.

Collection of the red-shifted (15800 ± 125 cm^{-1}) fluorescence yielded rise times that depended strongly on the excitation wavelength, but fall times ranging from 19 to 21 ns. If we assume that this decay has the same transition dipole as the free atom and take the mean emission energy as 15800 cm^{-1}, we predict a radiative lifetime of 20 ns, in excellent agreement with the observed value.

With respect to the rise times, when the excitation energy is to the blue of the atomic $J = 3/2$ line, the observed fluorescence is successfully fit to a model with a single rise time, which is found to be 70 ps, only slightly longer than the rise time observed for the atomic emission. This argues that following such excitation, the formation and desorption of the Na*-He exciplex occurs very rapidly. This suggests that the desorption is likely
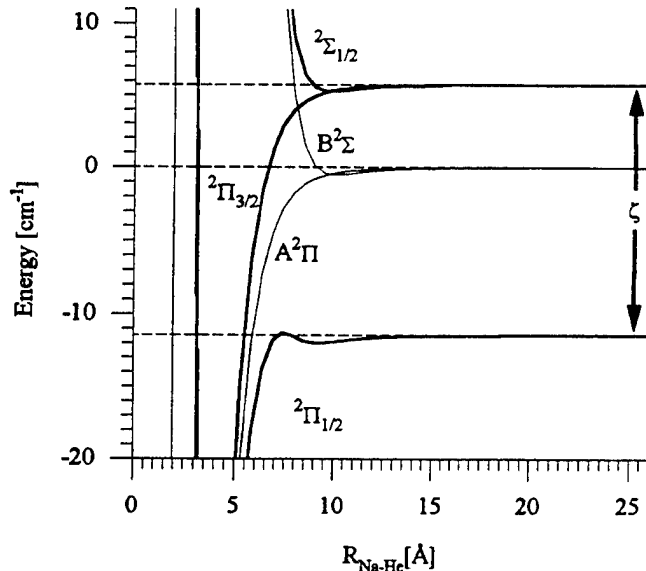
FIG. 6. Long range view of Na*-He potentials, neglecting (thin lines) and including (thick lines) the spin-orbit perturbation. Energies are relative to the unperturbed asymptotic value (16975.8 cm^{-1}).

to be directly coupled to the formation process. As we move the excitation wavelength to the red of the $J = 3/2$ atomic line, we find that to successfully fit the observed fluorescence signals, we must use two rise times. One component of the emission, with an amplitude decreasing as the excitation is moved to the red, also has a rapid rise time (70 ps). However, the second component has a much slower rise time of $\approx$ 700 ps. As will be discussed below, we assign the rapid rise time to formation of the Na*-He on the $^2\Pi_{3/2}$ surface (which correlates with the atomic $J = 3/2$ fine structure component) and the slow rise to formation of the Na*-He on the $^2\Pi_{1/2}$ surface (which correlates with the atomic $J = 1/2$ fine structure component).

Figure 6 shows an expanded view of the long range $A^2\Pi$ and $B^2\Sigma$ Na-He potentials as calculated by Pascale. This calculation neglects spin-orbit interactions, and thus produces a single $^2\Pi$ surface.

Following Takami [16], we will account for the spin-orbit effects by introducing a constant (i.e. independent of the bond length) perturbation equal to the atomic Na ^2P spin-orbit splitting constant $\zeta = 17.19$ cm^{-1}. This should be an excellent approximation at long range, where we expect negligible perturbation of the Na* electronic structure. In terms of the two potentials $V_\Pi(R)$ and $V_\Sigma(R)$, the effective Hamiltonian in terms of the basis states $[^2\Pi_{3/2}, ^2\Pi_{1/2}, ^2\Sigma_{1/2}]$ is:

$$\begin{bmatrix} V_\Sigma(x) & \frac{\sqrt{2}}{3}\zeta & 0 \\ \frac{\sqrt{2}}{3}\zeta & V_\Pi(x) - \frac{\zeta}{3} & 0 \\ 0 & 0 & V_\Pi(x) + \frac{\zeta}{3} \end{bmatrix} \quad (3)$$

We thus see that the spin-orbit operator mixes the $^2\Pi_{1/2}$ and $^2\Sigma_{1/2}$ states. Diagonalization of this Hamiltonian for each R leads to the three curves given in Figure 6 which are labeled by their dominant character at short R. We thus see that there are two curves, separated at short range by 2/3 of the atomic spin orbit splitting, that correlate with formation of the Na*-He exciplex. The most natural explanation for our experimental results is that excitation onto the upper, $^2\Pi_{3/2}$, surface leads to the rapid formation of the exciplex, while excitation to the lower, $^2\Pi_{1/2}$, surface leads to the slow formation of the exciplex.

Notice that unlike the $^2\Pi_{3/2}$ which is purely attractive at long range, the $^2\Pi_{1/2}$ surface has a small "outer" well of $\approx$ 0.5 cm^{-1} at $R = 9\text{Å}$, and centered near 8Å, a small barrier of height 0.19 cm^{-1} relative to the $^2\Pi_{1/2}$ asymptote (although the barrier height in relation to the minimum of the outer well is 0.7 cm^{-1}). It is interesting to note that the calculated cluster-Na* potential (in the frozen cluster approximation and using the sum of two-body potentials) predicts that the $^2\Pi$ excited state has a minimum with the Na* located $\approx 9\text{Å}$ above the 'dimple' in the He surface. Thus one would expect the closest He atoms to start at a distance from the Na* close to the outer minimum of the $^2\Pi_{1/2}$ potential. Physically, the barrier on the $^2\Pi_{1/2}$ surface can be understood as arising from the spin orbit mixing of the $^2\Pi_{1/2}$ and $^2\Sigma_{1/2}$, and from the fact that the Pauli repulsion on the $^2\Sigma_{1/2}$ curve becomes significant at larger R than the attraction on the $^2\Pi_{1/2}$ surface. A similar barrier in the Ag*-He exciplex curves was noted by Takami and used to explain the lack of exciplex formation when the $^2\Pi_{1/2}$ level of Ag was excited optically [16]. In that case, however, the barrier was much larger (66 cm^{-1}), as could be expected given the much larger atomic spin-orbit splitting (921 cm^{-1}). The quenching dynamics of the Rb D1 line in bulk liquid He have been explained by a barrier due to fine structure along the Rb-He $^2\Pi_{1/2}$ potential surface [17].

A natural explanation for the slower formation rate for the Na*-He exciplex on the $^2\Pi_{1/2}$ surface is the presence of this 0.7 cm^{-1} barrier. While this barrier is very small, it must be remembered that, at the T = 0.37 K He cluster temperature, $kT = 0.25$ cm^{-1} and thus a simple classical Boltzmann calculation would predict that a 0.7 cm^{-1} barrier could reduce the exciplex formation rate by a factor 16, which would account for the difference in exciplex formation rates observed for the two spin-orbit states. Such a calculation, however, ignores both zero point and tunnelling effects, both of which would be expected to increase the reaction rate. On the other hand, if there is a barrier for the extraction of a He atom from the cluster this further constraint would need to be included in the calculation of the overall formation rate of the exciplex.

We close this section with one last observation in which

132

we analyze the emission following excitation of Na on large H_2 clusters. As previously established (see above), Na* attached to H_2 clusters has a small quantum yield for emission (roughly 1%), and all of the observed emission appears at the gas phase wavelength, suggesting that only the small fraction of molecules that desorb from the cluster escape quenching [18,19]. The observed time dependent emission of Na* following excitation on the hydrogen clusters is successfully fit to a model with a free atom decay time (as expected), and a rise time of 20 ps. This result suggests that the desorption comes from atoms excited to bound-free transitions from the surface of the H_2 clusters. Previous theoretical calculations had predicted that Na would be solvated and reside inside of large H_2 clusters [21]. The present results demonstrate that at least the fluorescing fraction reside on the surface and, furthermore, lend support to the idea that the slower evaporation times measured for He clusters (50-70 ps) may be real.

IV. DISCUSSION

One of the main conclusions derived from the work described above is that in species with a P-type electronic structure, spin orbit coupling plays a role in the formation of dimers and, therefore, also higher clusters. The methods developed in our laboratory to study the formation and low T reactivity of metastable alkali complexes and excimers can be now applied to other species.

As an example, let us consider the formation of a diatomic Al_2 from two ground $^2P_{1/2}$ atoms. From two identical ^2P atoms, we can generate 36 microstates which lead to 12 singlet and 12 triplet states, which lead to a complicated mess of both attractive and repulsive curves at long range. The two atoms in the $J = 1/2$ fine structure levels have spherical charge distributions, sampling all orientations of the P orbital. As a result, at long range, we expect, in addition to the attractive van der Waals interaction, an average over all the possible states. In order to create states with electrons localized in definite s and p orbital, we must at least partially uncouple the spin-orbit interaction of the Al atoms. As for the case of the excited ^2P state of Na (see above), it is reasonable to expect that the need to uncouple the angular momenta will lead to long range barrier in the potential on the order of a modest fraction of the atomic spin-orbit splitting. Since in the 3 ^2P level of Al the atomic spin-orbit splitting is 112 cm^{-1}, even a barrier as small as 10% of this value will still represent $\approx 45\ kT$ at the temperature of He clusters, which should completely shut down the reaction. The implications of what is stated above for the loading of H_2 matrices with high concentrations of light metal atoms which has been one of the continuing goals of the HEDM program are clear.

More in general, we note that the introduction of rare gas matrix isolation spectroscopy [22,23] was an important step forward in the development of chemistry. For the first time, a large number of "reaction intermediates" that had been previously proposed by chemists could be isolated and studied. More importantly, a great many new, and previously unexpected, chemical species were detected and characterized [24]. Chemists felt the necessity to re-evaluate their definitions of what constituted a chemical species, since many molecules far too fragile to be isolated at room temperature could now be formed and stabilized, and held often for very long periods. The reason for this dramatic change was largely the change in temperature scale which from the values valid for solution chemistry, that previously extended from room temperature down to 200 K, moved down to the 40-80 K domain. Because of the typical exponential dependence of reaction rates on temperature, this modest change in absolute temperature scale led to dramatic changes in the chemistry that became thermally accessible.

The development of spectroscopy of species attached to, and dissolved in highly quantum clusters made of molecular hydrogen ($\approx$ 5 K) and atomic helium (0.37 K) promises another dramatic expansion in our understanding of chemical stability. The fractional change in temperature is even higher than in the case of the development of traditional cryogenic matrix spectroscopy. The size of a chemically significant energy drops from $\approx$ 1 Kcal/mole at room temperature to $\approx$ 1 cal/mole. This implies that a wide range of subtle and delicate chemical effects will dramatically alter the chemical reactivity in these media. As a result, it is expected that many atomic and molecular species that are viewed as unstable even by the standards of traditional matrix spectroscopy, could well be metastable under such conditions. This observation can have profound implications for a range of chemical phenomena, but perhaps none greater than for the HEDM field.

[1] M. Hartmann, R.E. Miller, J.P. Toennies, and A. Vilesov *Phys. Rev. Lett.* **75**, 1566 (1995).

[2] see the work from this group reported in previous HEDM Contractors' meeting proceedings.

[3] F. Stienkemeier, W.E. Ernst, J. Higgins, and G. Scoles *J. Chem. Phys.* **102**, 615 (1995).

[4] F. Stienkemeier, J. Higgins, W.E. Ernst, and G. Scoles *Phys. Rev. Lett.* **74**, 3592 (1995).

[5] F. Stienkemeier, J. Higgins, W.E. Ernst, and G. Scoles *Z. Phys. B.* **98**, 413 (1995).

[6] J. Higgins, W.E. Ernst, C. Callegari, J. Reho, K.K. Lehamnn, M. Gutowski, and G. Scoles *Phys. Rev. Lett.* **77**, 4532 (1996).

[7] J. Higgins, C. Callegari, J. Reho, F. Stienkemeier, W.E. Ernst, K.K Lehmann, M. Gutowski, and G. Scoles *Science* **273**, 629 (1996).

[8] e.g. in P. Botschwina, W. Meyer, I.V. Hertel, and W. Reiland *J. Chem. Phys.* **75**, 5438 (1981).

[9] S. Kanorsky, A. Weis, M. Arndt, R. Dziewior, T.W. Hänsch *Z. Phys. B* **98**, 371 (1995). J. Dupont-Roc *ibid.* p. 383

[10] F. Stienkemeier, J. Higgins, C. Callegari, S.I. Kanorsky, W.E. Ernst, and G. Scoles *Z. Phys. D.* **38**, 253 (1996).

[11] Pascale, J.; *Technical Report, Service de Physique des Atoms et des Surfaces* (C.E.N. Saclay, Gif sur Yvette-Cédex, France, 1983).

[12] M.D. Havey, S.E. Frolking, and J.J. Wright *Phys. Rev. Lett.* **45**, 1783 (1980).

[13] D.V. O'Connor and D. Phillips. *Time-correlated Single Photon Counting.* Academic Press (1984).

[14] A.A. Radzig, B.M. Smirnov: *Reference data on atoms, molecules and ions* (Springer-Verlag, New York 1985).

[15] S. Cova, M. Ghioni, and F. Zappa. *Rev. Sci. Instrum.* **62**, 2596 (1991).

[16] J.L. Persson, Q. Hui, Z.J. Jakubek, M. Nakamura, and M. Takami *Phys. Rev. Lett.* **76**, 1501 (1996).

[17] T. Kinoshita, K. Fukuda, T. Matsuura, and T. Yabuzaki *Phys. Rev. A* **53**, 4054 (1996).

[18] C. Callegari, J. Higgins, J. Reho, F. Stienkemeier, K.K Lehmann, and G. Scoles *unpublished data.*

[19] J. Reho, J. Higgins, C. Callegari, K.K. Lehmann, and G. Scoles *Farad. Discus.* **108** *submitted for publication.*

[20] R. J. LeRoy *Computer Physics Communications* **52** 383 (1989).

[21] F. Ancilotto, E. Cheng, M.W. Cole, and F. Toigo *Z. Phys. B* **98**, 323 (1995).

[22] N.J. Almond and A.J. Downs *Spectroscopy of Matrix Isolated Species.*

[23] R.J.H. Clark and R.E. Hester *Molecular Cryospectroscopy* (J. Wiley & Son).

[24] M.E. Jaycox, *J. of Phys. and Chem. Ref. Data*, Mono 3, Vibrational and Electronic Levels of Polyatomic molecules (AIP, 1995).

Spectroscopic Characterization of Non-bonding Interactions of the Boron Atom

Paul J. Dagdigian and Xin Yang
Department of Chemistry, The Johns Hopkins University
Baltimore MD 21218-2685

1. Introduction

In previous work, we have reported laser fluorescence excitation and depletion spectra of binary complexes of the boron atom with a rare gas atom (Ne, Ar, Kr) or hydrogen molecule. In collaboration with Millard Alexander and his group, these experimental data have been employed with theoretical work on their part to provide detailed information on the non-bonding interactions of the boron atom, in its ground $2s^22p$ ^2P and electronically excited $2s^23s$ ^2S Rydberg and $2s2p^2$ ^2D valence states, with a single atomic or molecular partner. We have also collaborated with David Yarkony in order to understand the mechanism of nonradiative decay of the BAr($C^2\Delta$) state.[1,2]

During the past year, we have extended our spectroscopic studies of weakly bound boron–rare gas diatomic species to complexes containing more than one rare gas atom. Specifically, we have observed in the BAr$_2$ complex the $^2S \leftarrow ^2P$ electronic transition by laser fluorescence excitation spectroscopy[3] and the $^2D \leftarrow ^2P$ transition by fluorescence depletion.

We have also extended our study of binary complexes to B$\cdots$N$_2$, specifically the observation and interpretation of its $^2S \leftarrow ^2P$ fluorescence excitation spectrum, with the help of calculations by Alexander. We previously reported that the B(^2S)$\cdots$H$_2$ state decays by fluorescence emission,[4] while the B(^2D)$\cdots$H$_2$ complex decays nonradiatively.[5] We have recorded and analyzed BH $A^1\Pi \rightarrow X^1\Sigma^+$ and $b^3\Sigma^- \rightarrow a^3\Pi$ chemiluminescence spectra from the reactive decay of this complex at various excitation energies. Finally, we have begun exploration of the non-bonding interactions of the ground $X^3\Sigma_g^-$ electronic state of the boron dimer.

The following sections present more detailed descriptions of this work.

2. The BAr$_2$ complex

The $2s^23s$ $^2S \leftarrow 2s^22p$ ^2P transition. In supersonic expansions of B atoms entrained in Ar at high source backing pressures, we observe a broad, asymmetric feature peaking at *ca.* 420 cm^{-1} to the blue of the $^2S \leftarrow ^2P$ atomic transition, as shown in Fig. 1.[3] This blue shift is about twice that of the strongest features (v$'$ = 8 and 9) in the excitation spectrum of the binary BAr complex. This feature cannot be assigned to the B atom or the diatomic BAr complex.
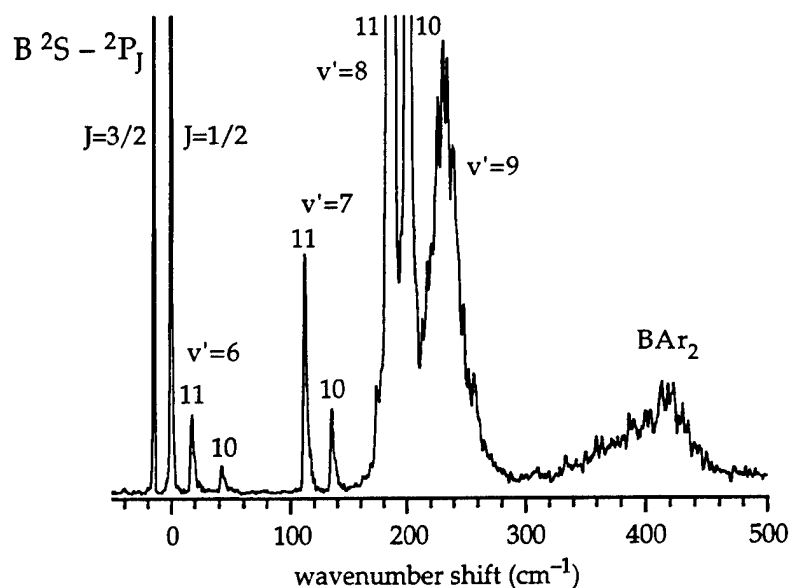
FIG. 1. Laser fluorescence excitation spectrum of a B/Ar beam (source backing pressure 9.1 atm). The B $^2S \leftarrow {}^2P$ atomic transition, the ^{11,10}BAr $B - X$ (v', 0) bands, and the feature assigned to BAr$_2$ are identified. The wavenumber is given relative to the atomic B $^2S \leftarrow {}^2P_{1/2}$ transition.

In collaborative theoretical work by Alexander and co-workers,[3] this feature has been assigned as the $^2S \leftarrow {}^2P$ electronic transition of the BAr$_2$ complex. These calculations employed a pairwise additive model for the interaction energies, with the BAr(X,B) potentials determined from fits to our observations. The ground B($2p$)Ar$_2$ vibrational wave function was determined by variational and diffusion Monte Carlo treatments of the nuclear motion, while the spectrum was simulated in a semiclassical treatment. The simulated spectra nearly quantitatively reproduces the experimental spectrum.

The $2s2p^2$ $^2D \leftarrow 2s^22p$ ^2P transition. We have also observed the transition to the $2s2p^2$ ^2D excited valence state in the BAr$_2$ complex by fluorescence depletion spectroscopy, using the assigned $^2S \leftarrow {}^2P$ transition as our probe. The fluorescence depletion spectrum, shown in Fig. 2, has 3 distinct features covering 800 cm^{-1} and extends both to the red and blue of the $^2D \leftarrow {}^2P$ atomic transition. The spectrum has been successfully modeled by Alexander and Krumrine[6] using BAr($C^2\Delta$, $D^2\Pi$) potentials derived in our previously reported[2] spectroscopic study of these diatomic electronic states and an estimated potential energy curve for the $E^2\Sigma^+$ state. It is interesting to note that the features in Fig. 2 cannot individually be associated with transitions to specific BAr electronic states, because of the mixing of these states in the ternary complex.

136

No $^2D \rightarrow {}^2P$ fluorescence is observed from the radiative decay of excited BAr_2, as was also found for the diatomic $BAr(C^2\Delta)$ state.[1] Nevertheless, we do observe a weak emission from the lower $2s^23s\ {}^2S$ state when BAr_n ($n \geq 2$) complexes are electronically excited to the ^2D state. This may be due to electronic quenching within the BAr_2 complex. Diatomic $BAr(C^2\Delta)$ decays nonradiatively because of predissociation induced by the repulsive state correlating with $B(2s2p^2\ {}^4P) + Ar.$[2]
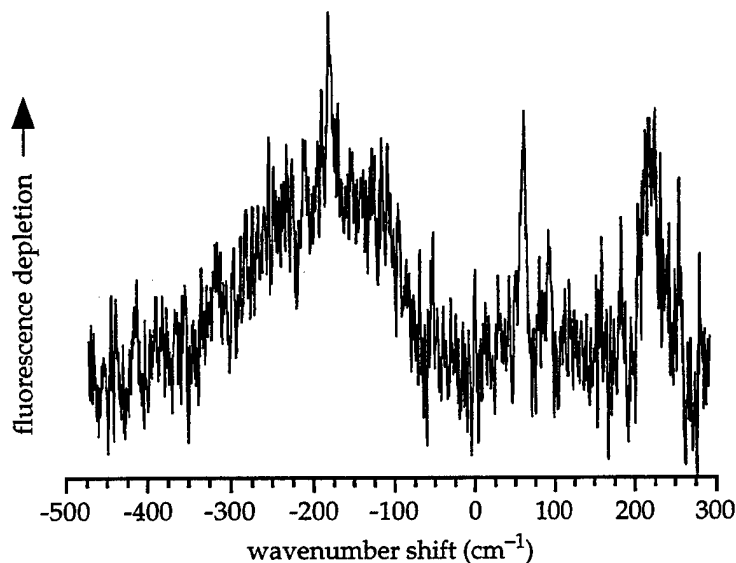

FIG. 2. Laser fluorescence depletion spectrum of the BAr_2 complex. The probe laser was tuned to excite the BAr_2 feature associated with the B atomic $^2S \leftarrow {}^2P$ transition (see Fig. 1).

3. The $B\cdots N_2$ Complex

The laser fluorescence excitation spectrum of the $3s \leftarrow 2p$ transition in this complex is shown in Fig. 3. All the observed emission corresponds to free $\leftarrow$ bound excitation since it appears at excitation energies greater than the $B(3s) + N_2$ dissociation asymptote, estimated from calculations by Alexander[6] of the $B(2p)\cdots N_2$ binding energy ($D_0'' = 154$ and 158 cm^{-1} for *ortho* and *para*–N_2, respectively). However, the $B\cdots N_2$ spectrum contrasts sharply with the corresponding free $\leftarrow$ bound $B\cdots H_2$ spectrum,[4] which has only a single broad, asymmetric peak.

In order to understand the structure seen in Fig. 3, we have carried out simulations of the $B\cdots N_2$ spectrum, using bend-stretch wave functions for the $B(2p)\cdots N_2$ state and a $B(3s)\cdots N_2$ potential energy surface calculated by Alexander.[6] One rather significant difference between the $B\cdots N_2$ and $B\cdots H_2$ complexes is that the anisotropies in both electronic states are large compared to the diatom rotor spacings in the former. This results in a

137

considerable polarization (mixing of rotor levels) of the N_2 rotor wave functions. This, in turn, allows electronic transitions to B(3s)···N_2 bender curves other than the lowest ($j' = 0$ and 1) of a given nuclear spin modification. The peaks in Fig. 3 are thus assigned as transitions to various bender curves correlating to different B(3s) + N_2 rotational asymptotes.
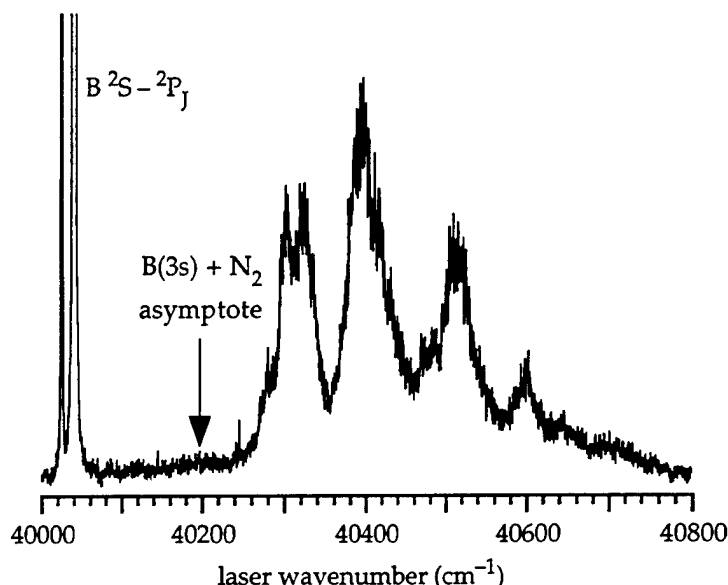

FIG. 3. Laser fluorescence excitation spectrum of the B···N_2 complex. The B $^2S \leftarrow$ ^2P atomic transition and the estimated excitation energy to the B(3s) + N_2 asymptote are identified.

4. BH Chemiluminescence from the B(^2D)···H_2 Complex

In other work, we have characterized the decay of electronically excited B(^2D)···H_2 complexes by observation and analysis of the BH $b^3\Sigma^- \rightarrow a^3\Pi$ and $A^1\Pi \rightarrow X^1\Sigma^+$ chemiluminescence spectra as a function of the excitation energy around the $^2D \leftarrow$ ^2P transition.

We have recorded the $b \rightarrow a$ and $A \rightarrow X$ chemiluminescence intensity as a function of the excitation energy. We find that chemiluminescence is observed predominantly for energies less than that of the corresponding B atomic $^2D \leftarrow$ ^2P transition, in the red end of the B(^2D)···H_2 fluorescence depletion spectrum.[5] This suggests that reaction within the complex to form radiating BH(b, A) products occurs on BH_2 potential energy surfaces which are attractive in the Franck-Condon region.

We have also estimated the excited BH(b, A) product rovibrational excitation by comparison of the observed spectra with simulations. We find that the A state product possesses considerable rotational excitation, with significant population in vibrational levels v' = 0–2. This suggests that there is considerable torque exerted on the departing BH product. The degree of

138

BH(A) vibrational and rotational excitation is roughly independent of the excitation energy of the B$\cdots$H$_2$ complex. By contrast, we observe BH(b) state in the v$'$ = 0 vibrational level only for low excitation energies of the B(^2D)$\cdots$H$_2$ complex and an onset for the formation of the v$'$ = 1 level. In addition, successful simulations of the $b - a$ (0,0) and (1,1) bands requires that a cutoff in the highest rotational level j' be imposed. These constraints result from the energetics of the B* + H$_2 \rightarrow$ BH(b) + H pathway. These observations have allowed us to estimate the energetic threshold for this channel. With this determination, we have been able to relate the energies of the BH singlet and triplet manifolds. Our value for the energy difference between the $a^3\Pi$ and $X^1\Sigma^+$ states is in good agreement with the theoretical value calculated by Yarkony and co-workers[7] and falls within the range calculated by Brazier[8] from extrapolation of measured $a^3\Pi$ vibrational energies.

At energies above the BH(b, v$'$ = 1) + H threshold, BH triplet and singlet products are formed in an approximately 1 : 4 ratio.

5. Preliminary study of non-bonding interactions involving B$_2$

In exploratory work, we have observed B$_2$ molecules in the v$''$ = 0 vibrational level of the ground $X^3\Sigma_g^-$ electronic state, formed in supersonic expansions of photolyzed B$_2$H$_6$/rare gas mixtures, through laser fluorescence excitation in the $2^3\Sigma_u^- - X^3\Sigma_g^-$ band system. With the addition of Ar to the seed gas, several new features, indicative of complexes involving Ar, appear in the spectrum. Work is continuing to characterize these complexes spectroscopically.

---

1. X. Yang and P. J. Dagdigian, J. Chem. Phys. **106**, 6596 (1997).

2. K. Sohlberg and D. R. Yarkony, J. Phys. Chem. A **101**, 3166 (1997); J. Chem. Phys. **106**, 6607 (1997).

3. M. H. Alexander, A. R. Walton, M. Yang, X. Yang, E. Hwang, and P. J. Dagdigian, J. Chem. Phys. **106**, 6320 (1997).

4. X. Yang, E. Hwang, and P. J. Dagdigian, J. Chem. Phys. **103**, 7966 (1995).

5. X. Yang, E. Hwang, and P. J. Dagdigian, J. Chem. Phys. **104**, 8165 (1996).

6. M. H. Alexander, abstracts *AFOSR 1996 HEDM Contractors Meeting*, Boulder, CO.

7. L. A. Pederson, H. Hettema, and D. R. Yarkony, J. Phys. Chem. **98**, 11069 (1994).

8. C. R. Brazier, J. Molec. Spectrosc. **177**, 90 (1996).

Structure, energetics, and excitation spectra of clusters containing B and other open-shell atoms

Millard H. Alexander, Andrew Walton, Moonbong Yang, and Jennifer Krumrine

Department of Chemistry and Biochemistry

University of Maryland, College Park, MD 20742-2021

I. Introduction

We have continued our investigation of weakly-bound clusters involving atomic B, carrying out further work on clusters with Ar and the BN_2 cluster. Additionally, we have initiated the investigation of B in solid Ar, and have determined the non-adiabatic electronic matrix elements crucial to the correct description of complexes of H_2 with atomic oxygen. Close contact continues with Dagdigian's group, who are reporting[1] related experimental investigations of BAr_2 and BN_2.

2. BAr_n clusters

Since the B atom has an open shell, the effective PES is obtained as the root of a 3×3 Hamiltonian.[2,3] With inclusion of spin-orbit coupling, the electronic states occur in three sets of degenerate pairs and are roots of the 6×6 Hamiltonian.

$$V(R) = T(\theta, \phi) \ H(R) \ T(\theta, \phi)^T \ , \qquad (1)$$

where $H(R)$ is a 6×6 matrix and $T(\theta, \phi)$ is the product of the two rotations which define the position of the Ar atom. In an uncoupled basis (l, m_l, s, m_s) $H(R)$ contains both diagonal and off-diagonal spin-orbit terms and diagonal contributions from the electrostatic BAr $X^2\Pi$ and $A^2\Sigma^+$ potential curves.[4] Following Balling and Wright[2] and our earlier paper,[5] we then describe the interaction of n Ar atoms with a single B atom by a 6×6 Hamiltonian which is a pairwise sum of n $V(R)$ matrices plus the $\frac{1}{2}n(n-1)$ Ar–Ar interactions. The lowest root of this Hamiltonian then defines the potential energy of the BAr_n cluster.

Stimulated by new work in Dagdigian's laboratory,[1] we completed[6] the simulation of the fluorescence spectrum of the BAr_2 trimer, subsequent to excitation in the vicinity of the atomic $(2s^23s \leftarrow 2s^22p)$ transition. We use the semiclassical expression for the total absorption cross section, namely[7,8]

$$\sigma(w) \sim \int dR \ |\psi_g(R)|^2 \ \delta\left[V_e(R) - E_g - \hbar\omega\right] \ . \qquad (2)$$

Here R designates, collectively, the 3 internal coordinates of the $B(Ar)_2$ complex, E_g is the energy of the lowest bend-stretch state of the complex in its electronic ground state, and $V_e(R)$ is the excited state PES. Since the electronic transition is localized on the B atom, we take the electronic transition moment to be constant.

In our simulation[6] we used, initially, the variational Monte-Carlo technique.[9-11] The resulting wavefunction was then used to guide a subsequent diffusion Monte-Carlo (DMC) calculation [12, 13] to determine the energy. Since the $B(2s^23s)$ excited state is nondegenerate, the $B(2s^23s)Ar_2$ PES is expressed as a simple pair-wise additive function, involving the $B(2s^23s)Ar$ diatomic potential, which we determined previously in prior collaborative work with Dagdigian.[4, 14]

Subsequently, we carried out entirely equivalent VMC calculations for the BAr_3 cluster. Here, it is impossible to locate the third Ar atom in a position which can avoid the repulsive interaction with the B $2p$ atom. The predicted spectrum of the ternary complex is shown below and compared with experiment.
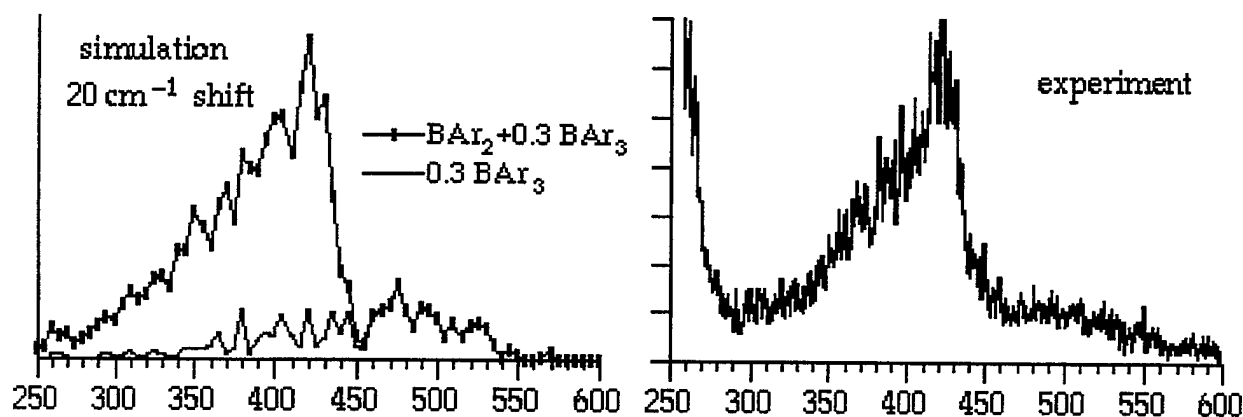

Fig. 1. Comparison of predicted excitation spectrum (upper panel) of a 10:3 mixture of BAr_2 and BAr_3 complexes with the observed spectrum. The position of both spectra are plotted relative to the $B(2p \rightarrow 3s)$ atomic transition. The high energy tail of the latter is evidence of the presence of the four-atom complex.

In more recent work, described in more detail by J. Krumrine in a poster presentation, we used the potential energy curves for the BAr $C^2\Delta$, $D^2\Pi$, and $E^2\Sigma^+$ states, reported this year by Yang and Dagdigian,[15] to simulate the excitation spectrum of the BAr_2 complex in the region of the atomic $[2s2p^2(^2D) \leftarrow 2s^22p]$ transition. Here the 10-fold degenerate excited state must be described with a pairwise Hamiltonian. The predicted excitation spectrum is shown below, and compared to experiment. The agreement is qualitatively good, although many fine differences remain. Likely this discrepancy is a manifestation of errors in the excited state $D^2\Pi$ and $E^2\Sigma^+$ potential curves, which could not be determined to high accuracy.
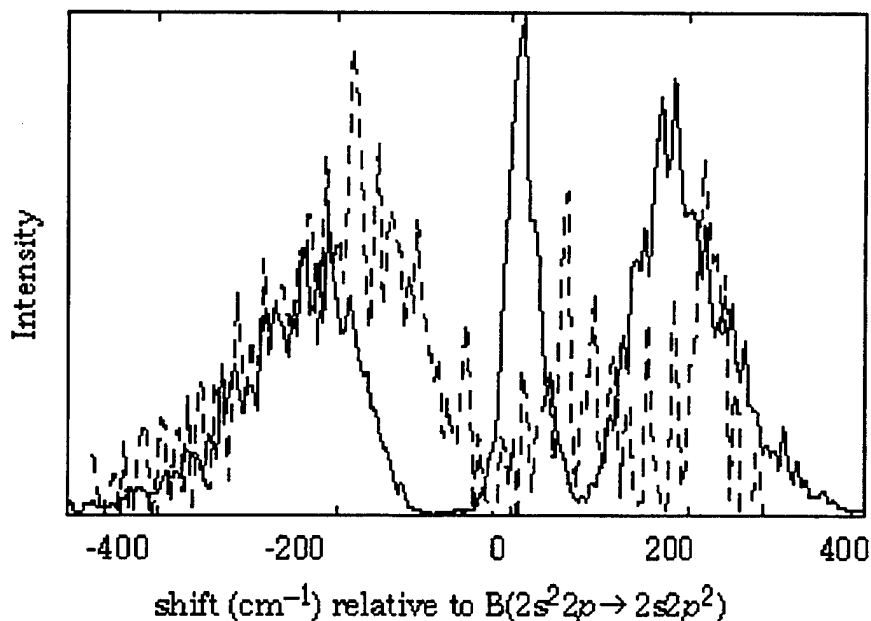
Fig. 2. Comparison of predicted excitation spectrum (solid) with observed spectrum (dashed).
The excitation accesses simultaneously *five* electronic states of the complex.

During the past year we have extended our Monte-Carlo simulations to a single B atom imbedded in a rigid Ar matrix. Following earlier work of Fajardo and Boatz[3] on Na in solid Ar, we used a 108 atom cluster and periodic boundary conditions to describe the fcc lattice. Again, we have used the pairwise Hamiltonian model to described the motion of the B atom. DMC calculations were carried out, involving 2000 replicas, with the B atom initially occupying one of the Ar sites. The predicted spectrum is shown in Fig. 3 (next page). The lineshape is predicted to be similar to that for the BAr_2 complex, but the peak is substantially more blue-shifted. Further work needs to be done before a definitive comparison is made with the earlier, unpublished spectrum taken by Fajardo and co-workers[16] for atomic B co-deposited in an Ar matrix.

4. BN_2 and OH_2 complexes

In a continuation of our earlier work on the BH_2 complex,[17-20] we have initiated the *ab initio* study of the BN_2 complex. This work is motivated by the fluorescence excitation investigation of this complex by Dagdigian and co-workers.[1]

Approach of the N_2 molecule to B leads to a mixing of the two electronic states corresponding to the two in-plane orientations of the B $2p$ orbital. We then reverse this mixing to transform the three *adiabatic* states into an electronically *diabatic* representation, defined by the three possible orientations of the $2p$ orbital along $\boldsymbol{R}$. To
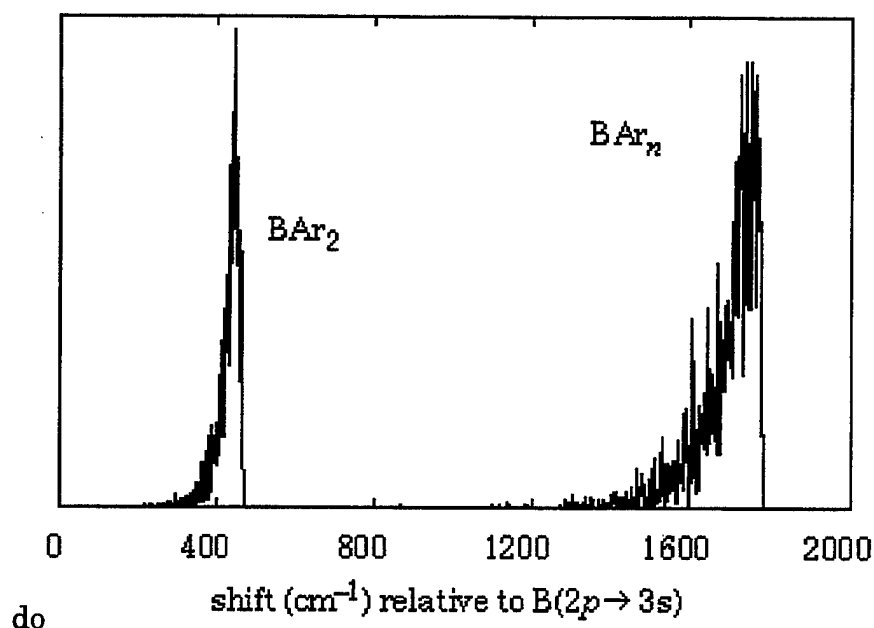
142

Fig. 3. Predicted excitation spectrum of a single B atom in a rigid fcc Ar matrix (right spectrum) compared with that for the ternary BAr_2 complex.

so, we have used[17, 18] both matrix elements of the electronic orbital angular momentum l as well as the coefficients in the CI expansion of the wavefunction.

In contrast to the BH_2 complex, the minimum energy geometry corresponds to a linear geometry, with $D_e \geq 170$ cm^{-1}. The diabatic PES's were presented at the 1996 HEDM Contractor's conference. Subsequently, we have carried out complete variational calculations of the lowest bend-stretch levels of the BN_2 complex. The lowest energy levels are given in the following table.

Table I. Energies of the BN_2 complex, relative to $B(2s2p^2, j = 1/2) + N_2(j = 0)$

o-N_2	E (cm^{-1})	p-N_2	E (cm^{-1})
$j = 0$	-144.8	$j = 1$	-144.8
$j = 2$	-143.1	$j = 1$	-143.5

The description of the excited state of the BN_2 complex is more involved. The $B(2s^23s)N_2$ state displays a barrier at long range with a substantial minimum farther in. This state is crossed by, and mixes with, a strongly attractive state which corresponds to the $^2\Delta(A')$ component of the $B(2s2p^2)N_2$ state. The determination of the excited states PES's is complicated by the large size of the reference space associated with these (and other) electron occupancies. Dagdigian has carried out modeling studies of the predicted excitation spectrum of the BN_2 complex based on simple assumptions about the form of the excited state PES's.[21]

143

In similar work we have investigated the potential energy surfaces for the interaction of $O(^3P)$ with H_2. This system has also been investigated by Apkarian and co-workers.[22] Our work is complementary to theirs, in that we have used the *ab initio* matrix elements of the electronic orbital angular momentum *l* and the coefficients in the CI expansion of the wavefunction to determine a transformation from the electronically adiabatic states into an approximate diabatic representation. The following figure shows the coupling between the two $O(^3P)$ diabatic states of A'' symmetry induced by approach of the H_2 wavefunction.
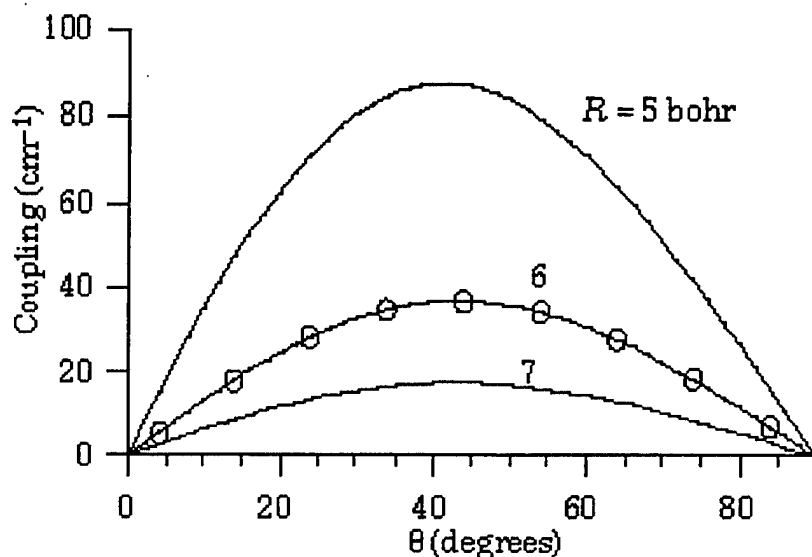

Fig. 4. Coupling between the two $O(^3P)$ states of A'' symmetry induced by approach of an H_2 molecules, as a function of the $O-H_2$ distance.

References

1. P. J. Dagdigian, E. Hwang, and X. Yang, abstracts *AFOSR 1996 HEDM Contractors Conference*, Boulder, CO, 1996, p. .
2. L. C. Balling and J. J. Wright, J. Chem. Phys. **79**, 2941 (1983).
3. J. A. Boatz and M. E. Fajardo, J. Chem. Phys. **101**, 3472 (1994).
4. E. Hwang, Y.-L. Huang, P. J. Dagdigian, and M. H. Alexander, J. Chem. Phys. **98**, 8484 (1993).
5. S. K. Gregurick, M. H. Alexander, and B. Hartke, J. Chem. Phys. **104**, 2684 (1996).
6. M. H. Alexander, M. Yang, A. Walton, X. Yang, E. Hwang, and P. J. Dagdigian, J. Chem. Phys. **106**, 6320–6331 (1997).
7. M. Lax, J. Chem. Phys. **20**, 1752 (1952).
8. R. Schinke, *Photodissociation Dynamics* (Cambridge University Press, Cambridge, UK, 1992).
9. M. H. Kalos and P. A. Whitlock, *Monte Carlo Methods* (Wiley, New York, 1986).
10. K. E. Schmidt and D. M. Ceperly in *The Monte-Carlo Method in Condensed Matter Physics*, Topics in Applied Physics, edited by K. Binder (Springer-Verlag, Berlin, 1992) 71, p. 205.
11. R. N. Barnett and K. B. Whaley, Phys. Rev. A **47**, 4082 (1993).
12. J. B. Anderson, J. Chem. Phys. **63**, 1499 (1975).
13. M. A. Suhm and R. O. Watts, Phys. Repts. **204**, 293 (1991).
14. E. Hwang, P. J. Dagdigian, and M. H. Alexander, Can. J. Chem. **72**, 821 (1994).

15. X. Yang and P. J. Dagdigian, J. Chem. Phys. **106**, 6596 (1997).

16. M. E. Fajardo, S. Tam, and M. Macler, private communication, 1993.

17. M. H. Alexander, J. Chem. Phys. **99**, 6014 (1993).

18. M. H. Alexander and M. Yang, J. Chem. Phys. **103**, 7956 (1995).

19. A. Vegiri, M. H. Alexander, S. Gregurick, A. McCoy, and R. B. Gerber, J. Chem. Phys. **100**, 2577 (1994).

20. X. Yang, E. Hwang, M. H. Alexander, and P. J. Dagdigian, J. Chem. Phys. **103**, 7966 (1995).

21. P. J. Dagdigian, abstracts *AFOSR 1997 HEDM Contractors Conference,* Chantilly, VA, 1997.

22. Z. Li, V. A. Apkarian, and L. B. Harding, J. Chem. Phys. **106**, 942 (1996).

FUNDAMENTAL INSIGHTS FROM HEDM STUDIES

David R. Yarkony

Department of Chemistry, Johns Hopkins University, Baltimore, MD 21218

Our research program considers spin-forbidden and electronically nonadiabatic processes as they relate to, the detection, the stability and the ultimate fate in a combustion process, of a high energy density material (HEDM). Recently our work has been motivated by the use of metal doped cryogenic hydrogen as a HEDM. In particular we have considered the detection of boron – rare gas van der Waals complexes[1,2] and the stability of the $Al-H_2$ and $B-H_2$ van der Waals complexes.[3] Our work on the detection of boron– rare gas van der Waals complexes was performed in collaboration with P. J. Dagdigian's experimental program at the Johns Hopkins University and the $M-H_2$ studies were performed in collaboration with M. S. Gordon's computational program at Iowa State University. The most exciting results of our research during the current performance period are: (i) our new insights into the nature of strong bonding in excited state van der Waals complexes[1] discovered in Dagdigian's laboratory,[3] and the resulting resolution of the much debated issue[4] of the origin of the fine structure splitting in metal -rare gas van der Waals complexes,[5] and (ii) the finding that seams of conical intersections normally thought of as accidental but symmetry-allowed may be more complicated involving several branches and trifurcations with important implications for the dynamics of $M-H_2$ reactions.[6]

Conical Intersections, Nonadiabatic Recrossing and the Kinetic Stability of Doped Cryogenic Hydrogen

Weakly bound van der Waals complexes between B or Al and molecular hydrogen are of interest in the HEDM program because of the possible role of metal doped cryogenic hydrogen as a propellant. The kinetic stability of a van der Waals complex with respect to formation of the dihydride, $M— H_2 \rightarrow MH_2$, is an important design criterion, as is the ultimate fate of the $M—H_2$ moiety in the combustion process. Gordon et al. have shown[7] that for M = Al the C_{2v} constrained reaction path from $M— H_2$ to MH_2 starts on the $^2B_2$ potential energy surface, passes through the minimum energy crossing point on the $^2B_2 - ^2A_1$ seam of conical intersection, and then moves on the $^2A_1$ potential energy surface to the $AlH_2(X^2A_1)$ state. The goal of our study was to understand how the kinetic stability of $M— H_2$ was effected by nonadiabatic interactions in the vicinity of the $^2B_2 - ^2A_1$ seam of conical intersection.

The $Al(^2P) + H_2$ seam of conical intersections would at first glance appear to be a straightforward $^2B_2 - ^2A_1$, accidental, but C_{2v} symmetry-allowed[8] seam of conical intersections. This turned out NOT to be the case! The seam of conical intersections was shown to exhibit an

unusual trifurcation pictured below. An exclusively C_{2v} region of the seam of conical intersection divides into a branch that preserves C_{2v} symmetry and two symmetry equivalent branches that have only C_s symmetry.
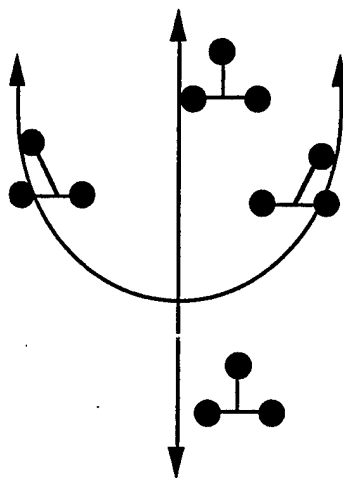

This trifurcation was found to occur in the region of the minimum energy point on the seam of conical intersections, which in turn lies near the transition state for the formation of AlH_2 from the van der Waals complex $Al-H_2$. Thus nonadiabatic interactions in general, and nonadiabatic recrossing in particular, will have important effects on the dynamics of the $Al + H_2$ reaction. Here 'nonadiabatic recrossing'[9] refers net reduction of reactive encounters produced by a nonadiabatically induced 'hop' onto a nonreactiive excited state potential energy surface and the subsequent 'rolling back' to the nonadiabatic region followed by recrossing onto the lower potential energy surface. Similarly wavepackets describing the decomposition of excited vibrational levels of $AlH_2(X^2A_1)$ are likely to pass quite close to the minimum energy point on the seam of conical intersections. Nonadiabatic recrossing could serve to increase the stability of these resonances. Consequently the decay of these resonances provides a valuable laboratory for the study of nonadiabatic effects.

Since the seam of conical intersections proposed above is nonstandard it is desirable to prove the existence of the points of conical intersection. A numerical search procedure cannot distinquish between a true intersection and a narrowly avoided crossing. With this in mind the existence of conical intersection points was proved by analyzing $X(C)$, the line integral of the derivative couplings, $f^{IJ}(R)$, along closed loops, C, containing the proposed point of conical intersection. The analysis depends on the observation[10,11] that $X(C) = \oint_C f^{IJ}(R) \cdot dR \xrightarrow{\rho \to 0} \kappa(C_\varepsilon)$ where $\kappa(C_\varepsilon) = 0$ if C_ε, the infinitesimal loop, contains 0 points of conical intersection and $\kappa(C_\varepsilon) = \pi$ if C contains 1 point of conical intersection.

This analysis is currently being extended to the B + H₂ system.

New and Unexpected Bonding in Open Shell van der Waals Complexes

For reasons outlined above Dagdigian and coworkers have studied the interactions of boron with the noble gases, Ne and Ar and with H_2.[12-15] Of particular concern were recent experiments in which the $C^2\Delta \leftarrow X^2\Pi$ transition was observed in BNe but not in BAr. It was suggested that the $C^2\Delta$ state in BAr is predissociated by spin-orbit induced coupling to a repulsive $^4\Pi$ state. To consider this hypothesis the potential energy curves for the van der Waals, $C^2\Delta$ state, and the repulsive $1^4\Pi$ state, were determined as was the $C^2\Delta \sim 1^4\Pi$ spin-orbit interaction, $H^{so}(C^2\Delta, 1^4\Pi)$.[2]
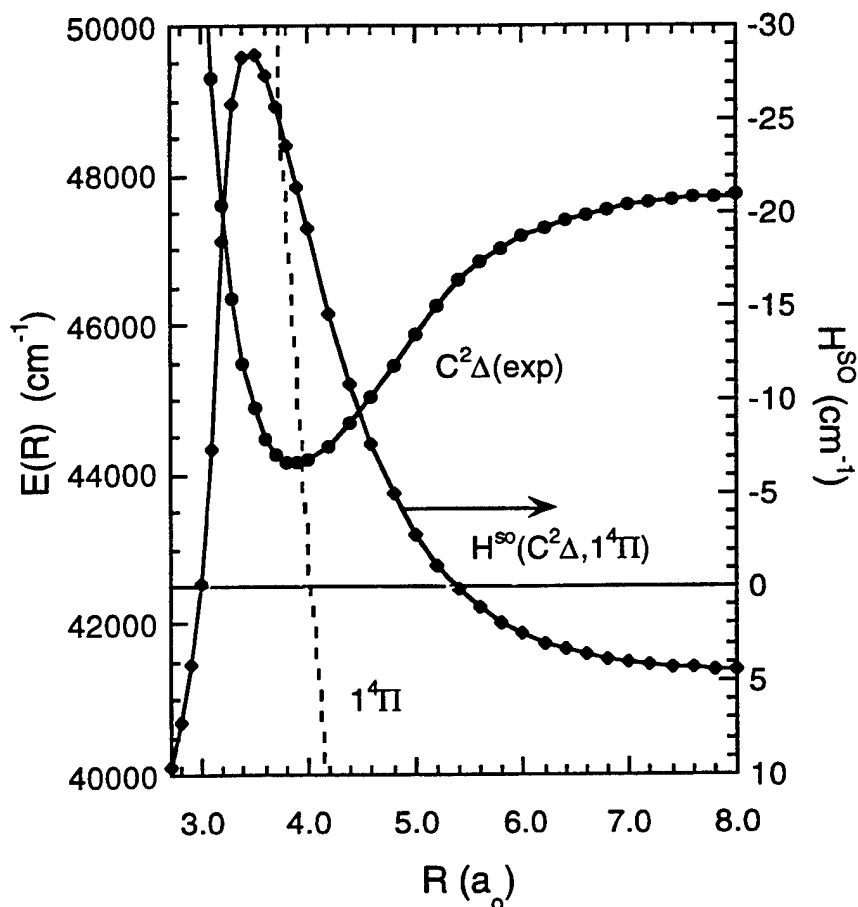
When compared with its asymptotic value, a remarkable 5 fold increase in $H^{so}(C^2\Delta, 1^4\Pi)$ was found in the vicinity of $R_e(C^2\Delta)$ - leading to a 25 fold increase in the computed predissociation rate. As a result of this large increase in $H^{so}(C^2\Delta, 1^4\Pi)$ the predicted predissociation rates[2] are in good agreement with the experimental inferences.[3] What is remarkable about these results is that: (i) the maximum in $H^{so}(C^2\Delta, 1^4\Pi)$ occurs for approximately the same value of $R(B-Ar)$ as $R_e(C^2\Delta)$ and (ii) $D_e(C^2\Delta) \sim 3700 cm^{-1},$[1,3] exceedingly large for a van der Waals complex.

Our analysis of R-dependence of $H^{so}(C^2\Delta, 1^4\Pi)$ leads to a novel and unexpected interpretation of these observations. We showed that:[1]

$$H^{so}(1^4\Pi, C^2\Delta) \approx \langle 8\sigma | h_x^{so} | 3\pi_y \rangle \approx s_1(R)p_1(R)\langle B_{2pz}|h_x^{so}|B_{2py}\rangle - s_2(R)p_2(R)\langle Ar_{3pz}|h_x^{so}|Ar_{3py}\rangle.$$

where the 3π and the 8σ orbitals have qualitatively the form:

$$8\sigma(R) = s_1(R)\, B2p_z + s_2(R)\, Ar3p_z$$

$$3\pi_y(R) = p_1(R)\, B2p_y - p_2(R)\, Ar3p_y$$

The origin of the R-dependence of $H^{so}(1^4\Pi, C^2\Delta)$ is now clear. At large R, $|s_1|$ and $|p_1|$ are large and $|s_2|$ and $|p_2|$ are small. The boron contribution to the spin-orbit coupling dominates and the value of $H^{so}(1^4\Pi, C^2\Delta)$ is close to the atomic boron limit. As R decreases, $|s_2|$ and $|p_2|$ increase and there is a contribution from the argon centered spin-orbit interaction. This is the external heavy atom effect.

Bonding in van der Waals complexes is usually explained in terms of dispersion forces or in the case of interpenetrating charge distributions, in terms of charge–induced-dipole models.[4] The above analysis of the spin-orbit interaction suggested the following alternative analysis of the bonding in the $C^2\Delta$ state. Since the 8σ orbital acquires Ar $3p_z$ character, in an antibonding manner, the corresponding doubly occupied argon like orbital, the 6σ orbital, should acquire the complementary <u>bonding</u> character by mixing in a B $2s2p_z$ hybrid. This can be viewed as Ar furnishing the electrons to the empty B $2s2p_z$ hybrid orbital to form a coordinate covalent, or <u>dative</u>, bond. B $2s2p_z$ hybridization facilitates the dative bonding by both orienting one B $2s$-$2p_z$ lobe toward the argon and by permitting the half occupied 7σ orbital (nominally the other B $2s$-$2p_z$ lobe) to point away from the region of the dative bond. This suggestion of dative bonding in BAr($C^2\Delta$) was born out by detailed calculations.

This analysis suggested an alternative explanation - again verified by explicit computation- for the heavy atom effect in alkali metal–rare gas complexes, an issue that had been the subject of considerable debate.[4] The σ orbital mixing described above implies similar, but smaller, π mixing

should also be present. In this case the heavy atom contribution to the fine structure splitting results from the antibonding mixture of <u>valence</u> p_π orbitals on the rare gas and metal atoms. Rydberg orbitals, previously suggested as the carrier of this effect, do not contribute significantly. The details of this argument can be found in Ref. 5.

REFERENCES

*(1)   K. Sohlberg and D. R. Yarkony, *J. Phys. Chem* (1997).

*(2)   K. Sohlberg and D. R. Yarkony, *J. Chem. Phys.* **106**, 6607-6611 (1997).

(3)   X. Yang and P. J. Dagdigian, *J. Chem. Phys.* **106**, 6596-6606 (1997).

(4)   W. H. Breckenridge, C. Jouvet, and B. Soep, *Adv. in Metal and Semiconductor Clusters* **3**, 1-83 (1995).

(5)   K. Sohlberg and D. R. Yarkony, *J. Chem. Phys.* , submitted (1997).

*(6)   G. Chaban, M. S. Gordon, and D. R. Yarkony, *J. Phys. Chem* submitted (1997).

(7)   M. S. Gordon, G. Chaban, and T. Taketsugu, *J. Phys. Chem.* **100**, 11512-11525 (1996).

(8)   T. Carrington, *Acc. Chem. Res.* **7**, 20-25 (1974).

(9)   G. C. G. Waschewsky, P. W. Kash, T. L. Myers, D. C. Kitchen, and L. J. Butler, *J. Chem. Soc. Faraday Trans* **90**, 1581 (1994).

(10)   D. R. Yarkony, *J. Chem. Phys.* **105**, 10456-10461 (1996).

(11)   D. R. Yarkony, *J. Phys. Chem.*, in press (1997).

(12)   E. Hwang, Y. L. Huang, P. J. Dagdigian, and M. H. Alexander, *J. Chem. Phys.* **98**, 8484 (1993).

(13)   X. Yang, E. Hwang, P. J. Dagdigian, M. Yang, and M. H. Alexander, *J. Chem. Phys.* **103**, 2779 (1995).

(14)   X. Yang, E. Hwang, and P. J. Dagdigian, *J. Chem. Phys.* **104**, 599 (1996).

(15)   X. Yang, E. Hwang, and P. J. Dagdigian, *J. Chem. Phys.* **104**, 8165 (1996).

Calorimetric Measurement of O Atom Recombination

P. Taborek and J. E. Rutledge

Department of Physics and Astronomy
Univeristy of California
Irvine, CA 92697-4575

We have continued our calorimetric study of the energy content of pure oxygen samples formed by quenching an RF discharge on a cold surface. The amount of stored energy in our samples is nearing technological significance. The form in which it is stored and the reaction path by which it is released have not yet been investigated.

The calorimeter used in these studies is similar to the one we described last year. The calorimeter consists of a copper substrate with a resistive heater and calibrated germanium thermometer. A thermal shield that is maintained near 25 K surrounds the calorimeter. An 8cm length of 1cm inner diameter quartz tubing penetrates the radiation shield and conducts the output stream of an RF plasma discharge onto the calorimeter. A mechanical heat switch allows the calorimeter to be placed in thermal contact with a closed cycle refrigerator with a base temperature of ~5 K or to be thermally isolated from the refrigerator. During sample deposition the calorimeter is connected to the refrigerator.

After a sample is deposited the oxygen flow and the RF power are turned off. When thermal contact to the refrigerator is broken, the temperature of the calorimeter begins to rise. The rate at which the temperature rises is determined by the heat capacity of the calorimeter and the rate at which energy is deposited in it. The heat capacity and the rate at which energy is deposited from external sources are measured in a separate experiment. The measured heat capacity is in good agreement with the value calculated from the specific heats and amounts of the materials comprising the calorimeter. The external heat leak is dominated by 300 K radiation from the quartz tube. Exothermic processes in the sample cause the temperature of the calorimeter to rise more quickly than the rate established by the external heat leak; endothermic processes cause the temperature to rise more slowly.

Figure 1 shows the temperature of the calorimeter, T, as a function of time for two successive openings of the heat switch. First an RF discharge was condensed on the calorimeter at a temperature between 5 and 6 K. Then at t = 0, the heat switch was opened. After 225 seconds the calorimeter had reached 35 K and the heat switch was closed. After the base temperature was reached, the heat switch was opened again. So that the subsequent thermal history can be more easily compared with the previous one, the second warm-up curve has been offset so that t = 0 also marks the time the heat switch was opened for this run. As shown in Fig. 1, the second warm-up to 35 K is considerably slower, taking more than 100 seconds longer than the first. This is

indisputably due to some exothermic process in the sample. If the experiment is repeated, subsequent warm-up curves are identical to the second one shown here.
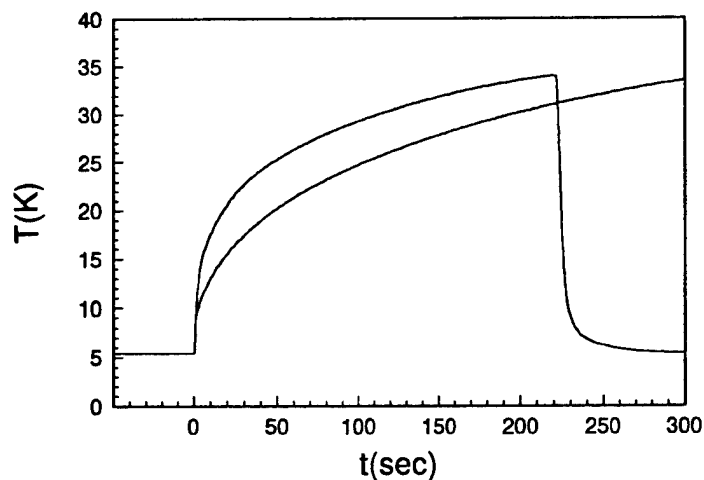

Figure 1.

If the sample is allowed to warm up past ~38 K, there is a downward break in the slope and a slower rate of warming for several degrees. The break in slope is due to the onset of evaporation, an endothermic process.
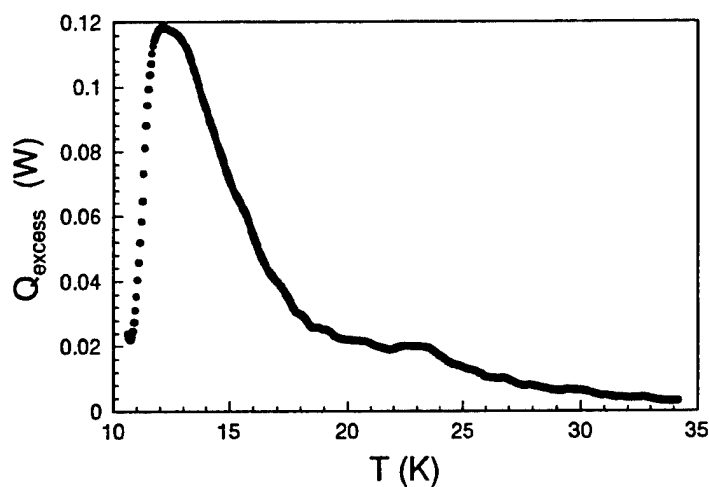
Figure 2.

The rate of heat production in the solid can be readily calculated from the data in Figure 1. The total heat deposited in the calorimeter is equal to the product of the known heat capacity of the calorimeter and dT/dt, which can be found by numerically differentiating data like those shown in Fig. 1. When this is done for the first warm-up curve in Figure 1, the result is $Q_{excess} + Q_{external}$, where Q_{excess} is the heat generated internal to the sample

152

and $Q_{external}$ is due to the external heat leak. Repeating the process for the second warm-up curve gives $Q_{external}$, which can be checked against the results of the runs that establish the heat capacity of the calorimeter. The difference, Q_{excess}, the exothermic heat from the sample is shown in Figure 2 as a function of temperature and in Figure 3 as a function of time. Figure 2 shows that most of the heat is liberated between 13 and 14 K. The integral of the curve in Figure 3 is the energy released by the sample during the warm-up. It is 1.5 J in the experiment shown. The data analysis done here relies on the assumption that $Q_{external}$ is a function of T only. Given its radiative origin and the constant temperature of its source this assumption is reasonable.
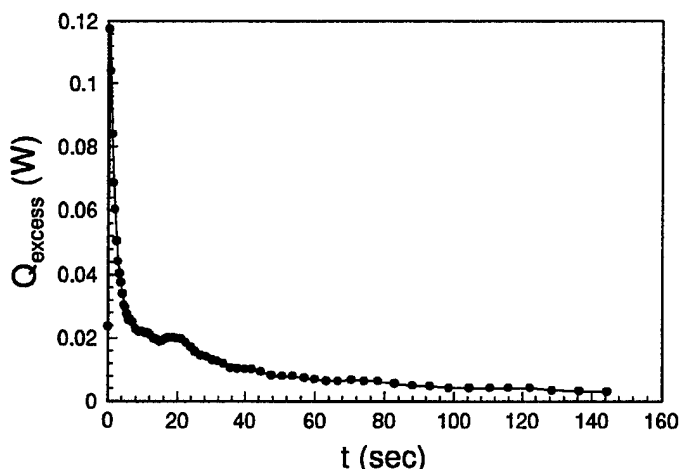

Figure 3.

A total of 5.8 x 10^{20} O_2 molecules passed through the RF discharge as the sample was deposited. The assumptions that the Qexcess is generated by O atom recombination at 5 eV per recombination and that all of the oxygen remains on the calorimeter imply an atomic O concentration of 0.64%.

Samples deposited with the RF discharge off also are exothermic, probably due to a sintering process in the poorly compacted oxygen. We have measured the sintering energy in several samples; it is on the order of 0.2 J. Taking this correction into account yields an estimated O atom concentration of 0.55%. We are able to reproducibly make and measure samples with excess energies comparable to those discussed here.

It is not clear that the deposition conditions that make these samples are optimal. Further increases in energy content are not ruled out by our experiment.

We believe that the Q_{excess} to sample size ratios that underlie our estimates of the atomic concentration are underestimates due to the open design of the calorimeter. First the sticking coefficient of the incoming RF discharged gas is less than one. Since we have used the total amount of oxygen passed through the discharge as the estimate of the sample size, that estimate is certainly too large by a factor that has yet to be measured. We believe we can exploit the heat of sublimation apparent in the data warm-up data above 38 K to refine the sample size estimate. Furthermore, we are likely to be

153

underestimating Q_{excess}. For example if atomic recombination is the source of Q_{excess}, it is likely that energetic O_2 molecules leave the sample as they are formed. Thus only a fraction of the recombination energy is absorbed by the calorimeter. Analogous energy loss accompanies other possible release mechanisms. Returning to a closed calorimeter design like the one we used a year ago may eliminate both of these problems. This will also affect the growth conditions of the sample and it is not clear what the consequences of that would be.

Although it is clear that the present samples contain excess energy, it is not clear that it is released by oxygen atom recombination. More complicated chemistry, perhaps involving ozone, may be involved. Properly executed spectroscopic studies might clarify these issues and suggest further steps to increasing the energy content to levels of true technological interest.

Note added since the meeting. It was suggested at the meeting that ions trapped in the sample might be responsible for the excess energy. We have added a magnetic trap between the calorimeter and the RF discharge to eliminate ions. The energy content of the samples was unaffected. Secondly it was suggested that O atoms in an O_2 matrix are unstable to ozone formation. Evidently the rate of this reaction has been measured at 15 K. We have attempted to grow samples at 15 K and indeed find that they contain no excess energy. A reaction barrier as small as 100 K (0.01 eV) would be sufficient to explain the qualitative differences in experiments at these two temperatures. It is tempting to speculate that the temperature dependence in Fig 2 suggests that ozone formation is responsible for Q_{excess}.

Characterization of Metal Atom-Doped Cryogenic Solids

W. Homsi, H. J. Maris, and G. M. Seidel

Physics Department, Brown University, Providence, RI 02912

We have constructed an apparatus for the study of the physical and thermal properties of films of molecular hydrogen incorporating light atoms produced by laser ablation. The temperature of the substrate upon which the films are deposited can be maintained and controlled down to 0.5 K using a ^{3}He cryostat. The substrate is backed by liquid helium to extract deposited principally by the ablation process. The energy with which the ablated atoms such as lithium hit the hydrogen film can be reduced by the presence of a dilute gas of helium within the deposition cell. The ablated atoms can make several collisions with the helium before reaching the substrate. The apparatus has optical windows not only for laser ablation but for measuring the film thickness and the spectroscopic properties of the incorporated atoms. We have developed a procedure whereby we can measure the heat capacity and thermal conductivity of the films using an ac temperature technique from 0.5 K to the temperature at which the hydrogen sublimates.

OZONE IN SOLID OXYGEN

Richard A. Copeland and Christian G. Bressler
Molecular Physics Laboratory, SRI International, Menlo Park, California 94025

INTRODUCTION

Storage of energetic species in cryogenic solids has been a goal of the High Energy Density Matter (HEDM) Program. Solid hydrogen and solid oxygen are the two host species that have received the most attention because of their excellent combustion properties. The increased density of these solid fuels gives modest improvements in the specific impulse, the key figure of merit, but crucial to a significant advance is incorporation of an energetic species in high concentrations into these hosts to dramatically enhance performance. This energetic-species generation and storage task is a difficult experimental challenge.

At SRI International we have focused our efforts on solid oxygen and incorporation of energetic species in that component of the propellant system. Specifically, we have investigated ozone, oxygen atoms and other O_x compounds as additives. In the case of ozone, the energized oxidizer may contain similar amounts of ozone and oxygen. Ozone is unique among potential HEDM materials because ton quantities can be generated with current technology and it contains significant chemical energy to "energize" the solid oxygen. However, ozone handling, storage, and shock sensitivity have limited its application to small-scale laboratory investigations. The use of solid ozone/oxygen mixtures in hybrid rocket systems is currently under study at Phillips Laboratory, and even if eventually its disadvantages are found to outweigh its potential use, it remains an important prototype system for the incorporation of high energy additives into a cryogenic solid. Because of the unique property that it is both experimentally tractable and practically useful, we are examining the properties of ozone/oxygen cryogenic mixtures to aid in its evaluation for the HEDM program.

Last year, we reported that irradiation of cryogenic oxygen matrices with ultraviolet light results in the production of ozone monomers and dimers locked in specific sites with unique orientations [1,2]. The spectroscopy, photophysics, and stability of these ozone species have been studied using Fourier-transform infrared (FTIR) spectroscopy. Over the past year, we have expanded the investigations to include mixtures with controlled concentrations formed via vapor deposition of O_3 seeded in oxygen gas. We have also examined the stability of $O(^3P)$ and $O(^1D)$ atoms in oxygen matrices deducing the behavior of these species at selected matrix temperatures and/or atom velocities. Before we describe these experiments we will briefly summarize previous experiments on solid ozone/oxygen mixtures.

OZONE/OXYGEN HISTORY

Solid ozone has a bad reputation for being shock sensitive. This reputation is well-deserved, but very difficult to study in a systematic way. In one of the few well-designed and controlled investigations, Wight [3] studied the sensitivity of both crystalline and amorphous solid ozone toward laser-induced detonation with pulsed 266-nm light. Crystalline ozone was

sensitive to laser-induced detonation while amorphous samples were more stable. An ozone solid seeded with 10 % O_2 was the least sensitive sample examined [3]. Irradiation at 266 nm dissociates the O_3 generating $O(^1D)$ atoms and heats the sample. Comparing this method of detonation with shock tests would be extremely instructive. The role the photogeneration of $O(^1D)$ atoms plays in the chain propagation is not well understood in ozone and ozone/oxygen mixtures. Sedlacek and Wight [4] have examined the quantum yield for $O(^1D)$ production in a single ozone photodissociation event, and found that the enormous gas phase value of 6 is significantly reduced in the condensed phase due to the cage effect. However, the value of 1.5 determined for solid ozone still emphasizes the reactive role of $O(^1D)$. Clearly, more knowledge of the detailed reaction sequence involving $O(^1D)$ atoms is required, and we report on interesting isotope experiments below.

In an investigation of the photochemistry of solid oxygen, Schriver-Mazzuoli *et al.* reported photogeneration of ozone in neat solid oxygen at 12 K with broad band UV light ($\lambda > 245$ nm) insufficient to dissociate O_2 with a single photon [5]. Two strong infrared (IR) absorption features were observed in each vibrational fundamental of O_3, of which they reported only the higher energetic feature was observed in ozone-seeded oxygen matrices and was accordingly assigned to an O_3 monomer in the O_2 lattice. The other absorption feature, located at 1031 cm^{-1} in the antisymmetric stretch region (ν_3) of ozone, was attributed to a novel complex, $O \cdots O_3$, with an $O(^3P)$ atom weakly bound to the center O atom of the O_3 molecule. The feasibility of storing $O(^3P)$ atoms in solid oxygen is of principal importance for the HEDM goals, and we report below on our conclusions regarding this weakly-bound species and O-atom stability above 15 K.

EXPERIMENTAL APPROACH

The details of the experimental approach are described elsewhere [1,2]; in this report, we will briefly outline the experiments. All the experiments are performed on thin films generated from room temperature gas phase deposition of oxygen or oxygen/ozone mixtures. The samples are deposited on a gold-coated copper substrate that is thermally connected with indium to the cooling finger of a closed-cycle He refrigerator. The lowest matrix temperature we obtain is 15 K. A Cr/Au thermocouple monitors the temperature and a heater stabilizes the temperature anywhere between 15 and 50 K. Ozone for the O_3-seeded samples is generated in a commercial ozonizer and condensed on silica gel inside a dry-ice cooled glass trap. Mixtures are prepared by standard barometric techniques. Deposition rates are estimated via the amount of gas admitted into the chamber. Typically, we use a flow rate of 3.5 mmol h^{-1} for 20 min. After deposition and prior to irradiation the pure O_2 matrices are annealed to about 30 K in order to reduce the number of defect sites.

Two pulsed lasers with markedly different characteristics are used for sample irradiation. The first laser system is an excimer-pumped, frequency-doubled dye laser. We use tunable nanosecond ultraviolet pulses with energies of about 200 μJ between 210 and 250 nm to illuminate the entire sample surface. In other experiments, we use the fundamental and frequency-doubled output of a mode-locked Nd:YAG laser with a pulse duration of 100 ps at a repetition rate of 78 MHz and an average power up to 20 W at 1.06 μ and 3 W at 532 nm.

The absorption spectrum of the samples are recorded using a Fourier-transform infrared (FTIR) spectrometer (Nicolet Co., Model 730) in the 500 - 4000 cm^{-1} range with a resolution of

0.5 cm^{-1}. The entire spectral region given above is acquired, but in the following sections we will focus our discussion on the v_3 region of ozone.

PHOTOGENERATED VERSUS SEEDED OZONE

Ozone infrared absorptions in solid oxygen change with the method of sample preparation. Figure 1 illustrates this difference showing representative spectra in the v_3 region following *in situ* creation of the ozone via 210 nm UV photolysis of solid oxygen and following deposition of ozone/oxygen mixtures directly from the gas phase. The 2 % concentration of ozone chosen in Fig. 1b ensures that we observe ozone dimers and higher aggregates. The labels above the spectra indicate the origin of the absorption feature, M for an ozone monomer and D for an ozone dimer. Numbered subscripts on the dimer designation are for dimers that are formed exclusively via treatment of solid O_2 with photons. The significance of the primes will become apparent in the following sections. Ascribing a specific orientation in the matrix to a specific absorption feature is not currently feasible given the complex shape of the monoclinic α–oxygen [6] together with the expected lattice distortions around the specifically-oriented ozone dimer species. However, previous signal growth studies clearly reveal that the D_x features stem from O_3 dimers [1,2]. Briefly summarizing those studies, which also show the wavelength dependence of ozone photogeneration in neat O_2, we find a limited mobility of hot $O(^3P)$ atoms following O_2 photodissociation in the
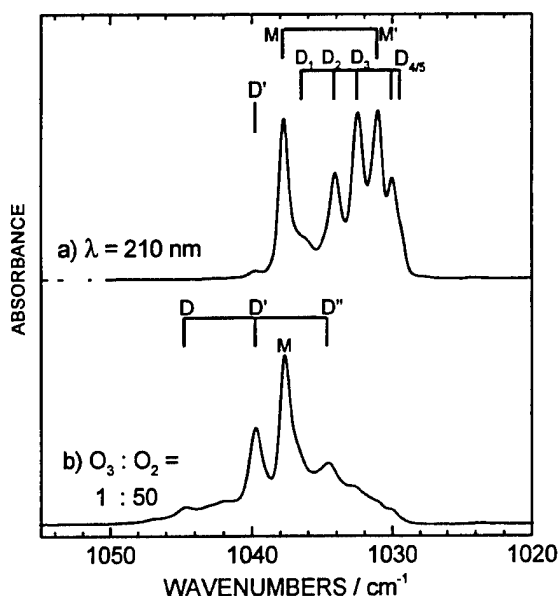

Figure 1: Comparison of the infrared spectrum of ozone in an oxygen matrix obtained via two methods. The top spectrum results from irradiation of neat solid oxygen with 210 nm laser light. The bottom spectrum results from gas-phase depostion of a 2 % ozone in oxygen mixture.. Both spectra are recorded at a sample temperature of 15 K.

Herzberg-continuum. In particular, both nascent $O(^3P)$ atoms with approximately 145 meV (1800 cm^{-1}) kinetic energy (corresponding to a photolysis wavelength of 232 nm) each react with a cage O_2 and form two O_3 molecules in close proximity. This reaction results in the 5 resolved D_x features after structural rearrangement of themselves together with the local environment. For small irradiation doses we observe no O_3 monomers (i.e., the M and M' features in Fig. 1a), but after prolonged irradiation they do grow in because of dimer photolysis in the Hartley-continuum of ozone. The dose-dependence of their growth exhibits an S-shaped curve, and their initial absence indicates complete reaction of both initial $O(^3P)$ fragments towards an ozone dimer.

The comparison with the highly enriched O_3/O_2 seeded sample (Fig. 1) verifies that these dimers are not stabilized under vapor deposition conditions. Here we observe three dimer features D, D', and D", which grow in with increasing concentration relative to the dominant monomer feature M, as shown in Fig. 2. The spectra have been normalized to the most intense

monomer feature, M, at 1037.8 cm^{-1}. This collection clearly shows the relative growth of dimer features and the slowly growing broad aggregate absorption extending from 1040 - 1030 cm^{-1}. In addition, we observe for the diluted samples (i.e., 1 : 10 000 and 1 : 1500) a weak M' feature. The M/M' intensity ratio remains 30 regardless of concentration, which supports its assignment to an ozone monomer. The ionization gauge inside the sample chamber forms O_3 under the high vacuum conditions during deposition of neat O_2, which results in the low concentration sample in Fig. 2e. The signal-to-noise ratio for this sample is too low to observe the weak M' feature.

The observed spectra for ozone seeded in O_2 matrices have proven to be extremely sensitive to deposition conditions. Samples grown at a slow rate (ca. 0.4 mmol h^{-1}) tend to favor aggregation of ozone leading to a dominant broad aggregate feature (width ca. 10 cm^{-1}) covering the 1040 - 1030 cm^{-1} range. High deposition rates on the order of 35 mmol h^{-1} suppress aggregation effects. The stability of the ozone features also de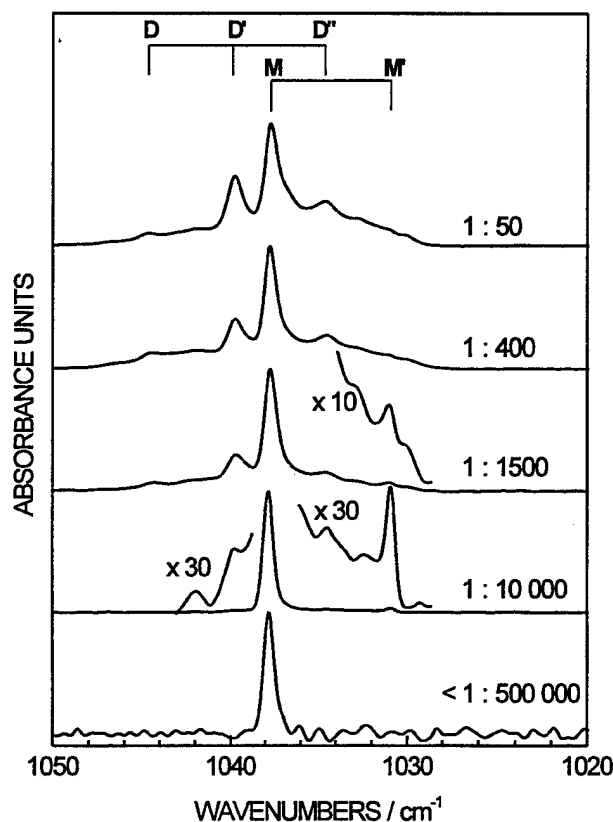pends on temperature. In order to preserve the generated features, we find that only the coldest accessible temperature, around 15 K, is suitable. The sample quality, i.e., the degree of disorder in the O_2 lattice, can be detected spectroscopically via the fundamental vibrations of O_2 host molecules in the IR [7,8]. While O_2 in the gas phase is not IR active, O_2 molecules adjacent to lattice imperfections (i.e., defect sites) experience an increased IR absorption cross section, and the intensity of these absorptions serves as a measure of the degree of uniformity in the molecular solid. We have carefully monitored the O_2 IR absorptions as an indicator of the structural quality of the crystal. Annealing to about 25 K for sufficient time (ca. 10 min.) leads to their permanent disappearance, indicating the healing properties of this annealing process. Prior to photolysis experiments of neat solid oxygen we have always performed an adequate annealing cycle to assure comparable structural quality from sample to sample.

Figure 2: Concentration dependence of the absorption features in the v_3 region of ozone. With decreasing ozone concentration (from a-e) the contribution of dimer features (labeled D, D' and D") decreases. The monomer features, M and M', remain at lower concentrations with a relative intensity of 30 : 1. The low concentration spectrum, shown in the bottom curve, is obtained after depositing neat oxygen with an ionization gauge operating in the sample chamber.

159

GENERATION AND STABILITY OF O(^{3}P) ATOMS IN OXYGEN

Our study of the wavelength-dependent formation of ozone in O_2 matrices has important implications regarding the recently reported storage of O atoms in solid oxygen [9]. Taborek and Rutledge found that condensation of oxygen gas pretreated in a discharge onto a ~ 4 K substrate results in a significant heat release upon warming. This heat release has been attributed to reaction of trapped O atoms in the cryo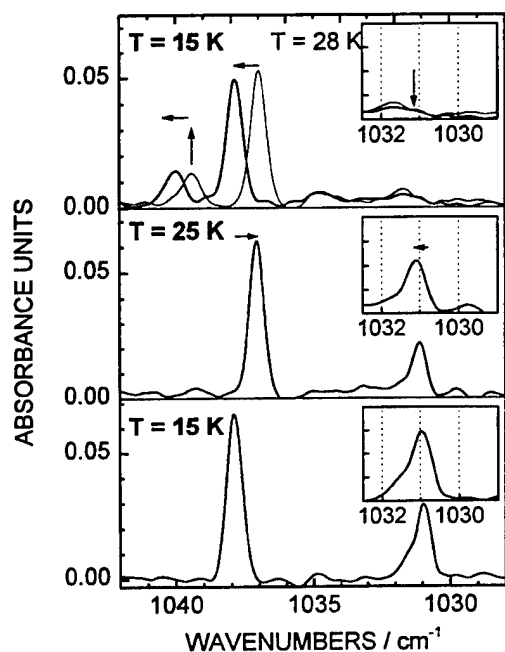genic solid. With monochromatic UV light in the 210 - 250 nm region we can generate O(^{3}P) atoms with controlled excess energies in the $0 \leq E_{exc} \leq 0.8$ eV range in a neat solid oxygen crystal. These excess energies correspond to O-atom kinetic energies in the 0 - 0.4 eV range. Right at the O_2 dissociation limit around 242 nm the O(^{3}P) fragments have little kinetic energy, and perhaps some O atoms remain stable in the solid. If this were the case, upon annealing we should observe some recombination to ozone leading to a larger O_3 IR absorption when the O atoms react.

We do not observe any measurable increase of the ozone monomer content in solid oxygen with increasing temperature for any of the photogenerated samples, i.e., those generated with light from 250 to 210 nm. The annealing sequence for a solid O_2 matrix irradiated near the dissociation limit is illustrated in Fig. 3 where the insets show an expanded region around the M' feature. The irradiated solid oxygen exhibits an IR spectrum shown in the bottom panel of Fig. 3. Heating to 25 K, which transforms the O_2 host into its hexagonal β phase [6] shows no increase in the v_3 absorption features (middle spectrum) indicating the absence of possible O(^{3}P) reactions. Only the strong red shift of M and the weak blue shift of M' is observed and indicated by the arrows. Further heating to 28 K leads to the disappearance of the M' feature accompanied by a simultaneous increase of the D' feature near 1040 cm^{-1}, while M remains unchanged in intensity. Recooling to 15 K demonstrates the irreversibility of this annealing cycle. Once formed the dimers do not dissociate without irradiation with photons. The lowest temperature our refrigerator-based cooling system can reach is 15 K, which is above the sample temperature of ~ 4 K reported by Taborek and Rutledge [9]. A possible weak barrier towards ozone formation may be already exceeded by the thermal energy of our samples thus preventing stable trapping of O atoms in the solid at 15 K. Therefore, it would be advantageous to repeat our measurements on colder samples near 4 K. Such a temperature study would eventually establish a quantitative value for the barrier of the reaction $O + O_2 \rightarrow O_3$ in the matrix.

Figure 3: Effect of annealing on the ozone absorption features in the v_3 region of a photogenerated sample. The bottom spectrum shows both monomer features M and M' after irradiation with 240 nm. This corresponds to an excess energy of ~ 20 meV for the O(^{3}P) atoms. The middle spectrum demonstrates the opposite shifts of M and M' with temperature. At 28 K, the M' feature disappears and the D' feature grows in. Recooling to 15 K demonstrates the irreversibility of this process.

OZONE STABILITY WITH TEMPERATURE

By changing the temperature of the oxygen matrix and observing the IR spectrum we can monitor processes occurring in the matrix and unravel some of the complexity surrounding the many absorption features. One temperature study concerns the assignment by Schriver-Mazzuoli *et al.* (SM) [5] of the feature at 1031 cm^{-1} to $O\cdots O_3$. Rather surprisingly, we observe the feature
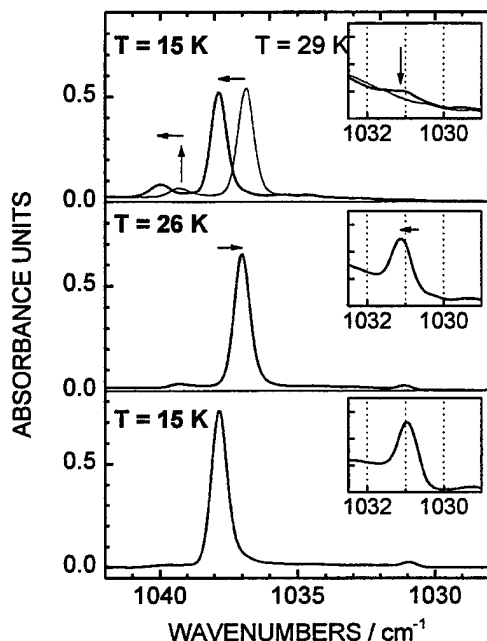

Figure 4: Effect of annealing on the ozone absorption features in the ν_3 region. The bottom spectrum shows both monomer features M and M' following deposition of an O_3/O_2 mixture (1 : 10 000). The middle spectrum demonstrates the opposite shifts of M and M' with temperature. At 29 K, the M' feature disappears and the D' feature grows in. Recooling to 15 K demonstrates the irreversibility of this process.
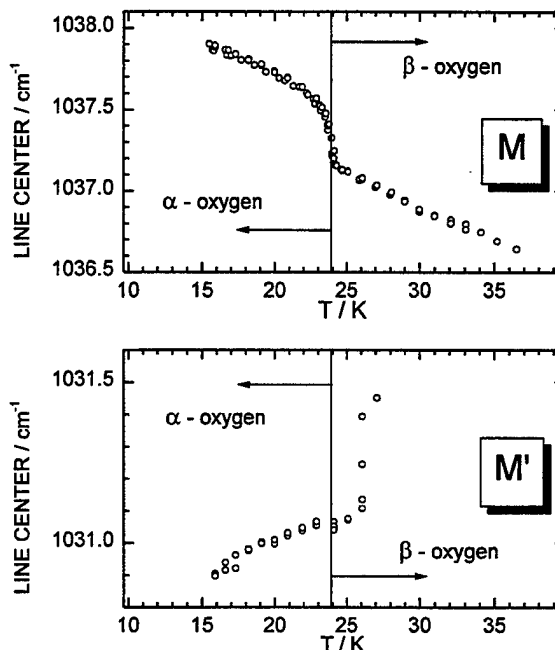
Figure 5: Temperature dependence of the line position of both ozone monomer absorptions in the ν_3 antisymmetric stretch region of O_3. The top panel shows the data for the M feature at 1037.8 cm^{-1} and the bottom panel shows the data for the M' feature at 1030.9 cm^{-1} (both values at 15 K). All data are successively taken moving from lower to higher temperature.

assigned to $O\cdots O_3$ by seeding O_3 in an O_2 matrix, even though no light source for O-atom generation is present. This observation contradicts those of SM who report the absence of the 1031 cm^{-1} feature in seeded samples. This contradiction may be due to different deposition rates or temperatures. Figure 4 shows the spectrum measured following deposition of a 1 : 10 000 mixture. The insets show the feature we call M' previously assigned to $O\cdots O_3$. The only possible source of O atoms in our system is ozone decomposition in the gas mixing chamber, especially during deposition. Since stabilization of $O\cdots O_3$ in the room temperature gas mixture has never been observed and is not expected, this complex would have to be formed during deposition. Under these conditions it seems highly unlikely that we would observe a constant intensity ratio between M and M' of 30 (as can be seen in Fig. 2) for concentrations ranging from

1 : 20 000 to 1 : 1500. Thus we conclude that O atoms do not contribute to the observed M' feature at 1031 cm^{-1}. More checks are needed to confirm that the feature in the seeded samples is identical in origin with the M' feature in the irradiated samples. In one check we examine the temperature dependence of the ozone infrared absorptions in a seeded sample (Fig. 4) and in a photogenerated sample (Fig. 3), where the latter generates the M' feature under comparable conditions to the SM study. Comparison of the thermal behavior of the 1031 cm^{-1} feature in both environments shows identical weak blue shifts with increasing temperature, a signal decrease around 25 K, and simultaneous appearance of a dimer absorption band around 1039 cm^{-1}. This identical behavior is unlikely to be accidental and we conclude that they are of the same origin. Together with the discussed absence of O atoms in the seeded samples we strongly believe that the M' feature in the photogenerated sample can not be due to O···O_3, thus we feel the identification reported by Schriver-Mazzuoli et al. [5] is in error.

We inspected the thermal induced frequency shift of the line center of the ozone features M and M', which is displayed in Fig. 5. For the M feature in the upper panel, we observe a linear slope for its red shift in the 15 - 23 K, and 25 - 30 K region. Around 24 K a steep decrease in frequency occurs, which we attribute to the α/β phase transition of solid oxygen located at 23.9 K [10]. This assignment is confirmed by investigating the temperature-dependent shift of other species we introduced into the molecular host, namely CO and N_2O, which both showed a similar drastic change at the phase transition of the otherwise moderately changing line centers. As an interesting side point, the exact position of this dramatic jump in the center postion shifts to 0.2 K lower temperature when we recool the sample from the higher temperatures where the O_2 host is in the β phase. This hysteresis in the phase transition was recently observed by heat capacity measurements of solid oxygen [10].

The M' feature exhibits a different behavior as shown in the bottom panel of Fig. 5. Its line center shift shows no pronounced change at the α/β phase transition. However, we do observe a change in its intensity, as soon as we enter the β phase. At this temperature (24 K) its intensity decreases with a rate that increases with further increasing temperature. Just below the phase transition within α oxygen (about 23.8 K) we observe no measurable decrease over a 20-h period. The decrease of the M' feature, as mentioned above, is accompanied with an increase of the D' feature. This important result implies thermal induced migration of this ozone species. Such a mobility is rather puzzling, when considering its large size relative to the lattice parameters. However, we may expect some influence of the molecular host material upon this property. Site interchanges between two adjacent O_2 molecules might stimulate an O_3 in a complex maneuver to change its lattice site as well. This would then be similar to interpretations of thermal mobility in solid Ar at elevated temperatures around 25 K, but in the case of solid O_2 this explanation remains tentative.

We observed a similar dimerization effect, though at a much slower rate, for the M species in the β phase. The dimerization rate of M increases with temperature as well, but this time we observe an increase mainly of the D dimer around 1045 cm^{-1} and the D'' feature at 1034.6 cm^{-1}. We can only heat the crystal to about 28 - 29 K. Above this temperature, the vapor pressure of solid O_2 is too large, and we observe vaporization of the solid at a similar rate to that of the dimerization of the M feature. Therefore, we cannot distinguish dimerization effects within the crystal and aggregation that occurs due to accumulation of residual O_3 on the sample surface during desorption of the host.

OZONE STABILITY WITH LIGHT

With laser irradiation, the concentration of ozone monomers and dimers in neat solid oxygen reach different limiting values at each wavelength. This wavelength-dependent maximum concentration of ozone species is caused by a dynamic equilibrium between formation and destruction. Decreasing the wavelength from 240 nm generates the D_x features with increasing concentration. The increase in dimers continues until our shortest wavelength of 210 nm. Subsequent irradiation with longer wavelength light leads to a decrease of the dimer features which is not fully compensated by the weak increase of the monomers, M and M'. We observe this phenomenon for longer wavelengths up to 308 nm. At this point we know that the longer wavelength light only dissociates the ozone and ozone dimers and does not generate O_3 species from the O_2 host. We believe that when the O_3 dimers are dissociated they can reform either a dimer or a monomer. This branching pathway results in the ultimate destruction of the dimers, while the ozone monomers upon photo-dissociation just reform monomers. We find it extremely interesting that the more unstable M' is not destroyed by photodissociation. More experiments on other samples should improve our understanding of this photodissociation process.
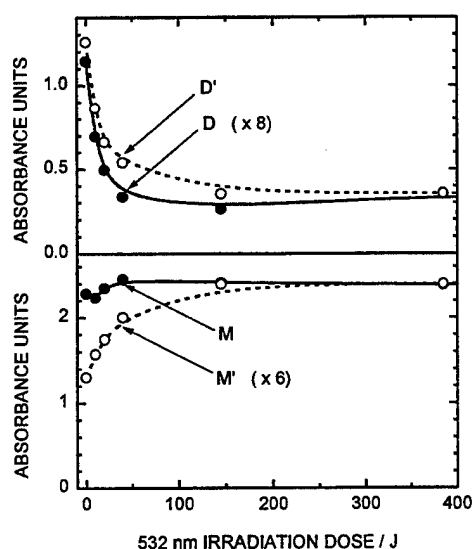
The majority of the photodissociation experiments are performed with nanosecond laser pulses, but we observe other interesting phenomena with picosecond pulsed light at 532 nm. Irradiating O_3-seeded O_2 matrices with visible 100-ps laser light, we observe the selective photodissociation of O_3 dimers into ozone monomers. Figure 6 shows the signals for the ozone monomers and dimers as a function of irradiation dose. The top panel shows the destruction of the dimers, D and D'. Both dimer signals are decreased to about 30 % of the initial values but with slightly different rates. After prolonged exposure no further destruction is observed. As shown in the bottom panel, we can enhance the concentration of the ozone monomer in the unstable site (M') about twofold. The rate of increase in that absorption seems to be correlated with a decrease in D' dimer. This D' dimer forms when M' disappears at higher temperatures in a thermally-induced change. Experiments are underway to see if this change is unique to picosecond light or would also be observed with pulses of longer duration. In the nanosecond pulsed photolysis in the UV we observe no M' increase in contrast to the picosecond experiments. Irradiation of matrices with picosecond light at 1.06 µm has resulted in severe heating of the sample due either to absorption of O_2 or to the higher intrinsic power of the laser at that wavelength. We have been able to monitor the heating via the temperature shift in the ozone absorption features.

Figure 6: Concentration of O_3 monomers and dimers in an O_3-seeded O_2 matrix (concentration 1 : 50) as a function of exposure to 532 nm picosecond light. The open circles are the M' and D' signals and the closed circles the results for M and D. The solid and dashed lines are smooth curves to guide the eye.

GENERATION AND REACTIONS OF O(^{1}D) IN OXYGEN

Photodissociation of ozone in the Hartley-continuum in the UV yields hot O(^{1}D) and O(^{3}P) atoms with a branching ratio of 0.9 to 0.1 [11]. Eventually these O atoms react with O_2 and reform ozone. We irradiate ozone-seeded O_2 matrices with 275 nm light, which only dissociates O_3, but does not interact with the host O_2 molecules. As a result, we observe no significant change of the ozone concentration with irradiation. Similar studies by SM at wavelengths greater than 360 nm and equal to 266 nm have yielded similar results.

We attempt to shed more light on this fundamental reaction involving O(^{1}D) atoms exploiting isotopic substitution. Previous experiments by SM on mixed isotopes gave less specific results [5]. Our experiment is performed on $^{16}O_3$ (shorthand 666) seeded $^{18}O_2$ (shorthand 88) matrices. Photolysis of one (666) yields a (6) atom, which can react with a cage (88) and form the isotopic (688), which we can distinguish IR spectroscopically from all the other ozone isotopes. For prolonged irradiation, we expect the isotopes containing (6) atoms to decrease to at least the numerical concentration of (6) in this seeded sample. We expect (888) to become the most abundant species. This production is what we observe in our experiments. Fig. 7 shows the dose-dependent growth curve of (888) together with the isotope (688). Interestingly, (668), and the symmetrical isotopes (686), and (868) remain a minor species throughout photolysis. We observe the decrease of (666) together with the growth of both (888) and (688). While this observation can be explained by the details of the bond breaking in ozone and reaction of the nascent atom to the terminal end of an O_2, the nearly identical initial linear growth curves of (688) and (888) remains puzzling. If at least two photons are required for (888) generation from (666), then the (888) concentration would depend on the (688) concentration. Thus, we would expect an S-shaped growth curve for (888), similar to what we observe for the M and D_x features when we photolyze a neat
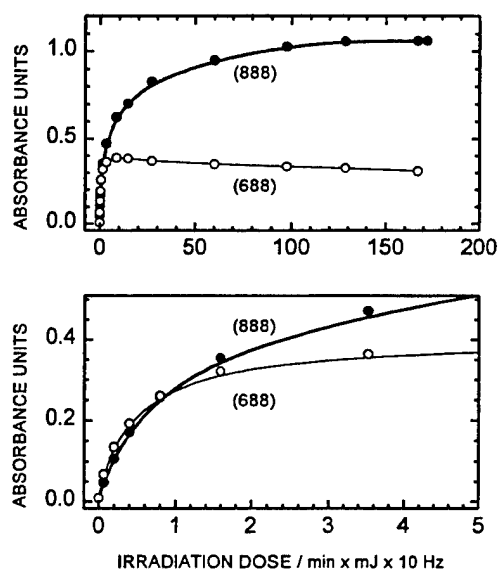

Figure 7: Growth of isotopic ozone IR absorptions (M feature) during irradiation of $^{16}O_3$ in $^{18}O_2$ (concentration 1 : 100) with laser light at 275 nm. The lower plot (enlarged region of the upper plot) shows the initial growth of $^{16}O^{18}O^{18}O$ (688) and $^{18}O_3$ (888) absorptions.

O_2 matrix with 232-nm light. The similar growth implies that the initial transient (688)* species undergoes fragmentation prior to stabilization, which may set an (8) atom free for further reaction with an (88), eventually creating (888) in this one-photon event.

This reaction sequence indicates a new process for propagating reaction energy through the O_2 lattice. Thus far, we cannot give a range for this propagation except a lower boundary of two nearest neighbor distances. More experiments to evaluate quantitative values for this sequence are needed. Similar to the case of O(^{3}P), we can exploit the broad Hartley-continuum with our tunable laser source to tune the excess energy of O(^{1}D) atoms.

164

CONCLUSIONS

These brief descriptions of an extensive list of investigations highlight some of the interesting effects we have observed during our investigations into ozone and oxygen atoms in oxygen. A detailed description of these phenomena will be presented in upcoming publications [12, 13]. These measurements impact the HEDM program on the ability to store oxygen atoms in oxygen matrices, the reactivity of $O(^3P)$ and $O(^1D)$ in O_2/O_3 mixtures, the movement of O_3 through solid samples, and the processes occurring in the oxygen phase transition. Experiments on discharge products, continuing the search for O_4, and trapping O atoms at low temperature in solid O_2 are planned for the future.

REFERENCES

[1]   R. A. Copeland, C. G. Bressler, and M. J. Dyer, in *Proc. of the HEDM Contractors Meeting, June 1996*, P. G. Carrick, N. T. Williams, eds., Air Force Material Command Report PL-TR-96-3037, p. 96 (1997).

[2]   M. J. Dyer, C. G. Bressler, and R. A. Copeland, Chem. Phys. Lett. **266**, 548 (1997).

[3]

[4]   A. J. Sedlacek and C. A. Wight, J. Phys. Chem. **93**, 509 (1988).

[5]   L. Schriver-Mazzuoli, A. de Saxcé, C. Lugez, C. Camey-Peyret, and A. Schriver, J. Chem. Phys. **102**, 690 (1995).

[6]   I. N. Krupskii, A. I. Prokhvatilov, A. Freiman, and A. I. Erenburg, Sov. J. Low Temp. Phys. **5**, 130 (1979); R. D. Etters, A. A. Helmy, and K. Kobashi, Phys. Rev. **B28**, 2166 (1983).

[7]   L. H. Jones, B. I. Swanson, S. F. Agnew, and S. A. Ekberg, J. Phys. Chem. **89**, 2982 (1985).

[8]   L. H. Jones, S. F. Agnew, B. I. Swanson, and S. A. Ekberg, J. Chem. Phys. **85**, 428 (1986).

[9]   P. Taborek and J. E. Rutledge, in *AFOSR High Energy Density Matter Contractor's Review*, 1 - 3 June, 1997.

[10]   L. Lipinski, A. Szmyrka-Grzebyk, and H. Manuszkiewicz, Cryogenics **36**, 921 (1996).

[11]   R. P. Wayne, *Chemistry of Atmospheres*, Oxford University Press, p. 84 (1985).

[12]   C. G. Bressler, M. J. Dyer, and R. A. Copeland, "Photochemical Studies of Ozone in Oxygen Matrices", in preparation (1997).

[13]   C. G. Bressler, and R. A. Copeland, "Temperature Effects on the Spectral Line Positions and Stability of Ozone Monomers and Dimers in Oxygen Matrices", in preparation (1997).

ADVANCED CRYOGENIC SOLID HYBRID ROCKET ENGINE DEVELOPMENTS FOR HEDM AND NON-HEDM DEMONSTRATIONS

Eric E. Rice, William H. Knuth, Christopher P. St.Clair,
and Daniel J. Gramer
Orbital Technologies Corporation (ORBITEC™)
Space Center, 1212 Fourier Drive
Madison, WI 53717
(608) 827-5000

Abstract

ORBITEC has conducted considerable R&D under various USAF and NASA contracts and company sponsored efforts to develop a new class of rocket propulsion devices. These advanced cryogenic solid hybrid rocket engines can be used in the future to both demonstrate the performance improvements provided by HEDMs and also demonstrate improved performance over conventional space propulsion systems. ORBITEC has been designing, developing and testing cryogenic solid hybrid rocket engines including the following propellant combinations: (1) solid oxygen/gaseous hydrogen; (2) solid hydrogen/gaseous oxygen; (3) solid methane/gaseous oxygen; and (4) solid methane-aluminum/gaseous oxygen. Work achieved to date includes: (1) a total of 90 solid cryogen test firings; (2) establishment of regression rate data for the different propellant combinations, where the rates can be a factor of 20 to 40 times higher than conventional HTPB-based hybrids; (3) achievement of burn durations from 1 to 15 seconds for no O/F ratio control and up to 30 seconds for O/F ratio control; (4) engine chamber pressures as high as 200 psi; and (5) results showing that both the unmetallized and metallized solid cryogenic hybrids obey the classical hybrid regression law, but with different constants and exponents reflecting the much higher regression rates. The potential applications include: research devices to test high-energy density matter (HEDM); hybrid rocket launch vehicle (LV); space-based propulsion; military high-thrust special weapons; high-thrust, high-performance sounding rocket applications; solid cryogen storage systems on ground-based vehicles; and technology that can contribute to the development of new freezer research tools. During a current sponsored USAF/PL project, ORBITEC is to design, develop and test a larger, SOX/LH$_2$ flight-type engine that will have throttling and O/F ratio control.

Overview

Orbital Technologies Corporation (ORBITEC™) first proposed cryogenic solid hybrid rocket engine applications to the USAF/PL under SBIR Program in 1991-1992 to support the HEDM Program. ORBITEC has had eight contracts in this technology area under USAF/PL and NASA funding. The key thrust area has been to conduct cryogenic solid oxidizer and fuel formation research, supporting analysis, and designing, developing, testing, and demonstrating engines in support of hybrid rocket engine developments for HEDM and non-HEDM propulsion applications. Solid cryogens have included: oxygen, hydrogen, and methane. ORBITEC has successfully first fired the following solid cryogen systems on the dates indicated below:

SOX/GH$_2$ Hybrid Rocket – August 21, 1995
SCH$_4$/GO$_2$ Hybrid Rocket – October 10, 1995
SH$_2$/GO$_2$ Hybrid Rocket – October 25, 1996
SCH$_4$-AL/GO$_2$ Hybrid Rocket – November 9, 1996.

Mark-II Engine and Supporting Hardware

The basic design approach for the cryogenic solid hybrid engines is depicted in Figure 1. The engine is encased in a vacuum chamber to allow the radiation shield (not shown) to function. A coolant (LHe or LN$_2$) fills the outer engine dewar. It is designed to allow cooling where the propellant is desired on the inner volume. The solid cryogen is admitted below the triple point pressure of the freezing cryogen. When the engine is ready to fire, the inner chamber is exposed to an atmospheric GHe purge and then an ignitor flame. The gaseous component of the propellant combination is then injected at the top of the grain. The firing begins and the grain is depleted over time, producing a hot gas emission/thrust. Figure 2 shows the side view

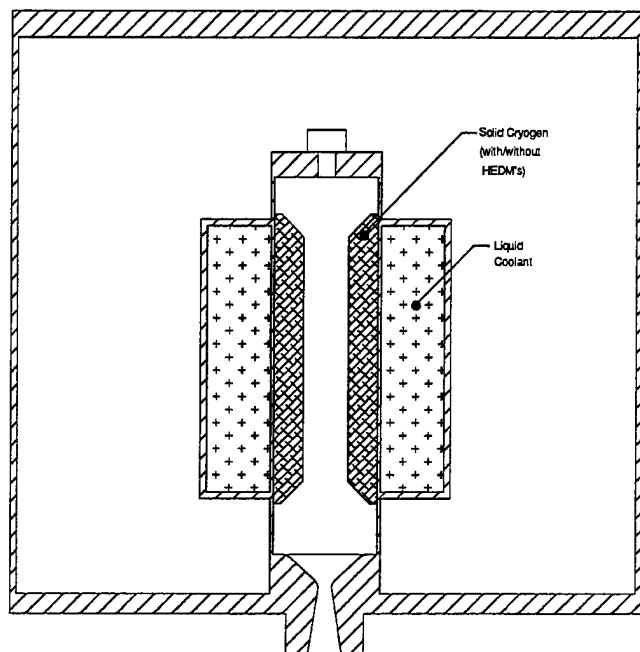of the Mark-II system located in ORBITEC's test facility.
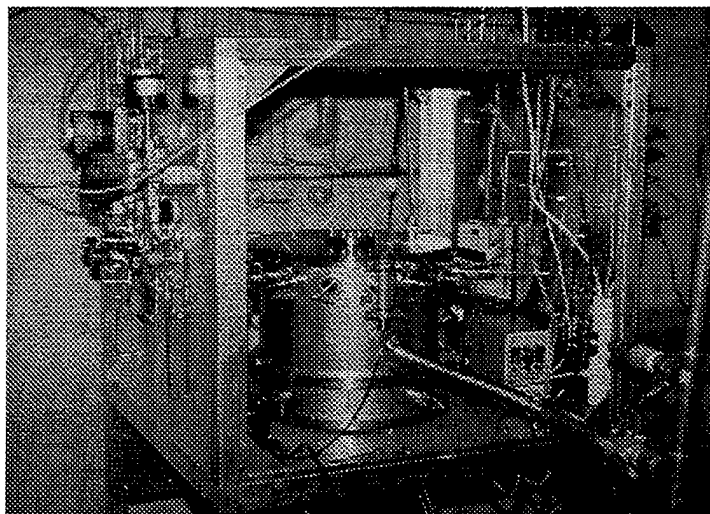

Figure 1. Engine Concept Design Sketch

Figure 2. ORBITEC's Mark-II Cryogenic Hybrid Engine

Summary of SOX/GH₂ Firings in Prototype and Mark -I Engine

A summary of the SOX/GH₂ firings in the Prototype and Mark-I engine is shown in Figure 3. Information is provided on grain mass, gaseous hydrogen mass flow, the maximum combustion chamber pressure achieved, the test duration, and the average O/F ratio for each of the test firings.

Firing #	Date	O_2 Mass (g)	N_2 Mass (g)	H_2 Source Pressure (psi)	H_2 Mass Flow (g/s)	Maximum Chamber Pressure (psia)	Burn Duration (sec)	Notes	Average O/F Ratio
1	17 Aug 95	30	50	125	--	--	--	Ignition failure, no burn.	--
2	21 Aug 95	30	50	125	0.40	48	2	First successful burn.	46
3	23 Aug 95	60	50	125	0.40	61	4	Successful burn.	41
4	29 Aug 95	90	50	125	0.40	73	7	Successful burn.	34
5 a	6 Sep 95	60	50	175	--	--	--	Ignition failure. No burn.	--
5 b	6 Sep 95	60	50	175	--	--	--	Ignition failure. No burn.	--
6	7 Sep 95	60	50	175	0.54	82	4	Successful burn.	28
7	13 Sep 95	60	50	350	1.03	135	5	Hard start, successful burn.	11
8	14 Sep 95	150	50	350	1.03	159	7	Successful burn.	20
9	15 Sep 95	90	10	500	1.46	199	4	Successful burn.	15
10	21 Sep 95	250	10	500	1.46	194	8	Successful burn.	21
11	8 Apr 96	27	10	300	0.85	119	1	Warm grain, brief burn.	19
12	11 Apr 96	60	50	175	--	--	--	Ignition failure, no burn.	--
13	15 Apr 96	26	50	175	0.52	54	1	Warm grain, brief burn.	42
PL-1	14 May 96	150	10	350	0.98	187	6	Successful burn.	24

Figure 3. Summary of SOX/GH₂ Firings in the Prototype and Mark-I Engine

Selected pressure plots for the firings given in Figure 3 are given in Figure 4. Test Firing #10 is worthy of note as the largest solid oxygen test firing performed to date.
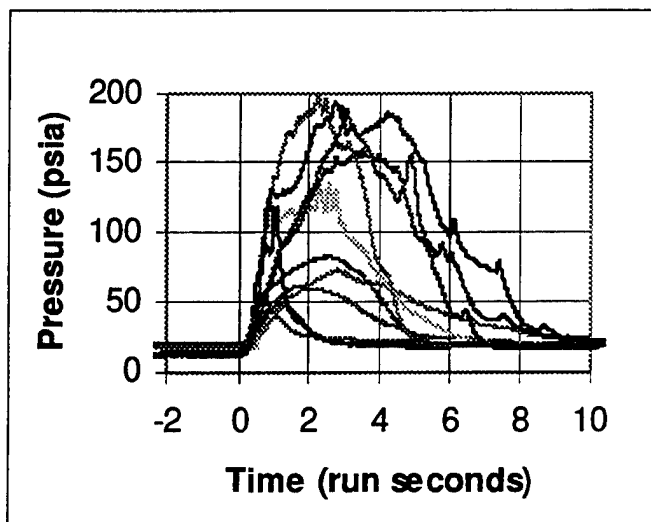
Figure 4. Summary of Pressure Traces for SOX/GH₂ Firings in the Prototype and Mark-I Engine

SOX/GH₂ Firings with O/F Control Measures

A summary of the SOX/GH₂ firings in the Mark-II engine with O/F control measures is shown in Figure 5. Figure 6 presents pressure traces for the same test firings. Note that the final test firing (#12) is not well represented in Figure 6 due to its extremely long duration.

Three different concepts for O/F ratio control have been tested. They are designated A, B, and C in Figure 5. All three approaches proved to be successful in reducing the O/F ratio. One concept in particular (B) is quite promising, and further testing is being conducted by ORBITEC to better characterize regression of solid oxygen using this technique.

Firing #	Date	O_2 Mass g	N_2 Mass g	Set-up Notes	H_2 Mass Flow g/s	Nozzle Dia. cm (in)	Max Steady Chamber Pressure N/cm^2(psia)	Burn Duration sec	Notes	Average O/F Ratio
1	3 Feb 97	50	2	A	1.2	0.69(0.27)	76 (110)	4.7	Hard start, successful burn.	8.9
2	4 Feb 97	50	2	A	1.2	0.69(0.27)	76 (110)	3.0	Hard start, successful burn.	14.1
3	5 Feb 97	50	2	A	2.1	0.69(0.27)	110 (160)	3.9	Hard start, successful burn.	6.1
4	10 Feb 97	50	2	B	1.6	0.69(0.27)	97 (140)	2.6	Hard start, successful burn.	12.3
5	11 Feb 97	100	2	B	2.4	0.69(0.27)	--	--	Very hard start, shut down.	--
6	13 Feb 97	50	2	B	1.6	0.69(0.27)	90 (130)	3.3	Successful burn.	9.6
7	14 Feb 97	50	2	B	2.6	0.69(0.27)	--	--	Ignition failure.	--
8	17 Feb 97	50	2	B	2.6	0.69(0.27)	140 (200)	2.5	Successful burn.	7.6
9	20 Feb 97	50	2	B	4.2	1.1(0.44)	48 (70)	2.7	Successful burn.	4.4
10	21 Feb 97	150	2	B	4.2	1.1(0.44)	76 (110)	5.7	Successful burn.	6.3
11	26 Feb 97	50	2	C	1.2	0.69(0.27)	17 (25)	--*	Successful but incomplete.	< 6
12	3 Mar 97	50	2	C	0.9	0.43(0.17)	59 (85)	16*	Successful but incomplete.	< 3

Figure 5. Summary of SOX/GH₂ Firings in Mark-II Engine with O/F Control Measures
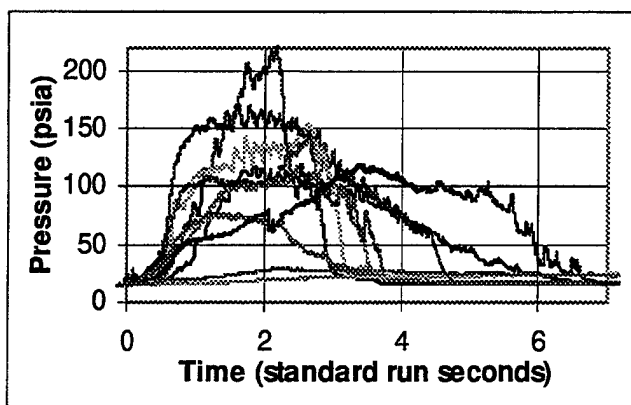
Figure 6. *Summary of Pressure Traces for SOX/GH₂ Firings in Mark-II Engine with O/F Control Measures*

Summary of SCH₄/GO₂ Firings in Prototype and Mark -I Engine

A summary of the SCH₄/GO₂ firings in the Mark II engine is shown in Figure 7. Figure 8 presents selected pressure traces for these firings. In general, solid methane exhibits more predictable and steadier burning behavior than oxygen.

Firing #	Date	CH₄ Mass (g)	O₂ Flow Rate (g/s)	Max Steady Chamber Pressure (psia)	Burn Duration (sec)	O/F Ratio	Notes
4	10 Oct 95	40	1.1	25	1	–	Brief burn, quenched.
5	10 Oct 95	58	2.0	29	1	–	Brief burn, quenched.
6	16 Oct 95	40	0.6	22	1	–	Brief burn, quenched.
7	18 Oct 95	40	2.0	26	1	–	Brief burn, quenched (LHe).
8	19 Oct 95	40	2.0 (s)	34	5	0.24	Successful burn (LHe).
9	19 Oct 95	100	2.4 (s)	41	15	0.37	Successful burn (LHe).
10	3 Nov 95	60	2.4 (s)	47	8	0.31	Successful burn.
11	9 Sept 96	60	3.6 (s)	52	7	0.42	Successful burn. *
15	13 Sept 96	60	7.2 (s)	98	4	0.50	Successful burn. *
16	16 Sept 96	60	7.2 (s)	101	4	0.53	Successful burn. *
22	3 Oct 96	80	3.6 (s)	59	8	0.40	Successful burn. *
30	16 Oct 96	60	7.2	101	5	0.67	Successful burn. *
31	16 Oct 96	80	7.2	102	7	0.64	Successful burn. *
32	17 Oct 96	60	14.9	185	4	–	Oxygen feed problem.
36	21 Oct 96	60	14.9	191	4	–	Oxygen feed problem.
37	21 Oct 96	60	14.9	200	4	1.1	Successful burn. *
38	22 Oct 96	80	14.9	198	5	0.98	Successful burn. *
39	22 Oct 96	100	7.2	108	9	0.63	Successful burn. *
40	23 Oct 96	100	3.6	55	13	0.50	Successful burn. *
42	25 Oct 96	80	7.2	92	11+	>0.98	Successful burn (LHe). *
44	29 Oct 96	100	14.9	203	5	0.93	Successful burn. *
45	31 Oct 96	100	21	98	3	0.58	Successful burn. *
46	4 Nov 96	100	28	125	2	0.71	Successful burn. *
48	6 Nov 96	100	35	157	3	1.1	Successful burn. *

Figure 7. *Summary of SCH₄/GO₂ Firings in Mark-II Engine*

169
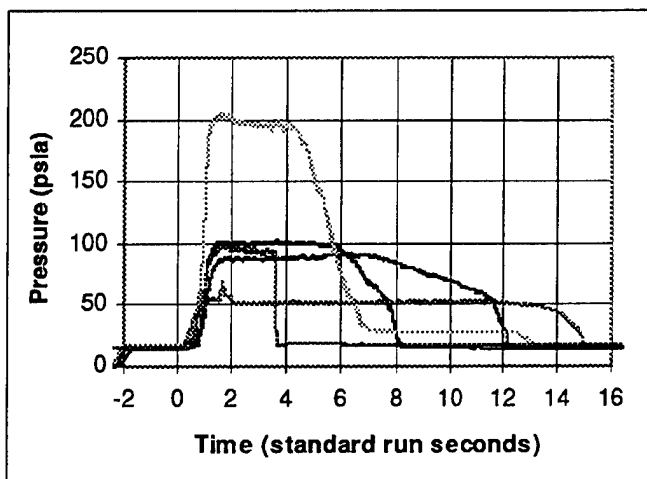
Figure 8. *Pressure Traces for Selected SCH₄/GO₂ Firings in Mark-II Engine with O/F Control Measures (Test Firings #31, 40, 42, 44, 45)*

Summary of SCH₄-Al/GO₂ Firings in Prototype and Mark -I Engine

A summary of the SCH₄-Al/GH₂ firings in the Mark II engine is shown in Figure 9. Figure 10 presents selected pressure traces for these firings. Aluminum wool grains were successfully burned at aluminum loading percentages as high as 30%. Combustion efficiency levels above 95% were obtained with aluminum loading percentages as high as 15%.

Firing #	Date	CH₄ Mass (g)	O₂ Flow Rate (g/s)	Max Steady Chamber Pressure (psia)	Burn Duration (sec)	O/F Ratio	Notes
51	8 Nov 96	100 (15%w)	7.2	94	14+	>0.84	Temperature shutdown.
52	11 Nov 96	100 (15%w)	14.4	240	6+	>0.70	Pressure shutdown.
54	13 Nov 96	100 (15%w)	21	86	9+	>1.6	Temperature shutdown.
55	14 Nov 96	100 (15%w)	21 (s)	105	6	1.17	Successful burn.
56	15 Nov 96	100 (15%w)	35 (s)	220	4	1.2	Successful burn; blowout.
57	27 Nov 96	120	21	105	2	0.35	Successful burn.
58	2 Dec 96	120 (15%w)	14 (s)	205	8	0.91	Successful burn.
59	3 Dec 96	72 (15%w)	21	110	9	2.2	Successful burn.
60	4 Dec 96	72 (15%w)	35	160	3	1.6	Successful burn.
62	6 Dec 96	72 (7.5%w)	35	150	3	1.9	Successful burn.
63	9 Dec 96	72 (30%w)	35	145	5+	>1.6	Temperature shutdown.

Figure 9. *Summary of SCH₄-Al/GO₂ Firings in Mark-II Engine*

Considerable insight into the burning behavior of SCH₄ and SCH₄-Al may be gained by comparing groups of test firings which are identical except for one variable. A series of six charts which compare such groups of firings follows. Figure 11 presents three pressure traces in which the grain size was varied and all other parameters were held constant. Observe the nearly identical pressure trace in the early part of the firing, and the manner in which each pressure trace successively drops down from the plateau as the firing proceeds, starting with the smaller grains. The abrupt

drop in pressure from the plateau region is attributed to one end of the grain burning back to the chamber wall. The grain length then decreases for the remainder of the test firing.

Figure 12 illustrates the effect of increasing oxygen mass flow rate for 100 g SCH₄ grains. As expected, the chamber pressure increases with the oxygen mass flow rate; the relation is nearly linear. Test firing duration decreases with increasing oxygen flow.

170
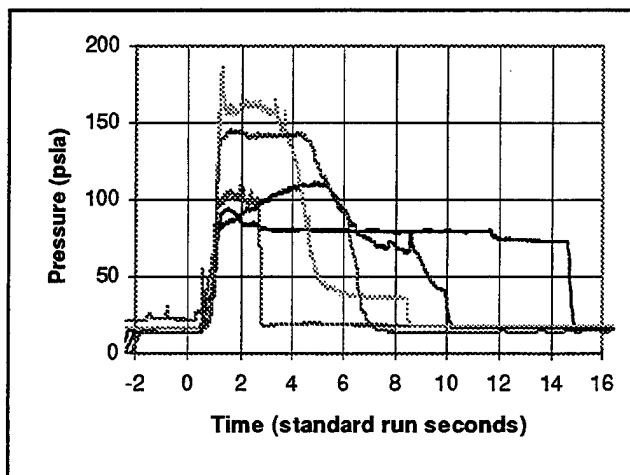
Figure 10. Pressure Traces for Selected SCH₄-Al/GO₂ Firings in Mark-II Engine (Test Firings #51, 57, 59, 60, 63)
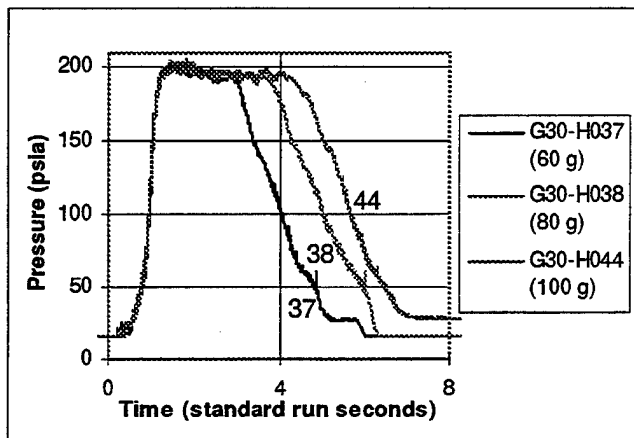
Figure 11. Effect of Grain Mass on Pressure Profile, SCH₄/GO₂
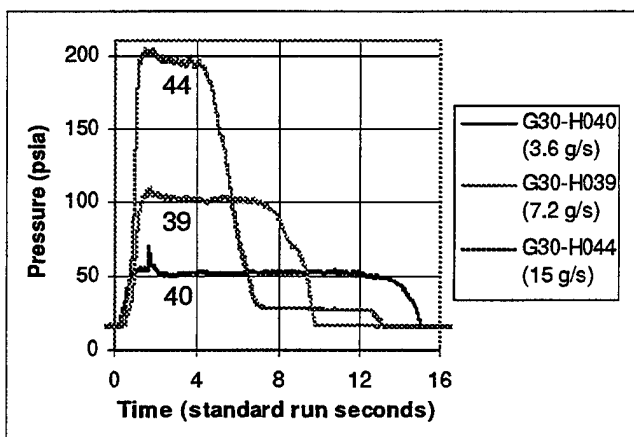
Figure 12. Effect of Oxygen Flow Rate on Pressure Profile, SCH₄/GO₂

Figure 13 shows the effect of loading aluminum wool into the methane grain. The pressure in the firing with the aluminized grain is substantially lower and the duration is longer, indicating a lower regression rate as a result of the aluminum. The aluminum wool test firing was terminated early as the result of excessive engine temperatures; inspection of the remaining aluminum wool suggested that the firing was only 55% complete at the time of shutdown.
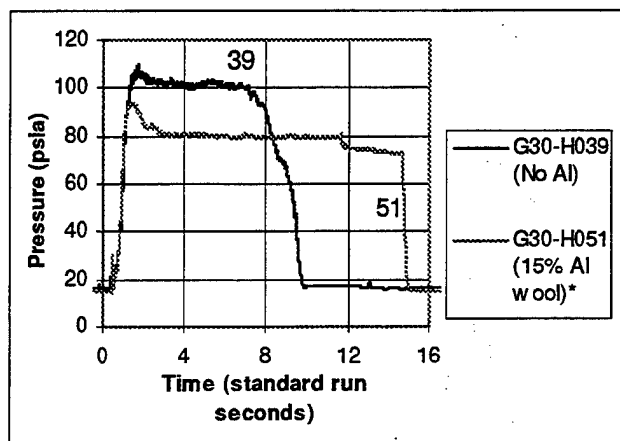
Figure 13. Effect of Aluminum Wool on Pressure Profile, SCH₄/GO₂ & SCH₄-Al/GO₂

Figure 14 shows the effect of aluminum wool loading density. Test firings were conducted with 7.5%, 15%, and 30% aluminum loadings, by mass. The 7.5% and 15% cases show similar durations, but the 15% case has a higher plateau pressure. The 30% case shows a pressure similar to the 7.5% case, but has a substantially longer duration. The 30% test firing was terminated early due to a temperature shutdown; at the end of the test, the Al wool was 90% consumed.
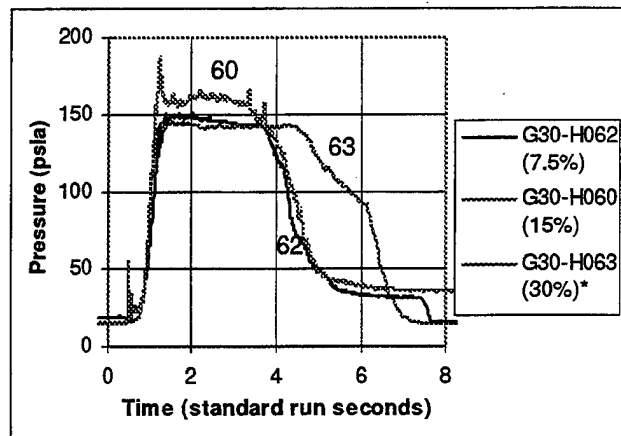
Figure 14. Effect of Aluminum Loading Percentage on Pressure Profile, SCH₄-Al/GO₂

Figure 15 shows pressure traces from two test firings with different injector types, a single-hole injector and a showerhead injector. The single-hole injector test firing has a slightly longer duration and a smoother burn. The showerhead injector has a less even burn and an abrupt end. Experience with the two injectors indicated that the singlet injector tended to burn away the bottom of the grain first, and the showerhead tended to burn away the top of the grain first.
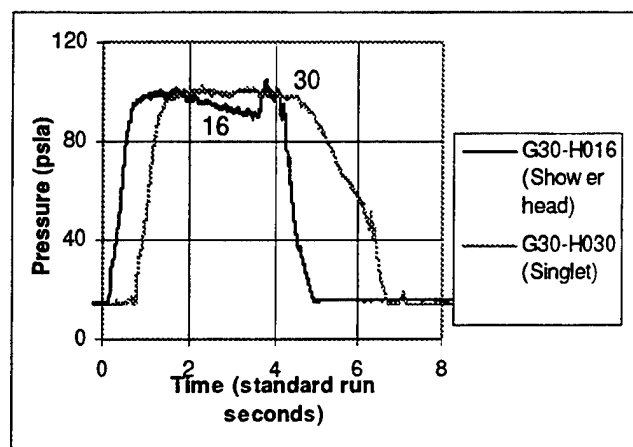
Figure 15. Effect of Injector Type on Pressure Profile, SCH₄/GO₂

Figure 16 shows the effect of initial grain temperature on the pressure profile. In Test Firing #31, the grain was frozen using liquid nitrogen (the standard coolant) and had an initial temperature of around 80 K. In Test Firing #42, the grain was frozen using liquid helium and had an initial temperature of approximately 10 K. The cooler grain resulted in lower chamber pressures and a nearly 50% extension of the burn duration.
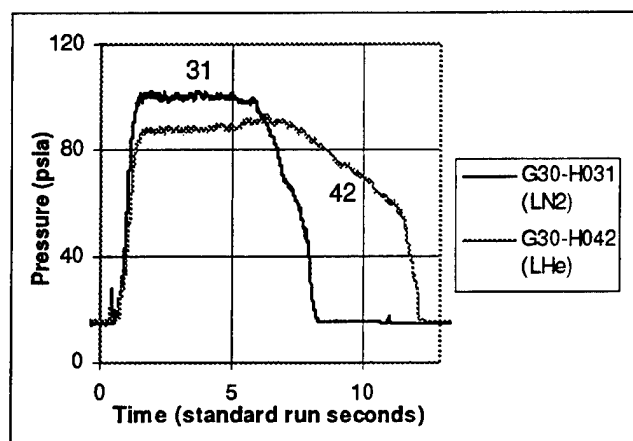
Figure 16. Effect of Initial Grain Temperature on Pressure Profile, SCH₄/GO₂

Summary of SH₂/GO₂ Firings in Prototype and Mark -I Engine

One solid hydrogen/gaseous oxygen test firing has been performed by ORBITEC in the Mark-II engine. It was performed on October 25, 1996, with a grain mass of 6 g, a duration of 3 seconds, and a gaseous oxygen flow rate of 3.5 g/sec. The maximum steady pressure obtained was 60 psia. Figure 17 presents the pressure trace for this test firing.
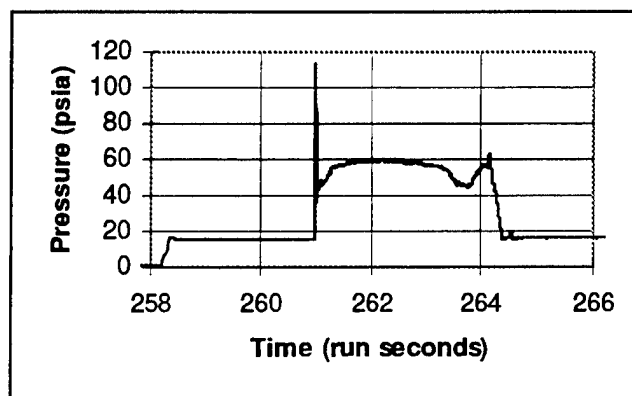
Figure 17. Pressure Trace for SH₂/GO₂ Firing in Mark-II Engine

Regression Rate Summary

The regression characteristics for ORBITEC's cryogenic hybrids are summarized in Figure 18. The vertical axis represents the average regression rate and the horizontal axis is the average oxygen mass flux or, in the case of the solid oxygen hybrids, the average hydrogen flux. Over 35 firings have been conducted including propellant combinations of SOX/GH₂, SCH₄/GO₂, SCH₄-Al/GO₂, and SH₂/GO₂.

As the graph shows, the most striking trait of these hybrids is that they regress more than an order of magnitude faster than conventional hybrids (HTPB) for a given port mass flux while still obeying the classical hybrid regression law. These high regression rates reduce the need for complex grain designs and provide increased mass fractions due to the smaller required initial port area. This result coupled with the high combustion performance of these propellants may allow substantial increases in overall hybrid engine efficiencies.

The first tests conducted were the solid oxygen, gaseous hydrogen firings which were all extremely

172

oxygen rich throughout the entire burn. Much of the work since then has focused on developing reliable methods for slowing down the regression rates such as the A - Control and B - Control methods shown in the plot. While the A - Method actually increased the regression rate, derivatives of the original concept still hold promise and are currently being pursued in a Phase II SBIR contract. Method B did succeed in slowing down the regression rates by up to 50%, but resulted in somewhat non-uniform burning of the grain. Control method C, not displayed on the plot, greatly slowed down the regression rates; however, we were not able to calculate a quantitative description of the results.
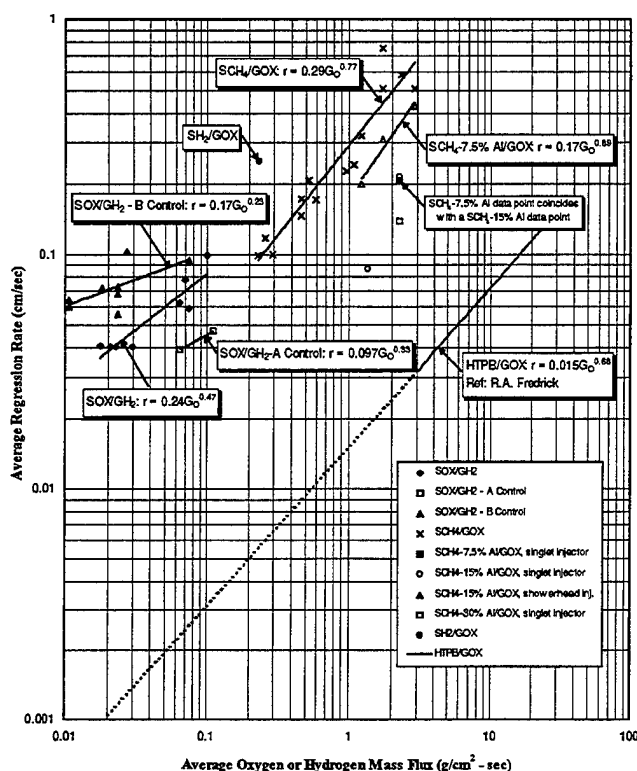
Figure 18. *Regression Rate Summary for ORBITEC's Solid Cryogen Hybrid Test Firings*

The one solid hydrogen, gaseous oxygen firing resulted in an extremely fuel rich burn. As can be seen in the plot, solid hydrogen regresses the fastest for a given port flux.

The solid methane, gaseous oxygen firings shown in the plot obey the hybrid regression law quite well and have flux exponents similar to those obtained for HTPB/GO$_2$. These firings also resulted in fuel rich

burns as well. This problem was solved by adding up to 30% aluminum by weight to the grains. This greatly reduced the regression rate and is some cases resulted in stoichiometric and even oxygen rich firings. In addition to providing an avenue for controlling the regression rate, burning the high energy Al also enhanced the engine's performance. It was also found that the regression characteristics of the aluminized grains are strongly affected by the geometry of the injector.

Current R&D Activity

ORBITEC's currently sponsored R&D in this area is by the USAF/PL under contract F04611-97-C-0020, titled "Advanced Cryogenic Rocket Engine for Testing High-Energy Propellants". We are currently in design of systems and approaches to control regression rates to optimize engine performance (O/F ratio and C*) . The Mark-II engine firings are on-going with SOX/GH$_2$ to prove best combustion control approaches. Our goal is to design, develop, test and demonstrate a flight-weight type system that uses LH$_2$ for the SOX freeze coolant and also as the fuel in the engine. The use of ozone is also being integrated into the design approach. We are working with Rocketdyne and Boeing to help assess our current and future systems applications.

Summary of Findings

This section provides a top-level summary and conclusions of our work.

- From cylindrical freezing tests, the SOX grain was shown to obtain a temperature of 7 to 10 K on a continued ~10 min of cooling with LHe.

- Through observation, it was noted that there is approximately a 45° bevel at the ends of the grain.

- Experience showed that approximately one liter of LHe will produce about one gram of solid oxygen and/or solid nitrogen in the engine or freezer configuration.

- ORBITEC successfully fired the first SOX/GH$_2$ hybrid rocket at Badger Army Ammunitions Plant (BAAP) on August 21, 1995, and conducted 14 SOX/GH$_2$ firing attempts, 10 of which were successful.

- Surface area appears to be the driving factor to the shape of the chamber pressure curve.

- Because of the high rate of SOX melting, O/F ratios remain high and seem to improve (decrease) with increased hydrogen flow rate.

173

- Solid methane (SCH$_4$) was easily formed in the freezer and engine hardware developed in this project using LN$_2$ at 77 K and LHe at 4.2 K. Grains as large as 140 g were achieved.

- Methane gas frozen using LN$_2$ is transparent; methane gas frozen using LHe is opaque and white in appearance, apparently due to microcracks.

- Methane gas will easily freeze into both aluminum wool (as high as 30% loading by mass) and aluminum foam without any voids being apparent, creating a uniform cryogen/metal grain.

- The freezing rate of methane in aluminum wool is very similar to that of pure methane. This indicates that the wool does not contribute much to the grain's overall thermal conductivity and heat flow to the wall of the freezing surface.

- The freezing rate of methane with aluminum foam in contact with the freezer wall effectively doubles. This indicates that there would be high heat transfer into the grain from the combustion process.

- Experience showed that approximately one liter of LN$_2$ would produce about one gram g of SCH$_4$.

- LHe-cooled grains (10 K), when burned, exhibit lower regression rates than LN$_2$-cooled grains (80 K).

- Aluminizing the methane grains substantially increased the combustion performance in terms of C*, exhibiting a peak in performance at 15% aluminum by mass.

- The CH$_4$/GOX and CH$_4$-Al/GOX exhibited high combustion (C*) efficiencies.

- Most of the CH$_4$/GOX and CH$_4$-Al/GOX hybrid firings had smooth, relatively flat chamber pressure traces.

- The regression rate, and consequently the O/F ratio, of the grains was strongly dependent upon the amount of aluminum and the geometry of the injector. The aluminum wool appeared to reduce the regression rate due to the fact that radiation could not penetrate the grain as it does in the pure methane grains.

- The initial temperature of a hybrid grain has a large effect on its regression rate, with lower temperatures giving rise to lower regression rates (more heat required to melt).

- Because of the high regression rate of SCH$_4$ grains, O/F ratios remain low but improve (increase) with increased flow rate of GOX and amount of Al present.

- There appears to be no limit to the possible use of this technology as applied to small (ACS), orbit transfer vehicles, high-thrust military ABMs, boosters, and single-stage-to-orbit vehicles.

- Booster concepts that look promising include: staged combustion topping cycle, pump-fed expander cycle, and pump-fed preburner cycle. Pressure-fed designs can also be used.

- The hybrid developed here should provide the hardware needed to evaluate high energy density matter (HEDM) additives to a variety of frozen matrix candidates.

- All three new approaches were successful in reducing the O/F ratio of the test firings for a given amount of hydrogen flow, thus extending burn duration times.

Acknowledgments

David Fordham and Jack Coyle, U.S. Army Badger Army Ammunitions Plant

Bibliography

Rice, E.E., Kohles, D.R., Knuth, W.H., Kellicut, A.J., and Richter, R.C., "Metallized Cryogen for Advanced Hybrid Engines", NASA Contract NASW-4789, OTC-G017-FR-93-1, Orbital Technologies Corporation, Madison, WI, August 1993.

Rice, E.E., Knuth, W.H., Kohles, D.R., Rothbauer, W.J., Heinen, G.W., St. Clair, C.P., Vermaak, A.G., "Cryogenic Hydrogen/Oxygen Solid Propellant Rocket Motor", OTC-G033-FR-95-1, NASA/LeRC Contract NAS3-27503, Orbital Technologies Corporation, Madison, WI, June 14, 1995.

Rice, E.E., St. Clair, C.P., Knuth, W.H., Gramer, D.J., Rothbauer, W.J., Van Roo, J.D., and Vermaak, A.G., "High-Energy Density Cryogenic Monopropellant Phase I SBIR Final Report", NASA/MSFC Contract NAS8-40678, OTC-G049-FR-96-1, Orbital Technologies Corporation, Madison, WI, July 10, 1996.

Rice, E.E., Gramer, D.J., St. Clair, C.P., Knuth, W.H., Bemowski, P.A., and Hermes, P.A., "Metallized Cryogen for Advanced Hybrid Engines", OTC-G030-FR-96-1, NASA/LeRC Contract NAS3-27382, Orbital Technologies Corporation, Madison, WI, December 1996.

Rice, E.E., Knuth, W.H., St. Clair, C.P., Gramer, D.J., Bemowski, P.A., Rothbauer, W.J., "Advanced Cryogenic Hybrid Rocket Engine for Testing High-Energy Propellants Phase I SBIR Final Technical Report", AF Contract F04611-96-C-0034, Orbital Technologies Corporation, Madison, WI, May 1997.

THE NEW BICYCLIC NITROGEN TETROXIDE CATION, NO4+ HAS A LOW DECOMPOSITION ENERGY.[*]

Anatoli A. Korkin[i], Rodney J. Bartlett[i] Marcel Nooijen[i] and Karl O. Christe[ii]

[i]*Quantum Theory Project, University of Florida, Gainesville, Fl 32611-843,*
[ii]*Phillips Laboratory, Edwards AFB, CA 93524-7680*

Nitrogen oxide cations, such as NO_2^+ and NO^+, are strong oxidizers and useful components for ionic High Energy Density Materials (HEDM) [1]. Their energy content and oxidizing power increase with increasing oxidation state of the nitrogen atom and the number of oxygen ligands. In our search for related, halogen-free, highly energetic cations we have become interested in the bicyclic NO_4^+ (I).

In view of the great challenge and the time consuming efforts which the synthesis of NO_4^+ would present, and the potential for low energy decomposition pathways, it was imperative to first pursue a feasibility study using *ab initio* methods. This contribution of theory offers the synthetic chemist the benefits of avoiding the unsuccessful pursuit of target molecules which are either vibrationally unstable or possess very low barriers towards decomposition, and provides guidance for their synthetic efforts.

The gas phase heat of formation of NO_4^+ (370 kcal/mol) has been estimated at the CCSD(T)/TZ2P level from the experimentally known heat of formation of NO_2^+ (233 kcal/mol) and the heat of the reaction:

$$NO_4^+ \quad \rightarrow \quad NO_2^+ \quad + O_2\,(^3\Sigma_g^-) \quad \Delta E = 137 \text{ kcal/mol} \qquad (1)$$
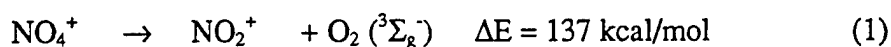
Although the minimum D_{2d} structure of **I** has short NO distances and long OO distances and is vibrationally stable at the HF, MBPT(2) and CCSD levels of theory (see Table 1), the decomposition barrier was suspected to be low because of the high exothermicity of reaction 1 (Scheme 1). The minimum energy C_{2v} path is a symmetry and spin (singlet-triplet) forbidden reaction. To model the transition barrier structure we searched for its TS and the minima at the lowest PES crossings by using the novel STEOM-CCSD method. An algorithm, which allows to locate intersystem crossing

minima efficiently, has been implemented into the ACES II program recently. It is based on minimization of the functional, $F = E_1 + E_2 + \alpha * (E_1 - E_2)$, where α is an adjustable penalty parameter (usually about 10^3).

The transition state, which has been found at the $^1A_1$ potential energy surface, and two intersystem crossing minima, singlet-singlet and singlet-triplet, have similar structures and close energies (see Table 2). The wave function has an essential multi-configurational character in the transition state and in other computed low lying excited states (Scheme 2).

The estimated decomposition barrier has been finally computed by using CASPT2, STEOM-CCSD [2], and CCSD(T) methods with extended basis sets at the STEOM-CCSD/DZP optimized geometries. All approaches show the decomposition barrier to be too low (10-20 kcal/mol) for this cation to have any reasonable stability. In addition NO_4^+ has a high vertical electron affinity (8.4 eV compared to 4.5 eV in NH_4^+), which would be another reason for a high instability of the cation.
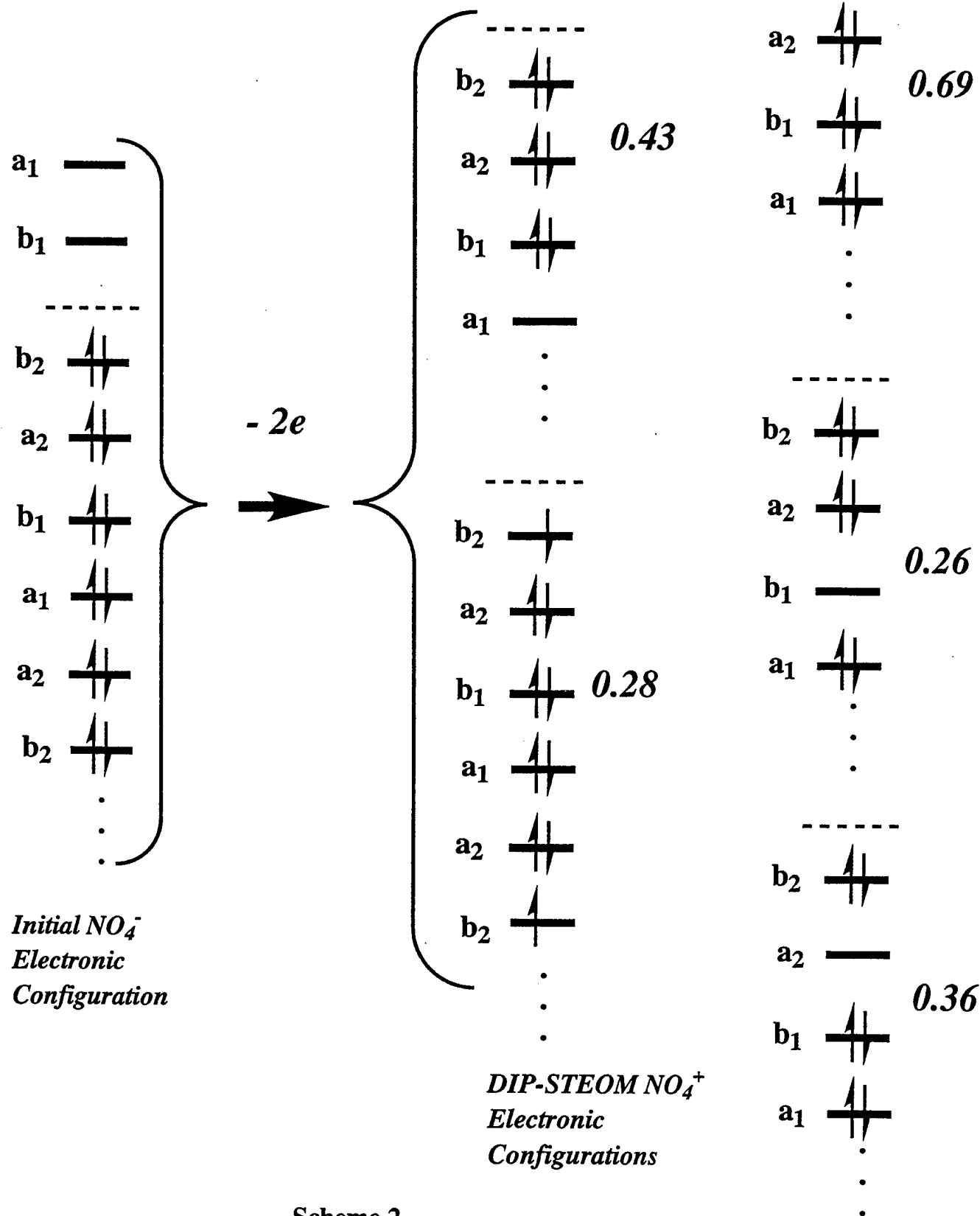
The structures of other bicyclic species, XY_4 ($X = B^-$, C, N^+; $Y = N$, O) (Scheme 3), have been computed at the MBPT(2)/6-31G* and at the CCSD/DZP levels (Scheme 3) and their energetics and reactivity are under investigation.

[1]   E.W. Lawless, I.C. Smith, Inorganic High-Energy Oxidzers (Marcel Dekker, Inc. New York, 1968).

[2]   M. Nooijen, R.J. Bartlett, J. Chem. Phys. 106 (1997) 6441.
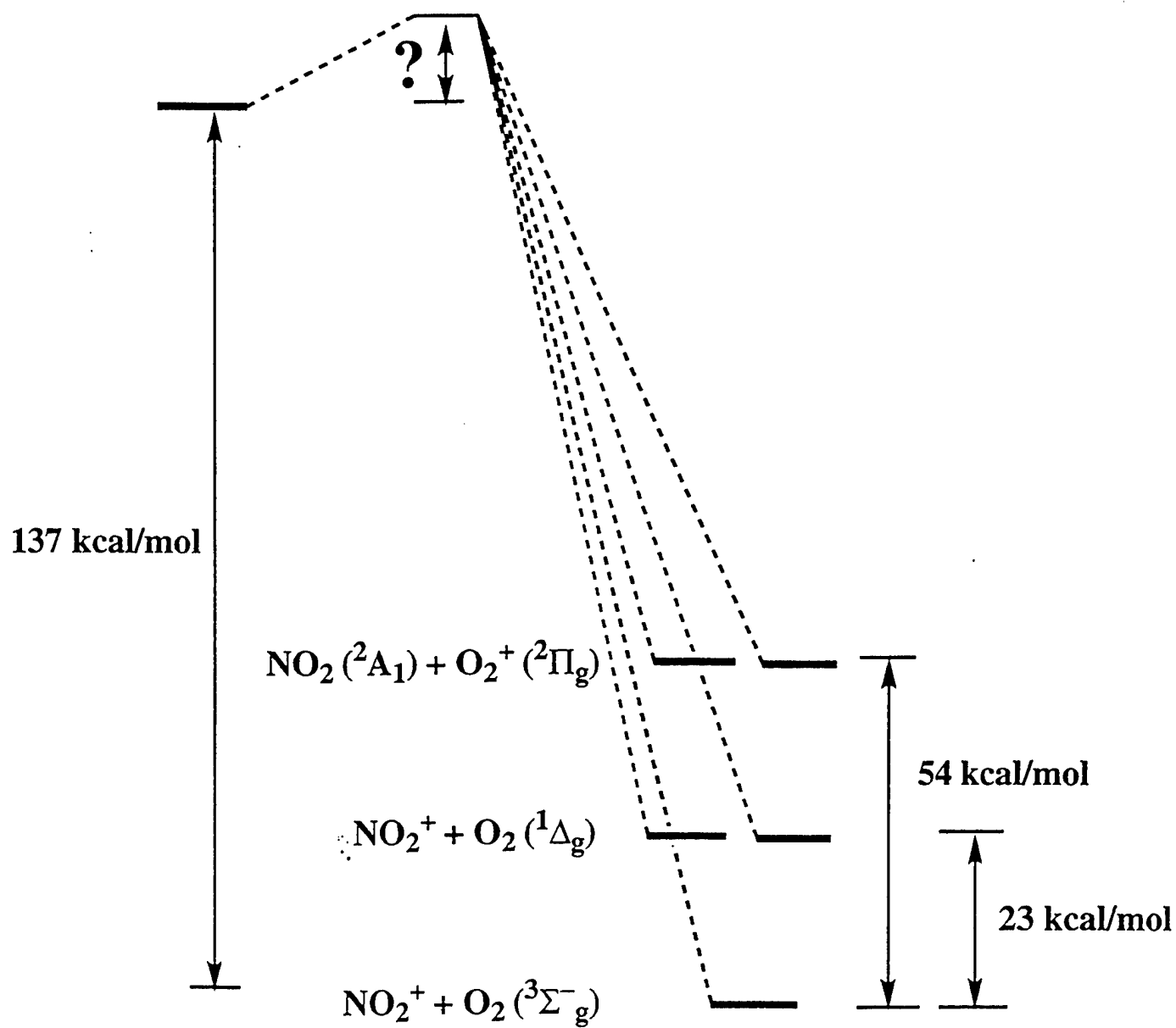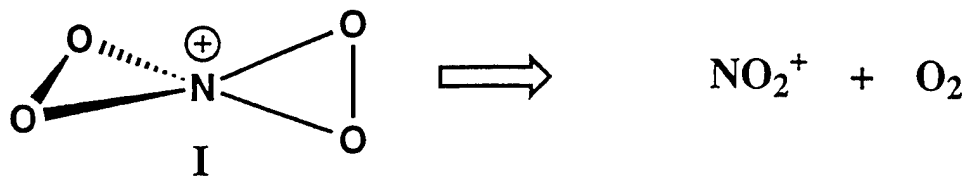
Scheme 1

TRANSITION STATE GEOMETRY:
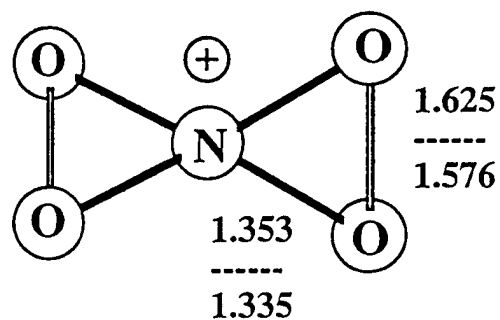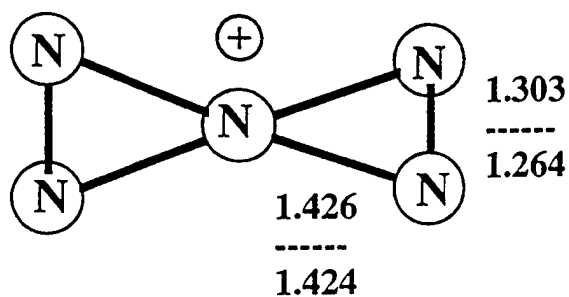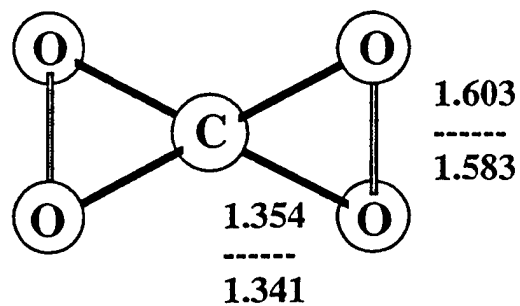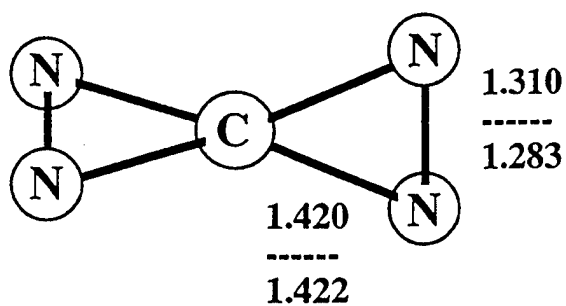## Weights of the electronic configurations

- 2e

0.43

0.28

0.69

0.26

0.36

Initial NO₄⁻
Electronic
Configuration

DIP-STEOM NO₄⁺
Electronic
Configurations

Scheme 2

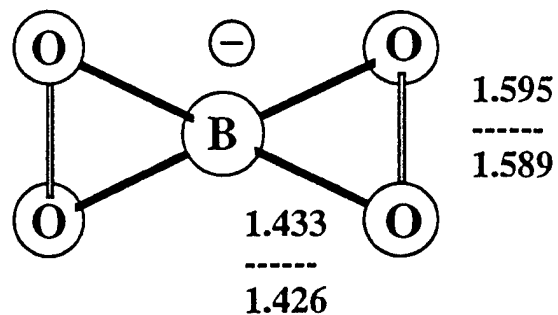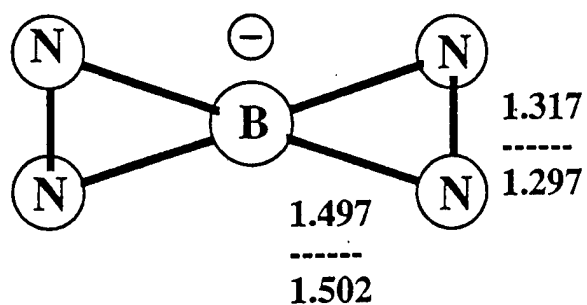# XN₄   VS   XO₄

$$XN_4 \quad vs \quad XO_4$$

MBPT(2)/6-31G*

CCSD/DZP

Scheme 3

Table 1.

Bond lengths (in angstroms) and harmonic vibrational frequencies (in cm^{-1}) of the D_{2d} NO_4^{+} [a]

Method:	HF/		MBPT(2)/		CCSD/	
	/DZP	/TZ2P	/DZP	/TZ2P	/DZP	/TZ2P
Bond lengths:						
R_{NO}	1.290	1.292	1.346	1.347	1.335	1.335
R_{OO}	1.455	1.467	1.620	1.613	1.576	1.571
Frequencies:						
B_1	472 (0)	466 (0)	341 (0)	340 (0)	376 (0)	377 (0)
E	556 (56)	553 (46)	511 (18)	499 (16)	505 (26)	499 (24)
A_1	696 (0)	689 (0)	563 (0)	571 (0)	554 (0)	567 (0)
B_2	942 (1)	942 (4)	664 (14)	692 (15)	679 (10)	716 (12)
E	1212 (24)	1173 (17)	967 (10)	949 (10)	1024 (16)	1005 (26)
A_1	1231 (0)	1218 (0)	913 (0)	929 (0)	981 (0)	998 (0)
B_2	1882 (100)	1832 (100)	1350 (100)	1355 (100)	1514 (100)	1502 (100)
Zero Point Energies:						
	12.52	12.29	9.70	9.70	10.24	10.25

[a] Relative intensities are given in parenthesis.

Table 2.

Relative energies (in kcal/mol) and structures (bond lengths in angström) of the transition state and minima at the PES crossings for a C_{2v} decomposition pathway at the STEOM-CCSD/PBS//CCSD-STEOM/DZP level.[a]

MO confuguration	Energy	$R_{NO}{}^1$	$R_{NO}{}^2$	$R_{OO}{}^1$	$R_{OO}{}^2$
D_{2d} $NO_4{}^+$ minimum	0.0	1.335		1.576	
Transition State	12.7	1.345	1.353	2.210	1.534
$^1A_1$ - $^1B_1$ crossing	12.6	1.343	1.353	2.196	1.532
$^1A_1$ - $^3B_1$ crossing	11.3	1.336	1.338	2.028	1.557

Lowest electronic state at the transition state geometry.

Multiplet	root	irrep	energy diff (eV)	% singles	total energy
Triplet	1	$^3B_1$	14.52026902	99.98	-354.00019085
Singlet	1	$^1B_1$	14.72766231	99.96	-353.99256929
Singlet	1	$^1A_1$	14.73537610	99.86	-353.99228581
Singlet	1	$^1A_2$	14.78197499	99.94	-353.99057334
Singlet	2	$^1A_1$	14.83184913	99.87	-353.98874050

[a] The D_{2d} minimum has been computed at the CCSD/DZP level.

THE INTERACTION OF Li ATOM WITH THE HYDROGEN MOLECULE IN GROUND AND IN LOW LYING EXCITED STATES. AN *AB INITIO* COUPLED-CLUSTER STUDY.

Anatoli A. Korkin, Marcel Nooijen and Rodney J. Bartlett
Quantum Theory Project, University of Florida, Gainesville, FL 32611-8435

Cryogenic solid hydrogen doped by atomic lithium is believed to be a potential energetic material with a high performance capacity. The system is very interesting and challenging in studying quantum effects of lithium dynamics in the solid hydrogen matrix. The van-der-Waals character of the interaction requires a very accurate approach for an adequate description, both in size of the basis set and the correlation energy treatment. The lithium atom electronic absorption spectra influenced by the interaction with hydrogen molecules and available from experimental studies provide a source of experimental data, which contain information about the ground and the excited state potential energy surfaces, as well as dynamic effects related to the process of light absorption and energy transformation.

The correct description and modeling of the experimental results require an accurate description of both the ground and the low excited states of a lithium atom embedded in the hydrogen matrix (cluster). In this study we present a coupled cluster equation-of-motion study of the Li-H_2 system in the ground state and in the first excited states, corresponding to the 2s $\rightarrow$ 2p electron excitation of the unperturbed lithium atom. As a result we provide reliable potential energy surfaces suitable for accurate quantum dynamics modeling, as well as precise characteristics of minimum energy structures and binding energies of the ground and excited state Li-H_2 van-der-Waals complexes and bound species, which give insights into the available experimental results and challenge new studies.

Rapid In-Vacuum Deposition of Thick, Optically Transparent, Solid Parahydrogen Samples

Simon Tam and Mario Fajardo
Propulsion Sciences Division, Propulsion Directorate, Phillips Laboratory
(OLAC PL/RKS Bldg. 8451, Edwards AFB, CA 93524-7680)

ABSTRACT

We have recently developed a method for in-vacuum deposition of solid parahydrogen (pH_2) samples that are several millimeters thick, and yet are amazingly transparent even at vacuum ultraviolet wavelengths. These experiments represent an increase of two to three orders-of-magnitude in sample sizes over our previous thin film solid hydrogen matrix isolation work.

We employ an ortho-to-para hydrogen converter consisting of an 1/8 inch OD by 1.5 m long copper tube packed with 1.4 g of APACHI catalyst wound (and potted with conductive epoxy) onto a copper bobbin which can be cooled to below 10 K by a closed-cycle cryostat. This setup allows for continuous H_2 flow rates at 15 K in excess of 1 mol/hr, yielding a flow of pre-cooled 99.99% pH_2 which is deposited directly onto a BaF_2 substrate cooled to 2 K by a separate liquid helium bath cryostat. Deposition rates in this apparatus are limited to < 1 cm/hour by the pumping speed of the small turbomolecular pump which maintains the cryogenic thermal isolation vacuum (P < 10^{-4} Torr uncondensed H_2); ultimate sample thickness is limited solely by the 2 liter capacity of the liquid helium bath cryostat.

Characterization of pure pH_2 samples by infrared (IR) absorption spectroscopy indicates a very low ortho-hydrogen content (consistent with complete ortho/para equilibration in the converter) and the exclusive formation of hexagonal close-packed (hcp) solid structures. The addition of atomic, molecular, and ionic dopants to these samples yields IR absorptions of the trapped species, as well as a panoply of novel H_2 absorption features induced by the dopants.

NOTE: No separate long-form abstract was submitted for this presentation. For more details please see the companion paper **Progress Towards the Production of Cryosolid HEDM Samples by Laser Ablation and Matrix Isolation Techniques** by M.E. Fajardo, M. Macler, and S. Tam.

Monte Carlo Simulations of the Structures and Optical Absorption Spectra of Al/Ar$_N$ Clusters: Applications of Spectral Theory of Chemical Binding

Jerry A. Boatz and Jeffrey A. Sheehy
Phillips Laboratory
Propulsion Sciences Division
OLAC PL/RKS
Edwards AFB, CA 93524-7680

and

Peter W. Langhoff[†]
Department of Chemistry
Indiana University
Bloomington, IN 47405-4001

ABSTRACT

Classical Monte Carlo simulation techniques have been used in conjunction with a recently developed spectral theory of chemical binding to predict the structures and optical absorption spectra of Al/Ar$_N$ clusters. The new spectral theory, for which the Balling and Wright model (B&W) for predicting the ^{2}P excited state potential energy surfaces of alkali atoms in the presence of an arbitrary number and arrangement of rare gas perturbers is a special limiting case, is based on the use of a direct product of complete sets of atomic eigenstates and an optical-potential analysis in finite subspaces of this representation. This technique extends the approximation of simple pairwise additivity to include interactions between several diatomic potential energy curves. The Al/Ar$_N$ simulations seek to understand several key issues regarding the experimental spectroscopic study of Al/Ar$_N$ clusters [James M. Spotts, Chi-Kin Wong, Matthew S. Johnson, and Mitchio Okumura, *Proceedings of the HEDM Contractors' Conference, 5-7 June 1996*], such as: (1) the location of the Al atom (surface or interior), (2) the role of the 4s and 4p states of Al in the putative 3p -> 3d transition, and (3) the origin of the spectral red shifts and splittings as a function of cluster size. The (17s12p5d4f)/[7s6p4d3f] atomic natural orbital basis set of Widmark et al. (supplemented with diffuse (1s1p1d1f) functions), in conjunction with internally contracted multireference configuration interaction (MRCI) calculations from [6331] (3 electrons in 13 orbitals) state-averaged complete active space reference wavefunctions, was used to calculate the Al-Ar diatomic potential energy curves which correlate with the 3p, 4s, 3d, and 4p atomic states of Al. The "HFDB2" potential of Aziz and Slaman was used in calculating the Ar-Ar interaction energies.

I. Introduction

As part of our ongoing effort to develop a general model for simulations of the structures and electronic spectra (absorption,[1] emission,[2] and magnetic circular dichroism (MCD)[3]) of doped clusters and cryogenic solids, we present here preliminary results of simulations of a series of Al/Ar$_N$ clusters. This work is primarily motivated by the recent experimental results of Spotts, Wong, Johnson, and Okumura,[4] in which the absorption spectra of several Al/Ar$_N$ clusters have been measured in the vicinity of the Al 3p -> 3d atomic transition. The main features of the observed spectra include both blue- and red-shifted peaks relative to the Al 3p -> 3d atomic transition at 308.2 nm. Some of the more detailed features include additional, partially resolved splittings of the blue- and red-shifted absorptions features for some clusters.

Some of the main questions to be resolved are as follows: Does the Al atom reside on the surface or the interior of the cluster? What is the origin of the observed spectral red shifts? Do the 4s and 4p states of Al play a role in the observed spectra?

II. Theoretical Methods

Our method for the simulation of the structures and absorption spectra of metal-doped argon clusters uses a combination of the classical Metropolis Monte Carlo algorithm[5] in conjunction with the recently developed spectral theory of chemical binding.[6] The latter, which is similar in spirit to diatomics-in-molecules (DIM) methods[7] and of which the Balling and Wright first-order degenerate perturbation theory model[8] and pairwise additivity approximations are special limiting cases, provides a systematic method for obtaining an increasingly accurate manifold of eigenstates via incorporation of non-additive contributions to the total energy. The foundation of the spectral theory is pairwise summation of projections of the fully antisymmetrized electronic wavefunctions of the diatomic components into a partially antisymmetrized atomic-product basis.[6] By expanding the number of diatomic and atomic-product states included in the spectral theory formalism, in principle one systematically increases the accuracy of the computed potential energy surfaces.

The following is a brief outline of the spectral theory (for more details, see ref. [6].) The spectral theory hamiltonian which describes the interaction of a single "guest" atom (e.g., the Al atom) with an aggregate of N "host" atoms (e.g., the Ar atoms) is given by

(1) $H = \Sigma_k \ D(\theta_k, \phi_k)^t \ U(R_k)^t \ E(R_k) \ U(R_k) \ D(\theta_k, \phi_k)$

where host atom "k" is located at position (R_k, θ_k, ϕ_k) relative to the guest atom at the origin. $E(R_k)$ is a diagonal matrix of Al-Ar interaction energies in the diatomic basis at internuclear separation R_k. $U(R_k)$ is the unitary transformation from the diatomic basis to the atomic-product basis. Finally, $D(\theta_k, \phi_k)$ is a direct product of Wigner rotation matrices which transforms the coordinates of atom k to the laboratory frame. The energy of the nth electronic state of the cluster is given by

(2) $E_n = \lambda_n + \Sigma_{k>1} V_{RG-RG} (R_{kl})$

where λ_n is the nth eigenvalue of $\mathbf{H}$ in Eq. (1); i.e.,

(3) $\lambda = \mathbf{V^t H V}$

The diatomic Al-Ar wavefunctions are written as superpositions of atomic product states constructed from the direct product of Al and Ar atomic states: Al $\{3P,4S,3D,4P,....\} \otimes$ Ar $\{^1S,....\}$. Since the excited states of Ar are much higher in energy than those of Al, it is assumed that the most important contributions to the diatomic wavefunctions will be described by atomic products containing Al atom excited states and the Ar atom ground state. In matrix/vector notation,

(4) $\Phi = \mathbf{U} \Psi$

where Ψ denotes the row vector of Al-Ar diatomic states (e.g., X $^2\Pi$, A $^2\Sigma^+$, B $^2\Sigma^+$,....), Φ denotes the row vector of atomic product states (e.g., $|3P_0> \cdot |^1S_0>$, $|4S> \cdot |^1S_0>$,....), and $\mathbf{U}$ is the unitary transformation connecting the diatomic and atomic-product representations. An important point to be noted is that the atomic-product basis is <u>not</u> used for computations. Rather, all computations are performed in the (fully antisymmetrized) diatomic basis, followed by projection onto the atomic-product basis via the unitary $\mathbf{U}$ matrix transformation defined in Eq. (1) (see ref. [6] for more details.)

In these preliminary simulations, the limiting case of pairwise matrix additivity is assumed (i.e., $\mathbf{U}$ is taken to equal to the identity matrix.) Furthermore, the effects of spin-orbit coupling are omitted. The many-body potential energy surfaces for the lowest twelve electronic states (i.e., the states which correlate with the Al 3p, 4s, 3d, and 4p atomic levels) are computed at each of the cluster configurations generated by the Monte Carlo sampling. The twelve lowest-energy doublet potential energy curves of Al-Ar (four $^2\Sigma^+$ states, three doubly-degenerate $^2\Pi$ states, and a doubly-degenerate $^2\Delta$ state) have been computed using the (17s12p5d4f)/[7s6p4d3f] atomic natural orbital basis set of Widmark et al. (supplemented with diffuse (1s1p1d1f) functions), in conjunction with internally contracted multi-reference configuration interaction (MRCI) calculations from a [6331] (3 electrons in 13 orbitals) state-averaged complete active space reference wavefunction. These curves, which correlate with the 3p, 4s, 3d, and 4p atomic states of Al, were used in constructing E(R) in Eq. (1). The Al-Ar interaction energy is obtained as the lowest eigenvalue of $\mathbf{H}$ in Eq. (1); the residual Ar-Ar interactions are obtained as a pairwise additive sum using the "HFD-B2" potential of Aziz and Slaman.[9]

At each configuration, the transition energies from the ground state "i" to the set of excited states "f" corresponding to the Al 4S, 3D, and 4P atomic levels are binned (using a bin width of 20 cm^{-1}) and weighted using the transition intensity matrix $\mathbf{T}$, given by

(5) $T_{if} = | \mathbf{V^t} \mu_0(R->\infty) \mathbf{V} |_{if}^2 + | \mathbf{V^t} \mu_+(R->\infty) \mathbf{V} |_{if}^2 + | \mathbf{V^t} \mu_-(R->\infty) \mathbf{V} |_{if}^2$

187

where $\mu_{0,+,-}$ (R->∞) are the matrices of Al atomic dipole-allowed transition moments in the atomic-product representation. The resulting histogram of weighted transition energies over the sampled configurations is taken to be the predicted absorption spectrum.

The radial probability distribution functions (RPDFs) and absorption spectra of three $AlAr_N$ clusters (N=6,12,54) have been predicted at classical temperatures of 10, 20, and 30K. Initial configurations were generated by placing each atom at an ideal fcc lattice site appropriate for pure solid argon at the specified temperature. After an "equilibration" period of 10,000 configurations, structures and absorption spectra were obtained from sampling over 40,000 configurations.

III. Results and Discussion

A. Diatomic potentials

The calculated X $^2\Pi$ and A $^2\Sigma^+$ curves (which dissociate to ground state ^{2}P Al and ground state ^{1}S Ar) are shown in the bottom panel of Figure 1. The minimum of the X state is located at R_e = 4.0 angstroms, with a well depth D_e of approximately 131 cm^{-1}. Although the calculated R_e is somewhat longer than the experimentally observed value of 3.79 angstroms,[10] the predicted D_0[11] of 115 cm^{-1} is in good agreement with the observed D_0, 122.4 cm^{-1}.[12]

The calculated Al-Ar curves which dissociate to ground state Ar and Al in its ^{2}S (4s), ^{2}D (3d), and ^{2}P (4p) excited states are shown in the top panel of Figure 1. Of particular importance is the avoided crossing between the (2) $^2\Pi$ (Al 3d) and (3) $^2\Pi$ (Al 4p) curves in the vicinity of R = 3.6 angstroms. This region of internuclear separation is sufficiently close to the ground state minimum (4.0 angstroms) to be sampled during the Monte Carlo iterations, particularly at the higher temperatures (20-30K.)

This strongly suggests that there may be significant interactions between the corresponding potential energy surfaces in the Al/Ar_N clusters, which in turn will have important effects on both the predicted and experimental absorption spectra. Furthermore, in the present limiting case of pairwise additivity (i.e., setting U equal to the identity matrix in Eqs.(1) and (4),) the change in configurational character of the (2) ^{2} Π and (3) ^{2} Π states resulting from the avoided crossing cannot be appropriately described. Rather, this limit implicitly assumes that each diatomic curve is described as a single atomic-product configuration for all internuclear distances R. (Note, however, that it is only the change in configurational character of the (2) ^{2} Π and (3) ^{2} Π states that is not appropriately described; the corresponding diatomic energies are correct at all R.) The implication is that only qualitative agreement between the simulated and experimental spectra should be expected.

B. Cluster geometries

The location of the Al-Ar radial probability distribution function (RPDF) peak maxima and the number of atoms per peak for Al-Ar$_N$, N=6,12,54 are summarized in Table I. In all cases, the

energetically preferred site of the aluminum atom is on the surface of the cluster. Simulations in which the Al atom was initially positioned in the cluster interior invariably resulted in either "diffusion" of the metal atom to the cluster surface or trapping in a metastable interior site. This raises the interesting possibility that inhomogeneous broadening effects due to multiple trapping sites may have an important role in the observed absorption spectra, although this issue is not addressed in this preliminary study.

C. Absorption spectra

The simulated absorption spectra of Al-Ar$_{6,12,54}$ at temperatures of 10, 20, and 30K are shown in Figure 2 and the absorption energies are summarized in Table II. (For each cluster, the predicted location of the absorption peak corresponding to the 3p -> 4s transition is in the 380-386 nm range and is not shown in Figure 2 or included in Table II.) The locations of the peak maxima are virtually independent of the simulation temperature, although the peak widths increase with increasing temperature.

The simulated spectra show the presence of a single red-shifted and two blue-shifted absorptions, although in the case of the N=12 and N=54 clusters the blue-shifted absorption is not fully resolved into two distinct peaks. Analysis of the wavefunctions of the AlAr$_N$ excited states in terms of the component atomic products (i.e., the eigenvector matrix V in Eq. (3)) reveals that all three absorptions arise from transitions in which the final electronic state is primarily described by the $|3D> \cdot |^1S_0>$ atomic product (i.e., the Al 3d atomic level.) Furthermore, the upper electronic state involved in the red-shifted absorption shows a slight predominance of the Δ components over the Π and Σ components of the $|3D> \cdot |^1S_0>$ atomic product, whereas in the blue-shifted absorptions it is the Π and Σ components of the $|3D> \cdot |^1S_0>$ atomic product which dominate. This is consistent with the calculated diatomic curves which dissociate to ground state Ar and Al in its ^2D Al (3d) state (top panel of Figure 1), which show the (1) $^2\Delta$ curve slightly lower in energy than the closely-spaced (2) $^2\Pi$ and (3) $^2\Sigma^+$ curves.

Included in Table II is a summary of the experimental absorption peak locations,[13] which fall into subsets of red-shifted and blue-shifted absorptions relative to the Al atomic 3p -> 3d transition wavelength of 308.2 nm. The magnitude of the experimentally observed red shift increases slightly with increasing cluster size, while the location of the centroid of the blue shift is approximately independent of cluster size. Furthermore, for the N=6 and N=12 clusters, there are two partially resolved red-shifted peaks, whereas for N=54 there is tentative evidence for two partially resolved blue-shifted peaks. For all three clusters, the red-shifted absorptions are more intense than the blue-shifted absorptions.

The relative intensities of the red and blue-shifted peaks in the simulated spectra are in qualitative agreement with the experimental relative intensities. However, there is no evidence for multiple red-shifted peaks in any of the simulated spectra, in contrast to the experimental results for N=6 and N=12. Furthermore, the locations of the red-shifted absorptions in the simulated spectra for N=12 and 54 are actually slightly shifted to the blue relative to the

corresponding absorption in N=6, whereas in the experimentally observed spectra the size of the red shift slightly increases with increasing cluster size.

IV. Conclusions

The structures and absorption spectra of $AlAr_N$ (N=6,12,54) have been predicted using a special limiting case of the spectral theory of chemical binding.[6] The energetically preferred site of the Al atom is on the surface of the cluster. Relative to the Al 3p -> 3d atomic transition energy, the predicted spectra show a single red-shifted absorption and two blue-shifted absorptions (which are only partially resolved for the N=12 and N=54 clusters.)

Although the simulated spectra show reasonably good qualitative agreement with experiment, the primary shortcomings of the simulated spectra relative to experiment are (1) underestimation of the splittings between the red and blue-shifted absorptions and (2) lack of an increasing magnitude of the red shift with respect to cluster size. These deficiencies are most likely due to the special limiting case of the spectral theory used in this preliminary study, in which there is no mixing of atomic product states (i.e., $U = I$ in Eqs. (1) and (4).) In particular, this limiting case precludes an appropriate description of the avoided crossing between the (2) $^2\Pi$ (Al 3d) and (3) $^2\Pi$ (Al 4p) Al-Ar diatomic curves (see top panel Figure 1.) Another possible factor which affects the accuracy of the present simulations is the exclusion of spin-orbit effects in the calculated diatomic curves. Both of these issues will be addressed in our future studies of $Al-Ar_N$ clusters. Nonetheless, the present calculations provide a useful benchmark for comparison with subsequent, more refined techniques.

References

1.   a) Boatz, J.A.; Fajardo, M.E. *J. Chem. Phys.*, **1994**, <u>101</u>, 3472-3487.
      b) Boatz, J.A.; Fajardo, M.; Langhoff, P.W. "Proceedings of the High Energy Density Matter (HEDM) Contractors' Conference", Patrick G. Carrick and Simon Tam, eds., 1995.
      c) Boatz, J.A.; Fajardo, M.; Sheehy, J.A.; Langhoff, P.W. "Proceedings of the High Energy Density Matter (HEDM) Contractors' Conference", Patrick G. Carrick and Lt. Neal T. Williams, eds., 1996.

d) Fajardo, M.E.; Boatz, J.A. *J. Comp. Chem.*, **1996**, <u>18</u>, 381-392.

2.   Boatz, J.A.; Fajardo, M. "Proceedings of the High Energy Density Matter (HEDM) Contractors' Conference", T.L. Thompson, ed., 1993

3.   Kenney, J.W. III; Terrill-Stolper, H.A. "Proceedings of the High Energy Density Matter (HEDM) Contractors' Conference", Patrick G. Carrick and Simon Tam, eds., 1995.

4.   James M. Spotts, Chi-Kin Wong, Matthew S. Johnson, and Mitchio Okumura, "Proceedings of the High Energy Density Matter (HEDM) Contractors' Conference", Patrick G. Carrick and Lt. Neal T. Williams, eds., 1996.

5.   Metropolis, N.; Rosenbluth, A.W.; Rosenbluth, M.N.; Teller, A.H.; Teller, E. *J. Chem. Phys.* **1953**, <u>21</u>, 1087-1092.

6.   a) Langhoff, P.W. "Proceedings of the High Energy Density Matter (HEDM) Contractors' Conference", T.L. Thompson and S.L. Rodgers, eds., 1994.
        b) Langhoff, P.W. "Proceedings of the High Energy Density Matter (HEDM) Contractors' Conference", Patrick G. Carrick and Simon Tam, eds., 1996.
        c) Langhoff, P.W. *J. Phys. Chem.*, **1996**, <u>100</u>, 2974-2984.
        d) Sheehy, J.A.; Boatz, J.A.; Fajardo, M.E.; Langhoff, P.W. "Proceedings of the High Energy Density Matter (HEDM) Contractors' Conference", Patrick G. Carrick and Lt. Neal T. Williams, eds., 1996.

7.   Tully, J. "Modern Theoretical Chemistry", G.A. Segal, ed., Plenum, NY, 1977, Vol. 7, 173-200.

8.   Balling, L.C.; Wright, J.J. *J. Chem. Phys.* **1983**, <u>79</u>, 2941-2944.

9.   Aziz, R.A.; Slaman, M.J. *Mol. Phys.* **1986**, <u>58</u>, 679-697.

10.   McQuaid, M.J.; Gole, J.L.; Heaven, M.C. *J. Chem. Phys.*,**1990**, <u>92</u>, 2733.

11.   Within the harmonic approximation, the predicted zero-point energy is $1/2\omega_e = 15.5$ cm^{-1}.

12.   Heidecke, S.A.; Fu, Z.; Colt, J.R.; Morse, M.D. *J. Chem. Phys.*,**1992**, <u>97</u>, 1692-1710.

13.   Spotts, J.M. and Okumura, M.; private communication.

Table I. Al-Ar Radial Probability Distribution Function Peak Locations.

Al-Ar$_N$ Peak Maxima Locations[a]

N = 6

T=10K	4.13(4)	6.75(2)			
T=20K	4.06(4)	6.79(2)			
T=30K	4.02(4)	6.74(2)			

N = 12

T=10K	4.16(6)	6.82(5)	8.10(1)		
T=20K	4.12(6)	6.92(5)	8.10(1)		
T=30K	4.20(6)	6.94(5)	8.07(1) (sh)[b]		

N = 54

T=10K	3.98(2)	4.65(4)	7.08(5)	7.60(7)	8.20(4)
	10.13(15)	11.17(1)			
T=20K	4.03(2)	4.69(4)	7.50(16)	10.26(15)	11.79(1)
T=30K	4.03(2)	4.70(4)	7.45(16)	10.32(15)	11.94(1)

[a] In angstroms. Number of atoms in the peak given in parentheses.
[b] Shoulder

Table II. Absorption Spectrum Peak Locations.

Al-Ar$_N$ Peak Maxima Locations[a]

N = 6	Red-shifted peaks		Blue-shifted peaks		
T=10K	310.0		306.4	304.1	303.2
T=20K	310.0		306.2	304.0[b]	303.4
T=30K	309.8		306.2		303.8
exptl[c]	316	312	302[c]		

N = 12					
T=10K	308.8		303.8[b]		
T=20K	308.8		303.8[b]		
T=30K	308.6		304.0[b]		
exptl[c]	318[b]	314	301		

N = 54					
T=10K	308.6		303.6	302.7	
T=20K	308.6		303.6	302.8	

T=30K	308.6	303.6	302.8[b]
exptl[c]	320	305[d]	295[d]

[a] In nm.

[b] Shoulder.

[c] Spotts, J.M. and Okumura, M., private communication.

[d] Tentative assignment.

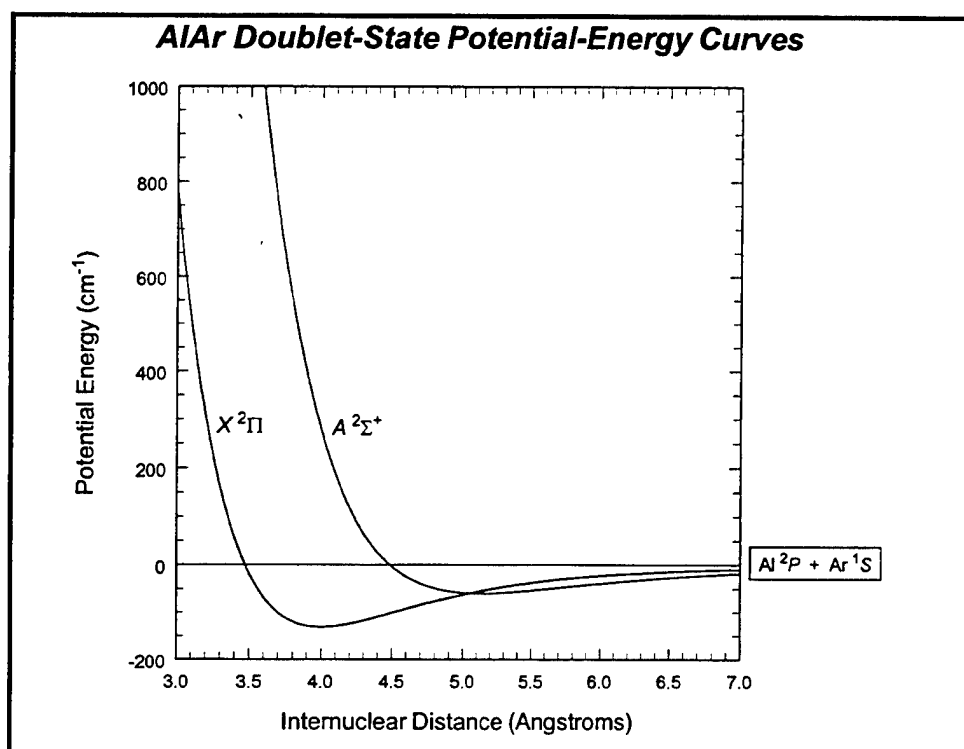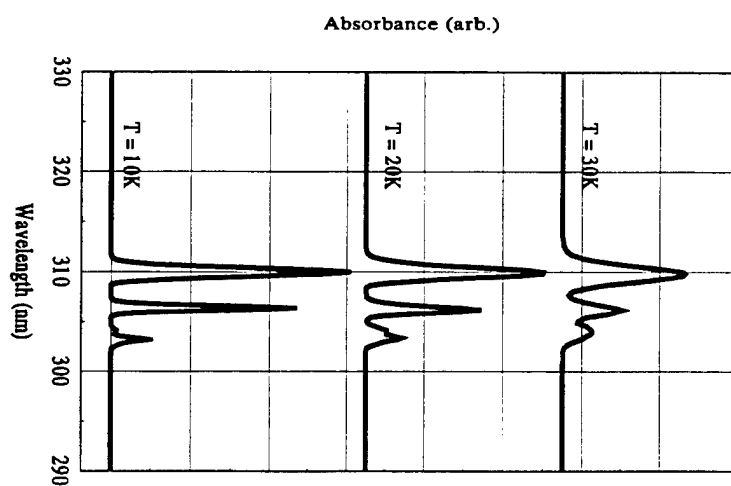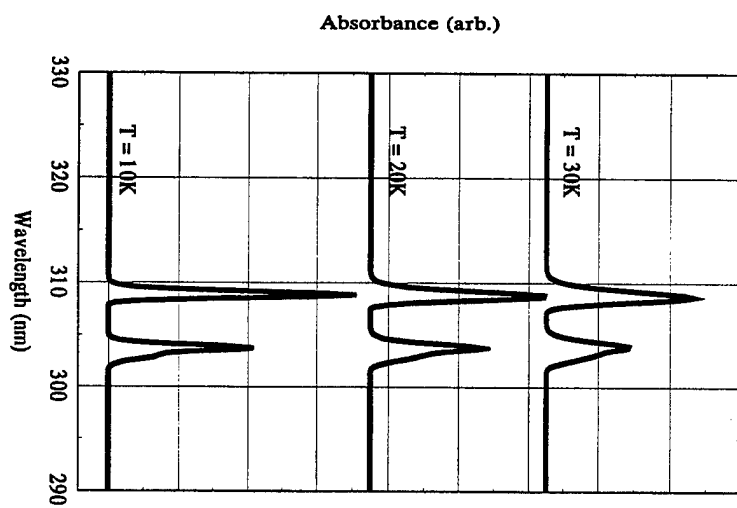[e] Approximate center of broad absorption band.

AlAr Doublet Excited-State Potential-Energy Curves

195

AlAr Doublet-State Potential-Energy Curves

Figure 1

Absorbance (arb.)
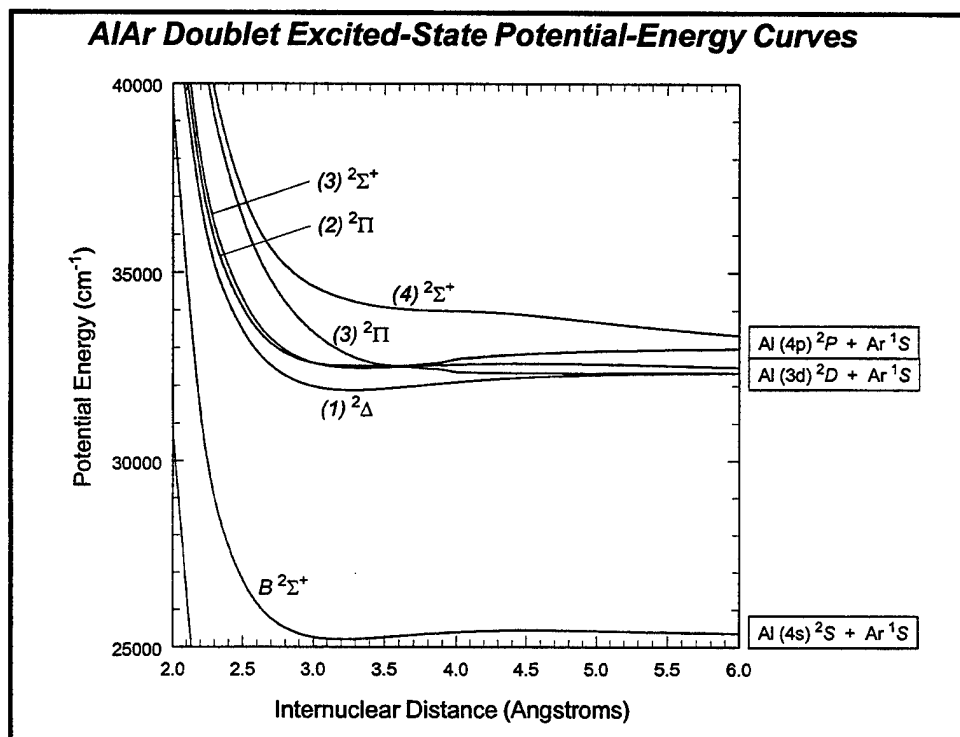
AlAr₆ Absorption Spectra

Figure 2

Absorbance (arb.)

AlAr12 Absorption Spectra

T = 10K
T = 20K
T = 30K

Wavelength (nm)

Absorbance (arb.)

AlAr54 Absorption Spectra

T = 10K
T = 20K
T = 30K

Wavelength (nm)
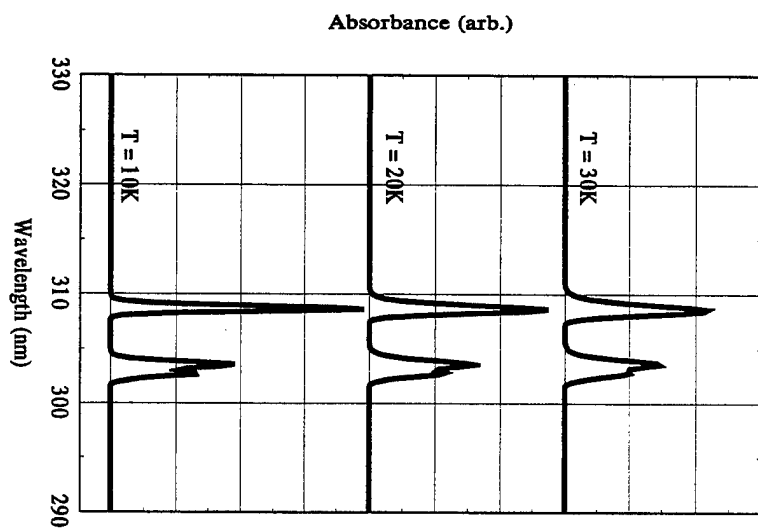
Cryogenic Solid Combustion*

M. E. DeRose, K. L. Pfeil, P. G. Carrick and C. W. Larson
Propulsion Directorate/Phillips Laboratory
Edwards AFB, CA 93524-7680

ABSTRACT

The tube burner was developed to quantify the regression rate and combustion efficiency of fast-burning cryogenic solids. The project objective was to demonstrate that fuels which are gases or liquids at room temperature could be condensed and burned as cryogenic solids in a controlled manner, which would support the idea that high energy density material (HEDM) could be burned as an additive in solid cryogenic fuel, e.g., solid hydrogen.

We have now measured regression rates and mixing/combustion efficiencies of ten cryogenic solid hydrocarbon fuels with the tube burner under conditions where hybrid rockets operate, i.e., pressure and mass flux up to 800-psi and 60-g/cm^2-s. Ported fuel cylinders with outside diameter of 0.9-inch, port diameter of 0.4-inch, and lengths of 3-inches and 6-inches have been burned with gaseous oxygen mass flow rates ranging from 5- to 30-grams per second.

Regression rates of the cryogenic solid hydrocarbons are between two and eight times faster than conventional hybrid rocket fuels, e.g., Plexiglas and HTPB. Pentane, the most extensively studied fuel, burns four times faster than HTPB. Combustion efficiency is degraded by incomplete mixing of fuel and oxidizer, which was more pronounced in burns of 6-inch fuel cylinders, where O/F ~ 1, than in burns of 3-inch fuel cylinders, where O/F ~ 2. Higher pressure burns improved combustion efficiency of the shorter cylinders more than the longer cylinders. Maximizing specific impulse in propulsion applications requires that hydrocarbons be burned fuel rich to produce the lightweight CO combustion product rather than CO$_2$. This paper reports on burns of 3-inch pentane cylinders at the near optimum O/F ~ 2.5.

LIST OF SYMBOLS, DEFINITIONS

$r(t)$ instantaneous fuel grain center port radius, cm

$r'(t)$ instantaneous radial regression rate, cm/s

ρ_f density of the solid fuel, g/cm^3. $\rho_{solid\,pentane}$ at 77 K ~ 0.85$\pm$0.02 g/cm^3.

$G(t,x,r)$ instantaneous mass flux in Marxman-Altman (MA) equation, g/cm^2 s

μ free stream viscosity of combustion gases in port in MA equation, g/cm s

x distance from oxidizer entrance port in MA equation, cm

B blowing coefficient in MA equation

n flux exponent in uniform burn approx

a_n empirical regression rate constant in uniform burn approximation, dimensions (mass flux)$^{1-n}$ per unit density

$G_{mid}(t)$ instantaneous mass flux in fuel cylinder port at the cylinder mid-point, g/cm^2 s

$F_f(t)$ fraction of fuel burned at time t, dimensionless

$m'_f(t)$ instantaneous fuel mass flow rate, g/s

$m'_{ox}(t)$ instantaneous oxygen mass flow rate, g/s

$P_c(t)$ instantaneous combustion pressure, psia

$P_{ambient}$ ambient pressure, 13.2 psia

t_b total burn time to $m'_f(t) = 0$, s

$m_{f,total}$ total mass of fuel grain, 20.5 or 41.0 g

L length of fuel cylinder, 7.5 or 15.0 cm

V_{tube} volume of tube burner, 152 cm^3

r_{max} radius of combustion chamber, 1.14 cm

r_o initial radius of fuel cylinder port, 0.48 cm

A_n area of nozzle, 0.097 to 0.206 cm^2

C_D nozzle discharge coefficient, ~ 0.9

c^*_{eq} equilibrium characteristic velocity, m/s

F^*_{eq} equilibrium characteristic thrust, lbf

I^*_{eq} equilibrium characteristic impulse, lbf s

$I^*_{sp.eq}$ equilibrium characteristic average specific impulse, lbf s/lbm

I_{exp} actual experimental impulse, lbf s

$I_{sp.exp}$ actual experimental average specific impulse, lbf s/lbm

η_I impulse based apparent combustion efficiency

$I_{exp,adiab}$ adiabatic experimental impulse, lbf s

γ heat capacity ratio, C_p/C_v

INTRODUCTION

During the past decade the Air Force has supported research on the use of high energy density matter (HEDM) as a high performance propellant[1]. More than 20% enhancement of specific impulse is predicted for the quintessential HEDM, solid hydrogen at 4 degrees Kelvin that is seeded with up to 8% atomic additive[2]. One approach envisions burning the cryogenic fuel in a hybrid rocket configuration. To demonstrate this feasibility, and to further understanding of combustion in hybrid rockets, we carried out laboratory scale experiments to evaluate combustion of cryogenically solidified lightweight hydrocarbons (liquid nitrogen temperature, 77K), fuels that are gases or liquids at ambient temperature and pressure. Compared to conventional hybrid rocket fuels, cryogenic solids are expected to have much faster burning rates because they require ten to twenty times less energy for vaporization into the oxidizer stream. Whereas conventional fuels must be pyrolyzed and vaporized, the cryogenic solids need only be melted and vaporized. In this paper we summarize previous results obtained during the past three years[3-6] and emphasize the achievement of near optimum O/F ~ 2.5 in burns of short cylinders (L/D = 3.0) of solid n-pentane. Other solid hydrocarbons burned to date include ethylene, quadracyclane, RP1, and 2,2,5-trimethylpentane. Solid acetone, isopropyl alcohol, and a mixed fuel of partially oxidized hydrocarbons (HF1, a mixture of 60% light alcohols and ketones, 30% hexanes, and 10% tetrahydrofuran) burn more slowly and relatively cleanly in the tube burner. Burning rates of the cryogenic fuels ranged from two to ten times faster than hydroxyl terminated polybutadiene (HTPB).

EXPERIMENTAL

Previously,[3-6] we described the laboratory scale tube burner depicted in figure 1. The tube burner was fabricated from a 14-inch length of 1-inch stainless steel tubing, 0.049-inch wall thickness. Gaseous oxygen was introduced at the top of the tube through a 0.375-inch o.d. tube at right angles to the tube burner axis. Six-inch and three-inch long fuel cylinders with 0.375-inch ports, 0.902-inch o.d. were produced with their tops located 3-inches from the burner top. A microtorch/spark assembly was located 1-inch from the top of the fuel cylinder. A 0.3-inch thick Pyrex window, 1.4-inches in diameter, was sealed to the top of the burner with a viton O-ring.

The tube was mounted inside a liquid nitrogen Dewar so that the bottom 5-inches of the tube burner extended through the bottom of the Dewar; thus a six-inch length of the tube could be cooled to 77 K. Five equally-spaced thermocouples (TC5, TC6, TC7, TC8, TC4) were clamped to the outside of the tube over the six-inch length within the LN2 and one thermocouple (TC3) was clamped to midpoint of the 5-inch section extending outside the Dewar. Two additional thermocouples (TC1, TC2) monitored the temperature deep within the nozzle, about 0.1-inch from the throat, and at the surface of the nozzle assembly as shown in figure 1. The instantaneous combustion chamber pressure, $P_c(t)$, was measured with a diaphragm pressure transducer with a frequency response around 300 Hz. Pressure and temperature data were acquired at the rate of 100 Hz with a computer.

The nozzle choked the flow ($P_{ambient}/P_c < 0.52$), which enabled use of the rocket equation[7], $c^* = P_c A_n C_D/m'$, where c^*, C_D and m' are the characteristic velocity, nozzle discharge coefficient and total mass flow rate, respectively. Converging nozzles with A_n of 0.015, 0.020, and 0.030 in^2 were used. The half-angle of the converging section was about 68-degrees so that C_D was substantially less than unity (i.e., $C_D \approx 0.9$), principally because the large half angle causes a significant departure from the one-dimensional approximation[7] embodied in the rocket equation.

The oxidizer mass flow rate, m'_{ox}, was metered with sonic chokes of 0.070-inch or 0.047-inch throat diameter from Flowdyne, Inc. The flow coefficient was such that about 500 psi upstream pressure on the 0.070-inch choke produced a constant flow of about 22-g/s. Second order corrections were applied to account for the non-ideal behavior of oxygen (variation of γ with pressure); for the 0.070-inch choke, $m'_{ox}(070) = 0.327[0.126 + 7.6 \times 10^{-6} P_{choke}]P_{choke}$, with m'_{ox} in g/s and P_{choke} in psia, whereas for the 0.047-inch choke, $m'_{ox}(047) = 0.1466[0.126 + 7.6 \times 10^{-6} P_{choke}]P_{choke}$.

No effort was made to condition the oxidizer flowfield prior to its injection into the fuel cylinder port. The tube burner head space was minimized to enable a close-up "down the tube" view of the fuel grain through the window on the burner head. Oxygen entered the combustion chamber at right angles to the combustion tube, 5 cm above the top of the fuel grain; tangential injection that would impart swirl to the oxidizer flow was thereby avoided.

The burning events were recorded in four views on SVHS video tape at 60-frames per second: (1) straight down the tube shot, (2) oblique down the tube shot, (3) plume close-up shot, and (4) plume and apparatus wide shot. The oblique down the tube shot was also recorded on high-speed video at 3000 frames per second.

A measured amount of liquid pentane was frozen into the tube with use of a mandrel to shape the centerline port. Fuel cylinders of mass 20.5-g (7.5-cm cylinders) or 41.0-g (15-cm cylinders) were produced in about 30-minutes. The fuel cylinder was ignited by synchronizing the Tesla coil ignition of a small methane/oxygen torch (0.015-cm diameter) with a 0.5 to 0.7 second staged increase of the oxygen mass flow to the final m'_{ox} of the experiment.

CALCULATED RESULTS

Marxman[8] modeled the regression rate of hybrid fuel cylinders more than thirty years ago. Altman recently modified the form that has appeared throughout the literature[9]:

(1) $r' = (0.030/\rho_f) (G)^{0.8} (\mu/x)^{0.2} B^{0.32}$

for $5 < B < 100$. Altman[10] produced a one-dimensional form by integrating equation (1) over the axial dimension. Our previous paper[5] introduced the uniform burn approximation to eliminate the weak 0.2 power dependence of r' on x,

(2) $r'(r,t) = a_n [G_{mid}(r,t)]^n$

where a_n is an empirical regression rate constant, and n is the flux coefficient, which takes on values of ½, ¾, and 1 in the calculations described below. $G_{mid}(t,r)$ is the mid-port mass flux: $G_{mid}(t,r) = (½ m'_f(t) + m'_{ox})/ \pi [r(t)]^2$. The mass balance relationship,

(3) $\rho_f r'(r,t) = m'_f(t)/2 \pi L r(t)$,

was used to produce

(4) $r'^{\frac{1}{n}} - a_n^{\frac{1}{n}}(\rho_f L)\left[\frac{r'}{r}\right] - a_n^{\frac{1}{n}} (m'_\infty / \pi)\left[\frac{1}{r^2}\right] = 0$.

Solutions to equation (4) were computed with use of a regression rate constant and density appropriate for pentane -- $a_n = (0.2 \text{ g/sec})/(7.5 \text{ g/cm}^2\text{-s})^n$ and $\rho_f = 0.85\text{-g/cm}^3$ -- and the two fuel

cylinder lengths of our experiments, L = 15 cm or 7.5 cm. Figures 2a and 2b show these solutions as plots of O/F(t) as a function of $F_f(t)$, the fraction of fuel burned at time t. Five solutions corresponding to m'_{ox} = 5-, 10-, 20-, 40-, and 80-g/s are shown for each value of n; burn time is also indicated by the time intervals between symbols, which decrease with increasing m'_{ox}.

The equilibrium properties of solid pentane (77K)/gaseous oxygen mixtures were computed[5,11] under the condition of combustion to the equilibrium state at constant enthalpy. The dependence of c^*_{eq} on O/F may be represented by figure 3. Soot was produced at O/F < ~ 1.1. The maximum c^*_{eq} ~ 1820 m/s is reached at O/F ~ 2.5.

The regression rate calculation, O/F(t) as a function of $F_f(t)$, may be combined with the c^*_{eq}(O/F) from figure 3 to obtain c^*_{eq} as a function of the fuel fraction burned as shown in figures 4a and 4b. Figure 4a shows that long cylinders do not burn near maximum c^*_{eq} unless n = ½ and m'_{ox} is greater than about 40 g/s. However, figure 4b indicates that short cylinders produce nearly constant c^*_{eq} at its maximum value only when $m'_{ox} \approx 20$ g/s.

We define the characteristic thrust, F^*_{eq}, by

(5) $F^*_{eq} = c^*_{eq}(m'_{ox} + m'_f)$

Figures 5a and 5b show flat thrust profiles with a weak dependence on the flux exponent. A non-linear increase with m'_{ox} is also apparent. Short cylinders produce about the same thrust as long cylinders.

The maximum total impulse produced in burn time t_b is defined by

(6) $I^*_{eq} = \int_0^{t_b} F^*_{eq} \, dt$,

which is plotted as a function of m'_{ox} in figure 6. Here it is seen that short cylinders produce more impulse than long cylinders when m'_{ox} is less than about 20 to 30 g/s.

EXPERIMENTAL RESULTS

Table 1 summarizes the experimental variables and calculated quantities discussed below. The experimental impulse of each burn, I_{exp}, was calculated by integration of the $P_c(t)$ trace,

$$(7) \quad I_{exp} = C_D A_n \int_0^{t_b} P_C \, dt.$$

Under cold flow conditions we measured discharge coefficients in the range of 0.88 to 0.95. An average discharge coefficient ($C_D \approx 0.9$) was used in equation (7) to reduce the measured P_c traces to the integrated I_{exp} listed in Table I. A variation of as much as $\pm$ 0.05 in C_D during the burn is expected because the boundary layer thickness decreases with decreasing temperature and the departure from the one-dimensional approximation increases with decreasing pressure ratio $P_c/P_{ambient}$[7]. Table I also lists the average specific impulse of the burn, defined by

$$(8) \quad I_{sp,exp} = I_{exp}/m_{total},$$

where m_{total} is the total mass of fuel plus oxygen consumed in burn time, t_b.

An impulse-based apparent overall oxidation efficiency, η_I, may be defined without accounting for energy loss to the burner:

$$(9) \quad \eta_I = I_{exp}/I^*_{eq}.$$

As defined, η_I is an average of the apparent c^* combustion efficiency, which is not necessarily constant during burns of fuel cylinders where O/F increases substantially (figure 2).

Figure 7 compares the $P_c(t)A_n$ (relative thrust) traces for three burns at similar m'_{ox} (11 to 14 g/s). The variables are normalized to $m'_{ox} = 12.2$ g/s to facillitate the comparison. Two short cylinders (run 128 at high pressure and run 122 at low pressure) show that higher pressure burns of short cylinders produce measurably higher thrust. The long cylinder burn (run 100) produces about the same thrust as the high pressure short cylinder burn (run 128). However, as shown below, pressure did not appreciably affect the thrust in long cylinder burns.

Figure 8 compares I^*_{eq} to I_{exp} over the experimental range of m'_{ox} extending to ~ 20 g/s. The experimental points are divided into two classes, those with long cylinders (runs 99 - 119) and those with short cylinders (runs 122-128). I_{exp} for the long cylinders was unaffected by pressure, whereas the higher pressure short cylinder burns produced about 20% more I_{exp}. The fuel cylinder of run 125 contained about 3 weight percent aluminum foam imbedded in the lower third of the cylinder; this low

pressure burn produced about 15% more I_{exp} than its counterparts (runs 122, 123, 124) in spite of ejection of burning aluminum particulate from the burner.

Figure 8 shows that the calculated I^*_{eq} of long cylinders is ~ 20 % less than short cylinders because the latter burn at near-optimum O/F: less fuel produces more total impulse. However, the experimental results show that slightly less I_{exp} is produced with the short cylinders primarily because the energy loss to the tube is greater in short cylinder burns.

Figure 8 shows that fuels burning with n = ½ or ¾ produce higher I^*_{eq} at higher m'_{ox}, whereas m'_{ox} does not affect the I^*_{eq} of fuels that burn with n = 1. The I_{exp} clearly increase more with m'_{ox} than I^*_{eq} for the n = ¾ and n=1 calculations. Since n ~ 0.8 to 0.9 for pentane[5], η_I and/or C_D increases with increasing m'_{ox}. At m'_{ox} ~ 10 g/s, I_{exp} is about 85% of I^*_{eq} for the long cylinders and about 75% of I^*_{eq} for the short cylinders at high pressure (runs 126,127,128).

Energy loss by heat transfer to the burner tube was analyzed[5] in our previous work with long cylinders and found be 25 to 35 KJ with about $\pm$ 15 KJ uncertainty due to insufficient thermocouple instrumentation. Given current results with more complete instrumentation (see below) we would revise these losses to their lower limit (i.e., to about 10 to 20 KJ) which amounts to about 15 to 20% of the total energy release of the burn. An experimental adiabatic impulse, $I_{exp,adiab}$, may be calculated by adding this loss to I_{exp}. Thus, accounting for the square root dependence of impulse on energy, $I_{exp,adiab}$ is about 7 to 9% larger than I_{exp}, placing it at 92 to 94% of I^*_{eq}.

In the current work with short cylinders, energy loss to the burner wall was measured at eight locations. Energy loss is larger in short cylinder burns because an additional length of 3-inches of tube burner wall is exposed to the hot combusting mixture and the combustion temperature is significantly higher. Figure 9 shows the temperature rise that occurred at each location during run 128. Figure 10 shows the temperature traces at the nozzle throat (TC1) for all of the short cylinder burns. TC1 was located in a thermocouple well whose bottom was about .04-inch from the nozzle throat. Nozzle throat temperature correlates with the I_{exp} shown in figure 8: burns with higher I_{exp} also produced higher nozzle throat temperatures.

In previous work with long pentane cylinders, temperature was measured only at two locations, denoted TC3 in figure 1 (external to the

LN2) and TC4 (in the LN2 at the bottom of the Dewar). The temperature traces at these locations are shown in figures 11a and 12a for the long cylinder burns and in figures 11b and 12b for the short cylinder burns. At TC3, short cylinders produced temperature increases of ~ 500 C and long cylinders produced temperature increases of ~ 300 C. At TC4, short cylinders produced temperature increases of ~ 600 C and long cylinders produced temperature increases of ~ 200 C. Comparison of these data shows that energy loss in the short cylinder burns is about twice that of the long cylinders and amounts to 30 to 40% of the total energy release. Thus, $I_{exp,adiab}$ is 14 to 18% greater than I_{exp} in short cylinder burns and amounts to ~ 89 to 93% of I^*_{eq}.

Video of the combustion zone (down the tube shot) showed a swirling luminous and turbulent reacting boundary layer, about 4 mm thick, with a dark zone in the center. The image bore a remarkable resemblance to a satellite view of a hurricane. Coherent structures within the luminous zone with lifetimes longer than about 20 ms were captured on the 60 sub-frame per second video. Nearer the fuel grain surface, coherent structures rotated more slowly and could be tracked; rotational speeds of ~ 10 revolutions per second were estimated. High speed video at rates up to 3000-frames per second revealed large and small scale coherent luminous structures with lifetimes up to several ms. Mixing appeared to be incomplete on a time scale < 10 ms.

CONCLUSIONS

A comparison of the burning of short fuel cylinders (L/D = 3) to the burning of long fuel cylinders (L/D = 6) showed the following:

- The burning time was barely affected and may increase slightly with short cylinders.
- The O/F ratio of short cylinders was about two times that of long cylinders.
- The total impulse produced by the shorter cylinders, after correction for energy loss to the burner, is actually as great as that produced by the longer cylinders, which contain twice the fuel.
- The effect of increased m'_{ox} on combustion efficiencies, based on measured total impulse, was the same for both the short and long cylinders. Increasing m'_{ox} increased combustion

efficiency from 85% to 95% over the m'_{ox} range of 5- to 20-g/s for both short and long cylinders.

- For the short cylinders, increase in pressure from 200-psig to 400-psig (at fixed m'_{ox}) caused $I_{exp,adiab}$ to increase from 75 to 90% of I^*_{eq}. For long cylinders, little or no pressure effect on I_{exp} was observed. This result is most likely due to an increase in η_l with pressure for the short cylinders. If I_{exp} increased due to an increase in C_D, the pressure effect would have been observed with both short and long cylinders.

This work shows conclusively that burning of fuel cylinders at optimum O/F can only occur at specific L/D that depends on the fuel burning rate. With single point injection of oxidizer, fast burning fuels like pentane require small L/D around 3 to achieve optimum combustion performance.

ACKNOWLEDGMENT

REFERENCES

1. Carrick, P. G., and Williams, N. T., eds., "Proceedings of the High Energy Density Matter (HEDM) Contractor's Conference," 5-7 June 1996, Boulder, CO, USAF Technical Report PL-TR-96-3037, and proceedings from 10 previous annual conferences.

2. Carrick, P. G., "Theoretical Performance of High Energy Density Cryogenic Solid Rocket Propellants," AIAA 31st Joint Propulsion Conference, July 1995, San Diego, CA, and USAF Technical Report PL-TR-93-3014.

3. Carrick, P. G., and Larson, C. W., "Lab Scale Test and Evaluation of Cryogenic Fuel Grains," AIAA 31st Joint Propulsion Conference, July 1995, San Diego, CA, Paper No. AIAA 95-2948.

4. Carrick, P. G., Larson, C. W. and Pfeil, K. L., "Characterization of Cryogenic Solid Hybrid Rocket Motors," Proceedings of the 1995 JANNAF Joint Propulsion Conference, Tampa, FL 3 - 7 December 1995, published by CPIA, Johns Hopkins University.

5. Larson, C. W., Pfeil, K. L., DeRose, M. E., and Carrick, P. G., "High Pressure Combustion of Cryogenic Solid Fuels for Hybrid Rockets," AIAA 32nd Joint Propulsion Conference, July 1996, Lake Buena Vista, FL, Paper No. AIAA 96-2594.

6. Larson, C. W., DeRose, M. E., Pfeil, K. L., and Carrick, P. G., "High Pressure Combustion of Cryogenic Hybrid Fuels in a Lab-Scale Burner," Proceedings of the 1996 JANNAF Joint Propulsion Conference, Albuquerque, NM, 9 - 13 December 1996, published by CPIA, Johns Hopkins University.

7. Zucrow, M. J., and Hoffman, J. D., "Gas Dynamics," Volume 1, (John Wiley, New York, c1977), p. 277ff. ; and Welty, J.R., Wicks, C.E., and Wilson, R.E., "Fundamentals of Momentum, Heat, and Mass Transfer," (John Wiley, New York, c1969), Chapter 11.

8. Marxman, G. A., "Boundary Layer Combustion in Propulsion," 11th International Symposium on Combustion, The Combustion Institute, August 1966, p. 269.

9. Recently, D. Altman stated during a discussion following presentation of Ref 3, that the exponent of B had been recalculated from a least squares fit to original data and found to be 0.32, not 0.23 as published throughout the literature. This also impacts the dimensionless constant, reducing it from 0.036 to 0.030.

10. Altman, D., "Space Propulsion Analysis and Design," Humble, Henry, Larson, Editors, Chapter 7, McGraw Hill, 1995.

11. USAF AFAL Theoretical Isp Code, originally written by Curtis Selph and Robert Hall, adapted for microcomputers by C. Beckman, R. Acree and T. Magee, Phillips Laboratory, Edwards AFB, CA

Table I. Summary of experimental data from solid pentane (77K) combustion experiments.

Run	An (in^2)	m'$_{ox}$ (g/s)	Burn time (sec)	Maximum chamber pressure (psig)	Total impulse (lbF-sec)	average specific impulse (lbF-sec/lbm)
128	0.0197	14.3	3.8	400	20.6	125
127	0.0197	6.9	5.8	200	14.7	110
126	0.0197	7.3	5.5	225	15.4	115
125	0.0320	13.5	4.5	250	19.5	109
124	0.0320	15.6	3.5	250	17.5	105
123	0.0320	20.1	3.0	350	22.3	125
122	0.0320	10.8	3.8	200	13.3	98.0
119	0.0320	10.0	4.3	200	17.9	93.8
118	0.0320	5.0	7.5	90	12.6	74.1
117	0.0150	10.0	4.3	450	18.0	94.7
111	0.0150	5.0	6.0	205	12.0	77.9
103	0.0155	20.0	3.0	800	24.6	110
102	0.0155	10.2	4.5	420	18.2	95.7
101	0.0320	22.0	3.0	440	24.0	101
100	0.0320	11.6	4.5	225	19.5	95.5
99	0.0320	11.6	4.5	220	19.2	95.4
98	0.0320	11.6	4.5	220	19.3	94.6
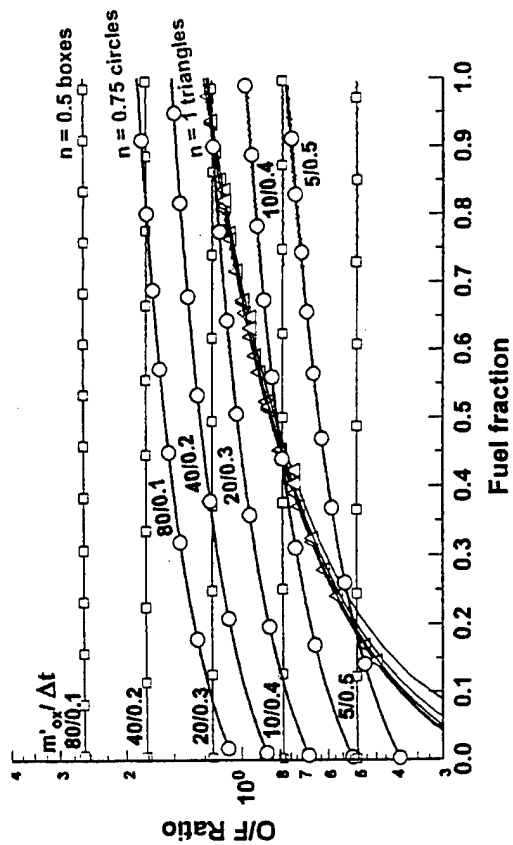
Figure 2a. Calculated O/F ratio for uniform burns of solid cryogenic pentane, L = 15 cm. Symbols are printed at intervals varying between 0.1 sec for m'_{ox} = 80 g/s and 0.5 sec for m'_{ox} = 5 g/s.
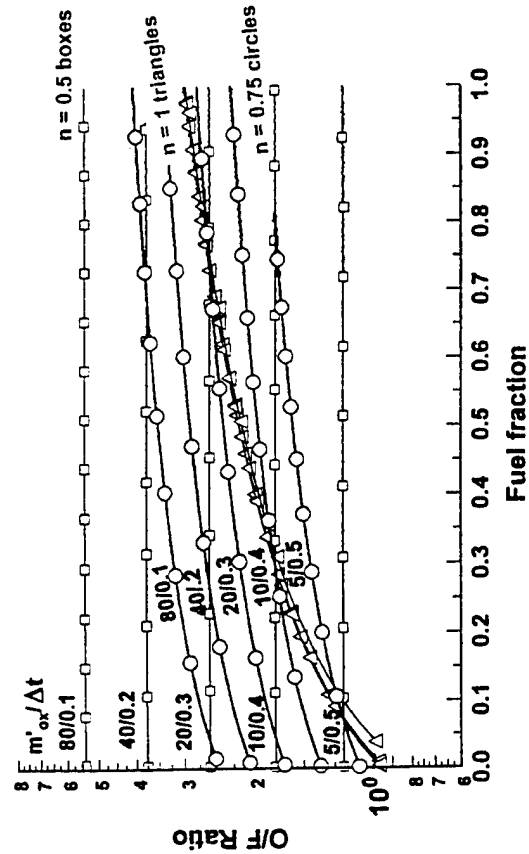

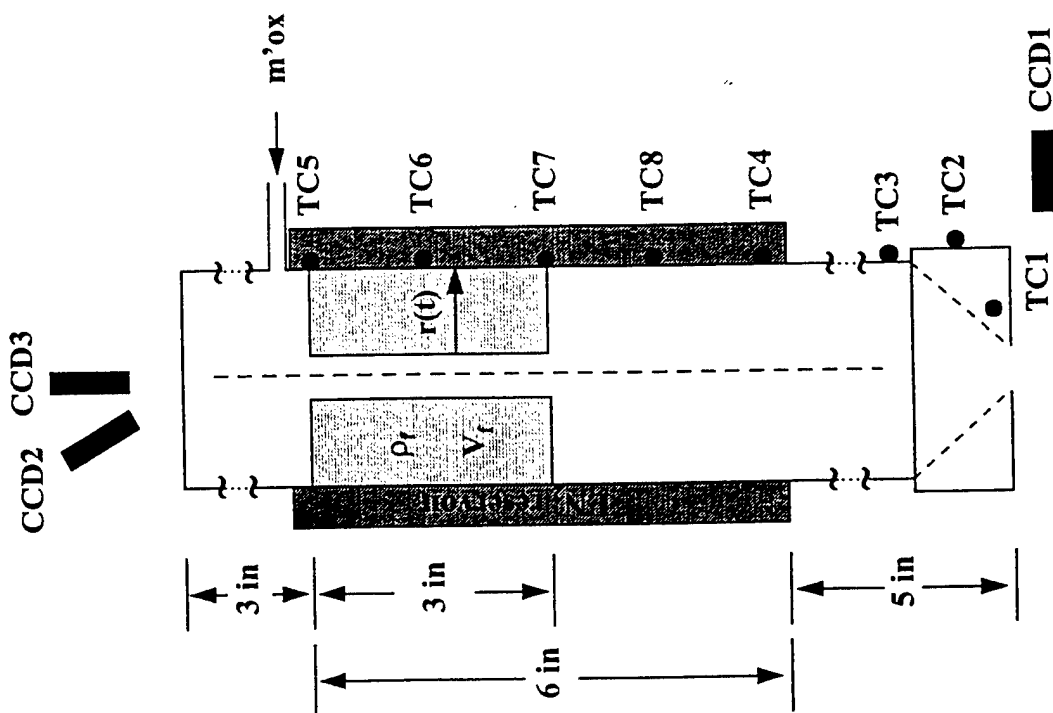Figure 2b. Calculated O/F ratio for uniform burns of solid cryogenic pentane, L = 7.5 cm.

Figure 1. Fourteen-inch lab-scale tube burner, shown with 3-inch fuel cylinder. Placement of video cameras (CCDs) is shown.
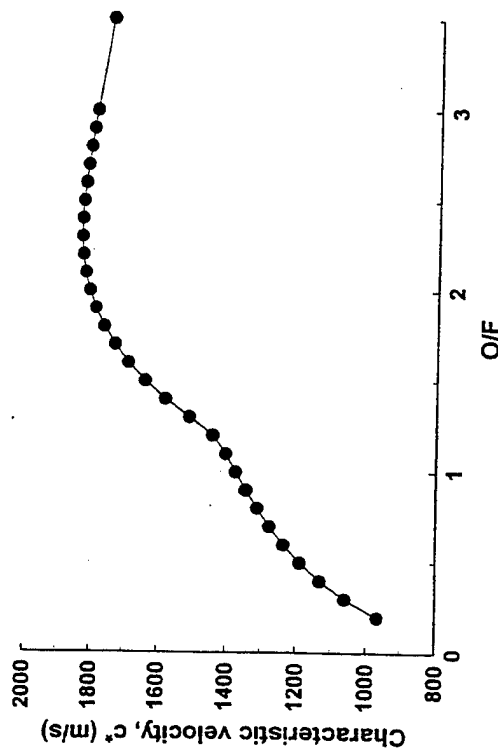
Figure 4a. Calculated c^*_{eq} for uniform burns of solid pentane, L = 15 cm.
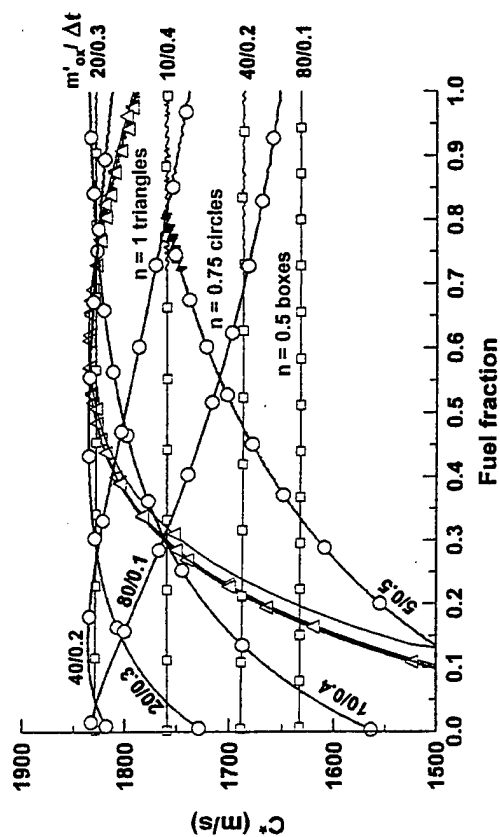
Figure 4b. Calculated c^*_{eq} for uniform burns of solid pentane, L = 7.5 cm.

Figure 3. Calculated c^*_{eq} for combustion of solid cryogenic pentane (77 Kelvin) with gaseous oxygen.

Figure 6. Calculated I*eq for uniform burns of solid pentane, L = 15 and 7.5 cm.
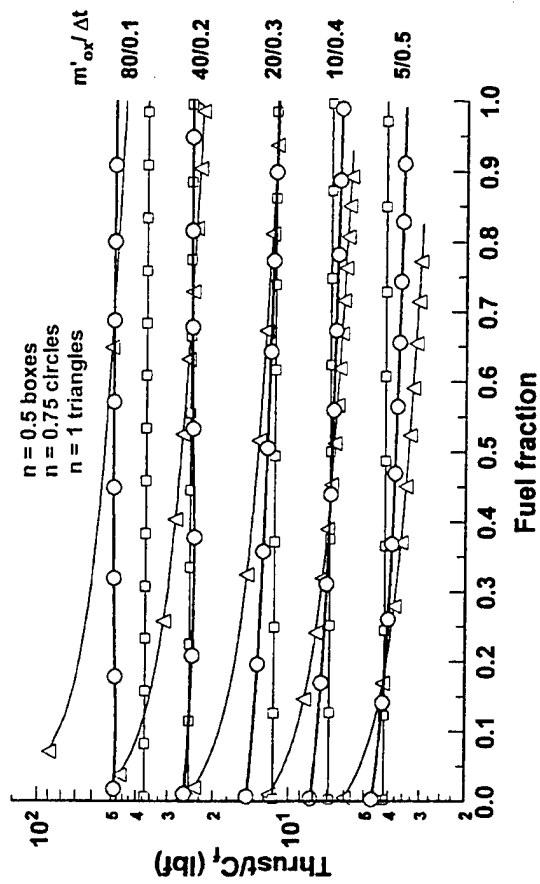
Figure 5a. Calculated F*eq for uniform burns of solid pentane, L = 15 cm.
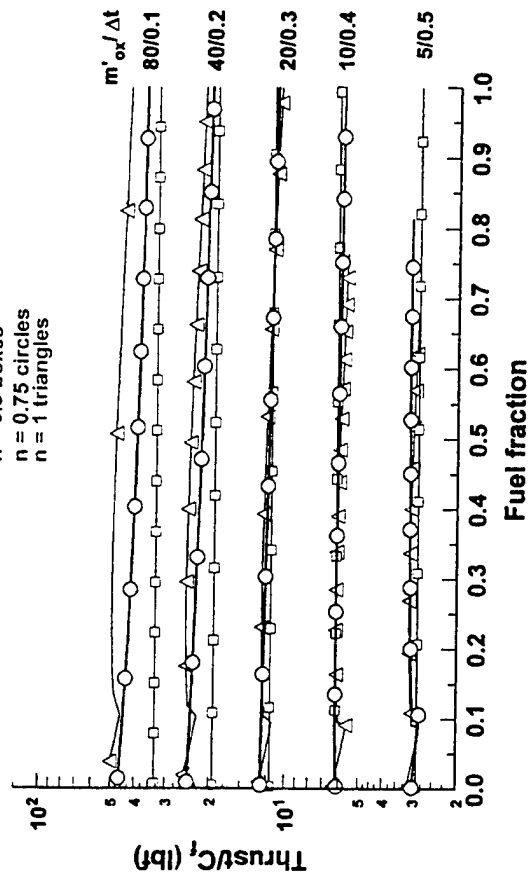
Figure 5b. Calculated F*eq for uniform burns of solid pentane, L = 7.5 cm.

Figure 9. Experimental traces of outside tube wall temperatures for Run 128.
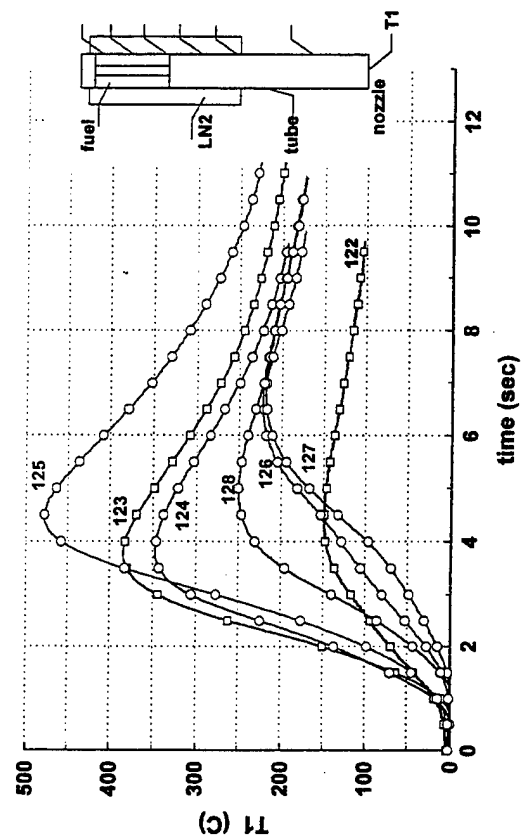
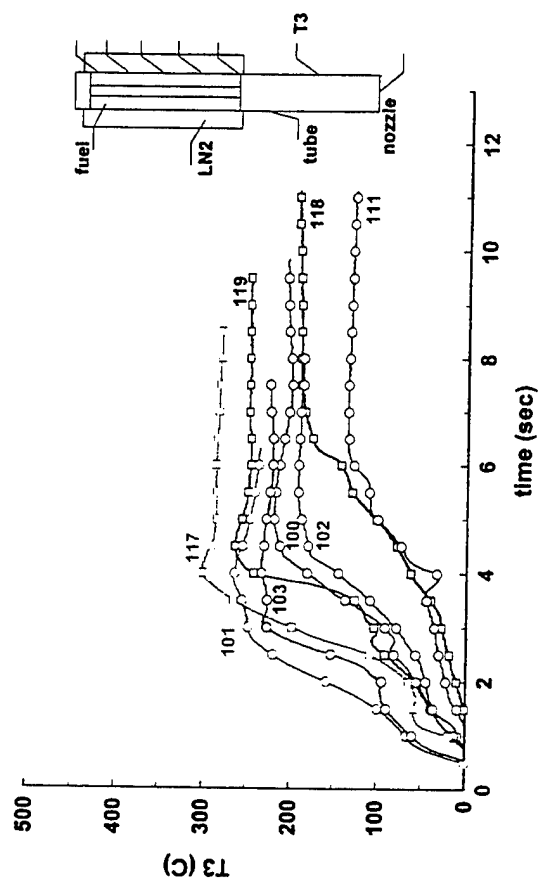Figure 10. Experimental traces of nozzle throat temperature for short fuel cylinders.

Figure 7. Comparison of normalized experimental thrust profiles for runs 128, 122 and 100 with m'_{ox} of 14.3, 10.8 and 11.6 g/s, respectively.

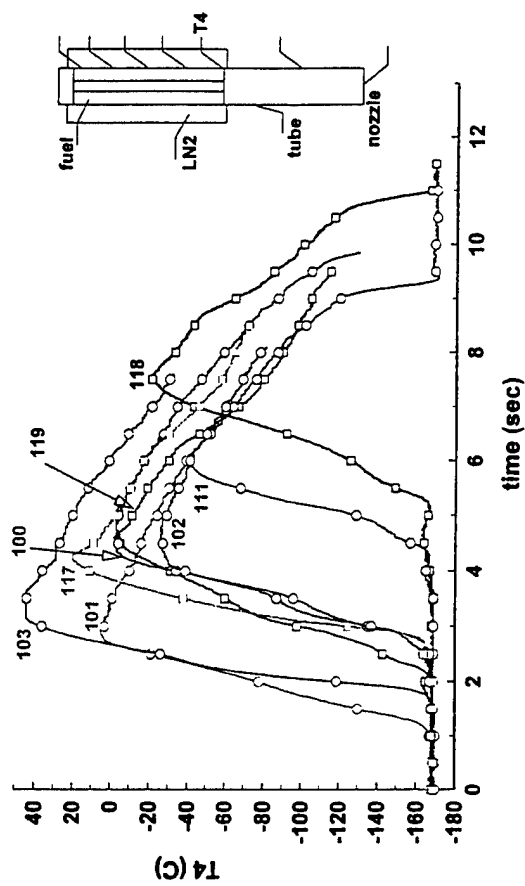Figure 8. Comparison of calculated I^*_{eq} and experimental I_{exp}.

205

Figure 12a. Experimental traces of T4 in burns of 15 cm pentane cylinders.

Figure 12b. Experimental traces of T4 in burns of 7.5 cm pentane cylinders.

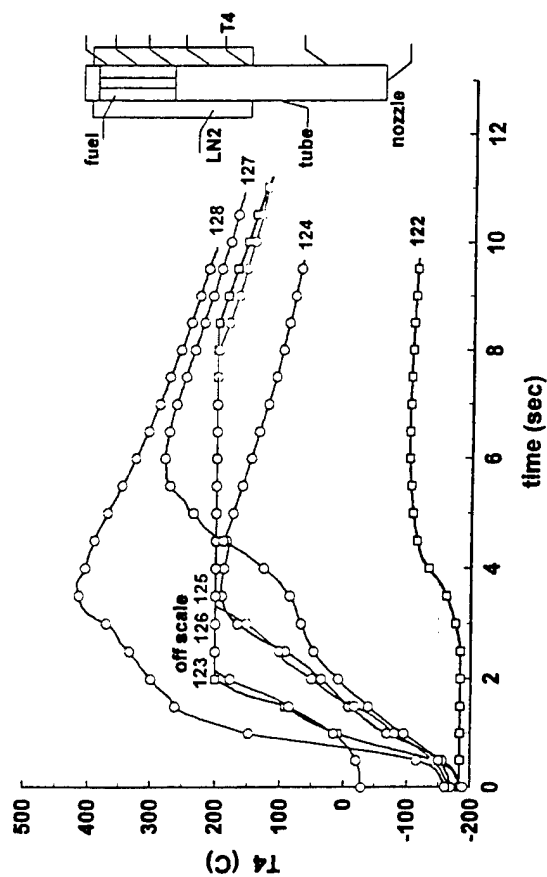Figure 11a. Experimental traces of T3 in burns of 15 cm pentane cylinders.

Figure 11b. Experimental traces of T3 in burns of 7.5 cm pentane cylinders.

206

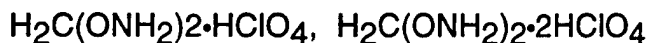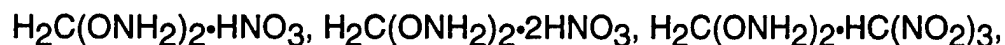# Progress in the Synthesis of Novel Energetic Salts

Mark A. Petrie, Tom W. Hawkins, Karl O. Christe,
Jeffrey A. Sheehy, Jerry A. Boatz, and Paul Jones
Hughes STX and Propulsion Sciences Division, Edwards Air Force Base,
CA 93524-7680

Progress was made in the synthesis of new energetic salts which may be useful as energetic additives to liquid monopropellant and bipropellant formulations. Several salts of the energetic trinitromethanide anion, $C(NO_2)_3^-$ were prepared, $H_3NOH^+C(NO_2)_3^-$ (HANF), $MeONH_3^+C(NO_2)_3^-$ (MOANF), and $H_2C(ONH_2)_2H^+$ $C(NO_2)_3^-$ (MBOANF). Two of the salts exhibit thermal stability rarely observed for the ammonium salts of trinitromethanide. Other salts of the interesting methylene bisoxyamine, $H_2C(ONH_2)_2$ (MBO) were synthesized and characterized. The nitrocyanamide anion, O_2NNCN^- was synthesized and charcterized.

The undesirable long-term decomposition characteristics of the $HONH_3^+$ salt of $C(NO_2)_3^-$ led to the synthesis of substituted $RONH_3^+$ and $HONRH_2^+$ salts. The addition of an O-methyl group $MeONH_3^+$ increases the sensitivity of the nitroformate salt. The addition of water to the salt substantially decreases the impact sensitivity. The salt dissociatively evaporates ($MeONH_2$ + $HC(NO_2)_3$) at ambient temperature and exhibits relatively high thermal stability (<2% mass loss at 60°C for 72h). The compound was further characterized by Raman, FT-IR, DSC, and TGA.

Encouraged by the thermal properties of MOANF, we sought similar salts with reduced volatility. The higher basicity and lower volatility of the methylene bisoxyamine, $H_2C(ONH_2)_2$ (MBO) (b.p. 47-50°C/0.3 mmHg) molecule compared to $MeONH_2$ (b.p. 48/760 mmHg) led to the preparation of several new salts of MBO. Dr. C. Merrill of Phillips Laboratory first prepared MBO and its diperchlorate salt in 1969. MBO was proposed to be a higher performing monopropellant replacement for hydrazine, however, the slight impact sensitivity of MBO (60 kg•cm) quenched efforts in this area. Methylene bisoxyamine is synthesized[1] from readily available starting materials. Since

other salts of this molecule have not been reported, the following salts were synthesized by acid-base reaction of MBO and the corresponding acid;

$$H_2C(ONH_2)_2 \cdot HNO_3, \quad H_2C(ONH_2)_2 \cdot 2HNO_3, \quad H_2C(ONH_2)_2 \cdot HC(NO_2)_3,$$

$$H_2C(ONH_2)2 \cdot HClO_4, \quad H_2C(ONH_2)_2 \cdot 2HClO_4$$

These salts were characterized by X-ray crystallography, IR, Raman, DSC, TGA, impact and friction sensitivity, and short term thermal stability studies. The x-ray crystal structure of the MBO salt of $HC(NO_2)_3$ shows that the acidic protons are located between bridging $H_2C(ONH_2)_2$ molecules. I_{sp} calculations have shown that these salts in alcohol solution offer significant performance potential ($I_{sp} > 300s$) over that of hydrazine ($I_{sp} \sim 232s$).

There is interest in using the energetic nitrocyanamide anion as an additive in monopropellant formulations or eutectics. It was first prepared in 1950 by A.F. McKay[2] and co-workers. Several salts of nitrocyanamide were prepared by S.R. Harris[3] to test their suitability as initiating explosives under contract by the U.S. Army. Since structural and spectroscopic data were not available, we have thoroughly characterized the O_2NNCN^- anion. The X-ray crystal geometry of the O_2NNCN^- anion and vibrational spectra for KO_2NNCN, NaO_2NNCN and Me_4NO_2NNCN were obtained, and compared to the geometry and vibrational spectra calculated at the SCF/cc-pVDZ, B3LYP/cc-pVDZ and CCSD(T)/cc-pVDZ levels of theory. Experimental and calculated data indicate that in the minimum-energy structure of O_2NNCN^-, the NO_2 group is essentially coplanar with the plane defined by the atoms NNCN. In nitrocyanamide, the substitution of one NO_2 group with a nearly linear cyano group removes the steric repulsion between the NO_2 groups observed in the structure of dinitramide, $N(NO_2)_2^-$. The NCN moiety is nonlinear due to repulsion between the non-bonded electron pairs on the central nitrogen and the electrons of the CN triple bond. Large thermal motion parameters for the position of the O(2) atom were observed. Two single crystal X-ray data sets of KO_2NNCN collected at different temperatures (123K and 173K), rule out thermal effects since the O(2) atom deviations

were very similar. The O(2) atom probably occupies two or more positions in the crystal due to lattice effects. The bands in the Raman and IR spectra of O_2NNCN^- anion have been assigned by comparison to computed frequencies. Splitting of some bands associated with the stretching modes of the NO_2 group are thought to occur from solid state effects. Despite numerous attempts, the X-ray crystal structure of the Me_4NO_2NNCN salt gave a disordered structure indicative of crystal twinning.

---

1) C.S. McDowell, C.I. Merrill, and M.W. Barnes, Technical Report AFRPL-TR-69-174, September 1969.

2) A.F. McKay et al., Can. J. Research, 28B, 683 (1950).

3) S.R. Harris, JACS, 80, 2302, (1958).

Chemistry at the Limits of Coordination

Drake, G. W. ; Christe, K. O. ; Wilson, W. W. ; Petrie, M. A. ; Gnann, R. Z. ; Wagner, R. I. ; Dixon, D. A.

National Research Council, Washington, D.C., 20418; Hughes STX, Edwards Air Force Base, CA, 93524; Loker Hydrocarbon Research Institute, University of Southern California, Los Angeles, CA; Pacific Northwest National Laboratories, Richland, WA, 99352.

High coordination anion chemistry has developed rapidly in the last decade most notably in the field of binary fluorides. The discovery of a truly anhydrous fluoride source, tetramethylammonium fluoride, $(CH_3)_4NF$ [1], has led to a renaisssance in main group chemistry. Tetramethylammonium fluoride is thermally stable, soluble in organic solvents, and surprisingly resistant to powerful oxidizers such as ClF_3, BrF_5, and IF_7. Many new anions have been synthesized and characterized through the use of this fluoride source. [2-6] However, relatively few dianions have been studied and characterized to date, including XeF_8^{2-} [7-10], $TeOF_6^{2-}$ [4], TeF_8^{2-} [5], and MF_5^{2-} (M = As, Sb, Bi) [11]. Problems plaguing the study of new dianions include poor solubility in solution, and the equilibrium between the dianion and its monoanion and fluoride precursors. Several new fluorodianions have been synthesized, characterized through vibrational spectroscopy, and compared to theoretical calculations.

The reinvestigation of an original sample of "Cs_3IF_6" [12] found strong evidence that the sample is actually a mixture of Cs_2IF_5 and CsF rather than Cs_3IF_6. This conclusion has been drawn from the fact that the sample had a Raman band pattern very similar to that reported for the recent, structurally characterized XeF_5^- [13]. The infrared spectrum and x-ray powder spectrum of "Cs_3IF_6" contained bands indicative of large amounts of CsF.

The IF_5^{2-} dianion can also be formed in acetonitrile at low temperatures through the reaction of tetramethylammonium fluoride and IF_3. It can be made either stepwise through the well known IF_4^-, or by the reaction of two equivalents of tetramethylammonium fluoride with IF_3. Theoretical calculations were carried out at the SCF/ECP level of theory where a minimum was found for the pentagonal planar D_{5h} structure. The observed vibrational spectra are in excellent agreement with those calculated for pentagonal planar IF_5^{2-} and with those found for isoelectronic, pentagonal planar XeF_5^-.

The IF_7^{2-} dianion has been prepared by several routes in our laboratory. Two routes involve vacuum pyrolyses, which were carried out in sapphire tube reactors. It was first found that heating a mixture of $KIF_6 \cdot nIF_7$ resulted in the formation of K_2IF_7 with IF_7 and IF_5. Later, it was found that heating pure KIF_6 led to K_2IF_7 and IF_5. The IF_7^{2-} dianion can also be synthesized through the reaction of $(CH_3)_4NF$ with IF_5 in acetonitrile at room temperature. The vibrational spectra of K_2IF_7 are very similar to those of the structurally characterized and isoelectronic $CsXeF_7$[14], indicating the same C_{3v} monocapped octahedral structure.

Presently, there are no nine-coordinate main group AX_9 species known. Theoretical calculations for IF_9^{2-} show that a slightly distorted D_{3h} structure is vibrationally stable. This structure is very reminiscent of the well known ReH_9^{2-}[15] structure. To date, laboratory efforts have not been successful. The reaction of either two or three equivalents of CsF with IF_7 at high temperatures in a monel cylinder under a fluorine

atomsphere has failed. The reactions of $(CH_3)_4NF$ with IF_7 in cold acetonitrile, either stepwise through IF_8^- [4], or all at once, also were unsuccessful.

SbF_5 and BiF_5 are strong Lewis acids which react quantitatively with a fluoride ion source forming the well known octahedral SbF_6^- and BiF_6^- species. From the known existence of TeF_8^{2-} [4, 16-17], whose precursor TeF_6 has a similar fluoride affinity as BiF_5 [18], the formation of SbF_7^{2-} and BiF_7^{2-} through the reaction of excess CsF with the corresponding Lewis acid seemed reasonable. In the case of SbF_5, only partial conversion to SbF_7^{2-} was achieved with a 2:1 CsF/SbF_5 reaction mixture. Even using a 3:1 CsF/SbF_5 ratio, the product still contained some $CsSbF_6$. For Bismuth, it was found that a 2:1 ratio of CsF/BiF_5 gave a high conversion to Cs_2BiF_7, but there was still some $CsBiF_6$ present., The Raman signals due to BiF_6^- diminished by raising the temperature of the reaction to 300 °C. Bismuth pentafluoride reacted smoothly with $(CH_3)_4NF$ at low temperatures in acetonitrile to form the BiF_7^{2-} dianion. In the case of SbF_5, reaction with a large excess of $(CH_3)_4NF$ in acetonitrile or sufur dioxide, gave exclusively the SbF_6^- anion. The vibrational frequencies for the SbF_7^{2-} dianion were calculated at the SCF/ECP level of theory with a minimum being found for the pentagonal bipyramidal D_{5h} structure. The calculated frequencies and intensities agreed well with the ones found for Cs_2SbF_7. The vibrational frequencies for the BiF_7^{2-} dianion were calculated at the HF level of theory using DZP(F) and ECP/DZP(Bi) basis sets, which also found a minimum for the pentagonal bipyramidal D_{5h} structure. Again, the calculated frequencies and intensities agreed well with the observed ones.

In summary, several new doubly charged anions, IF_5^{2-}, IF_7^{2-}, SbF_7^{2-}, and BiF_7^{2-} have been prepared and characterized. IF_5^{2-} and IF_7^{2-} are only the second known examples of a pentagonal planar AX_5E_2 and a monocapped octahedral main group AX_7E species, respectively. BiF_7^{2-} and SbF_7^{2-} are the first examples of seven coordinate AX_7 pnictogens, and both dianions adopt a pentagonal bipyramidal structure.

References

1. Wilson, W. W. ; Christe, K. O. ; Feng, J. ; Bau, R. J. Amer. Chem. Soc. **1990**, *112*, 7619.

2. Christe, K. O. ; Curtis, E. C. ; Dixon, D. A. ; Mercier, H. P. ; Sanders, J. C. P. ; Schrobilgen, G. J. J. Am. Chem. Soc. **1991**, *113*, 3351.

3. Christe, K. O. ; Wilson, W. W. ; Chirakal, R. V. ; Sanders, J. C. P. ; Schrobilgen, G. J. Inorg. Chem. **1990**, *29*, 3506.

4. Christe, K. O. ; Sanders, J. C. P. ; Schrobilgen, G. J. ; Wilson, W. W. J. Chem. Soc. Chem. Commun. **1991**, 837.

5. Christe, K. O. ; Wilson, W. W. ; Dixon, D. A. ; Mercier, H. P. ; Sanders, J. C. P. ; Schrobilgen, G. J. ; Majjoub, A. R. ; Seppelt, K. J. Am. Chem. Soc **1993**, *115*, 2696.

6. Christe, K. O. ; Wilson, W. W.; Schrobilgen, G. J.; Dixon, D. A. J. Amer. Chem. Soc. **1997**, *119*, 3918.

7. Peacock, R. D. ; Selig, H. ; Sheft, I. J. Inorg. Nucl. Chem. **1966**, *28*, 2561.

8. Moody, G. J. ; Selig, H. Inorg. Nucl. Chem. Lett. **1966**, *2*, 319.

9. Peterson, S. W. ; Holloway, J. H. ; Coyle, B. A. ; Williams, J. M. Science **1971**, *173*, 1238.

10. Christe, K. O. ; Wilson, W. W. Inorg. Chem. **1982**, *21*, 4113.

11. Greenwood, N. N. ; Earnshaw, A. "Chemistry of The Elements" Pergamon Press, Oxford, **1984**, pp 659-661.

12. Schmeisser, M. ; Sartori, P. ; Naumann, D. Chem. Ber. **1970**, *103*, 590.

13. Christe, K. O. ; Curtis, E. C. ; Dixon, D. A. ; Mercier, H. P. ; Sanders, J. C. P. ; Schrobilgen, G. J. J. Amer. Chem. Soc. **1991**, *113*, 3351.

14. Ellern, A. ; Mahjoub, A-R. ; Seppelt, K. Angew. Chem. Int. Ed. Engl. **1996**, *35*, 1123.

15. Abrahamas, S. L. ; Ginsberg, A. P. ; Knox, K. Inorg. Chem. **1964**, *3*, 558.

16. Muetterlies, E. L. J. Amer. Chem. Soc. **1957**, *79*, 1004.

17. Selig, H. ; Sarig, S. ; Abramowitz, S. Inorg. Chem. **1974**, *13*, 1508.

18. Christe, K. O. ; Dixon, D. A. ; Wilson, W. W. unpublished results.

Theoretical Determination of the Heats of Formation of Prospective Strained-Ring Rocket Fuels

J.A. Boatz and J.D. Mills

OLAC PL/RKS
Propulsion Directorate
Propulsion Sciences Division
US-AFRL/Phillips Laboratory
Edwards AFB, CA 93524-7680

ABSTRACT

The gas-phase heats of formation of seven unusual strained and substituted organic molecules ranging in size from C_6H_8 to $C_{17}H_{24}N_4O_8$ have been determined using the parallel version of the GAMESS quantum chemistry code. Molecular energies obtained by a number of methods, ranging from the semi-empirical through Hartree-Fock, 6-31(d) geometry optimization and force-constant evaluation with MP2, 6-31(d) single-point energy calculation, have been combined with experimental information to provide the necessary composite thermodynamic parameters. In addition, a variety of resource-tailored strategies for employing these values, some relying upon investigation of the target compound alone and others involving suitable isodesmic reactions, have been critically evaluated and compared with results obtained from the wholly empirical Benson additivity rules. Within the present set of reference molecules, this computation-free approach compares favorably with all but the highest level theoretical treatments.

A. Introduction

As a measure of the intrinsic energy content of a substance, the standard enthalpy of formation, the energy required for its formation from the elements in their standard states under conventional thermodynamic conditions, constitutes a critical parameter for the evaluation of a candidate propellant's likely performance. Since chemical synthesis of even small quantities of novel chemical compounds can be extremely resource intensive, it is desirable to narrow the search for new materials to only those candidates which show particular promise. In order to be of use to propellant chemists, theoretical predictions of molecular heats of formation must meet the often conflicting criteria of timeliness, affordability, and accuracy. Thus, when encountering a set of perhaps rather speculative proposed fuels, a rapid and approximate preliminary screening procedure might be productively employed in advance of initial experimental investigations and more extensive, and presumably more accurate, theoretical treatments. To these ends the research reported herein is not merely motivated by the quest for the heats of formation of a few specific molecules of present interest but, with a view toward future needs, also gives particular emphasis to evaluating and comparing a variety of established, progressively more expensive theoretical methods within a diverse set of strained molecules of the sort of interest as high-energy propellants.

Specifically, this work reports results of calculations of the ideal-gas enthalpies of formation, $\Delta H_f^\ddagger \equiv \Delta H_{f,\text{id gas}}^{298\,\text{K}}$, of the following seven compounds made

or proposed by synthetic chemists in the Propulsion Sciences Division of the Propulsion Directorate, Air Force Research Laboratory.
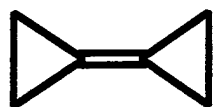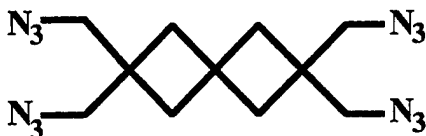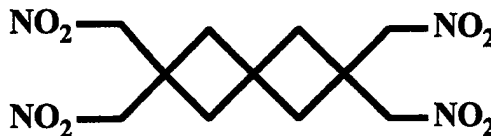

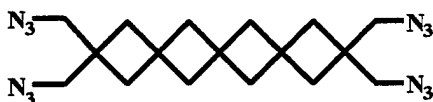1: bicyclopropylidene
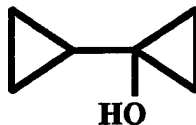
2: 1-cyclopropyl-
   cyclopropan-1-ol

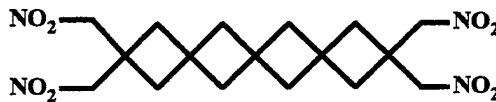3: 2,6-dioxa-
   spiro[3.3]heptane

4: 2,2,6,6-tetra(azidomethyl)-
   spiro[3.3]heptane

5: 2,2,6,6-tetra(nitromethyl)-
   spiro[3.3]heptane

6: Higher spiro analogue of 4

7: Higher spiro analogue of 5

In addition, the specific impulse, a parameter derived from the enthalpy of formation and more directly indicative of the performance of a molecule in a rocket application, is reported for each.

B. Theoretical Methods for the Calculation of Heats of Formation

There follows a brief survey of some of the more common methods devised for the prediction of molecular heats of formation. A more complete account is provided in a subsequent publication.[1] These approaches may be broadly classified in a number of ways; for present purposes, they are discriminated according to their methodological nature or scope as well as by the more practical criteria of the expense of the calculations which supply their requisite composite parameters.

1. Broad Methodological Classes

Two criteria may be used to classify the methodology of a determination of the molecular heat of formation. First of all, some approaches involve characterization of only the molecule of primary interest (hereafter the "target molecule"), in contrast to those to be discussed subsequently, which seek some cancelation of errors by utilizing the change in energy of a reacting set of molecules.

Of the single-molecule methods considered here, the second criterion, that of additivity, can be employed to further discriminate between those which rely upon the approximate transferability of energetic contributions of chemical moieties such as atoms, bonds, or functional groups (hereafter labeled as *ab lateribus* (literally "from the bricks")) and those which conceive of molecules as complete, fully interacted systems, indivisible to the level of fundamental quantum-chemical

---

[1] J.D. Mills, *Technical Report*, in preparation.

215

particles ("single-whole-molecule" approaches). In these latter methods, the calculated quantum-chemical molecular energy, that is, the energy of interaction of the composite electrons and nuclei, may differ from the enthalpy of formation, referenced to the energies of the elements, by several orders of magnitude. Therefore it is common to adjust the molecular energies by a variety of means in order to correct relatively small errors, either in conjunction with or in advance of incorporation of elemental energies and thermodynamic effects.

An alternative means of correcting minor errors in whole-molecule energies is to broaden the calculation to include a group of well-characterized reacting compounds containing, in some sense, similar chemical environments or groups ("reaction-based" approaches) and to take advantage thereby of a partial cancelation of errors between the calculated energies of fully interacted reactants and products. These approaches then separately include the thermodynamic effects of non-zero temperature.

As ordered here, the methods become generally more complicated and, other things being equal, are expected to be more accurate. They also, however, become progressively more subjective, as for example in the selection of the most appropriate reaction between "most similar" reactants and products. Each of the three classes already described are more definitively characterized by the following formulae.

a. Class A–*Ab Lateribus* Methods

The enthalpy of formation of the target molecule may be composed as a simple sum of the combined energetic and thermodynamic contributions of composite chemical groups as:

$$\Delta H_f^\dagger = \sum_{j,\,groups} \Delta H_{f,j} \tag{1}$$

where the groups may be operationally defined in a number of ways so as to ensure maximum accuracy and transferability between different molecules.

b. Class B–Additively Corrected Single-Whole-Molecule Methods

Within this work, methods limited to the fully interacted target combine whole-molecule energies with additivity-based corrections, as:

$$\Delta H_f^\dagger = E_{mol} + \sum_{j,\,groups} \Delta H_j \tag{2}$$

somewhat in the spirit of *ab lateribus* approaches. These undifferentiated adjustments are designed to incorporate thermodynamic effects as well as ameliorate calculational deficiencies.

c. Class C–Reaction-Based Methods

In the present research isodesmic or "bond-preserving" reactions, those in which there are the same number and type of formal bonds in the sets of reactants and products,[2] are used to determine molecular heats of formation from

---

[2] W.J. Hehre, R. Ditchfield, L. Radom, and J.A. Pople, *J. Am. Chem. Soc.*, **92**, 4796 (1970).

calculated reaction energies. The procedure by which this is effected is perhaps best illustrated with a specific example. The third target compound, 2,6-dioxaspiro[3.3]heptane, could be isodesmically deconstructed as:

$$4\,CH_4 + O\!\!\diagdown\!\!\diagup\!\!\diagdown\!\!\diagup O \rightarrow 2\,CH_3\text{-}O\text{-}CH_3 + C(CH_3)_4, \qquad (3)$$
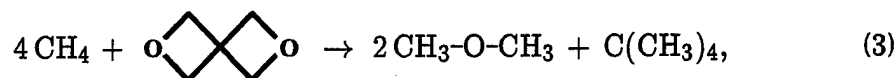
the corresponding reactions for the remaining target molecules being suggested by the list of "non-target" or isodesmic-partner compounds listed in Table (D). For each target molecule, the ideal-gas enthalpy of formation is then constructed from:

$$\Delta H_f^{\dagger} = \Delta(\Delta H_f'^{\dagger}) - \left[\Delta E_{eq} + \Delta E_{zp} + \Delta(H_{298K} - H_{0K})\right] \qquad (4)$$

where each component is defined below, first in general notation, and then, as seems illuminating, in application to the example reaction. The first parameter:

$$\Delta(\Delta H_f'^{\dagger}) \equiv \sum_{\substack{i' \text{ molecules,} \\ \text{not target}}} \nu_{i'}\, \Delta H_f^{\dagger}(i')$$

$$= 2\,\Delta H_f^{\dagger}(CH3\text{-}O\text{-}CH3) + \Delta H_f^{\dagger}(C(CH_3)_4) - 4\,\Delta H_f^{\dagger}(CH_4) \qquad (5)$$

is just the stoichiometrically weighted difference of known heats of formation of all molecules in the reaction except the target. The quantity enclosed in square brackets in equation (4) is just the standard-temperature reaction enthalpy and is composed of three parts:

$$\Delta E_{eq} \equiv \sum_{i, \text{molec.}} \nu_i\, E_{eq}(i)$$

$$= 2\,E_{eq}(CH3\text{-}O\text{-}CH3) + E_{eq}(C(CH_3)_4) - 4\,E_{eq}(CH_4) - E_{eq}(O\!\!\diagup\!\!\diagdown\!\!\diagup\!\!\diagdown O)$$

$$\Delta E_{zp} \equiv \sum_{i, \text{molec.}} \nu_i\, E_{zp}(i)$$

$$\Delta(H_{298K} - H_{0K}) \equiv \sum_{i, \text{molec.}} \nu_i\, (H_{298K}(i) - H_{0K}(i)) \qquad (6)$$

which are similar differences, this time including all participants in the reaction, of, respectively, the energies of the molecules at their theoretical equilibrium geometries, shifts due to zero-point energy, and the "heat capacity correction" which incorporates the enthalpic effects of the standard temperature. To the extent that the structural environments are similar on both sides of the reaction and errors in a calculation are similar for any given type of environment, much of any error is expected to cancel in the indicated differences.

2. Calculational Method

Within each methodological class, specific approaches can be further divided according to the means employed to supply the parameters just described. In the interests of determining the relative value of each method in a resource-limited environment, it seems appropriate to organize the approaches in terms of their computational expense. Therefore, labels indicating the final step in a

Table (A)	
Calculation Type by Computational Expense	
Label	**Terminal Calculation Step**
I	No computation
II	Semi-Empirical Geometry Optimization and Hessian
III	Hartree-Fock Geometry Optimization
IV	Hartree-Fock Hessian at Minimum Energy Geometry
V	MP2 Energy at HF Optimum Geometry

succession of calculations (Table (A)) will be used hereafter, in addition to the methodological class index already described, to delineate each specific approach; in the same context, the label, Exp, will be used to denote an experimental value.

For the computations performed for this study, the semi-empirical calculations, although involving the same effort as their more sophisticated counterparts to specify the geometry and prepare the input files, consumed negligible computer time. In contrast, each succeeding step (III-V) described in Table (A) was found to require a significant and roughly comparable additional expenditure of resources.

3. Details of Present Methods

a. Method IA–Benson Group Additivity

Although a number of computation-free, *ab lateribus* methods have been devised, this work considers only the most common, the Benson group-additivity prescription.[3] Based wholly upon comparison with experiment, representative enthalpic contributions of chemical groups, each generally a single atom discriminated according to its bonding partners, have been tabulated and may be quite readily applied to many molecules with classical chemical structures.

b. IIB Methods–Semi-Empirical Values

A number of computational codes directly report semi-empirical enthalpies of formation after shifting the fully interacted molecular energy by atom-based adjustments derived from experimental and theoretical considerations.[4] Results of this type are denoted hereafter with the label IIB followed by a parenthetical indication of the semi-empirical Hamiltonian used.

c. Method IIIB–Ibrahim/Schleyer Hartree-Fock Atom Equivalents

Similarly, Ibrahim and Schleyer,[5] within a reference set of molecules for which accurate experimental values are known, found an optimum set of atom-based shifts which yield heats of formation from the total, Hartree-Fock molecular energy. These factors subsume energetic and thermodynamic effects, as well as corrections for computational deficiencies.

[3] S.W. Benson, *Thermochemical Kinetics*, Second Ed., (Wiley, New York, 1976), references cited therein, and H.-D. Beckhaus, C. Rüchardt, S.I. Kozhushkov, V.N. Belov, S.P. Verevkin, and A. de Meijere, *J. Am. Chem. Soc.*, 117, 11854 (1995).

[4] J.J.P. Stewart, *J. Comput. Chem.*, 10, 209 (1989).

[5] M.R. Ibrahim and P.v.R. Schleyer, *J. Comput. Chem.*, 6, 157 (1985). A few additional parameters were determined by the present author.

Table (B)				
Origin of Parameters (Eqns. (5) and (6)) for Reaction-Based Methods by Calculation Level				
Method	$\Delta H_f^\dagger(i')$	$E_{eq}(i)$	$E_{zp}(i)$	$H_{298K}(i)-H_{0K}(i)$
IIC	Exp/G2	SE	SE(sc)	Exp/SE(sc)
IIIC	Exp/G2	HF	SE(sc)	Exp/SE(sc)
IVC	Exp/G2	HF	HF(sc)	Exp/HF(sc)
VC	Exp/G2	MP2	HF(sc)	Exp/HF(sc)

d. Reaction-Based Methods–Class C

The sources of the parameters described in equations (5) and (6) for each of the reaction-based methods are summarized in Table (B). The labels, SE, HF, MP2, and G2 denote calculation by semi-empirical, Hartree-Fock, second-order Møller-Plesset, or G2 methods, respectively. Semi-empirical calculations utilized the MNDO, AM1, and PM3 Hamiltonians, as will be indicated by a parenthetical addition to the method label, and Hartree-Fock and MP2 calculations were performed in the 6-31G(d) basis. The label, Exp, followed by a theoretical level indicates the use of available experimental values, either direct or indirect,[6] in preference to those of theory and (sc) marks theoretical thermodynamic values for which the vibrational frequencies have been multiplicatively scaled (Hartree-Fock/6-31G(d)-0.89[7] and semi-empirical: MNDO-0.91, AM1-0.95, PM3-0.97, as determined by the present author by comparison of the zero-point energies of target and non-target molecules with scaled Hartree-Fock values).

4. Computational Considerations

All calculations utilized the serial and parallel versions of the GAMESS computational code[8] and were performed on IBM RS/6000 workstations at AFRL and tens of nodes of the IBM SP machines at the Maui High Performance Computing Center and the Aeronautical Systems Center, Major Shared Resource Center. The largest *ab initio* calculations involved molecules with no symmetry and 483 basis functions and consumed several node-months on the IBM SP.

Quick turn-around and high through-put are enabled by the extensive parallelization implemented in the program. For example, as compared with sequential mode, one sample MP2 calculation ran with around ninety-percent efficiency on eight nodes.

C. Results and Discussion

1. Molecular Geometries

Hartree-Fock optimization indicates that molecules 1 and 3 have the respective D_{2h} and D_{2d} configurations suggested by chemical intuition and that

---

[6] Experimental values from correlation of, J.B. Pedley, R.D. Naylor, S.P. Kirby, *Thermochemical Data of Organic Compounds*, Second Ed., (Chapman-Hall, London, 1986), pp. 89ff.

[7] J.A. Pople, H.B. Schlegel, R. Krishnan, D.J. Defrees, J.S. Binkley, M.J. Frisch, R.A. Whiteside, R.F. Hout, and W.J. Hehre, *Int. J. Quantum Chem.: Quantum Chem. Symp.*, 15, 269 (1981).

[8] M.W. Schmidt, K.K. Baldridge, J.A. Boatz, S.T. Elbert, M.S. Gordon, J.H. Jensen, S. Koseki, N. Matsunaga, K.A. Nguyen, S. Su, T.L. Windus, M. Dupuis, and J.A. Montgomery, Jr., *J. Comput. Chem.*, 14, 1347 (1993).

these minima constitute the only thermodynamically relevant geometries. In contrast, molecule 2 seems to have no symmetry and the Hartree-Fock potential energy surface exhibits three degenerate pairs of closely lying (within ~1 kcal/mol) enantiomeric minima. This is expected to modestly degrade the quality of the thermodynamic predictions reported herein, as they assume a single harmonic minimum.

The four remaining compounds were initially subjected to an optimization constrained by D_{2d} symmetry with, on each end of the molecule, the nitrogen-containing groups directed away from one another and the distal methylene hydrogens eclipsed after the manner of propane. Although computation of the full Hessian revealed only real frequencies for one of the molecules, the remaining three had "imaginary frequencies" (magnitude ≤ 34 cm^{-1}) indicating that these are not equilibrium, minimum-energy structures. By sampling a number of geometries resulting from rotation about the distal C-C and C-N bonds, for each molecule an almost degenerate pair of "constrained minima" of D_2 and S_4 symmetry were found to have an energy fully 4 to 7 kcal/mol below the corresponding D_{2d} structures. However, vibrational analysis indicated that each was not a local minimum on the full potential energy surface. Only by allowing non-planarity in the spiro-linked cyclobutane rings (as in cyclobutane itself) were true local minima discovered. A number of combinations of physically justifiable ring-bending distortions starting from both the D_2 and S_4 geometries were sampled and several nearly iso-energetic minima were elucidated. For each molecule the most stable geometries have no symmetry and lie fully 5 to 11 kcal/mol below the D_{2d}-constrained optima. The principal hope that these indeed constitute global minima rests upon the progressive diminution of the stabilization energy with each successive type of distortion from D_{2d} and the extensive, but admittedly not exhaustive, sampling of the alternatives. In any case, deficiencies in the thermodynamic predictions due to the presence of multiple, low-lying minima and an anharmonic, relatively flat potential energy surface are again likely to be manifest.

2. Enthalpies of Formation

Calculated heats of formation for both target and non-target molecules are presented in Tables (C)-(E). For the first two classes of methods, those limited to a single molecule (A and B), results for the target molecules, Table (C), may be compared with those for the non-target molecules, Table (D). As evidenced by the root-mean-squared deviations from either experimental values (RMS(Exp)) or (in lieu of experimental information) the highest level theoretical predictions (RMS(VC)), the computation-free, *ab lateribus* method of Benson clearly outperforms the other tabulated approaches. This appears to be true, not only for the non-target set containing relatively small and simple systems expected to be well-represented among the reference molecules of parameterized empirical methods, but also for the target compounds as well. Although these latter systems have well-characterized classical chemical structures, they, not unexpectedly, manifest predicted heats of formation with a much stronger overall variance, either by virtue of their size or because of the unique character of their strained binding.

The predicted target heats of formation displayed in Table (E) for the reaction-based methods (class C) indicate that the use of isodesmic reactions
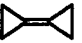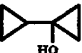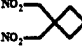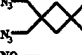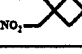
Table (C)
Target-Molecule $\Delta H_f^\ddagger$ (kcal/mol)
Ab Lateribus (A) and Single-Whole-Molecule (B) Methods

Molecule	IA	IIB(MNDO)	IIB(AM1)	IIB(PM3)	IIIB
1:	86.6	61.8	79.9	74.0	83.8
2: (HO)	-8.5	-12.4	-0.4	-5.4	-9.1
3: (O...O)	-26.9	-62.0	-36.8	-44.6	-30.2
4: (N₃ substituents)	320.6	307.3	342.7	306.8	281.1
5: (NO₂ substituents)	-19.8	68.5	1.6	-26.1	-27.4
6: (N₃ substituents)	354.3	313.8	365.5	316.2	308.7
7: (NO₂ substituents)	13.9	73.3	24.9	-18.1	-1.4
RMS Dev. vs. VC, RMS(VC)	11.9	52.9	23.5	13.2	19.0

Table (D)
Non-Target-Molecule $\Delta H_f^\ddagger$ (kcal/mol)
Ab Lateribus (A) and Single-Whole-Molecule (B) Methods Compared with Experiment

Molecule	IA[a]	IIB(MNDO)	IIB(AM1)	IIB(PM3)	IIIB[a]	Exp
CH_4	-15.3[b]	-11.9	-8.8	-13.0	-17.0	-17.8 ± 0.1
CH_3N_3		66.4	76.7	69.9	60.7	71.0[c]
CH_3NO_2		3.3	-9.9	-15.9	-17.9	-17.8 ± 0.1
C_2H_6	-20.4	-19.7	-17.4	-18.1	-20.1	-20.0 ± 0.1
CH_3OCH_3	-43.6	-51.2	-53.2	-48.3	-43.6	-44.0 ± 0.1
$CH_3CH_2CH_3$	-25.3	-24.9	-24.3	-23.6	-25.2	-25.0 ± 0.1
cyclopropane	12.8	11.2	17.8	16.3	13.6	12.7 ± 0.1
$C(CH_3)_4$	-40.3	-24.6	-32.8	-35.8		-40.2 ± 0.2
t-BuOH	-75.1	-64.3	-71.6	-71.3	-68.8	-74.7 ± 0.2
(structure)	-17.1	-13.2	-16.3	-21.9	-10.1	-16.3 ± 0.3
RMS(Exp)	1.0	9.6	6.0	3.6	4.5	

[a] Absent results constitute the sole value in a parameter reference set and so are identical to the experiment by definition.
[b] From bond additivity rules.
[c] G2 theoretical result from: D.W. Rogers and F.J. McLafferty, *J. Chem. Phys.*, **103**, 8302 (1995).

tends to increase the quality of the results obtained using a given calculational level. Further, none of the methods, including the next most sophisticated requiring the rather expensive Hartree-Fock optimum geometry and Hessian, significantly out-performs the Benson *ab lateribus* method. In addition, it will be noted that the method labeled IIC(PM3) seems roughly competitive with the Benson rules. Although this computationally economical semi-empirical method

does require more human effort, it may be useful in cases in which suitable *ab lateribus* parameters are not available. Its utility for systems lacking classical chemical structures certainly bears further examination.

It must be conceded, however, that all characterizations of target-molecule results, heretofore, rest upon the assumption that the most expensive method, VC (or, in conventional notation, MP2/6-31G(d)//HF/6-31G(d)), closely, or at least best, represents experiment. In a similar study[9] of a variety of strained hydrocarbons of the type which provide the framework of the target molecules, it was found that methods essentially identical to those here labeled IVC (or HF/6-31G(d)//HF/6-31G(d)) and VC predicted isodesmic heats of formation with RMS deviations from experiment of 10.4 and 2.1 kcal/mol, respectively. These values seem at least consistent with the 11.7 kcal/mol deviation of the IVC results from those of the highest level. Further, it has been found[10] in a different test set that electron-correlation treatments of a sophistication just beyond the MP2 can, in fact, lead to reaction energies of reduced accuracy. In any case, until experimental values or significant additional computational resources become available, the current results would seem to provide the best measure of target-molecule formation enthalpies.

Table (E)					
Target-Molecule $\Delta H_f^{\ddagger}$(kcal/mol) by Reaction-Based Methods (C)					
Molecule	IIC(MNDO)	IIC(AM1)	IIC(PM3)	IIIC(PM3)[a]	IVC	VC
1	61.4	70.8	82.1	82.5	75.1	76.5
2	-19.7	-9.0	-12.2	-9.9	-9.9	-10.2
3	-45.1	3.3	-25.4	-27.4	-29.8	-28.8
4	318.9	362.3	332.5	333.9[b]	329.3	315.8
5	-22.4	12.9	-12.5	-15.7[b]	-18.8	-34.7
6	312.0	400.2	348.0	365.0[b]	358.0	342.7
7	-31.0	51.2	1.5	13.7[b]	8.4	-8.6
RMS(VC)	17.7	42.0	11.6	15.7	11.7	

[a] For brevity only IIIC(PM3) results are provided. See, J.D. Mills, *Technical Report*, in preparation, for IIIC(MNDO) and IIIC(AM1) values.
[b] Optimized, semi-empirical structure differs qualitatively from the Hartree-Fock. Thermodynamic parameters are calculated for the local-minimum geometry most resembling the Hartree-Fock.
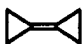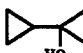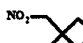
3. Specific Impulse
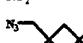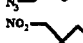
The implications of the theoretical results for actual propellant performance may be illuminated in a number of ways. Most simply, a candidate's mass-normalized energy content seems a more appropriate measure of its lifting capability than the common molar value; mass-adjusted heats of formation for the highest level theoretical results are given in Table (F). Further, calculation[11] of

[9] R.L. Disch, J.M. Schulman, M.L. Sabio, *J. Am. Chem. Soc.*, **107**, 1904 (1985).
[10] J.R. Van Wazer, V. Kellö, B.A. Hess, Jr., and C.S. Ewig, *J. Phys. Chem.*, **94**, 5694 (1990).
[11] C. Selph, R. Hall, C. Beckman, R. Acree, T. Magee, "Theoretical ISP Code," *Computer Program*, Phillips Lab., Edwards AFB, CA.

the specific impulse, I_{sp},[12] provides a more direct measure of the probable utility of a prospective fuel. Even though the target molecules are envisioned as solid- or liquid-propellant additives, the present study does not address the energetics or properties of their condensed phases. Therefore, Table (F) is limited to the specific impulse of each fuel as a gas combusted with liquid oxygen under fixed reference conditions.[13] It was hoped that these values would provide at least a relative measure of likely performance; under the same conditions, RP-1, a common, kerosene-based hydrocarbon fuel, has a theoretical specific impulse of 299.8 sec.

Table (F) Target-Molecule, Mass-Based Enthalpies of Formation (Method VC) and Specific Impulse		
Molecule	$\Delta H_f^\ddagger (cal/g)$	$I_{sp}(sec)$
1:	955	313.2
2: (HO)	-104	300.7
3:	-288	295.5
4: (N$_3$)	998	301.6
5: (NO$_2$)	-104	287.8
6: (N$_3$)	864	301.8
7: (NO$_2$)	-21	292.4

Somewhat surprisingly, the majority of the proposed fuels seem to manifest relatively poor performance or only modest performance gains compared to RP-1. Additional calculations[14] reveal that their specific impulses even show a generally disappointing relationship with those of the non-target isodesmic counterparts– molecules which might be characterized as containing the same functional groups as, but, for the most part, lacking the energy-bestowing strain of, the targets. It was initially supposed that the relatively unsaturated target molecules might simply lack sufficient hydrogen to produce significant quantities of favorable, light exhaust products when burned with oxygen alone and that they might therefore manifest a cooperative enhancement with a relatively hydrogen-rich fuel. However, no tripropellant combination of liquid oxygen and a target fuel with either liquid hydrogen or RP-1 leads to any predicted performance increase. (That is, in each case the optimum specific impulse is just that of a binary mixture of oxygen, and whichever of the other two components has the best performance with oxygen alone.) It appears that condensation energetics and densities must be determined, or at least sensibly hypothesized, in advance of optimization of realistic specific formulations in order to more definitively rank these candidates.

---

[12] G.P. Sutton, *Rocket Propulsion Elements: An Introduction to the Engineering of Rockets*, Sixth Ed., (Wiley, New York, 1992).

[13] Sea level expansion with 1000 psi chamber pressure.

[14] J.D. Mills, *Technical Report*, in preparation.

D. Conclusions

The accuracies of a series of progressively more expensive and sophisticated theoretical methods for calculating gas-phase enthalpies of formation have been evaluated in a specialized reference set of strained and substituted molecules in an effort to justify means by which valuable experimental and theoretical resources may be more efficiently focussed on candidates of particular promise. It appears that the computation-free, *ab lateribus* Benson prescription based upon correlations with experimental values can be expected to predict the formation enthalpies of these types of molecules with an error on the order of 10 kcal/mol. As an alternative to very lengthy calculations, facile, semi-empirical computation with the PM3 Hamiltonian in conjunction with isodesmic reactions may provide roughly comparable results for the relatively rare systems to which the simpler method can not be applied. After an initial screening with either of these two approaches, it appears that the progressively sophisticated theoretical methods considered here do not yield significant improvements in accuracy, at least until the level at which energies from a Hartree–Fock–optimized vibrational analysis and MP2 single-point–energy calculation (MP2/6-31G(d)//HF/6-31G(d)) are combined in accord with an appropriate isodesmic reaction.

By themselves, theoretical, gas-phase heats of formation constitute parameters determinative of a simple relative specific-impulse ranking of candidate fuels under reference conditions. Nonetheless, condensed-phase properties and more interaction with researchers in propellant formulations appear to be necessary in order to fully actualize the potential of these investigations to support the effort to reduce the time and expense required to develop and deploy propellants capable of higher performance and increased payload.

E. Acknowledgments

Cryogenic Oxidizers: Solid Oxygen and Ozone-Doped Solid Oxygen

Michelle E. DeRose and Lt. Jessica Harper
Propulsion Directorate/Phillips Laboratory
OLAC PL/RKS
10 East Saturn Blvd.
Edwards AFB, CA 93524-7680

Introduction

One approach to the task of increasing the energy of a propellant system is to freeze gaseous oxygen into a solid grain and then trap energetic additives, such as ozone, in the grain. This technique would serve to create a denser, more compact fuel or oxidizer grain with more energy than current systems such as LOX/LH$_2$.

The first step in this process was illustrated with the Solid Oxygen (SOX) engine, which was the result of a Phase II SBIR with Orbital Technologies Corporation (ORBITEC). The objective of this SBIR, to develop an apparatus which would freeze and combust solid oxidizers with gaseous hydrogen, was demonstrated at ORBITEC with freezer and firing tests and was further carried out at the Phillips Laboratory.

The next step is to find a way to safely handle ozone and to demonstrate that ozone can be trapped in solid oxygen in significant concentrations. Unfortunately 100% ozone, especially in the liquid and solid phases, is notoriously dangerous because of its tendency to explode. However, numerous reports from the 1950's state that liquid oxygen/ozone mixtures can be produced and handled safely without incident. Additionally, the recent work of Chuck Wight has shown that solid ozone can be safely handled as an amorphous solid.[1] This information leads us to believe that solid mixtures of oxygen and ozone could be stable and safe enough to handle, thus providing a feasible additive to solid oxygen. Before ozone can be integrated into a solid oxygen grain, small scale experiments to explore its properties must be performed and evaluated. An apparatus has been designed and built to not only test sensitive ozone/oxygen mixtures, but any solid cryogenic propellant or oxidizer sample.

SOX Engine Demonstrations

The SOX engine was delivered to the Phillips Laboratory in April 1996. Prior to the engine's delivery, ORBITEC performed numerous freezer and firing tests in the engine as part of the contract requirements. After delivery, 6 runs were performed at the PL. The objective of these experiments was to demonstrate that the engine's chamber pressure could be controlled during combustion by varying the main hydrogen pressure. Oxygen grains as large as 275g have been frozen and combusted at chamber pressures as high as 200 psi.

Figure 1 shows a representative chamber pressure vs. time plot. It can be noted that the incoming hydrogen pressure does seem to have an effect on the resulting chamber pressure, although some fine-tuning still needs to be done to reliably control the chamber pressure.

Improved video techniques for the last 3 runs allowed us to observe a disturbing and reproducible occurrence. Within 1 - 2 seconds of the start of combustion, pieces of solid oxygen can be seen breaking off of the grain. Approximately half-way into the combustion, the grain is also observed to slip 1-2 cm down the tube. Preliminary analysis shows that the slipping can be correlated to a drop in the chamber pressure, though more analysis needs to be done before this can be stated with certainty. One possible solution for the slipping problem is to place a support ring at the bottom of the tube, directly under the grain, to prevent the grain from sliding. An approach to the sloughing problem may be to add a metal (such as Al) foam or matrix to the grain. This would have the added benefit of providing additional energy to the system.

Increasing the Energy of Solid Oxygen

Following the successful demonstration of solid oxygen combustion, we turned our attention to increasing the energy of this oxidizer--a goal of the HEDM program. Ozone has long been considered as an energetic additive to liquid oxygen and more recently as an additive to solid oxygen. Calculations show that 50 mole % ozone in oxygen will increase the I_{sp} to 410 sec, a 20 sec increase over that of pure solid oxygen.[2] This energy benefit, along with ozone being relatively easy to produce and measure, makes ozone our primary additive candidate.

Gaseous and liquid ozone are well-characterized, and methods exist to handle it safely at any concentration. Much work was done on liquid ozone and liquid oxygen mixtures in the 1950's, when these liquid mixtures were considered for high energy liquid rocket oxidizers. A considerable amount of data on liquid ozone and liquid ozone/oxygen mixtures exists and explains that these mixtures can be produced and handled safely:

- "The minimum concentration of liquid ozone in oxygen which can be made to explode by passage of an electric spark through the body of the liquid has been determined to be 47 percent ozone by weight."[3]
- "Detonation data indicate that 30 percent by weight ozone in liquid oxygen if properly handled can be run safely in a rocket."[4]
- "The investigations of Mahieux [in a French patent] indicated that in the temperature range between 123 and 93 K, liquid ozone-oxygen mixtures are stable up to an ozone concentration of 60 mole percent with no tendency to explosion on the application of any kind of shock effect."[5]
- "It has been the experience of the staff of Armour Research Foundation that highly concentrated ozone, as either a gas or a liquid, can be produced and handled in pilot plant quantities with care and without mishap."[6]
- "100% liquid ozone and all liquid ozone/oxygen mixtures, if properly prepared and very carefully handled, are relatively stable."[6]

Considerably less literature exists on solid ozone; no literature could be found dealing with solid ozone/oxygen mixtures. Ozone, notoriously dangerous because of its tendency to detonate when not handled carefully, is sometimes said to be even more hazardous in the solid state.

> "It is, therefore, recommended that ozone should not be stored or transported as a solid and that its presence should be avoided at all times."[7]

"Solid ozone with solid carbon dioxide, nitrous oxide, and argon present has the same impact sensitivity as solid ozone alone. The use of solid ozone is to be avoided."[8]

On the other hand, a conflicting report states that "solid ozone (at -320° F) was compressed to 22.5 atm without any difficulty. Slight impact and slight friction at that temperature did not cause an explosion."[9]

More recent research into the properties of solid ozone has been conducted by Chuck Wight at the University of Utah and shows that solid ozone can be desensitized. Thick films (1 mm or greater) of the crystalline structure are highly unstable, detonating explosively under slight provocation. Yet amorphous samples of solid ozone formed at temperatures below 20K are stable to laser irradiation. (Because temperatures at which solid ozone was formed were not reported in the references above, this may explain the discrepancies.) Thin films of amorphous, polycrystalline, or crystalline structure are all stable, giving an indication of the critical diameter of solid ozone.[1]

Proposed Sensitivity Testing

Because of the dearth of literature on solid O_3/O_2 mixtures and the inconsistency of solid O_3 reports, we determined it necessary in the interest of safety to establish the limits of ozone's stability. An apparatus has been designed and built in which we will perform various sensitivity tests. Although these tests were designed with ozone/oxygen mixtures in mind, any cryogenic solid sample could be tested in the chamber. Ozone samples will be small, on the order of 10 - 100 mg. Initial ozone concentrations will be low and then gradually increased, to build a comprehensive data base of sensitivity information. The entire operation will be remotely controlled.

Initial tests will be cryogenic adaptations of conventional propellant tests such as drop or impact tests, hot-wire, and friction tests which have not been previously performed at temperatures near absolute zero. Standards will be tested along with the ozone/oxygen samples to use as a basis of comparison.

If the tests show that solid ozone/oxygen mixtures are safe enough to handle, the mixtures will be scaled up to a size suitable for combustion in the SOX engine. If not, this research will at least answer fundamental questions which are currently not addressed in literature.

Summary/Conclusions

- The Solid Oxygen Engine is a valuable tool for testing cryogenic HEDM propellant systems. Engine firings have demonstrated that pure, undoped solid oxygen/gaseous hydrogen can be combusted in the engine and that the chamber pressure can be controlled during combustion by varying the H_2 pressure.

- Theory predicts that adding 50% ozone to solid oxygen will increase the I_{sp} by 20 sec. We will determine experimentally if ozone is a feasible additive to solid oxygen.

- Based on the literature on liquid and gaseous ozone, extreme caution will be used when testing ozone/oxygen mixtures. An apparatus has been designed and built and conventional propellant tests

have been adapted for our cryogenic environment. Specific milestones will have to be passed before proceeding to each new step in the testing sequence.

References

[1] C.A. Wight, "Desensitization of Energetic Materials," in <u>Proceedings of the High Energy Density Matter Contractors' Conference</u>, Michael R. Berman, ed., (Air Force Office of Scientific Research, Bolling AFB DC, 1992).

[2] Calculations of P.G. Carrick, private communication.

[3] "Handling of Concentrated Liquid Ozone," Armour Research Foundation Formal Report No. 16, Contract No. AF33(038)-16174; Project No. C 015-5; 13 November 1953.

[4] Miller, R.O.; Brown, D.D., "Effect of Ozone Addition on Combustion Efficiency of Hydrogen - Liquid Oxygen Propellant in Small Rockets," NASA Memorandum 5-26-59E, June 1959.

[5] Horvath, M.; Bilitzky, L.; Huttner, J.; <u>Ozone</u>, Elsevier, N.Y. 1985, p.254.

[6] Platz, G.M.; Hersh, C.K., "Preparation of Liquid Ozone and Ozone-Oxygen Mixtures for Rocket Application," Ind. Eng. Chem. **48(4)**, 742 (1956).

[7] "Engineering Study of Tonnage Production and Handling of Liquid Ozone, "Armour Research Foundation Final Report, Contract AF04 611 2316, Project ARF C100, 1 June 1957, p. 8.

[8] Gerald M. Platz and Robert I. Brabets, "Handling of Concentrated Liquid Ozone," ASD-TR-56-228 (was WADC Technical Report 56-228), December 1956, p. 53.

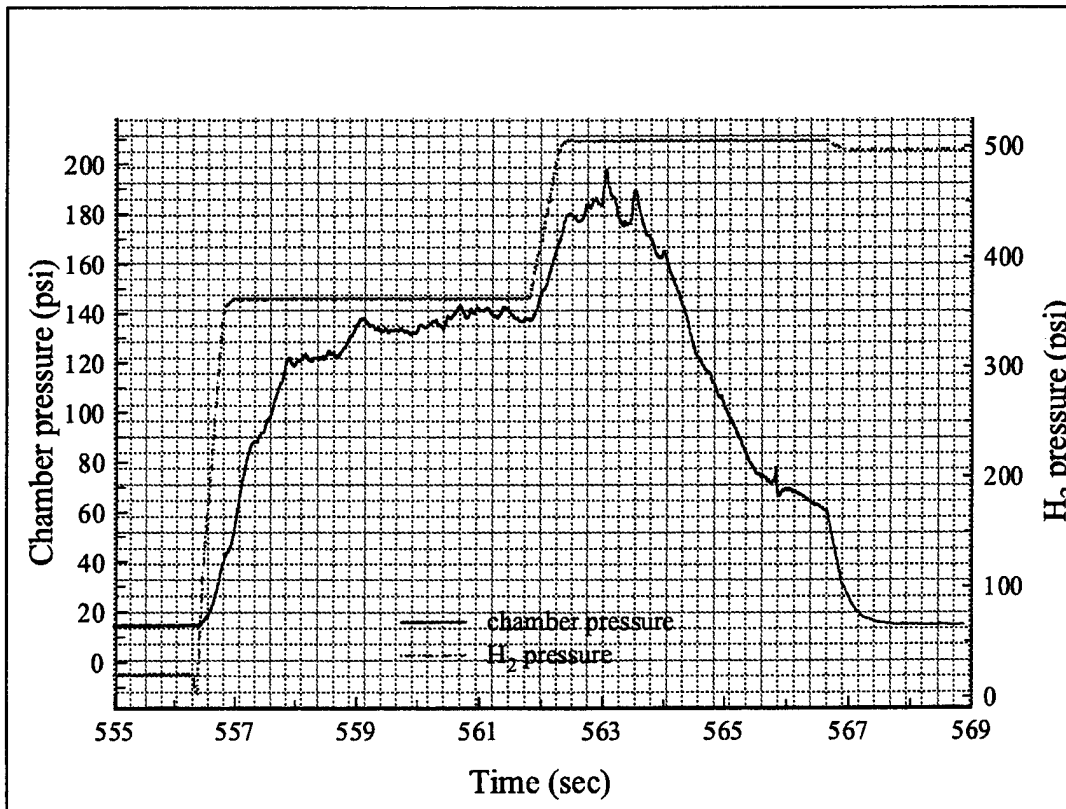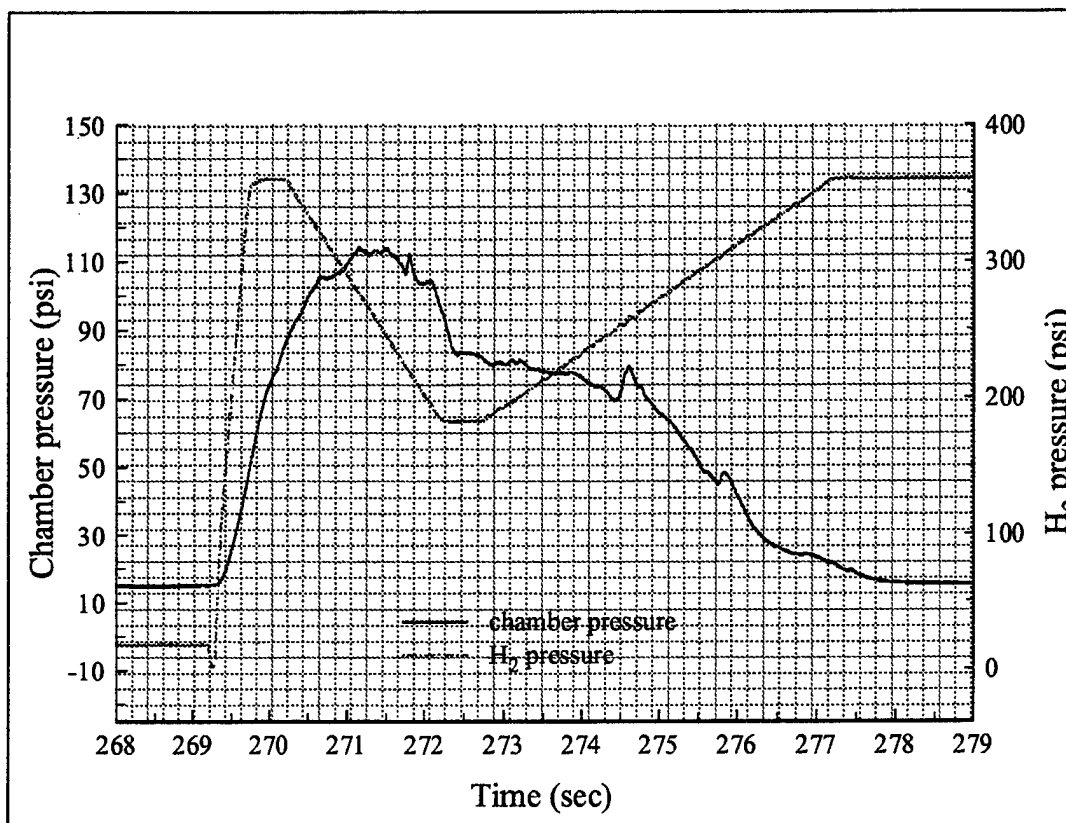[9] "Handling Hazardous Materials," <u>Ozone</u>, Chapter 5, NASA SP-5032, NASA Technology Utilization Division.

Figure 1. a.) Chamber pressure vs. time with corresponding hydrogen pressure for a 150g solid O_2 grain. b.) Similar plot, but for a 275g solid O_2 grain.

Excited State Structures with Equation-of-Motion Coupled-Cluster Methods

Steven R. Gwaltney, Janet E. Del Bene[†], and Rodney J. Bartlett

Quantum Theory Project

University of Florida

Gainesville, Florida 32611-8435

One of the most important tools which quantum chemistry has developed is the ability to calculate analytical gradients for ground states of molecules. Analytical gradients make it possible to routinely study the potential energy surfaces of molecules, as well as to efficiently calculate harmonic vibrational frequencies and intensities and to calculate properties such as multipole moments. However, these methods are generally applicable to only the ground state and a few excited states (the lowest of a given symmetry and multiplicity) of a molecule.

Only recently have analytical gradients become available for methods which include dynamic correlation and which can be applied to arbitrary excited states. The Equation-of-Motion Coupled-Cluster Singles and Doubles (EOM-CCSD) method is such a method. Another is the partitioned EOM-CC method based on a MBPT[2] reference function (P-EOM-MBPT[2]) which we have developed. The P-EOM-MBPT[2] method is a less expensive approximation to the full EOM-CCSD method and is therefore applicable to larger systems. For both of these methods we can calculate the energy and the gradient of the energy with respect to any number of perturbations in about twice as long as it takes to calculate just the energy.

In this poster we present excited state structures and frequencies for some diatomic molecules where we can compare to experiment. Included are also structures for the first two excited states of pyridine. Finally we give structures for protonated and hydrogen bonded formaldehyde and methyleneimine in their first excited state.

POTENTIAL ENERGY SURFACES FOR DISSOCIATION REACTIONS OF HIGH ENERGY ISOMERS OF N_2O_2

Galina Chaban, Mark S. Gordon, and Kiet A. Nguyen

Department of Chemistry
Iowa State University
Ames, Iowa 50011

The possible existence of high energy isomers of NO dimer has been of considerable experimental and theoretical interest recently due to their potential role as new high energy density materials (HEDM)[1-6]. Stimulated emission pumping experiments of Wodtke and co-workers[1], and studies of photoelectron spectra of $N_2O_2^-$ by Arnold and Neumark[2] provide indirect evidence for the existence of several high energy N_2O_2 species. A number of metastable N_2O_2 isomers have also been predicted recently in theoretical papers [4-6]. Relative energies of these isomers are in the range of 40-80 kcal/mol above the energy of 2 NO fragments. However, in order to be useful as high energy compounds, these species must be kinetically stable; that is, they must be separated from the lower energy isomers and dissociation products by relatively high barriers on the potential energy surfaces. Besides the adiabatic kinetic stability, the possibility of surface crossings must also be considered, to ensure that there is no lower energy path to products due to non-adiabatic couplings that can decrease the stability of such compounds[7]. An example is the high energy asymmetric NNOO isomer [5,6]. This structure corresponds to a local minimum on the $^1A'$ potential energy surface and is stable to the spin-allowed decomposition a-N_2O_2 -> $N_2O(X\ ^1\Sigma^+) + O\ (^1D)$. However, the minimum energy crossing point for the singlet and triplet surfaces lies only 2 kcal/mol above the a-N_2O_2 isomer, leading to its predissociation to $N_2O\ (X\ ^1\Sigma^+) + O$ (^3P) products [5]. Consequently, this isomer is not a viable HEDM candidate.

Here we present minimum energy reaction paths for dissociation of several previously predicted[4,6] high energy N_2O_2 species to 2 NO fragments, including potential energy barriers separating them and approximate minimum energy crossing points between nearby singlet and triplet states.

The N_2O_2 potential energy surfaces have been studied using *ab initio* electronic structure methods employing multi-configurational self-consistent-field (MCSCF)[8] wavefunctions. MCSCF wavefunctions are necessary for a qualitatively correct description of dissociation processes that involve bond breaking. Two kinds of wavefunctions were used. One, denoted MCSCF(10,10), included all possible configurations, consistent with the appropriate symmetry and spin, that may be obtained

by distributing 10 active electrons in 10 active orbitals. Generally speaking, five NO and NN bond orbitals, and the five corresponding anti-bonding orbitals were included in the active space for various isomers. The second active space, MCSCF (14,12), included two oxygen lone pair orbitals (one on each oxygen atom) in addition to the (10,10) space. Inclusion of oxygen lone pairs is necessary to obtain a consistent description of some reactions. The stationary points on the N_2O_2 potential energy surface have been identified using analytic gradients of MCSCF energies. Minimum energy paths (MEPs) were determined using the intrinsic reaction coordinate (IRC) method with the second order algorithm developed by Gonzalez and Schlegel[9] and a step size of 0.15 amu$^{1/2}$ bohr. Stationary point searches and IRC calculations were performed using MCSCF(10,10) and MCSCF(14,12) wavefunctions and the 6-31G(d)[10] basis set . These calculations were done using the GAMESS[11] electronic structure program. The energies of stationary points, as well as selected points along the MEPs, were recalculated with the multi-configurational second order perturbation theory method (CASPT2[12]) to account for dynamic correlation. The CASPT2 wavefunctions were based on MCSCF(10,10) (denoted as CASPT2(10,10)) and MCSCF(14,12) (denoted as CASPT2(14,12)) reference wavefunctions with 6-31G(d) and 6-311+G(2d)[13] basis sets. These calculations were performed using the MOLCAS[14] program.

RESULTS AND DISCUSSION

The four high energy singlet isomers of N_2O_2 are shown in Figure 1, with the structural parameters obtained at the MCSCF(10,10)/6-31G(d) level of theory. The structure and energetics of isomers **1-3** have been studied previously [4] at several levels of theory including the MCSCF(10,10) and CASPT2(10,10) levels used in this paper. The Hartree-Fock and MP2/6-31+G(d) structures for isomer **4** have been reported by Arnold and Neumark [2]. All four isomers are relatively high in energy: planar isomers **1, 2**, and **4** are about 50 kcal/mol higher than 2 NO, and the bicyclic isomer **3** is about 80 kcal/mol above the energy of 2 NO. Here we consider the kinetic stability for each of these isomers with respect to dissociation to two NO molecules.

1. Dissociation of D_{2h} cyclic isomer 1.

Isomer **1** in Figure 1 has a planar ring structure with four equal N-O bonds (D_{2h} symmetry). This isomer is 50 kcal/mol higher in energy than 2 NO molecules at the CASPT2(14,12)/6-311+G(2d) level of theory. The geometry of the transition state for decomposition of **1** to 2 NO is predicted to have C_s symmetry. Energetics along the dissociation path **1** $\rightarrow$ 2 NO are presented in Figure 2a. The barrier height for this reaction is about 40 kcal/mol at the best, CASPT2(14,12)/6-311+G(2d), level used here.

This reaction is Woodward-Hoffmann forbidden which leads to the high reaction barrier. Figure 2a illustrates the CASPT2(14,12)/6-31G(d) energies for the lowest singlet (^{1}A') and triplet (^{3}A") states at selected geometries along the ground singlet state MEP. The repulsive ^{3}A" state crosses the singlet before the transition state (that is, on the reactant side), but this crossing is predicted to occur at an energy that is about 32 kcal/mol above the reactant well. So, it is likely that singlet-triplet interaction will not destroy the stability of isomer **1**. We conclude that the D_{2h} isomer is kinetically stable with respect to dissociation to two NO molecules. Other possible dissociation channels (for example, to $N_2 + O_2$) are likely to contain even higher potential energy barriers since considerably more electronic and geometric rearrngements would be involved; therefore, this isomer should be considered to be a possible candidate for isolation and use as a source of energy.

2. Dissociation of C_{2v} planar cyclic isomer 2.

Isomer **2** is also quite high in energy, about 45 kcal/mol above the two NO fragments at the highest level of theory. This isomer has an N=N double bond, two single N-O bonds, and a single O-O bond. The reaction path for dissociation of this isomer is shown in Figure 2b. Also shown are CASPT2 single point energies for singlet and triplet states calculated at several points along the IRC path. The transition state structure is not planar; it is twisted by about 15° (due to the broken O-O bond) and has no symmetry (although it is very close to C_2). The height of the barrier is estimated to be about 19 kcal/mol. The reaction proceeds by breaking the O-O bond first, and then breaking the N-N bond. The lowest triplet state is higher in energy than the singlet state for all points along the reaction path at the CASPT2(10,10) level of theory . When the single point energies are calculated using the larger MCSCF(14,12) active space (along the same MCSCF(10,10) reaction path), the CASPT2(14,12) triplet is found to be 4 kcal/mol *lower* than the corresponding singlet, at the transition state geometry. Although the triplet state is close to the singlet in energy in the transition state region, the triplet energy is much higher in the reactant channel. Again, it is unlikely that the singlet-triplet crossing will prevent detection of isomer **2.**

3. Stability of bicyclic isomer 3.

Bicyclic isomer **3** (Figure 1) is one of the highest isomers on the N_2O_2 potential energy surface: its relative energy with respect to 2 NO is about 82 kcal/mol. It has a strained structure of two three-membered N-O-N rings with an O-N-N-O dihedral angle equal to 107°. This isomer, as well as the part of the potential energy surface connecting this isomer with the planar ring **1**, was studied in detail previously [6]. The two isomers were found to be separated by a barrier of 40 kcal/mol. Therefore, the stability of the

bicyclic isomer with respect to isomerisation to **1** was established. In an attempt to find a reaction path leading to the dissociation of the isomer **3**, we found that breaking one of the N-O bonds leads to a transition state connecting this isomer to another planar isomer **4**. The dissociation to two NO molecules occurs here in two steps: first, **3** isomerizes to **4** through a barrier of about 20 kcal/mol, and then, isomer **4** dissociates to 2 NO with a rather small barrier of about 7 kcal/mol.

The MCSCF(10,10)/6-31G(d) IRC path for the first (isomerisation) part of the potential energy surface is shown in Figure 2c. When dynamic correlation (CASPT2) is included, isomer **4** is predicted to be 26 kcal/mol lower in energy than **3**, and the **3** -> **4** barrier height is 19 kcal/mol. The lowest triplet state is about 4 kcal/mol lower than singlet at the transition state geometry and is much higher in energy for both isomers (see Figure 2c). Therefore, the bicyclic isomer **3** is probably kinetically stable with respect to rearrangement to isomer **4**, although the barrier for this channel is lower than for the rearrangement **3** -> **1**. Breaking one of the N-O bonds of **3** leads to rearrangement to isomer **4**, and breaking of the N-N bond leads to **1**. Since both processes involve substantial barriers, the bicyclic isomer may be a good candidate for a metastable high energy species. Its isolation, however, may be difficult because very high energy (at least 100 kcal/mol) has to be provided to 2 NO to overcome the lowest barrier leading to this isomer.

4. Dissociation of C_S planar isomer 4.

Isomer **4** has C_S symmetry, short (almost double) N-N (1.23 Å) and N-O (1.20 Å) bonds, one single N-O bond (1.4 Å), and one very weak N-O bond (1.7 Å). Our MCSCF structural parameters are close to those found at the MP2/6-31+G(d) level by Arnold and Neumark[2]. This isomer is about 48.5 kcal/mol higher in energy than 2 NO at the highest, CASPT2(14,12)/6-31+G(2d), level of theory. The dissociation reaction **4** -> 2 NO is shown in Figure 2d, along with single point CASPT2 energies for both the lowest singlet and triplet states obtained at several selected points on the MCSCF(14,12) IRC path. The transition state structure shows that the first stage of the dissociation process involves transfer of the (single bond) oxygen atom from one nitrogen atom to another. This requires only a small amount of energy, resulting in a barrier height of about 7 kcal/mol (CASPT2). During the second part of this reaction, the N-N bond breaks, with the π (N-N) and π*(N-N) orbitals rearranging into two singly occupied π* (N-O) orbitals of the dissociation products. The triplet ($^3A''$) state is higher in energy than the singlet in the region of the minimum and transition state, and becomes close to the singlet state in the product (2 NO) part of the reaction . The small barrier for this reaction suggests that structure **4** may be stable only at low temperatures. On the other hand, this isomer has

the lowest barrier for the reverse reaction, 2 NO → isomer **4**, and may be responsible for the enhanced vibrational relaxation observed by Wodtke and coworkers[1] for excitation energies above vibrational quantum number $\upsilon \approx 12$. The barrier height is about 56 kcal/mol (2.4 eV), which is in the region where vibrational relaxation accelerates[1]. Two NO molecules at large separation, with one in its ground vibrational state and the other with the N-O bond stretched to 1.55 Å (corresponding to $\upsilon \approx 15$), have an energy that is about 4 kcal/mol above the 2NO → **4** reaction barrier height. This supports the suggestion made in reference 1 that the trajectory for collision NO($\upsilon = 0$) + NO($\upsilon \geq 12$) may pass near the transition state for formation of isomer **4** or other high energy isomers.

ACKNOWLEDGMENTS

REFERENCES

1. (a) Yang, X.; Kim, E. H.; Wodtke, A. M. *J. Chem. Phys.* **1992**, *96*, 5111; (b) Yang, X.; Price, J. M.; Mack, J. A.; Morgan, C. G.; Rogaski, C. A.; McGuire, D.; Kim, E. H.; Wodtke, A. M. *J. Phys. Chem.* **1993**, *97*, 3944.
2. Arnold, D. W.; Neumark, D. M. *J. Chem. Phys.* **1995**, *102*, 7035.
3. Michels, H. H.; Montgomery, J. A. *J. Chem. Phys.* **1988**, *88*, 7248.
4. Nguyen, K. A.; Gordon, M. S.; Montgomery, J. A.; Michels, H. H. *J. Phys. Chem.* **1994**, *98*, 10072.
5. Nguyen, K. A.; Gordon, M. S.; Montgomery, J. A.; Michels, H. H.; Yarkony, D. R. *J.Chem. Phys.* **1994**, *98*, 3845.
6. Nguyen, K. A. ; Gordon, M. S.; Boatz, J. A. *J. Am. Chem. Soc.*, **1994,** *116*, 9241.
7. (a) Yarkony, D. R. *J. Am. Chem. Soc.* **1992**, 114, 5406; (b) Yarkony, D. R. *J. Chem. Phys.* **1990**, 92, 2457.
8. (a) Ruedenberg, K.; Schmidt, M. W.; Gilbert, M. M.; Elbert, S. T. *Chem. Phys.* **1982**, *71*, 41; (b) Lam, B.; Schmidt, M. W.; Ruedenberg, K. *J. Chem. Phys.* **1985**, *89*, 2221.
9. (a) Gonzalez, C.; Schlegel, H. B. *J.Chem.Phys.* **1989**, 90, 2154; (b) *J.Phys.Chem.* **1990**, 94, 5523; (c) *J.Chem.Phys.* **1991**, 95, 5853.
10. Hehre, W. J.; Ditchfield, R.; Pople, J. A. *J. Chem. Phys.* **1972,** *56*, 2257.
11. Schmidt, M. W.; Baldridge, K. K.; Boatz, J. A.; Elbert, S. T.; Gordon, M. S.; Jensen, J. H.; Koseki, S.; Matsunaga, N.; Nguyen, K. A.; Su, S.; Windus, T. L.; Dupuis, M.; Montgomery, J. A. *J. Comp. Chem.* **1993**, 14, 1347.
12. (a) Anderson, K.; Malmqvist, P.-Å.; Roos, B. O. *J. Chem. Phys.* **1992**, 96, 1218; (b) Anderson, K. Malmqvist, P.-Å., Roos, B. O. *J. Phys. Chem.* **1990**, 94, 5483.
13. (a) Hariharan, P. C.; Pople, J. A., *Theor. Chim. Acta*, **1973**, 28, 213; (b) Krishnan, R.; Binkley, J. S.; Seeger, R.; Pople. J. A. *J. Chem. Phys.* **1980,** 72, 650; (c) Frisch, M. J.; Pople, J. A.; Binkley, J. S. *J. Chem. Phys.* **1984**, 80, 3265.
14. Anderson, K.; Blomberg M. R. A.; Fülscher, M. P.; Kellö, V.; Lindh, R.; Malmqvist, P.-Å.; Noga, J.; Olsen, J.; Roos, B. O.; Sadlej, A. J.; Siegbahn, P. E. M.; Urban, M.; Widmark, P.-O. MOLCAS version 3, University of Lund, Sweden, 1994.

MCSCF(10,10)/6-31G(d) geometry

1. D$_{2h}$

2. C$_{2v}$

Relative energy, kcal/mol

	1. D$_{2h}$	2. C$_{2v}$
MCSCF(10,10)/6-31G(d)	71.0	41.6
CASPT2/MCSCF(10,10)/6-31G(d)	49.0	47.7
MCSCF(10,10)/6-311+G(2d)	71.7	47.0
CASPT2/MCSCF(10,10)/6-311+G(2d)	48.7	53.1

3. C$_{2v}$

D(ONNO)=57.6 deg.

4. C$_s$

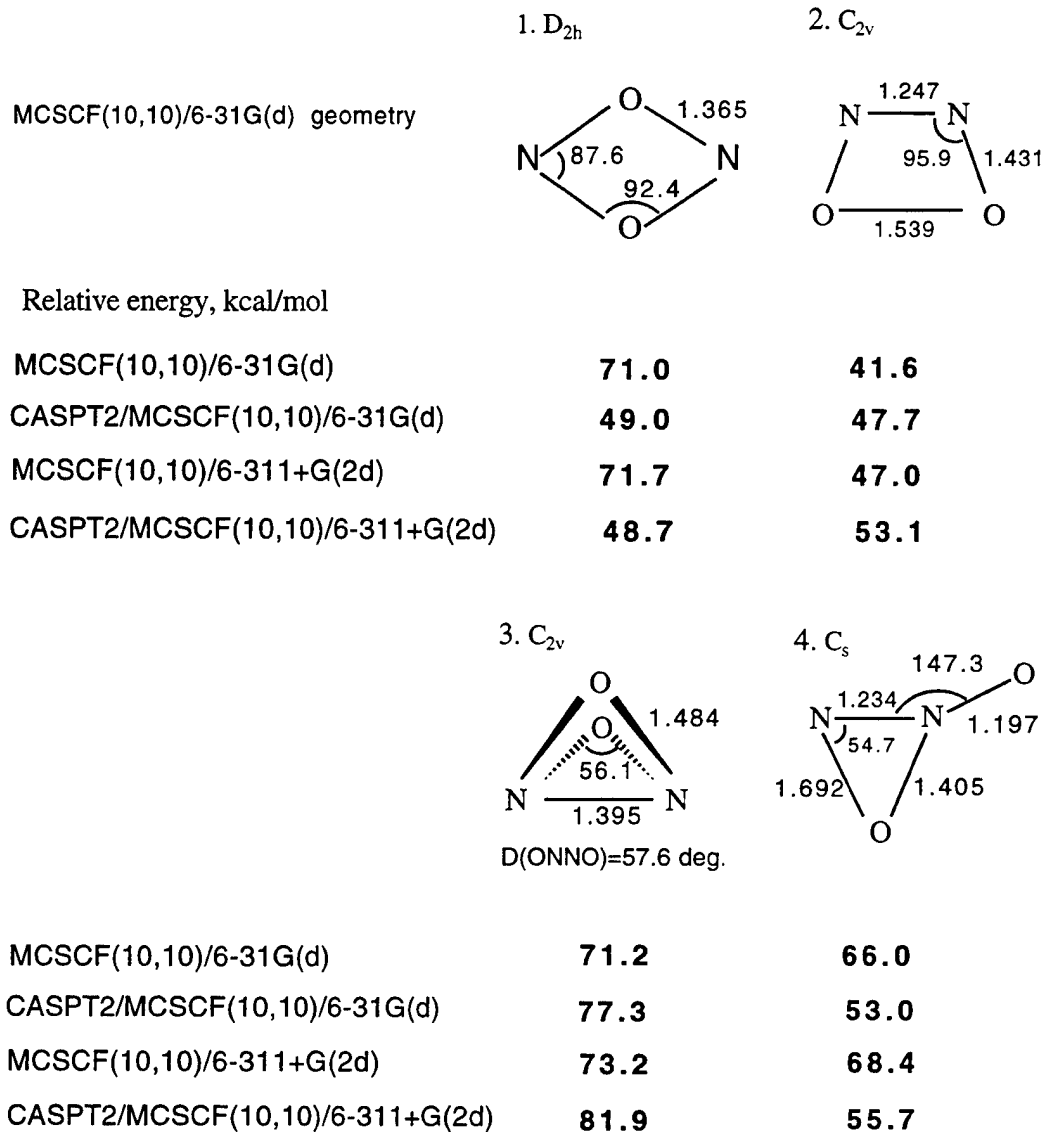|	3. C$_{2v}$	4. C$_s$
MCSCF(10,10)/6-31G(d)	71.2	66.0
CASPT2/MCSCF(10,10)/6-31G(d)	77.3	53.0
MCSCF(10,10)/6-311+G(2d)	73.2	68.4
CASPT2/MCSCF(10,10)/6-311+G(2d)	81.9	55.7

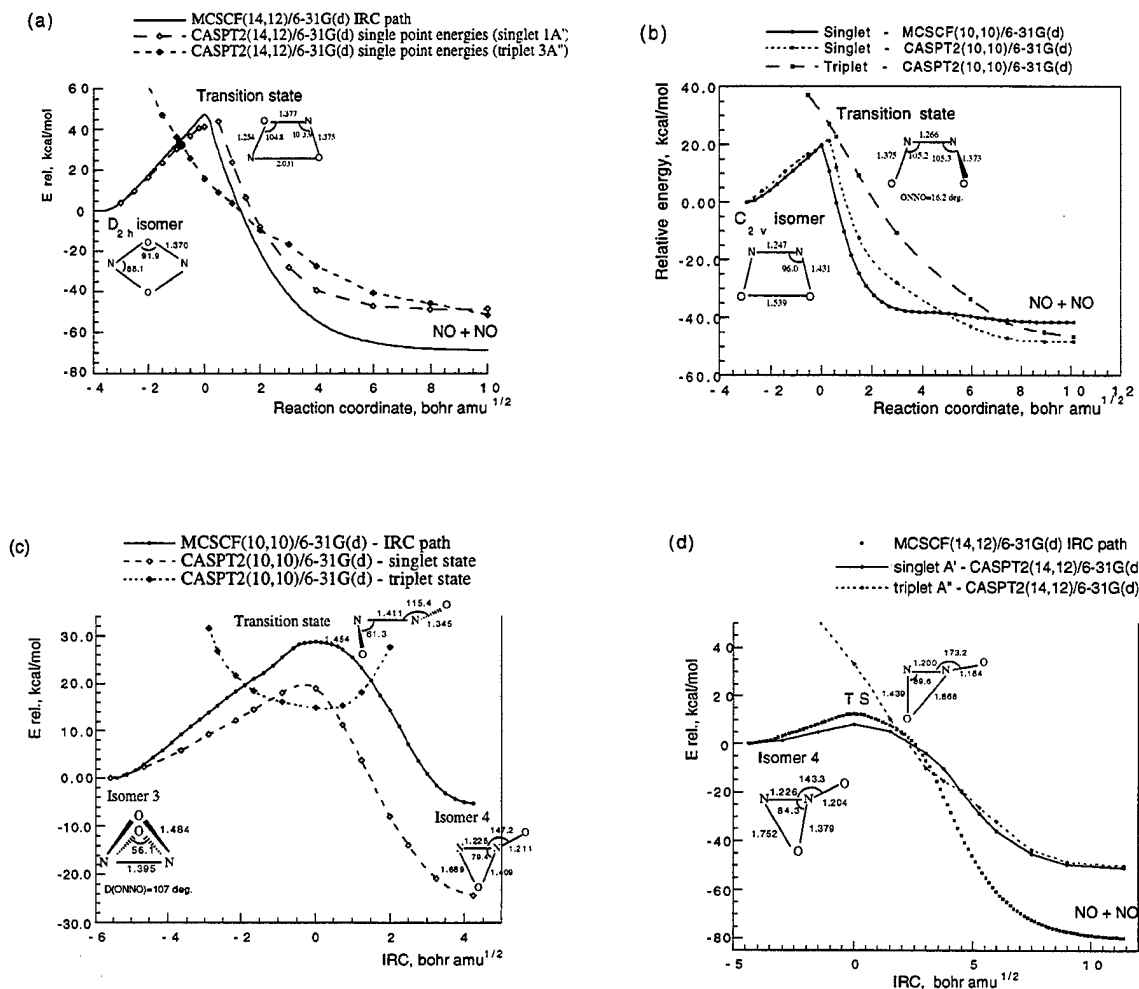Figure 1. N$_2$O$_2$ high energy isomers

Figure 2. Reaction paths for a) dissociatian of isomer 1 to 2 NO;
b) dissociation of isomer 2 to 2 NO;
c) isomerisation betwwen isomers 3 and 4;
d) dissociation of isomer 4 to 2 NO.

Theoretical investigation of features of the BAr_2 excitation spectrum

Jennifer R. Krumrine[a] and Millard H. Alexander

Department of Chemistry and Biochemistry
University of Maryland
College Park, MD 20742-2021

Simulation of the spectrum of the BAr_2 $2s2p^2\,{}^2D \leftarrow 2s^2 2p$ transition qualitatively reproduces the features seen in the fluorescence excitation spectrum of the $B(Ar)_2$ van der Waals complex. These features, observed by Yang and Dagdigian, cannot be assigned to the BAr diatom. Previous work by Alexander assigns satisfactorily the feature in the experimental spectrum, in the neighborhood of the B $3s \leftarrow 2p$ transition, which is not assignable to BAr. Here, using excited state potential energy surfaces constructed by Dagdigian and coworkers, transitions in the region of the five-fold degenerate $2s2p^2\,{}^2D$ state are investigated. A variational Monte-Carlo method is used to approximate the ground state wavefunction of BAr_2. The square of the wavefunction is projected onto the excited state potential energy surfaces. We consider excitation to each of the five electronic states of the complex. We predict both red and blue shifted features which are in good agreement with experiment. Our investigation lends insight into the energetics of the approach of B to multiple Ar atoms, and how the orientation of B 2p orbitals governs the stability of the complex.

Diatomic Boron Compounds Studied by
Multireference Configuration - Interaction Methods

Friedrich Grein

Department of Chemistry, University of New Brunswick, Fredericton, NB, E3B 6E2, Canada

Over the last years, multireference CI studies have been performed on B_2 [1], BO [2], BO^+ [3], BN [4,5], and the ions of BN with charges from +3 to -2 [5-12]. In all cases, high-level basis sets including polarization, semidiffuse and Rydberg functions were used. Potential energy curves, spectroscopic constants, relative stabilities, UV-visible excitation energies and oscillator strengths, vibrational frequencies, ionization and photodissociation behavior, and other properties were investigated. Attention was also directed towards low-lying doubly excited states of such molecules.

For B_2, the ground state is clearly established to be $X^3\Sigma_g^-$ ($2\sigma_g^2 2\sigma_u^2 1\pi_u^2$). The experimentally observed $A^3\Sigma_u^-$ is the second $^3\Sigma_u^-$, not the first one. The ground state of BN is $X^3\Pi$ ($4\sigma^2 1\pi^3 5\sigma$), but $1^1\Sigma^+$ ($4\sigma^2 1\pi^4$) is very close in energy (0.10 eV according to [4], 0.01 to 0.02 eV in more recent work). In the osoelectronic BO^+ ion, the ground state is $X^1\Sigma^+$ ($4\sigma^2 1\pi^4$), and $1^3\Pi$ ($4\sigma^2 1\pi^3 5\sigma$) lies about 0.3 eV higher. BN^+ has a $X^4\Sigma^-$ ground state ($4\sigma^2 1\pi^2 5\sigma$) and low-lying excited states $1^2\Sigma^-$ and $1^2\Delta$ arising from the same configurat6ion, as well as $1^2\Pi$ from $4\sigma^2 1\pi^3$. BN^{2+} is predicted to have 14 quasibound states, the lowest being $X^3\Sigma^-$ ($4\sigma^2 1\pi^2$), followed by a strongly bound $1^5\Sigma^-$ ($4\sigma 5\sigma 1\pi^2$). BN^{3+} still has 3 metastabhle states, $1^4\Sigma^-$, $1^2\Delta$ and $2^2\Sigma^+$, all arising from $4\sigma 1\pi^2$. Of the anions, BN^- has 3 bound states, with $X^2\Sigma^+$ ($4\sigma^2 5\sigma 1\pi^4$) being the lowest. BN^{2-} in the gas phase is not stable with respect to BN^- or BN, but BN^{2-} may well be stabilized within a crystal environment. These, and other interesting properties of B_2, BN, BO and their ions will be reviewed.

1. M. Hackey, S.P. Karna and F. Grein, J. Phys. B.: At. Mol. Opt. Physics 25, 1119 (1992).
2. S.P. Karna and F. Grein, J. Mol. Spectrosc. 122, 356 (1987).
3. S.P. Karna and F. Grein, Mol. Phys. 61, 1055 (1987).
3. S.P. Karna and F. Grein, Chem. Phys. 98, 207 (1985).
5. S.P. Karna and F. Grein, Chem Phys. Letters 144, 149 (1988).
6. S.P. Karna and F. Grein. Mol Phys. 56, 641 (1985).
7. R.C. Mawhinney, P.J. Bruna and F. Grein. Can. J. Chem. 71, 1581 (1993).
8. R.C. Mawhinney, P.J. Bruna and F. Grein. J. Phys. B: At. Mol. Opt. Phys. 28, 4015 (1995).
9. R.C. Mawhinney, P.J. Bruna and F. Grein. Chem. Phys. 199, 163 (1995).
10. R.C. Mawhinney, P.J. Bruna and F. Grein. J. Chem. Phys. 103, 8944 (1995).
11. P.J. Bruna, R.C. Mawhinney and F. Grein. Int. J. Quant. Chem.: Quant. Chem. Symp. 29, 455 (1995).
12. P.J. Bruna, R.C. Mawhinneyk and F. Grein. J. Phys. B: At. Mol. Opt. Phys. 29, 2413 (1996)

SIMULATION OF PROTON AND HYDRIDE TRANSFER IN SOLUTION

Sharon Hammes-Schiffer

Department of Chemistry and Biochemistry, University of Notre Dame
Notre Dame, IN 46556
e-mail: hammes-schiffer.1@nd.edu

We have simulated the real-time quantum dynamics of proton and hydride transfer reactions in solution. The processes we are studying include proton transport along protonated linear water chains, model proton-coupled electron transfer reactions, and NADH (nicotinamide adenine dinucleotide) hydride transfer reactions. Both adiabatic and nonadiabatic mixed quantum/classical molecular dynamics simulations have been performed. The transferring hydrogen atoms are treated quantum mechanically, while the remaining degrees of freedom are treated classically. The nonadiabatic simulations utilize the stochastic surface hopping method "molecular dynamics with quantum transitions" (MDQT). The advantages of MDQT are that branching processes (i.e. processes involving multiple pathways) are accurately described and nonequilibrium real-time dynamical processes can be simulated. We have also developed the new "multiconfigurational MDQT" (MC-MDQT) method, which combines a multiconfigurational self-consistent-field (MC-SCF) approach with MDQT for the simulation of multiple proton transfer reactions. We have derived MC-SCF wavefunctions for vibrational modes and have proven that the Hellmann-Feynman forces on the classical particles are rigorously exact for an appropriate choice of basis functions. MC-MDQT has been shown to incorporate the important correlation between quantum protons. We have applied MC-MDQT to proton transport along chains of water molecules. Our simulations indicate that the multiple proton transfer reactions are strongly coupled and that quantum dynamical effects play an important role in the proton transport mechanism. Moreover, we have extended MDQT to study model proton-coupled electron transfer reactions in solution, where both a proton and an electron are treated quantum mechanically. Photoinduced proton-coupled electron transfer reactions have also been investigated. These simulations provide insight into the fundamental physical principles and the dynamical aspects of proton-coupled electron transfer reactions in solution. In addition, we have developed a general augmented molecular mechanical potential for proton and hydride transfer in solution. This potential allows specified bonds to break and form and incorporates changes in charge distribution, bond order, and hybridization. We have utilized this methodology to study the solvent effects for NADH hydride transfer reactions in water and acetonitrile.

An Application of the Interaction Picture to Calculate S-Matrix Elements for Reactive Scattering

Michael J. MacLachlan
Air Force Research Laboratory

David E. Weeks
Air Force Institute of Technology

September 11, 1997

1. Introduction

Accurate quantum calculations of matrix elements of the scattering operator **S** remain computationally prohibitive for reactions involving more than a few atoms. We have developed a time-dependent quantum computational approach that employs the interaction picture, together with the channel-packet method, to calculate these matrix elements with improved efficiency. The channel-packet method is based on the Møller-operator formulation of scattering theory, and divides the computational process into two parts. The first is the application of Møller operators to initial reactant and product wavepackets, producing two Møller states. The second is the computation of the time-dependent correlation function of the Møller states. The Møller operators are single time-evolution operators in the interaction picture, instead of the paired operators required in the Schrödinger picture. The interaction picture reduces the memory requirements for the first step of the channel-packet method by decreasing the size of the computational grid. Initial results indicate that in one dimension, the interaction picture requires several times more computation time than propagation in the Schrödinger picture. For higher dimensions, the effect of a reduced grid on FFT speed is expected to lead to improved computational efficiency relative to the Schrödinger

241

picture.

2. The S Matrix and the Channel Packet Method

For purposes of illustration, the simplest collision to describe is that of two structureless particles with no angular momentum. In this case, the configuration of the system can be described completely using a single spatial coordinate. The Hamiltonian for this system can be written

$$\mathbf{H} = \mathbf{H}_0^\gamma + \mathbf{V}(x), \tag{2.1}$$

where the potential operator $\mathbf{V}(x)$ describes the interaction of the two particles, and the asymptotic Hamiltonian,

$$
\begin{aligned}
\mathbf{H}_0^\gamma &= \lim_{x \to \pm \infty} \mathbf{H} \\
&= \frac{\hbar^2 \mathbf{k}_\gamma^2}{2\mu} + \mathbf{V}_0^\gamma,
\end{aligned}
\tag{2.2}
$$

is obtained in the asymptotic limit where $\lim_{x \to \pm \infty} \mathbf{V}(x) = \mathbf{V}_0^\gamma$. Here the index γ labels the two reaction channels, and k_γ represents the relative momentum.

The scattering operator $\mathbf{S}$ relates the reactant and product states $|\psi_{in}^\gamma\rangle$ and $\left|\psi_{out}^{\gamma'}\right\rangle$ of an interaction as

$$
\begin{aligned}
\left|\psi_{out}^{\gamma'}\right\rangle &= \mathbf{S}^{\gamma'\gamma} |\psi_{in}^\gamma\rangle \\
&= \Omega_-^{\gamma'\dagger} \Omega_+^\gamma |\psi_{in}^\gamma\rangle,
\end{aligned}
\tag{2.3}
$$

where the Møller operators are defined as

$$\Omega_\pm^\gamma = \lim_{t \to \mp\infty} e^{i\mathbf{H}t} e^{-i\mathbf{H}_0^\gamma t/\hbar}. \tag{2.4}$$

In terms of the Møller operators, the probability of scattering from a given reactant state $|\psi_{in}^\gamma\rangle$ to a given product state $\left|\psi_{out}^{\gamma'}\right\rangle$ is given by

$$
\begin{aligned}
\mathbf{P}^{\gamma'\gamma} &= \left| \left\langle \psi_{out}^{\gamma'} \left| \mathbf{S}^{\gamma'\gamma} \right| \psi_{in}^\gamma \right\rangle \right|^2 \\
&= \left| \left\langle \psi_{out}^{\gamma'} \left| \Omega_-^{\gamma'\dagger} \Omega_+^\gamma \right| \psi_{in}^\gamma \right\rangle \right|^2 \\
&= \left| \left\langle \psi_-^{\gamma'} \left| \psi_+^\gamma \right\rangle \right|^2.
\end{aligned}
\tag{2.5}
$$

242

The states $\left|\psi_-^{\gamma'}\right\rangle = \Omega_-^{\gamma'}\left|\psi_{out}^{\gamma'}\right\rangle$ and$= \Omega_+^{\gamma}\left|\psi_{in}^{\gamma}\right\rangle$ are called Møller states.

Weeks and Tannor[1] have shown that S-matrix elements can be calculated efficiently from channel packets by a two-step process. First, two initial Gaussian wavepackets

$$\left|\psi_{in(out)}^{\gamma}\right\rangle = \int_{-\infty}^{\infty} dk_\gamma \eta_\pm\left(k_\gamma\right)\left|k_\gamma\right\rangle, \qquad (2.6)$$

are constructed at $t = 0$ (Figure 1), and propagated using the Møller operators to create the Møller states $\left|\psi_+^{\gamma}\right\rangle$ and $\left|\psi_-^{\gamma'}\right\rangle$ (Figures 2-3). The coordinate representations of the states $\left|\psi_{in}^{\gamma}\right\rangle$ and $\left|\psi_{out}^{\gamma'}\right\rangle$ are chosen to be in the interaction region of the potential at time $t = 0$, and the momentum representations are chosen to cover energies of interest while remaining positive or negative definite. The effect of the Møller operator Ω_+^{γ} on $\left|\psi_{in}^{\gamma}\right\rangle$ is to propagate the state backward in time under the asymptotic Hamiltonian $\mathbf{H}_0^{\gamma}$ until the resulting intermediate state (Figure 2) exits the interaction region, and then to propagate the intermediate state forward in time again under the full Hamiltonian (Figure 3). Similarly, the product state $\left|\psi_{out}^{\gamma'}\right\rangle$ is propagated forward in time under $\mathbf{H}_0^{\gamma'}$, and back in time under $\mathbf{H}$.

In the second part of the process, the time-dependent correlation,

$$C^{\gamma'\gamma}(t) = \left\langle\psi_-^{\gamma'}\left|e^{-i\mathbf{H}_0 t/\hbar}\right|\psi_+^{\gamma}\right\rangle, \qquad (2.7)$$

between the two Møller states is calculated as one of them continues to evolve in time. The Fourier transform $F^{\gamma'\gamma}(E)$ of the correlation function is then used to compute a set of S-matrix elements,

$$S_{\pm k_{\gamma'}',\pm k_\gamma}^{\gamma',\gamma} = \frac{\hbar^2}{2\pi}\sqrt{\frac{\left|k_{\gamma'}'\right|\left|k_\gamma\right|}{\mu_{\gamma'}\mu_\gamma}}\frac{F^{\gamma'\gamma}(E)}{\eta_-^*\left(\pm k_{\gamma'}'\right)\eta_+\left(\pm k_\gamma\right)}, \qquad (2.8)$$

relating one of the four combinations of positive and negative reactant and product momenta (Figure 4).

3. Application of the Interaction Picture

Wavepacket propagation methods which use fast Fourier transforms (FFTs) unfortunately tend to demand generously sized computational grids. Shrinking the grids through the use of the interaction picture can lead to improved efficiency.

The transformation from the Schrödinger picture to the interaction picture is

$$\left|\psi(t)\right\rangle_I = e^{i\mathbf{H}_0 t/\hbar}\left|\psi(t)\right\rangle_S, \qquad (3.1)$$

where the subscript I labels the interaction picture, and the subscript S refers to the Schrödinger picture[3]. It is seen readily from equation (3.1) that $|\psi(0)\rangle_I = |\psi(0)\rangle_S$. The interaction-picture Hamiltonian is defined as

$$\mathbf{H}_I(t) = e^{i\mathbf{H}_0 t/\hbar} \mathbf{V} e^{-i\mathbf{H}_0 t/\hbar}, \tag{3.2}$$

and the time-evolution operator is,

$$\mathbf{U}_I(t, t_0) = e^{i\mathbf{H}_0 t/\hbar} e^{-i\mathbf{H}(t, t_0)/\hbar} e^{-i\mathbf{H}_0 t_0/\hbar}, \tag{3.3}$$

where $\mathbf{H}$, $\mathbf{H}_0$, and $\mathbf{V}$ are given by equation (2.1).

Since Møller states are defined in the Schrödinger picture at time $t = 0$, they are equal to their counterparts in the interaction picture:

$$\left|\psi_\pm^\gamma\right\rangle_I = \left|\psi_\pm^\gamma\right\rangle_S. \tag{3.4}$$

The asymptotic reactant and product states are likewise invariant:

$$\left|\psi_{in(out)}^\gamma\right\rangle_I = \left|\psi_{in(out)}^\gamma\right\rangle_S. \tag{3.5}$$

Therefore, it can be shown that the Møller states are simple propagations in the interaction picture:

$$\left|\psi_\pm^\gamma\right\rangle_I = \lim_{t \to \mp\infty} \mathbf{U}_I(0, t) \left|\psi_{in(out)}^\gamma\right\rangle_I.$$

Tannor and his collaborators achieved a reduction in the number of required grid points when propagated in the interaction picture by creating "nested" interaction pictures, which optimize the grid width in coordinate and momentum space[4]. The PR-adapted interaction picture shifts the origins of both the momentum and the coordinate representations, defining the state vector,

$$|\psi\rangle_I'' = e^{i\langle\mathbf{R}\rangle\mathbf{P}_S/\hbar} e^{-i\langle\mathbf{P}\rangle\mathbf{R}_S/\hbar} e^{i\mathbf{H}_0 t/\hbar} |\psi\rangle_S, \tag{3.6}$$

where $\langle\mathbf{R}\rangle = \langle\psi|_I \mathbf{R}_I |\psi\rangle_I = \langle\psi|_S \mathbf{R}_S |\psi\rangle_S$ is the expectation value of the position operator, and $\langle\mathbf{P}\rangle$ is that of the momentum operator. The equation of motion is given by

$$i\hbar \frac{d}{dt} |\psi\rangle_I'' = \mathbf{H}'' |\psi\rangle_I'', \tag{3.7}$$

where

$$\mathbf{H}'' = e^{i\langle\mathbf{R}\rangle\mathbf{P}_S/\hbar} e^{-i\langle\mathbf{P}\rangle\mathbf{R}_S/\hbar} e^{i\mathbf{H}_0 t/\hbar} \mathbf{V}(\mathbf{R}_S) e^{-i\mathbf{H}_0 t/\hbar} e^{i\langle\mathbf{P}\rangle\mathbf{R}_S/\hbar} e^{-i\langle\mathbf{R}\rangle\mathbf{P}_S/\hbar}. \tag{3.8}$$

Wavepackets can be propagated using fewer grid points in the nested interaction picture because they remain centered on the grid.

The most accurate and reliable version of the nested interaction picture is the simplest, so-called "sequential," approach. The sequential method accepts the computational overhead of evaluating each of the component operators in (3.8) in turn, leading to computational times which may be several times longer than an equivalent Schrödinger-picture propagation in one dimension. However, the reduction in grid size is expected to lead to computational savings as the number of degrees of freedom increases.

4. Conclusion

The interaction picture has been shown to be useful for calculating S-matrix elements on reduced computational grids[4]. However, previous use of the interaction picture has been restricted to single scattering channels, limiting its application to non-reactive scattering problems[5]. In this paper, we have outlined how, through the use of the channel-packet method, the interaction picture can be used to compute reactive scattering matrix elements.

References

[1] (a) Weeks, D. E.; Tannor, D. J. *Chem. Phys. Lett.* 207, 301 (1993). (b) Weeks, D. E.; Tannor, D. J. *Chem. Phys. Lett.* 224, 451 (1994). (c) Tannor, D. J.; Weeks, D. E. *J. Chem. Phys.* 98, 3884 (1993).

[2] Leforestier, C., *et. al. J. Comput. Phys.* 94, 59 (1991).

[3] Shankar, R. *Principles of Quantum Mechanics;* Plenum: New York, p. 612 (1980).

[4] (a) Tannor, D. J.; Besprozvannaya, A.; Williams, C. J. *J. Chem. Phys.* 96, 2998 (1992). (b) Das, S.; Tannor, D. J. *J. Chem. Phys.* 92, 3403 (1990). (c) Williams, C. J.; Qian, J.; Tannor, D. J. *J. Chem. Phys.* 95, 1721 (1991).

[5] Taylor, J. R. *Scattering Theory: The Quantum Theory of Nonrelativistic Collisions;* Krieger: Malabar, FL (1987).

[6] Calfas, R., and Weeks, D. E. *Chem. Phys. Lett.* 263, 292 (1996).

Figure 1. The initial channel packets $\Psi_{in}(x)$ and $\Psi_{out}(x)$ (solid line), are the same in the interaction and Schrödinger pictures, since they are evaluated at $t = 0$. The potential (dotted line) is the sum of two Gaussian barriers, a Gaussian well, and a ramp function which is zero for $x < -4$, 0.01 for $x > 4$, and rises linearly in between.
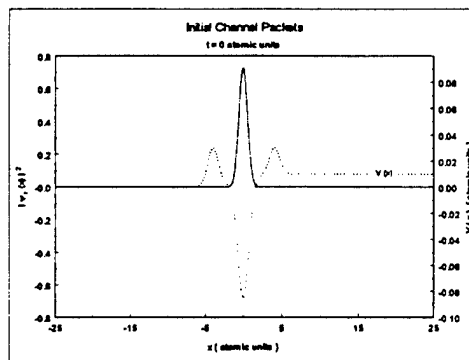

Figure 2. The reactant channel packet propagated backward in time to $t = -2000$ atomic units, and the product channel packet propagated forward in time to $t = 2000$ atomic units. Since the propagation occurs under a free-particle Hamiltonian, the wavepackets are unaffected in the interaction picture (solid line). The Schrödinger-picture packet (dashed lines) translates to the left (reactant, long dashes) or right (product, short dashes), and spreads, requiring a larger grid.
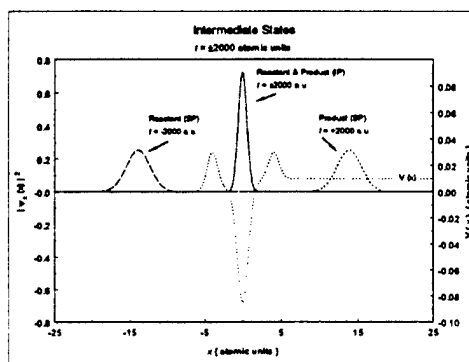

Figure 3. The reactant Møller state, $\Psi_+(x)$ (solid line), is the result of propagating the intermediate reactant state forward in time to $t = 0$, where the interaction and Schrödinger pictures are again identical. The dashed line is the product Møller state, $\Psi_-(x)$, the result of propagating the intermediate product state backward in time to $t = 0$.
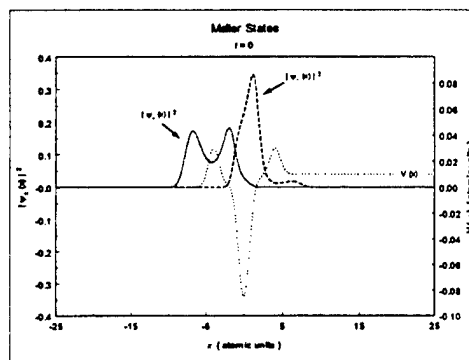

Figure 4. The transmission coefficient, computed from Møller states generated using the interaction picture (dotted line) and the Schrödinger picture (solid line). The interaction-picture S-matrix elements were computed on a grid half the size required for the Schrödinger-picture matrix elements.

246